Novel Polymerisation Approaches for Future Batteries

Holly Yeo



Magdalen College

Department of Chemistry

University of Oxford

December 2023

A thesis submitted in partial fulfilment of the requirements for the degree of Doctor of Philosophy in Chemistry

Declaration

The work described in this thesis was conducted between September 2019 and December 2023 at the University of Oxford. This is the work of the author unless otherwise stated.

The copyright of this thesis rests with the author and is made available under a Creative Commons Attribution Non-Commercial No Derivatives licence. Researchers are free to copy, distribute or transmit the thesis on the condition that they attribute it, that they do not use it for commercial purposes, and that they do not alter, transform or build-upon it. For any reuse or distribution, researchers must make clear to others the licence terms of this work.



Holly Yeo

Abstract

This thesis describes the synthesis of block copolymers featuring polycarbonates and polyesters and their optimisation and application in all-solid-state Li-ion batteries. All of the new polymers are prepared by one-pot, selective switchable polymerisation catalysis, combining lactone or cyclic carbonate ring-opening polymerisation (ROP) and epoxide/CO_2 or anhydride ring-opening copolymerisation (ROCOP) cycles using a single catalyst.

Chapter 1 provides an introduction to the role of polymers in all-solid-state batteries. Polymer binders and electrolytes are discussed; particularly, polycarbonate, polyester and block copolymer electrolytes. Switchable polymerisation catalysis to selectively produce poly(carbonate-*b*-ester)s from a one-pot monomer mixture is introduced.

Chapter 2 produces ABA- and AB-block copolymers by switch catalysis, where the 'A' block is poly(4-vinyl cyclohexene carbonate) (PvCHC) and the 'B' block is poly(ε-caprolactone-*r*-trimethylene carbonate) (P(CL-*r*-TMC). PvCHC is a 'hard' block (T_g = 106 °C) and P(CL-*r*-TMC) is soft (T_g = -56 °C). Systematic variation of polymer molar mass, composition and block structure identifies trends relating these features to Li-ion conductivity. The lead polymer is an ABA polymer with a molar mass of 50 kg mol^{-1} and an A-block weight fraction of 0.35. These trends are probed using thermal and structural information obtained from differential scanning calorimetry (DSC) and small-angle X-ray scattering (SAXS). This polymer had high Li-ion conductivity (2.2×10^{-4} S cm^{-1} at 60 °C), excellent oxidative stability (5.2 V) and compliant viscoelasticity for all-solid-state battery application. It is applied in a composite cathode comprising of single-crystal $LiNi_{0.8}Mn_{0.1}Co_{0.1}O_2$ cathodes, Li_6PS_5Cl solid electrolyte and carbon nanofibres. Compared to traditional fluorinated polymer binders, improved discharge capacities (186 mAh g^{-1}) and capacity retention (96.7% over 200 cycles) are achieved.

Chapter 3 produces a systematic series of polyester electrolytes with different functionalities by anhydride/epoxide ROCOP. The materials include polymers with both fluorinated or non-fluorinated backbones; and with oligoether side chains of varying lengths. To study the effect of a fluorinated polymer backbone, the anhydride is diglycolic anhydride (DGA) or 2,2,3,3,4,4-hexafluoropentanedioic anhydride (HFA). To study the effect of the ether side chain, epoxides featuring oligoether units of varying lengths (3, 5 or 12 CH_2CH_2O units) are used. Next, ABA block polymers are synthesised by one-pot switch catalysis, where the outer hard block is poly(dimethyltrimethylene carbonate), PDTC. The effect of these structural differences on Li-ion conductivity are studied: polymers with longer ether side chains have a higher Li-ion conductivity. The backbone fluorination has a small and inconsistent effect on Li-ion conductivity. The block copolymers generally have lower Li-ion conductivity than the polyesters. The lead block copolymer, poly(DTC-*b*-DGA-*alt*-MGE-$(PEG)_{12}$-*b*-DTC), has a Li-ion conductivity of 5.6×10^{-4} S cm^{-1} at 80 °C and an oxidative stability of 5 V.

Chapter 4 investigates an ABA poly(carbonate-*b*-ester-*b*-carbonate): poly(DTC-*b*-DGA-*alt*-AGE-*b*-DTC). The polymer is formed by switch catalysis from an anhydride/epoxide/cyclic carbonate monomer mixture, by selective and sequential DGA/ allyl glycidyl ether (AGE) ROCOP and DTC ROP. The PDTC block is hard (T_m = 109 °C) and the P(DGA-*alt*-AGE) block is soft (T_g = -14 °C). The block copolymer molar mass is varied between 4 and 19 kg mol^{-1}; PDTC weight fraction is varied between 0.2 and 0.5. Polymers with the lower PDTC weight fraction, ≈ 0.2, are approximately 5× more conductive than those with a PDTC weight fraction ≈ 0.5. The overall polymer molar mass does not have a significant effect on Li-ion conductivity in this regime. The polymer of molar mass 18 kg mol^{-1} and PDTC weight fraction of 0.2 has the highest Li-ion conductivity ($\sigma = 5.27 \times 10^{-5}$ S cm^{-1} at 70 °C). Fluorinated, sulfonated and nitrile functionalities are then incorporated into the polymer. Small

improvements in ionic conductivity are achieved with the fluorinated functionality: a ten-fold increase at 30 °C but insignificant differences at higher temperatures.

Chapter 5 outlines the key work of this thesis and suggests future work to build on this research.

Chapter 6 provides experimental details for Chapter 2−4.

Chapter 7 is an appendix that provides supplementary information, figures and data that supports the work and discussion through Chapters 2−4.

Acknowledgements

Firstly, thank you to my supervisor, Professor Charlotte Williams, for the pleasure of conducting my research in your group. It has been a privilege to be guided by you and to witness your excitement for science.

Thank you to George. Your patient support and scientific prowess has been invaluable.

The Williams' Group has been a wonderful place to work and I would like to thank everybody for the fun and for their support: Kam, Fran, Kat, Kristian, Ploy, Balu, Bonny, David, Diego, Edward, Gemma, Greg, Kate, Kira, Maddie, Mantas, Mati, Nora, Ryan and Thom. Kam, thank you for being an empathetic ear for my gripes and inanities. Ploy, I am inspired and humbled by your generosity and kindness. Thank you to the Gregory Group: Kieran, Zoé and especially Freddie, for your excellent baking.

Thank you to my dugout, of past and present; Wouter, Sandy, Víctor, Lukas, Rachel and Rosie. It has been the honour of my life to collect water for you throughout the day and I hope you will remain well-hydrated in my absence. A further thank you to Lukas for providing chewing gum and original perspectives on chemistry and life.

I have enjoyed being part of numerous outreach projects during my DPhil and I would like to thank Saskia O'Sullivan for her enthusiasm and support in pursuing these. I would also like to thank Oxford University Taekwondo School and the Cowley Road Condors Cycling Club: membership to these clubs have richly supplemented my time in Oxford.

Thank you to my family; I am emboldened by, and grateful for, your support.

List of Publications

Yeo, H., Gregory, G. L., Gao, H., Yiamsawat, K., Rees, G. J., McGuire, T., Pasta, M., Bruce, P. G., Williams, C. K., Alternatives to Fluorinated Binders: Recyclable Copolyester/Carbonate Electrolytes for High-Capacity Solid Composite Cathodes. ***(Under Review)***

Williams, C. K., Gregory, G. L., **Yeo, H.**, Bruce, P. J., Pasta, M., Polycarbonate-based di-/triblock copolymers for battery applications, UK Patent Application.

List of Abbreviations

AB	Diblock
ABA	Triblock
AGE	Allyl glycidyl ether
ASSB	All-solid-state battery
BCP	Block copolymer
BDM	1,4-Benzyl dimethanol
CL	ε-caprolactone
CNF	Carbon nanofibre
CTA	Chain transfer agent
CV	Cyclic voltammetry
d	Domain spacing
DGA	Diglycolic anhydride
DOSY	Diffusion-ordered spectroscopy
DP	Degree of polymerisation
DSC	Differential scanning calorimetry
DMTA	Dynamic thermal mechanical analysis
DTC	2,2-dimethyltrimethylene carbonate
E_a	Activation energy
EIS	Electrochemical impedance spectroscopy
G'	Storage modulus
G''	Loss modulus
HFA	Hexafluoroglutaric anhydride
LiTFSI	Lithium bis(fluorosulfonyl)imide
LSV	Linear sweep voltammetry
Me-BnOH	4-Methylbenzyl alcohol
ME_3MO	2-[(2-(2-(2-meth-oxyethoxy)ethoxy)ethoxy)methyl]oxirane
MGE	Methyl glycidyl ether
M_n	Number average molar mass
NBR	Nitrile butadiene rubber
NMC	Nickel manganese-cobalt oxide
NMC811	$LiNi_{0.8}Mn_{0.1}Co_{0.1}O_2$

NMR	Nuclear magnetic resonance
OCV	Open-circuit voltage
PBMA	Poly(benzyl methacrylate)
PC	Poly(carbonate)
PCL	Poly(ε-caprolactone)
PEG	Poly(ethylene glycol)
PEO	Poly(ethylene oxide)
PFG	Pulsed-field gradient
PO	Propylene oxide
PS	Poly(styrene)
PTFE	Poly(tetrafluoroethylene)
PTMC	Poly(trimethylene carbonate)
PvCHC	Poly(vinylcyclohexene carbonate)
PVDF	Poly(vinylidene fluoride)
$\mathbf{R_1}$	Alkyl group/chain
RI	Refractive index
ROCOP	Ring-opening copolymerisation
ROP	Ring-opening polymerization
SAXS	Small angle X-ray scattering
SBR	Styrene butadiene rubber
SEC	Size-exclusion chromatography
SLIC	Single lithium-ion conductor
SPE	Solid polymer electrolyte
$\boldsymbol{T}$	Temperature
$\boldsymbol{T_c}$	Crystallisation temperature
$\boldsymbol{T_{d,\,5\%}}$	Degradation temperature (5% mass loss)
$\boldsymbol{T_g}$	Glass-transition temperature
TGA	Thermal gravimetric analysis
$\boldsymbol{t_{Li+}}$	Lithium-ion transference number
$\boldsymbol{T_m}$	Melt temperature
TMC	Trimethylene carbonate
TTS	Time-temperature superposition
vCHO	Vinyl cyclohexene oxide

VFT	Vogel-Fulcher-Tammann
WLF	Williams-Landel-Ferry
w_{PC}	Polycarbonate weight fraction
χ	Flory-Huggins interaction parameter

List of Figures, Schemes and Tables

Chapter 1: Introduction

Figure 1.1 Illustration of a Li-ion battery during discharge.

Figure 1.2 Illustration of a composite cathode containing a polymer binder, conductive carbon and the active material

Figure 1.3 Structure of two fluorinated polymer binders: PVDF and PTFE.

Figure 1.4 Structure of non-fluorinated polymers applied as cathode binders: PAA, carboxymethyl cellulose and PFFOMB.

Figure 1.5 Structure of PEO and illustration of Li^+ solvation in PEO.

Figure 1.6 Structure of four polycarbonates studied as polymer electrolytes: PVIC, PVICOX, PEC and PPC.

Figure 1.7 Structure of three polycarbonates studied as polymer electrolytes: PTMC, PHEC and PBEC.

Figure 1.8 Structure of polyester electrolytes, PCL and P(CL-*r*-TMC).

Figure 1.9 Structure of five polyesters studied as polymer electrolytes: PEA, PBA, PHA, PE-2,4 and PE-2,10.

Figure 1.10 A series of six polyesters studied as polyester electrolytes, with systematic backbone (GA or DGA) and side chain (PO, AGE or ME_2MO) variations.

Figure 1.11 Theoretical phase diagram for a linear AB diblock copolymer and 2D illustrations of the equilibrium morphologies.

Figure 1.12 Structure of two block copolymers studied as polymer electrolytes: PS-*b*-PEO and P(BMA-*b*-CL-*r*-TMC).

Table 1.1 Li-ion conductivity of reported electrolyte materials.

Scheme 1.1 CO_2/CHO ring-opening copolymerisation (ROCOP) and CL ring-opening polymerisation (ROP) cycles accessed by a single switchable catalyst to produce block copolymers.

Figure 1.13 Illustration of the aims of this thesis: using switchable polymerisation catalysis to systematically vary polymer block structure, molar mass, composition, constituent monomers and pendant functionalities to produce

polymers for use in all-solid-state Li-ion batteries, as either a cathode binder or an electrolyte.

Chapter 2: Structural Optimisation of Poly(carbonate-*b*-ester) Electrolytes and their Application as Cathode Binders

Scheme 2.1 CO_2/CHO ring-opening copolymerization (ROCOP) and CL ring-opening polymerization (ROP) cycles accessed by a single switchable catalyst to produce block copolymers.

Figure 2.1 Structure of PvCHC-*b*-P(CL-*r*-TMC)-R_1, the polymer investigated in this project, and depiction of the three systematic series of polymers targeted.

Table 2.1 Poly(ester-*b*-carbonate)s and their compositions.

Scheme 2.2 The structure of the catalyst used in polymerisations, [LZn_2Ph_2], and its initiation with the bifunctional alcohol BDM.

Scheme 2.3 CL/TMC ring-opening polymerization (ROP) and vCHO/CO_2 ring-opening copolymerization (ROCOP) cycles accessed by a single switchable catalyst to produce triblock (ABA) or diblock (AB) block copolymers.

Scheme 2.4 Switchable polymerisation from a TMC/CL/vCHO monomer mixture to produce block copolymer poly(vCHC-*b*-CL-*r*-TMC).

Figure 2.2 Crude ^{1}H NMR spectra ($CDCl_3$) of the polymerisation process, identifying the signals used to calculate monomer conversions (labelled).

Figure 2.3 Assigned ^{1}H NMR spectrum ($CDCl_3$) of the purified polymer ABA(47, 0.30), poly(vCHC-*b*-CL-*r*-TMC-*b*-vCHC).

Figure 2.4 $^{13}C\{^1H\}$ NMR spectrum ($CDCl_3$) of poly(vCHC-*b*-CL-*r*-TMC-*b*-vCHC).

Figure 2.5 $^{13}C\{H\}$ NMR spectrum of the CL (top) and TMC (bottom) carbonyl regions of poly(vCHC-*b*-CL-*r*-TMC-*b*-vCHC) with the triads labelled.

Figure 2.6 Exemplar $^{31}P\{^1H\}$ NMR spectra ($CDCl_3$) after reaction of the polymer hydroxyl end groups with 2-chloro-4,4,5,5-tetramethyldioxaphospholone.

Figure 2.7 Exemplar DOSY NMR spectrum of ABA(47, 0.30), showing a single diffusion coefficient.

Figure 2.8 SEC traces from aliquots of the switch polymerisation of CL, TMC and vCHO, showing the growth in polymer molar mass after CL/TMC ROP

(P(CL-*r*-TMC)) and after the subsequent vCHO/CO_2 ROCOP (P(vCHC-*b*-CL-*r*-TMC-*b*-vCHC)).

Figure 2.9 DSC traces of ABA(50, 0.35), without (top) and with (bottom) 17 wt.% LiTFSI, upper and lower T_g's labelled.

Figure 2.10 Dynamic mechanical temperature analysis (DMTA) temperature sweep experiment for ABA(50, 0.35)/LiTFSI.

Figure 2.11 TGA trace for ABA(50, 0.35) polymer electrolyte with 17 wt.% LiTFSI.

Figure 2.12 SAXS data for (a) Series II ABA(M_n, 0.50) and (b) Series III ABA(50, w_{PC}) of polymer electrolytes.

Figure 2.13 Li-ion conductivity as a function of temperature, with varying LiTFSI concentrations.

Figure 2.14 DSC traces for ABA(50, 0.28) electrolytes with different LiTFSI contents.

Figure 2.15 Representative Nyquist curves, where points are the collected data and lines represent the fits to the data.

Figure 2.16 Li-ion conductivity as a function of temperature for ABA(50, 0.35)/LiTFSI, obtained by electrochemical impedance spectroscopy.

Figure 2.17 VTF fit for ABA(50, 0.35)/LiTFSI.

Figure 2.18 Top: M_n-dependence of ionic conductivity (σ) at T = 30 °C for AB vs. ABA polymers/LiTFSI at fixed w_{PC} ~0.5. Bottom: Corresponding DSC $T_{g,\,B}$ values.

Figure 2.19 (a) Hard wt. content (w_{PC}) dependence of Li-ion conductivity (σ), with M_n fixed at 50 kg mol^{-1}. (b) Corresponding SAXS data for the polymer electrolytes.

Figure 2.20 Oxidative stability vs Li metal and stainless-steel counter electrode measured by LSV at 60 °C, 0.1 mV s^{-1} scan rate, for ABA(50, 0.35) and PEO.

Figure 2.21 Oxidative stability vs Li metal and stainless-steel counter electrode measured by CV at 0.5 mV s^{-1} scan rate recorded over 35 cycles.

Figure 2.22 (a) ^{7}Li NMR spectrum of ABA(50, 0.35)/LiTFSI, showing the spectrum deconvoluted into two distinct peaks; (b) ^{7}Li NMR spectrum of PvCHC and P(CL-r-TMC) homopolymer electrolytes.

Figure 2.23 (a) ^{19}F NMR spectrum of ABA(50, 0.35)/LiTFSI, showing the spectrum deconvoluted into two distinct peaks; (b) ^{19}F NMR spectrum of PvCHC and P(CL-*r*-TMC) homopolymer electrolytes.

Figure 2.24 Diffusion coefficients of ABA(50, 0.35)/LiTFSI by ^{7}Li pulsed field NMR spectroscopy.

Figure 2.25 Diffusion coefficients of ABA(50, 0.35)/LiTFSI by ^{19}F pulsed field NMR spectroscopy.

Figure 2.26 Elastic behaviour of ABA(50, 0.35)/LiTFSI. Cyclic tensile testing (20% strain, 10 mm min^{-1} extension rate). A

Figure 2.27 Rheological data obtained for ABA(50, 0.35)/LiTFSI. (a) Storage and loss modulus as a function of temperature, conducted at a frequency of 1 Hz and a strain of 1%. (b) Time-temperature superposition (TTS) graph collated by measuring the storage and loss moduli as a function of oscillation frequency and repeating this at 10 °C intervals between 30 and 120 °C.

Figure 2.28 Electrochemical impedance plots of a Ni|PE|Li_6PS_5Cl|PE|Ni cell, at 60 °C, with one measurement recorded per hour and where PE is ABA(50, 0.35)/LiTFSI.

Figure 2.29 Fabrication of composite cathode and solid-state cell configuration, LTO| Li_6PS_5Cl |NMC-PE composite.

Figure 2.30 Specific discharge capacity vs. cycle number at T = 60 °C, 1 MPa stack pressure.

Figure 2.31 Initial discharge capacity, and capacity retention after 200 cycles.

Figure 2.32 Charge-discharge profiles for the LTO|Li_6PS_5Cl|NMC-PE cell where PE is ABA(50, 0.35)/LiFSI, at cycle numbers 1, 50, 100, 150 and 200.

Figure 2.33 Potential vs. capacity at cycle 1 for the LTO| Li_6PS_5Cl |NMC-PE cell, where PE is either ABA(50,0.35)/LiFSI, ABA(50,0.35)/LiTFSI or PTFE.

Chapter 3: Investigation of Block Copolymers with Fluorinated and PEG-ylated Functionalities.

Figure 3.1	The epoxides, anhydrides and cyclic carbonate to be polymerised in this study
Scheme 3.1	Anhydride/epoxide ROCOP, conducted at 100 °C under an anaerobic atmosphere
Table 3.1	Polyester characterisation data
Figure 3.2	^{1}H NMR spectra ($CDCl_3$, 500 MHz) from aliquots of DGA/ME_3MO ROCOP
Figure 3.3	SEC data from aliquots of DGA/ME_3MO ROCOP
Figure 3.4	Growth in polymer molar mass and change in dispersity index *Đ*, recorded by SEC, with increasing DGA conversion
Figure 3.5	Assigned ^{1}H NMR spectrum ($CDCl_3$, 500 MHz) of the purified polymer, poly(DGA-*alt*-ME_3MO)
Figure 3.6	SEC trace for the purified polymer poly(DGA-*alt*-ME_3MO)
Figure 3.7	^{19}F NMR spectra ($CDCl_3$, 500 MHz) from aliquots of HFA/ME_3MO ROCOP
Figure 3.8	DSC data for polyesters as listed in Table 3.1
Figure 3.9	DSC data for polyester electrolytes as listed in Table 3.1
Table 3.2	Polyester electrolyte VFT parameters and thermal data
Figure 3.10	Li-ion conductivity as a function of temperature for the polyester electrolytes
Table 3.3	Polyester electrolyte Li-ion conductivity
Figure 3.11	VFT fit for poly(DGA-*alt*-ME_3MO) polymer electrolyte
Scheme 3.2	Polymerisation of anhydride, epoxide, and DTC via switch catalysis
Table 3.4	Block copolymer characterisation data
Figure 3.12	^{1}H NMR spectra ($CDCl_3$, 500 MHz) from aliquots of DGA/ME_3MO/DTC copolymerisation
Figure 3.13	^{1}H NMR spectra ($CDCl_3$, 500 MHz) from aliquots of HFA/ME_3MO/DTC copolymerisation
Figure 3.14	^{19}F NMR spectra ($CDCl_3$, 500 MHz) from aliquots of HFA/ME_3MO/DTC copolymerisation

Figure 3.15 In-situ ATR-IR spectroscopy monitoring the switchable polymerisation catalysis of HFA, ME_3MO and DTC, catalysed by P_2-*t*-Bu, illustrating firstly HFA/ME_3MO ROCOP, followed by DTC ROP after 1 h

Scheme 3.3 Ring-opening copolymerization (ROCOP) and ring-opening polymerization (ROP) cycles accessed by a single switchable catalyst to produce block copolymers

Figure 3.16 SEC traces from aliquots of the switch polymerisation of DGA, ME_3MO, and DTC

Figure 3.17 Assigned ^{1}H NMR spectrum of poly(DTC-*b*-DGA-*alt*-ME_3MO-*b*-DTC)

Figure 3.18 Assigned $^{13}C\{H\}$ NMR spectrum of poly(DTC-*b*-DGA-*alt*-ME_3MO-*b*-DTC)

Figure 3.19 SEC trace for the purified polymer poly(DTC-*b*-DGA-*alt*-ME_3MO-*b*-DTC)

Figure 3.20 ^{1}H DOSY NMR spectrum of poly(DTC-*b*-DGA-*alt*-ME_3MO-*b*-DTC

Figure 3.21 $^{31}P\{H\}$ NMR spectra ($CDCl_3$) after reaction of the polymer hydroxyl end groups with 2-chloro-4,4,5,5-tetramethyldioxaphospholone

Figure 3.22 DSC data for block copolymers as listed in Table 3.2

Figure 3.23 DSC data for block copolymers electrolytes as listed in Table 3.3

Table 3.5 Block copolymer electrolyte VFT parameters and thermal data

Table 3.6 Li-ion conductivity and VTF parameter data for block copolymer electrolytes

Figure 3.24 Nyquist curves generated from the electrochemical impedance spectroscopy of poly(DTC-*b*-DGA-*alt*-ME_3MO-*b*-DTC)

Figure 3.25 Li-ion conductivity as a function of temperature for the block copolymer electrolytes

Figure 3.26 VFT fit of the temperature dependence of Li-ion conductivity for poly(DTC-*b*-DGA-*alt*-ME_3MO-*b*-DTC)

Figure 3.27 Oxidative stability of poly(DTC-*b*-DGA-*alt*-MGE-$(PEG)_{12}$-*b*-DTC) and poly(DTC-*b*-HFA-*alt*-MGE-$(PEG)_{12}$-*b*-DTC)

Chapter 4: ABA Triblock Polymers from Anhydride, Epoxide and Cyclic Carbonate: Properties and Modifications for Battery Applications.

Scheme 4.1	Ring-opening copolymerisation (ROCOP) and ring-opening polymerisation (ROP) cycles accessed by a single switchable catalyst to produce block copolymers.
Figure 4.1	Catalysts tested for DGA/AGE ROCOP and DTC ROP.
Table 4.1	Reaction conditions for the catalyst testing of DGA/AGE ROCOP.
Figure 4.2	^{1}H NMR spectra ($CDCl_3$, 500 MHz) from aliquots of DGA/AGE ROCOP.
Table 4.2	Reaction conditions for catalyst screening of DTC ROP.
Figure 4.3	^{1}H NMR spectra ($CDCl_3$, 500 MHz) from aliquots of DTC ROP.
Scheme 4.2	Polymerisation of DGA, AGE, and DTC via switch catalysis.
Scheme 4.3	Ring-opening copolymerisation (ROCOP) and ring-opening polymerisation (ROP) cycles accessed by a single switchable catalyst to produce block copolymers.
Figure 4.4	In-situ ATR-IR spectroscopy monitoring the switch polymerisation of DGA, AGE, and DTC.
Figure 4.5	^{1}H NMR spectra ($CDCl_3$, 500 MHz) from aliquots of the copolymerisation of DGA, AGE and DTC.
Figure 4.6	SEC traces from aliquots of the copolymerisation of DGA, AGE, and DTC.
Figure 4.7	^{13}C{H} NMR spectrum ($CDCl_3$, 500 MHz) of poly(DTC-*b*-AGE-*alt*-DGA-*b*-DTC).
Figure 4.8	DOSY NMR spectrum of poly(DTC-*b*-DGA-*alt*-AGE-*b*-DTC).
Table 4.3	Overview of the poly(DTC-*b*-DGA-*alt*-AGE-*b*-DTC) characterisation data.
Figure 4.9	Exemplar assigned ^{1}H NMR spectrum of the purified polymer, poly(DTC-*b*-DGA-*alt*-AGE-*b*-DTC), ABA(18, 0.20).
Table 4.4	Overview of the poly(DTC-*b*-DGA-*alt*-AGE-*b*-DTC) thermal data.
Figure 4.10	DSC data for ABA(18, 0.20) and its polymer electrolyte.
Figure 4.11	TGA data for ABA(18, 0.20) and its polymer electrolyte.
Table 4.5	Ionic conductivity data for the polymer electrolytes.
Figure 4.12	Li-ion conductivity as a function of temperature for the poly(DTC-*b*-DGA-*alt*-AGE-*b*-DTC) electrolytes.

Figure 4.13 VFT fit for ABA(18, 0.20) polymer electrolyte.

Figure 4.14 DSC data for poly(DTC-*b*-DGA-*alt*-AGE-*b*-DTC), before and after the diisocyanate coupling reaction.

Figure 4.15 TGA data for poly(DTC-*b*-DGA-*alt*-AGE-*b*-DTC), before and after the diisocyanate coupling reaction.

Scheme 4.4 General reaction mechanism for thiol-ene addition reactions.

Scheme 4.5 Functionalisation of P(DTC-*b*-DGA-*alt*-AGE-*b*-DTC).

Figure 4.16 ^{1}H NMR spectra of poly(DTC-*b*-DGA-*alt*-AGE-*b*-DTC), before and after functionalisation at the vinyl group.

Table 4.6 Characterisation data for functionalised poly(DTC-*b*-DGA-*alt*-AGE-*b*-DTC).

Table 4.7 Thermal-Mechanical and Li-ion conductivity data for poly(DTC-*b*-DGA-*alt*-AGE-*b*-DTC), before and after functionalisation.

Figure 4.17 DSC traces for unfunctionalised (vinyl) and functionalised (CF_3, nitrile, and sulfone) polymer electrolytes.

Figure 4.18 TGA data for the unfunctionalised (vinyl) and functionalised (CF_3, nitrile and sulfone) polymer electrolytes.

Figure 4.19 Storage moduli G' at 30 °C and 70 °C; and the T_g's, for the unfunctionalised (vinyl) and functionalised (CF_3, nitrile, sulfone) polymer electrolytes.

Figure 4.20 Li-ion conductivity as a function of temperature for the unfunctionalised (vinyl) and functionalised (CF_3, nitrile, sulfone) polymers.

Chapter 5: Outlook.

Figure 5.1 Strategies for producing new polymers for battery applications.

Figure 5.2 Strategies for producing new solid electrolytes for battery applications.

Chapter 6: Experimental.

Figure 6.1 Structure of LH_2 and $[LZn_2Ph_2]$.

Figure 6.2 Structure of $L_{van}AlOAc$ and $[L_{van}AlK(OAc)_2]$.

Figure 6.3 Structure of PvCHC-*b*-P(CL-*r*-TMC)-R_1.

Table 6.1 Reagent quantities for the synthesis of PvCHC-*b*-(CL-*r*-TMC)(-*b*-PvCHC).
Table 6.2 Characterisation Data for PvCHC-*b*-(CL-*r*-TMC)(-*b*-PvCHC).
Figure 6.4 Structure of P(DGA-*alt*-ME_3MO),
Figure 6.5 Structure of P(HFA-*alt*-ME_3MO),
Table 6.3 Reaction Conditions for the Polyesters Synthesised in Chapter 3.
Table 6.4 Characterisation Data for the Polyesters Synthesised in Chapter 3.
Figure 6.6 Structure of PDTC-*b*-P(DGA-*alt*-ME_3MO)-*b*-PDTC,
Figure 6.7 Structure of PDTC-*b*-P(HFA-*alt*-ME_3MO)-*b*-PDTC
Table 6.5 Reaction Conditions for the Synthesis of the Block Copolymers in Chapter 3.
Table 6.6 Characterisation Data for the Block Copolymers Synthesised in Chapter 3.
Figure 6.8 Structure of PDTC-*b*-P(AGE-*alt*-DGA)-*b*-PDTC,
Table 6.7 Reagent Quantities for the Synthesis of P(DTC-*b*-DGA-*alt*-AGE-*b*-DTC).
Table 6.8 Characterisation Data for P(DTC-*b*-DGA-*alt*-AGE-*b*-DTC).
Figure 6.9 Structure of PDTC-*b*-P(AGE-*alt*-DGA)-*b*-PDTC with CF_3, nitrile, and sulfone functionalities incorporated.

Table of Contents

	Declaration	2
	Abstract	3
	Acknowledgements	6
	List of Publications	7
	List of Abbreviations	8
	List of Figures, Schemes and Tables	11

Chapter 1: Introduction

1.1.	Li-ion Batteries	25
1.2.	Polymers in Batteries	27
1.2.1.	Polymer Binders	27
1.2.1.1.	Fluorinated Binders	28
1.2.1.2.	Non-fluorinated Binders	29
1.2.2.	Polymer Electrolytes	30
1.2.2.1.	Polyether Electrolytes	31
1.2.2.2.	Polycarbonate Electrolytes	33
1.2.2.3.	Polyester Electrolytes	36
1.2.2.4.	Block Copolymer Electrolytes	39
1.3.	Ring-Opening Polymerisation and Ring-Opening Copolymerisation	43
1.4.	Switch Catalysis	44
1.5.	Aims and Objectives	47
1.6.	References	50

Chapter 2: Structural Optimisation of Poly(carbonate-*b*-ester) Electrolytes and their Application as Cathode Binders

2.1.	Introduction	58
2.2.	Aims	62
2.3.	Polymer Optimisation	62
2.3.1.	Polymer Synthesis	62
2.3.2.	Polymer Characterisation	68
2.3.3.	Thermal Properties	74
2.3.4.	Small Angle X-Ray Scattering	78
2.3.5.	Li-ion conductivity	80
2.4.	Polymer Electrolyte Properties	87
2.4.1.	Electrochemical Properties	87
2.4.1.1.	Oxidative Stability	87
2.4.1.2.	Li-ion Transference Number	90
2.4.2.	Mechanical Properties	94
2.4.2.1.	Elastic Recovery	94
2.4.2.2.	Rheology	98
2.5.	Cell Performance	98
2.5.1.	Chemical Stability	95
2.5.2.	Cell Cycling	99
2.6.	Conclusions and Future Work	103
2.7.	References	105

Chapter 3: Investigation of Block Copolymers with Fluorinated and PEG-ylated Functionalities.

3.1. Introduction 110
3.2. Aims 112
3.3. Anhydride/Epoxide ROCOP to Produce Fluorinated and PEG-ylated Polyesters 113
3.3.1. Polymer Synthesis and Characterisation 113
3.3.2. Polyester Electrolyte Properties 122
3.4. Switchable Polymerisation of Anhydride/Epoxide/Cyclic Carbonate to Produce Fluorinated and PEG-ylated Block Copolymers 127
3.4.1. Synthesis and Characterisation 127
3.4.2. Block Copolymer Electrolyte Properties 143
3.5. Conclusions and Further Work 153
3.6. References 155

Chapter 4: ABA Triblock Polymers from Anhydride, Epoxide and Cyclic Carbonate: Properties and Modifications for Battery Applications.
4.1. Introduction 159
4.2. Aims 162
4.3. Anhydride/Epoxide/Cyclic Carbonate-based Polymers: Synthesis and Characterisation. 163
4.3.1. Catalyst Testing for ROCOP and ROP 163
4.3.2. Poly(DTC-*b*-DGA-*alt*-AGE-*b*-DTC) by Switch Catalysis. 168
4.4. Polymer Composition Optimisation 176
4.4.1. Synthesis and Characterisation 176
4.4.2. Polymer Thermal Properties 178
4.4.3. Li-ion Conductivity 182

4.5. Polymer Modification 184
4.5.1. Polymer Cross-Linking 184
4.5.2. Polymer Post-Functionalisation 188
4.5.2.1. Functionalised Polymer Synthesis and Characterisation 189
4.5.2.2. Functionalised Polymer Thermal-Mechanical Properties 192
4.5.2.3. Li-ion Conductivity of the Functionalised Polymers 195
4.6. Conclusions and Further Work 197
4.7. References 199

Chapter 5: Outlook.

5.1. Thesis Summary 203
5.2. Outlook 204
5.3. References 208

Chapter 6: Experimental.

6.1. General 211
6.2. Experimental Procedures 212
6.3. Analytical Techniques 225

Chapter 7: Appendices.

7.1. Chapter 2 230
7.2. Chapter 3 235
7.3. Chapter 4 247

CHAPTER 1

Introduction

1.1. Li-ion Batteries

In 2019, John Goodenough, Stanley Whittingham and Akira Yoshino won the Nobel Prize in Chemistry for the development of the lithium-ion battery. The battery consists of an electrolyte which separates two electrodes: the anode and cathode (Figure 1.1). Their role is to store and release lithium ions. Whittingham produced the first battery driven by lithium ions; the $LiCoO_2$ cathode was proposed by Goodenough in 1980 and was used in the first commercialised lithium-ion battery. Yoshino applied a carbon anode which then formed the prototype for current Li-ion batteries.[1] The electrolyte is usually comprised of a salt and an organic liquid carbonate (typically $LiPF_6$ and ethylene carbonate) and it facilitates ion transport between the electrodes. During discharge, the anode releases lithium ions that move through the electrolyte and into the cathode. The electric current flows via an external circuit. During charge, this process occurs in reverse.[2]

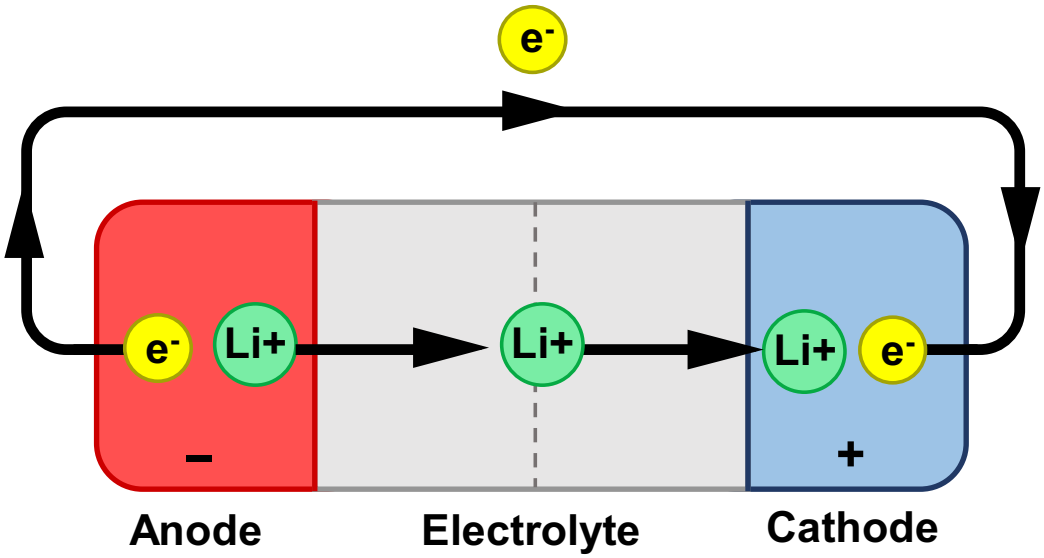


Figure 1.1. Simplified illustration of a Li-ion battery during discharge. Dashed line represents the separator.

The lithium-ion battery remains in favour due to its high energy density, low self-discharge rates, long-term cyclabilities and fast charging speed.[3] Other battery chemistries are the subject of academic research, such as Na-ion and K-ion. They are more abundant in the Earth's crust (2.3 and 1.5 wt%, compared to 0.0017 wt% for Li) and they are cheaper than lithium.[4] The larger size of these anions presents challenges: volume change on cycling and ion diffusivity are both negatively affected; and they suffer from intrinsically lower energy density.[4, 5]

There is demand for advanced Li-ion batteries with higher capacity and improved safety features. This is largely due to electric vehicles and large-scale energy storage: from 2035, all new cars and vans sold in the EU must have net-zero CO_2 emissions; from 2050, the EU aims to have net-zero greenhouse gas emissions.[6, 7]

To achieve these aims, all-solid-state batteries (ASSBs) should be developed: these use solid-state electrolytes that potentially allow use with high-capacity electrodes.[8] Li-metal anodes have an extremely high theoretical specific capacity – the amount of electricity that can be produced per gram of the active material, assuming 100% conversion – but have increased propensity for Li dendrite growth, causing short-circuiting and fires.[9] They are not used in current commercial Li-ion batteries. Li metal can be used with a solid-state electrolyte, such as Li_6PS_5Cl; this strategy can improve safety by impeding dendrite growth and replacing the highly flammable liquid electrolyte in the battery.[10, 11] However, it is challenging to maintain the appropriate interfacial contact between the solid electrolyte and the electrodes.[12] On the cathode side, high-capacity cathodes are also sought, such as nickel-rich manganese-cobalt oxides (NMC). Cobalt is a scarce resource thus it is desirable to decrease the cathode's cobalt content, to enhance sustainability.[13] However, these cathodes undergo volume change (6 vol.%) on cycling, causing contact loss and capacity fade.[14] The issue of maintaining interfacial contact and improving capacity retention in all-solid-state batteries can be resolved by

incorporating functional polymers into the battery: as an electrolyte or as a cathode binder material.

1.2. Polymers in Batteries

1.2.1. Polymer Binders

In lithium-ion batteries, the cathode consists of the active cathode material, plus conductive additives (carbon black) on a current collector to facilitate electron transport to the external circuit. A polymer binder is used to bind these components together and to improve processability (Figure 1.2).[15] The binder enables a homogenous distribution of the cathode components, facilitates Li-ion transport and provides mechanical integrity.[16] Whilst binders typically comprise just 2 – 5 mass% of the cathode composite, they have a significant impact on battery performance.

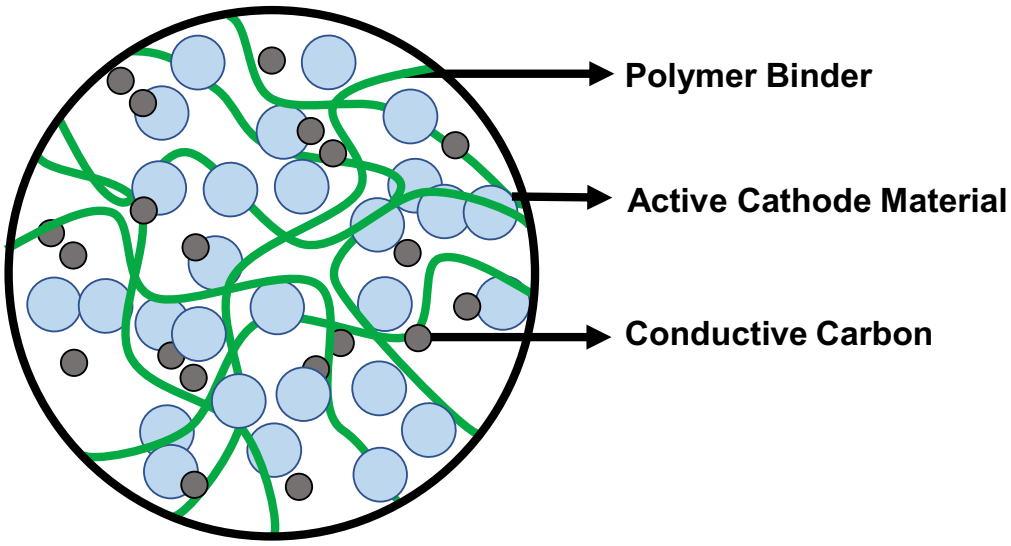


Figure 1.2. Illustration of a composite cathode containing a polymer binder, conductive carbon and the active material.

Practically, the capacity of $LiCoO_2$ is around 140 $mAhg^{-1}$. Alternative $LiMO_2$ cathodes, where M is a metal, have been investigated, such as $LiNi_{0.8}Mn_{0.1}Co_{0.1}O_2$, which show superior

capacity (200 mAh g^{-1}).[17] However, it undergoes significant structural changes during cycling; this can result in delamination, cracking and contact loss in the cathode, lowering its capacity.[14, 18] New polymer binders are proposed to overcome these issues.[16] To maintain excellent interfacial contact, binders should be elastomeric and adhesive; to enable compatibility with high-performance electrodes and solid state electrolytes, they should have high electrochemical, chemical and thermal stability; to maximise energy density, they should be ionically conductive.[16] Additional factors to consider include their cost, ease of manufacture and environmental impact.

1.2.1.1. Fluorinated Binders

Polyvinylidene fluoride (PVDF) is widely used as a cathode binder due to its electrochemical stability (Figure 1.3).[19] Its binding arises through weak van der Waals forces, so its adhesion strength is poor. Consequently, with new, high capacity cathodes, fracture and delamination occurs, resulting in capacity fade.[20] Fluorinated polymer binders have been modified to improve their performance.[16] Crosslinking the terpolymer poly(vinylidene fluoride-tetrafluroethylene-propylene) significantly improved its mechanical performance: it showed 150% strain before breaking, compared to 5% for PVDF.[21] Using non-conductive components in a battery, like poly(tetrafluoroethylene) (PTFE) and PVDF limits its capacity; chemically modifying PTFE with ionomeric groups resulted in a 20% capacity gain, compared to unmodified PTFE.[22]

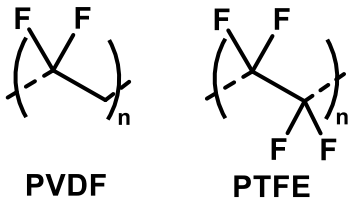


Figure 1.3. Structure of two fluorinated polymer binders: PVDF and PTFE.

However, fluorinated polymers present issues at end-of-life, as the binders are either burned or buried when discarded.[19] This can release hydrofluoric acid or organic fluorine compounds into the environment.[23] These are known as 'forever chemicals' which cause persistent pollution. Consequently, the European Chemicals Agency have recommended that many fluorinated substances are banned; non-fluorinated alternatives are sought.[24]

1.2.1.2. Non-fluorinated Binders

Elastomeric binders can mitigate electrode volume changes that occur during battery charge/discharge cycles.[25] Styrene butadiene rubber (SBR) and nitrile butadiene rubber (NBR) are commercial rubbers which have been applied as cathode binders but they have low polarity and are insufficiently adhesive; they form unstable interfaces and experience contact loss.[26] SBR was functionalised with carboxylic acid groups; this made the binder 1.4× more adhesive and produced a cell with 20% greater capacity retention.[27] An elasticomeric, Li-ion conductive polymer with covalent and dynamic hydrogen bonding crosslinks combined mechanical resilience with room temperature Li-ion conductivity, and was incorporated into an all-solid-state battery which achieved 94% capacity retention after 100 cycles.[28]

Bio-based polymers have been studied as cathode binders due to their high density of functional groups, which can improve adhesion.[15, 16] Alginate, cellulose, chitosan, guar gum, gelatin and xanthan gum binders have all exhibited comparable or improved performance

compared to PVDF (Figure 1.4).[29-34] Naturally-occurring sodium alginate was functionalised with 3,4-propylenedioxythiophene-2,5-dicarboxylic acid (ProDOT) to form the multifunctional binder SA-ProDOT. The carboxyl, hydroxyl, and ester functional groups improved the binding ability and helped to maintain electrode integrity on cycling; the conjugated backbone was electronically conductive, thus conductive additives were not required. This enabled an initial discharge capacity of 163 mAh g^{-1}, compared to 130 mAh g^{-1} for SA and 145 mAh g^{-1} for PVDF.[35]

The performance of a high-capacity cathode composite, using $LiNi_{0.8}Mn_{0.1}Co_{0.1}O_2$ (NMC811) active material, was improved when the PVDF binder was replaced with a polyimide binder with fluorinated and carboxylic acid functionalities; improved adhesion of the binder to the cathode particles was achieved due to its carboxylate groups.[36] Li and coworkers compared the use of poly(acrylic acid) (PAA) and PVDF binders with $LiMn_2O_4$ cathodes; PAA's adhesion strength was 10× greater than PVDF's (Figure 1.4). Consequently, the capacity retention of $LiMn_2O_4$ cathodes with the PAA binder was 87% after 200 cycles, compared to 75% PVDF.[37] Similarly, an electronically conductive polyfluorene binder with alcohol functionalities exhibited strong adhesion; used in a battery, it showed 88% capacity retention after 100 cycles, compared to 64% for a similar binder without alcohol groups.[38]

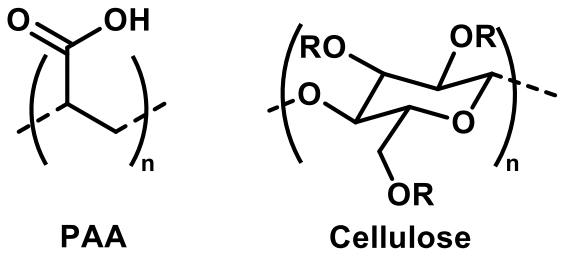


Figure 1.4. Structures of some leading non-fluorinated polymers applied as cathode binders: PAA and carboxymethyl cellulose.

1.2.2. Polymer Electrolytes

Electrolytes for Li-ion batteries should meet the following performance requirements: high ionic conductivity (10^{-2} – 10^{-3} S cm^{-1}); a Li-ion transference number (t_{Li+}, ratio of Li^+ migration to total ion migration) close to unity; wide electrochemical stability window (> 4.5 V); good chemical and thermal stability.[39, 40] This will enable effective Li-ion transport between the electrodes.

Liquid electrolytes are insufficiently electrochemically stable for use with high-capacity electrodes; they pose safety risks due to their flammability; and they have a limited lifetime due to the inherent reactivity of liquids.[12] Solid-state electrolytes could solve these issues. They can be broadly categorised as inorganic or polymeric. Sulfide-based inorganic electrolytes, such as Li_6PS_5Cl, have excellent conductivity ($2 – 5 \times 10^{-3}$ S cm^{-1} at ambient temperature) but face issues with contact loss during cycling.[41, 42] Whilst this can be overcome by cycling at high pressures (50 MPa), this is impractical for most applications.[43]

Where inorganic electrolytes fail, polymer electrolytes largely succeed. Polymer electrolytes have enhanced resistance to variations in electrode volume and improved processability and flexibility. They can be a dry solid or gel: dry solid polymer electrolytes (SPEs) are a mixture of polymer and salt, whereas gel incorporates plasticiser or solvent into the polymer matrix.[39] Gels often have better ionic conductivity but they can have poorer mechanical properties and involves the use of liquid.[39]

1.2.2.1. Polyether Electrolytes

Ionic conductivity in alkali salt complexes of poly(ethylene oxide) (PEO) was first reported by Fenton and coworkers in 1973.[44] Armand suggested that PEO could be used as an

electrolyte and it has since been extensively studied.[45] PEO has a flexible backbone, and its ether oxygens are able to coordinate Li-ions (Figure 1.5). Above its T_g (-60 °C), local segmental motion creates free volume around the chain segment and enables ion movement via a hopping mechanism.[46] Ion conduction is thus described as being coupled to the segmental motion of the polymer chains. It has high ionic conductivity at elevated temperatures (10^{-3} – 10^{-4} S cm^{-1} at 70 °C) and is processable.[46] However, a key limitation of PEO is its low room temperature conductivity (≈10^{-8} S cm^{-1} at 25 °C). PEO is semicrystalline but only the amorphous regions significantly contribute to ion conduction as the crystalline phase has a high energy barrier to Li^+ motion.[46, 47]

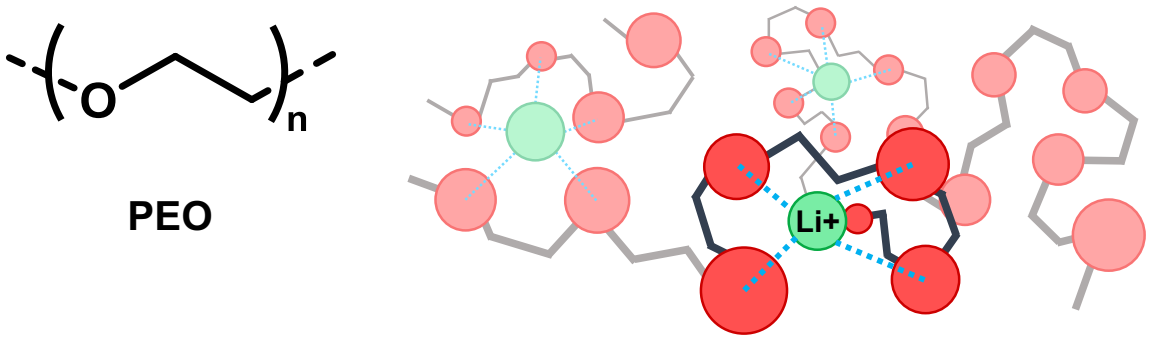


Figure 1.5. Structure of PEO (left) and illustration of Li^+ solvation in PEO (right).

Various approaches for inhibiting PEO's crystallinity, and thus improving its ionic conductivity, have been investigated: copolymerisation with glycidyl ethers; alternative polyether matrices such as polypropylene oxide and poly[bis(methoxy-ethoxy-ethoxy)phosphazene]; incorporation of plasticisers; polymer-in-salts (> 50 wt% salt); and producing organised polyether-type electrolytes with anisotropic conduction pathways.[3, 48-51] Regardless of any improvements to ionic conductivity, polyethers have sub-optimal electrochemical properties. They are generally unstable above 3.9 V, making them incompatible with high-voltage cathodes and restricting energy density, and their mechanical properties, such as elasticity and adhesion, are not optimal for mitigating cathode volume

change.[58] Their t_{Li+} is typically below 0.2 and this results in ion migration towards the anode, causing concentration polarisation and conductivity decay.[52] Carbonyl-coordinating polymer electrolytes, like polycarbonates and polyesters, could surpass these limitations.

1.2.2.2. Polycarbonate Electrolytes

Traditional Li-ion battery electrolytes are liquid carbonates, such as ethylene carbonate, vinylene carbonate and dimethyl carbonate.[53] Polycarbonates are thus an intuitive choice for solid polymer electrolytes: they are the linear polymerised version of these liquid electrolytes so are proposed to coordinate and conduct Li-ions similarly.[54]

Solvation in polycarbonates is mostly by the carbonyl oxygen; it binds to Li^+ less strongly than PEO, resulting in faster decoupling and Li-ion transport.[18] Carbonyl-coordinating SPEs typically have an oxidation onset of 4.5 – 5 V and they have an enhanced Li salt dissociation ability, translating to high t_{Li+} (> 0.5) and better battery performance.[55, 56] Aliphatic polycarbonates are preferred as aromatic moieties increase T_g thus restrict ion migration.[55]

Poly(vinylene carbonate) (PVIC) and poly(1,3-dioxolan-2-one-4,5-diyl oxalate) (PVICOX) were among the first polycarbonates investigated as polymer electrolytes (Figure 1.6). Despite their crystallinity, they achieved a room-temperature ionic conductivity of 10^{-6} and 10^{-4} S cm^{-1}, respectively; PVICOX had higher conductivity due to its larger free volume, despite having a higher T_g than PVIC. This indicated that the conductivity could be partially decoupled from polymer chain segmental motion.[57] The conductivity of PVIC was increased by copolymerising vinylene carbonate with vinyl ether. By varying the length of the oligoether chain, copolymers with T_g values between -60 and +11 °C were accessed.[58] Conductivity increased with increasing length of the oligoether side chain, to a maximum of 1.2×10^{-4} S cm^{-1}, consistent with their lower T_g facilitating Li-ion transport.

Polyethylene carbonate (PEC) is one of the simplest polycarbonates but it only has acceptable ionic conductivity in combination with an ionic liquid (2×10^{-5} S cm^{-1} at 90 °C) or at very high salt loadings (4.7×10^{-4} S cm^{-1} at 20 °C with 80 wt% LiTFSI) (Figure 1.6).[59, 60] However, at these high salt concentrations mechanical robustness is lost and a reinforcing matrix is required to produce a solid electrolyte. Tominaga and coworkers synthesised a series of PECs with modified side groups.[61] This included rigid and flexible groups, and those with hydrocarbon, ether and aromatic functionalities. Rigid side groups impeded backbone free movement, resulting in a high T_g and low conductivity: with a phenyl side group, T_g = 45 °C and $\sigma = 10^{-8}$ S cm^{-1} at 80 °C. The highest conductivity (2.2×10^{-6} S cm^{-1} at 30 °C, T_g = -33 °C) was achieved with a methoxyethyl side group due to its facile segmental motion.[62, 63]

Polypropylene carbonate (PPC) is amorphous and at a low M_n, it has a low T_g (5 °C) which results in high flexibility and insufficient mechanical strength for battery applications (Figure 1.6).[64] This can be overcome with PPC composites; a PEO/PPC blend had improved mechanical properties with good ionic conductivity (6.8×10^{-5} S cm^{-1} at 25 °C). A PPC/polybutadiene rubber (BR) cross-linked network, with a polyethylene glycol (PEG) plasticiser, had high ionic conductivity (1.3×10^{-3} S cm^{-1} at 25 °C) and mechanical integrity. Cellulose-reinforced PPC had an ionic conductivity of 3.0×10^{-4} S cm^{-1}, at 20 °C.[65-67] A PPC-based copolymer was produced by the terpolymerisation of CO_2, propylene oxide (PO) and allyl glycidyl ether (AGE), yielding poly(propylene carbonate-*ran*-allyl glycidyl ether carbonate) (PPCAGE). This copolymer was functionalised, via its pendant vinyl groups, to produce a single lithium-ion conducting polymer electrolyte. The material featured tethered anions, thus only the Li^+ should be responsible for ion transport and t_{Li+} was able to approach unity. The resulting electrolyte had an ionic conductivity of 1.6×10^{-4} S cm^{-1} at 80 °C, had good electrochemical stability (4.3 V), and a high t_{Li+} (0.86).[68]

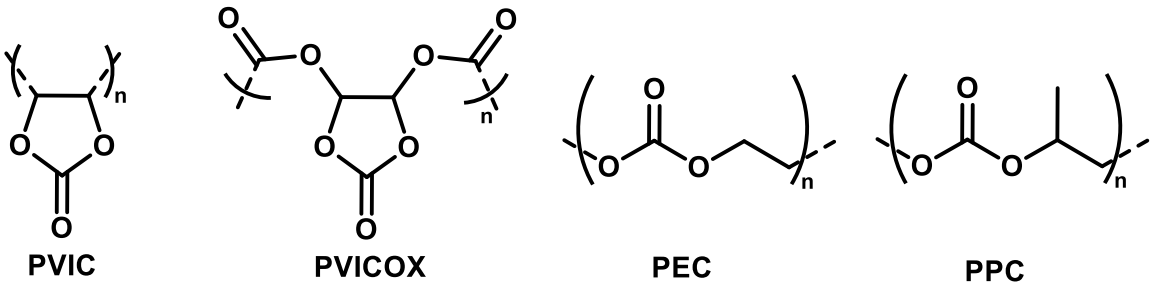


Figure 1.6. Structure of four polycarbonates studied as polymer electrolytes: PVIC, PVICOX, PEC and PPC.

Polytrimethylene carbonate (PTMC) has a lower T_g than PEC (-15 °C vs 13 °C) and has an amorphous structure (Figure 1.7).[53] It is widely studied in the biomedical field due to its biodegradability and biocompatibility. It has low room temperature conductivity (10^{-8} S cm^{-1}), however, it has a high t_{Li+} (up to a maximum of 0.8) and good electrochemical stability (4.5 – 5 V).[69] By randomly copolymerising TMC and CL, in a 3/2 ratio, its ionic conductivity was increased to 7.9 × 10^{-7} S cm^{-1}, at 25 °C. PCL has a lower T_g (-60 °C), thus, the random copolymer showed enhanced chain mobility (T_g = -26 °C).[70]

Brandell and coworkers studied numerous PTMC-based polymers, with pendant side groups, to observe how they affected Li-ion conductivity.[71-73] PTMC was functionalised with allyl-ether side groups and cross-linked to improve its mechanical stability. The ionic conductivity was enhanced (4.3 × 10^{-7} S cm^{-1} at 25 °C) which was attributed to the allyl ether groups' plasticising effect (T_g = - 20 °C).[71] However, a TMC-based copolymer featuring both pendant allyl-ether and heptyl ether groups (PHEC-*co*-PAEC) had poor ionic conductivity (10^{-7} – 10^{-8} S cm^{-1}) despite its low T_g (-49°C). The long and bulky heptyl ether side chains were proposed to hinder ion movement.[72, 73] This was further studied by molecular dynamics simulations, comparing PTMC, poly(2-butyl-2-ethyltrimethylene carbonate) (PBEC) and poly(2-heptyloxymethyl-2-ethyltrimethylene carbonate) (PHEC): whilst the polymers with longer alkyl side chains, PBEC and PHEC, had lower T_g values, they also had lower Li-ion

conductivity as their long alkyl chains restricted Li^+ motion (Figure 1.7). PTMC had more interchain Li^+ coordination, better conduction pathways and faster Li^+ transport, reflected by the residence time of Li^+ coordinated to a PTMC carbonyl group being three times shorter than with PBEC and PHEC.[68]

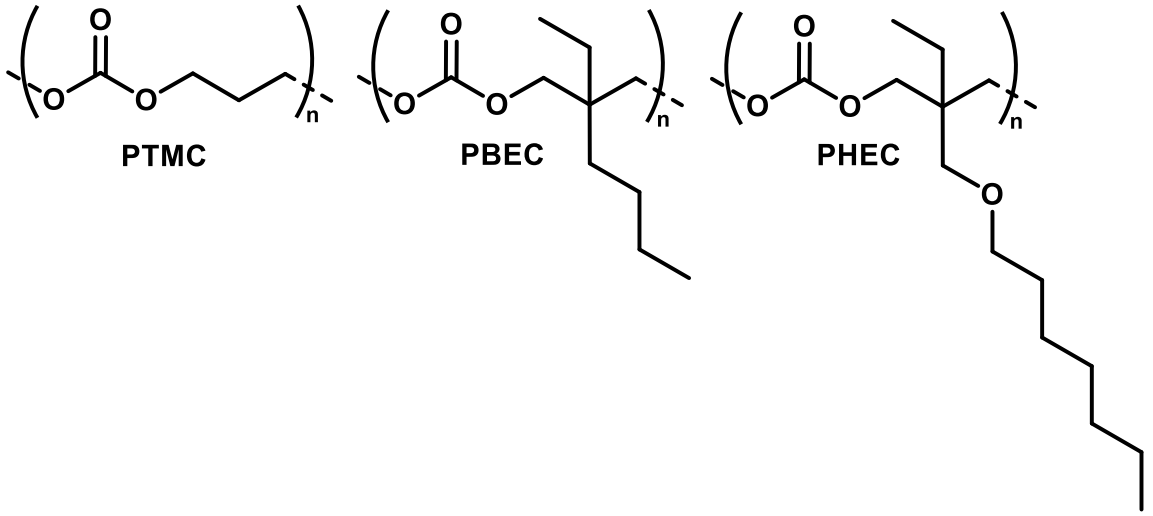


Figure 1.7. Structures of three polycarbonates studied as polymer electrolytes: PTMC, PHEC and PBEC.[72]

1.2.2.3. Polyester Electrolytes

As with polycarbonates, Li-ion conduction in polyesters is proposed to occur via the carbonyl oxygen.[74] Most of the polyesters studied are semicrystalline, with the amorphous region being responsible for conduction.[74]

There is increasing interest in using aliphatic polymers, including the biodegradable poly(ε-caprolactone) (PCL) (Figure 1.8).[55] It was studied as a polymer electrolyte with a variety of lithium salts.[75-77] It showed high oxidative stability (5 V) and a low T_g (-65 °C), but its conductivity was rather limited (~ 10^{-6} S cm^{-1} at ambient temperature) due to its semicrystallinity. Brandell and coworkers sought to improve the Li-ion conductivity of PCL by inhibiting its crystallinity.[78] To achieve this, 20 mol% of TMC was randomly incorporated

into PCL's backbone to produce poly(CL-*r*-TMC), successfully supressing its melting point (T_m) and increasing its conductivity from 1.1×10^{-6} S cm^{-1} to 4.1×10^{-5} S cm^{-1} at 25 °C (Figure 1.8).[78]

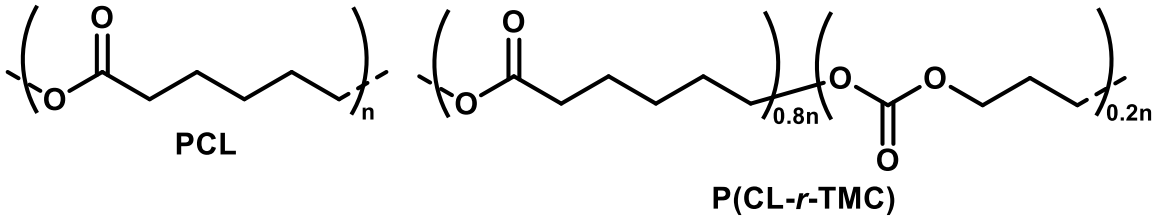


Figure 1.8. Structures of polyester electrolytes, PCL and P(CL-*r*-TMC).[78]

A series of polyester electrolytes, with increasing distance between the carbonyl groups, were also investigated: poly(ethylene adipate) (PEA) ($\sigma = 1.1 \times 10^{-5}$ S cm^{-1} at 30 °C, T_g = -25 °C), poly(1,4-butylene adipate) (PBA) ($\sigma = 1.3 \times 10^{-6}$ S cm^{-1} at 30 °C, T_g = -43 °C), poly(1,6-hexamethylene adipate) (PHA) ($\sigma = 9.5 \times 10^{-7}$ S cm^{-1} at 30 °C, T_g = -48 °C) (Figure 1.9).[79] PEA had the highest conductivity, despite its T_g being 20 °C higher than the other polyesters studied. This was proposed to be due to there being more carbonyl groups to solvate Li^+ and due to the carbonyl having a greater Li^+ coordination ability. However, when comparing polymers with a larger T_g difference, chain mobility can become the most important factor.[80] For example, comparing poly(ethylene succinate) (PE-2,4) and poly(ethylene sebacate) (PE-2,10), revealed that PE-2,4 had a much higher T_g (-3 vs -37 °C) and thus a lower conductivity (10^{-8} vs 10^{-7} S cm^{-1} at 60 °C). Despite the PE-2,4 having a greater proportion of Li^+ solvating groups, it did not compensate for the stiffer polymer chain (Figure 1.9).[80]

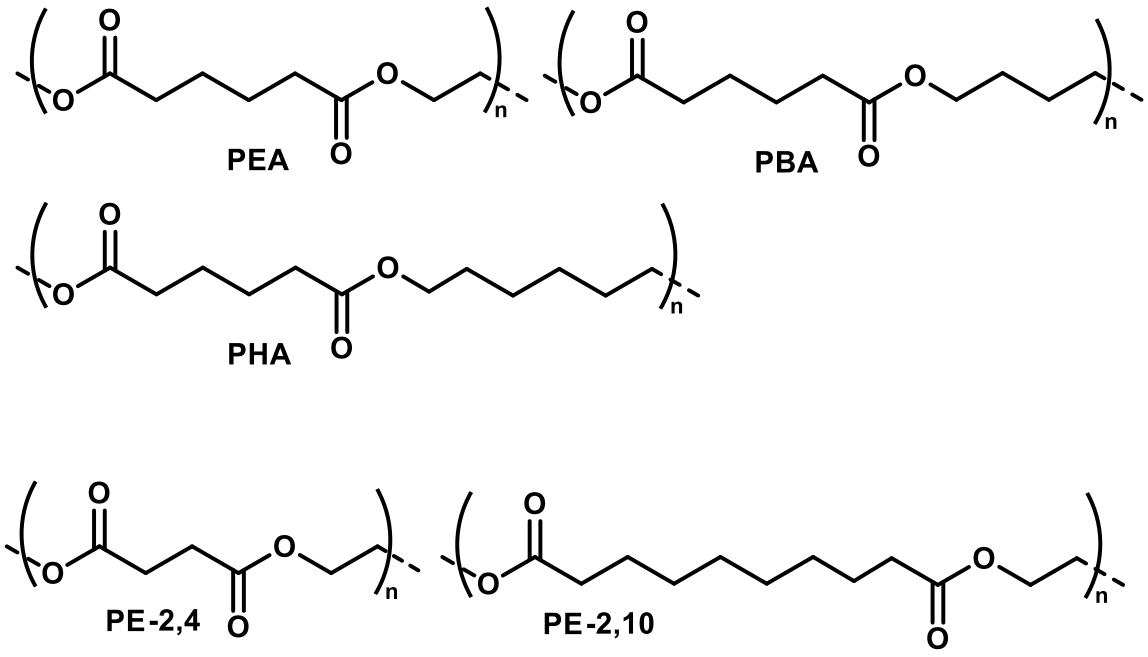


Figure 1.9. Structure of five polyesters studied as polymer electrolytes: PEA, PBA, PHA, PE-2,4 and PE-2,10.[79, 80]

A series of polyesters were studied by Balsara and co-workers, where the number and location of oxygen atoms were systematically changed using different polymeric backbones and sidechains, to elucidate the relationship between molecular structure and ionic conductivity.[81, 82] Six different polyesters were produced by anhydride/epoxide ring-opening copolymerisation (ROCOP): the anhydrides used were either glutaric anhydride (GA) or diglycolic anhydride (DGA). The epoxides were propylene oxide (PO), allyl glycidyl ether (AGE) or 2-[(2-(2-(2-meth-oxyethoxy)ethoxy) methyl]oxirane (ME_2MO) (Figure 1.10). When polymers had ether side-chains, Li^+ solvation occurred by the side-chains only, as studied by molecular dynamic simulations, resulting in a two-fold conductivity increase (1.5×10^{-4} S cm^{-1} for P(GA-*alt*-PO), 3.0×10^{-4} S cm^{-1} for P(GA-*alt*-ME_2MO) at 90 °C). The effect of a DGA- or GA-based backbone on conductivity varied depending on the epoxide comonomer used. Conductivity was still lower than PEO by an order of magnitude; molecular dynamic

simulations showed that in PEO, Li^+ transport occurred by intrachain hopping but in these polyesters Li^+ transport was dependent on intrinsically slower interchain hopping, accounting for their lower conductivity.[81, 82]

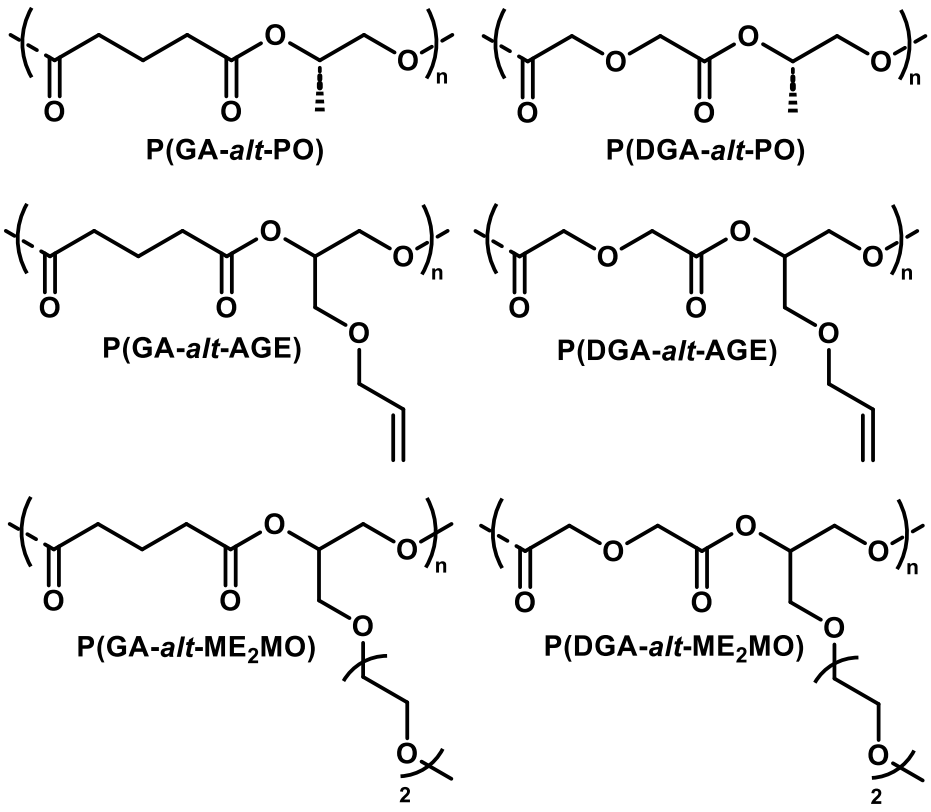


Figure 1.10. A series of six polyesters studied as polyester electrolytes, with systematic backbone (GA or DGA) and side chain (PO, AGE or ME_2MO) variations.[81, 82]

1.2.2.4. Block Copolymer Electrolytes

Block copolymers are of interest due to the parameters which can be varied, including the block structure (e.g. diblock and triblocks), molar mass and block composition (Figure 1.11).[83] For battery applications, block copolymers with a hard (T_g > ambient temperature) or crystalline (T_m) block are combined with a soft block (T_g < ambient temperature) to produce a polymer electrolyte which is ionically conductive whilst also having mechanical integrity. The structure is proposed to help inhibit the growth of lithium dendrites and improve interfacial

contact.[8] Additionally, some block copolymers exhibit microphase separation, subject to their molar mass (M_n), the interaction parameter between the constituent blocks (χ_{AB}) and the block composition (f_A).[84] Phase diagrams have been constructed which show how different block copolymer phase morphologies can be accessed by changing these parameters. For a given block copolymer, a range of morphologies can theoretically be accessed by varying molar mass and block compositions (Figure 1.11). This can result in improved mechanical properties, such as elasticity, and perhaps improved Li-ion conductivity through the formation of ordered Li-conducting channels.[85-88]

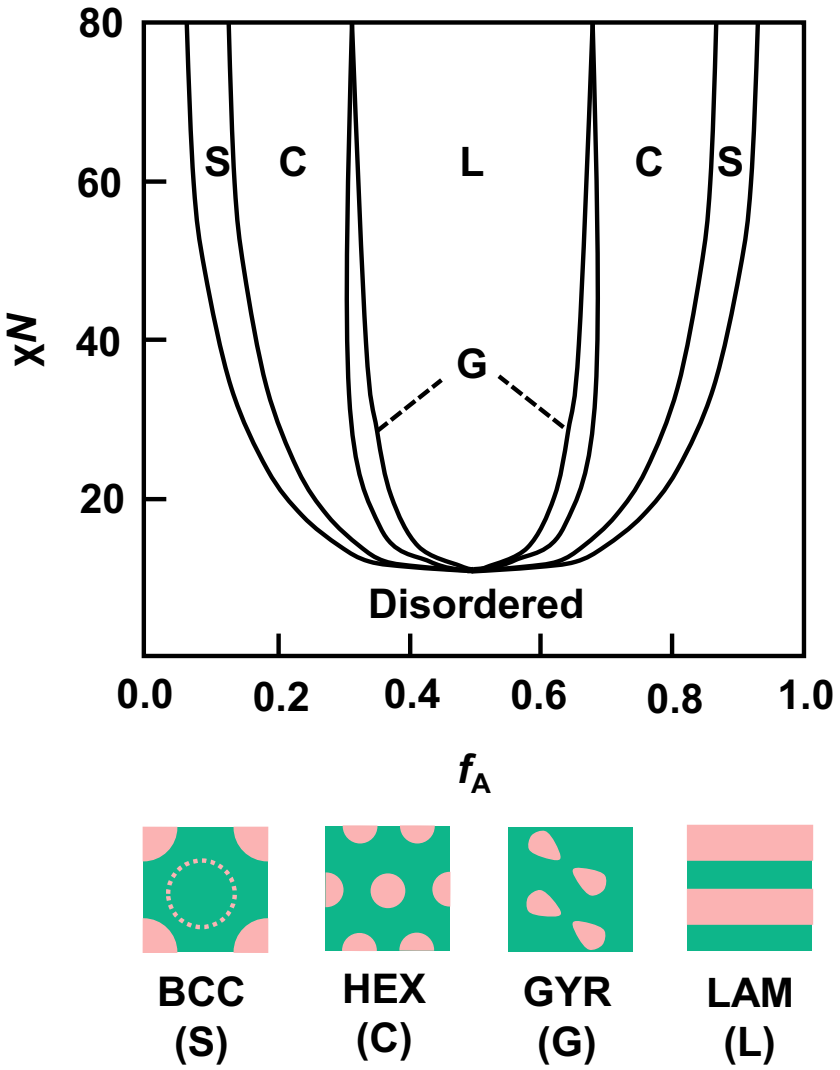


Figure 1.11. Theoretical phase diagram for a linear AB diblock copolymer and 2D illustrations of the equilibrium morphologies: spherical (BCC/S), cylindrical (HEX/C), bicontinuous gyroid (GYR/G) and lamellar (LAM/L). Morphologies dependent on block composition (f_A), Flory-Huggins interaction parameter (χ) and degree of polymerisation (N).[84]

Block copolymers involving PEO are well-studied for battery applications, particularly poly(styrene)-*b*-PEO (PS-*b*-PEO) (Figure 1.12).[89] The PS block imparts mechanical integrity – it has a high Young's Modulus (~3 GPa) and a high T_g (~90 °C) – whilst the PEO block enables Li-ion conductivity (~10^{-5} S cm^{-1} at ambient temperature). Balsara and coworkers have extensively studied phase-separated PS-*b*-PEO.[90, 91] They discovered that the conductivity of

lamellar microstructures of PS-*b*-PEO increased with molar mass (16 – 98 kg mol^{-1}).[89] This finding was contrary to PEO homopolymers, where a lower molar mass had increased chain mobility thus higher conductivity.[87] This difference was rationalised by considering the PS/PEO interfaces: EO units near the block interfaces have limited mobility; higher molar mass polymers have a lower proportion of these interfaces.[92, 93] In a lower molar mass range (2.7 – 13.7 kg mol^{-1}), conductivity decreased with increasing molar mass: this was proposed to be due to enhanced chain mobility at lower masses and the large number of Li-ions affected by the block interfaces.[94] A single lithium-ion conducting PS-*b*-PEO-*b*-PEO-based electrolyte was produced, where the PS blocks were functionalised with LiTFSI salt; it had moderate conductivity (1.3×10^{-5} S cm^{-1}) and excellent t_{Li+} (> 0.85).[95]

PS hard blocks are non-polar and insulating – there is interest in using carbonyl-coordinating hard blocks which can contribute to conductivity. Polycarbonate (PC) blocks have been studied, including poly(ditrimethylene carbonate) (PDTC) and poly(vinyl cyclohexene carbonate) (PvCHC); the former is crystalline (T_m = 109 °C) and the latter has a high T_g (106 °C). PDTC-*b*-PEO-*b*-PDTC achieved a good ionic conductivity of 10^{-4} S cm^{-1} at 60 °C.[96] The PvCHC-*b*-PEO-*b*-PvCHC electrolyte's composition was optimised to be adhesive, elastomeric and highly conductive (1.1×10^{-4} S cm^{-1} at 30 °C); consequently, it was successfully applied as a composite cathode binder.[97]

The semicrystalline polyester PCL has been applied as a hard block in PCL-*b*-PEO-*b*-PCL, which was crosslinked via the chain ends to improve its mechanical properties.[98] This resulted in an electrolyte which had a good ionic conductivity and formed a free-standing film ($\sigma = 5 \times 10^{-4}$ S cm^{-1} at 60 °C). PCL was rendered more conductive by incorporating 20 mol% TMC into the backbone, and then, the mechanical properties of P(CL-*r*-TMC) were improved by using it in block copolymers. For example, PS-*b*-P(CL-*r*-TMC) had a Li-ion conductivity of 5.0×10^{-6} S cm^{-1} at 30 °C.[99] When the PS was replaced with a polar, carbonyl-coordinating

hard block, P(BMA-*b*-TMC-*r*-CL), where BMA is benzyl methacrylate, the Li-ion conductivity increased to 9.1×10^{-6} S cm^{-1} .[100] (Figure 1.12).

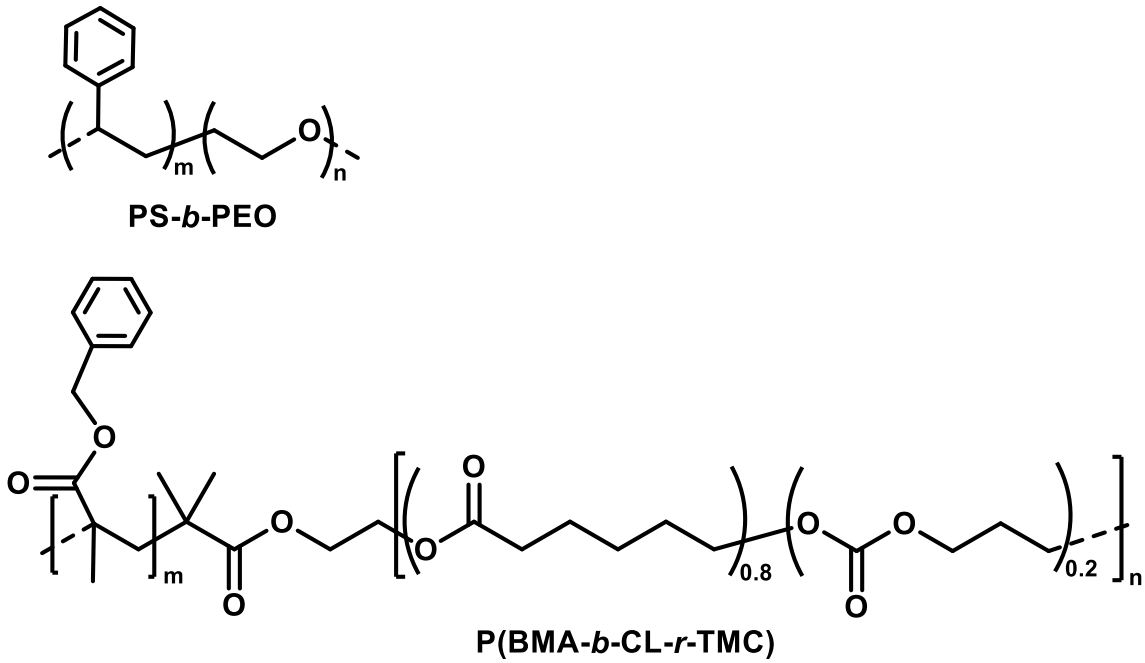


Figure 1.12. Structure of two block copolymers studied as polymer electrolytes: PS-*b*-PEO and P(BMA-*b*-CL-*r*-TMC).[87, 100]

Table 1.1. Li-ion conductivity of reported electrolyte materials.

Classification	Material	Conductivity (S cm^{-1}) [a]	Temperature (°C) [b]
Inorganic	Li_6PS_5Cl [41]	$2 – 5 \times 10^{-3}$	30
Polyether	PEO [46]	$10^{-3} – 10^{-4}$	70
	PEO [46]	10^{-8}	30
Polycarbonate-based	PVIC [57]	10^{-6}	30
	PVICOX [57]	10^{-4}	30
	PEC / Ionic liquid [59]	2×10^{-5}	90
	PEO/PPC blend [65]	6.8×10^{-5}	25
	PPC/BR + PEG [66]	1.3×10^{-3}	25
	PPC (cellulose reinforced) [67]	3.0×10^{-4}	20
	PPCAGE [68]	1.6×10^{-4}	80
	PTMC [69]	10^{-8}	30
	PTMC-*co*-PCL (3:2) [70]	7.9×10^{-7}	25
	PHEC-*co*-PAEC [72]	$10^{-7} – 10^{-8}$	25
Polyester-based	PCL [75-77]	10^{-6}	30
	PCL-*co*-PTMC (4:1) [78]	4.1×10^{-5}	25
	PEA [79]	1.1×10^{-5}	30
	PBA[79]	1.3×10^{-6}	30
	PHA[79]	9.5×10^{-7}	30

	PE-2,4 [80]	10^{-8}	60
	PE-2,10 [80]	10^{-7}	60
	P(GA-*alt*-PO) [81]	1.5×10^{-4}	90
	P(GA-*alt*-ME_2MO) [81]	3.0×10^{-4}	90
Block copolymers	PS-*b*-PEO [89]	10^{-5}	30
	PDTC-*b*-PEO-*b*-PDTC [96]	10^{-4}	60
	PvCHC-*b*-PEO-*b*-PvCHC [97]	1.1×10^{-4}	30
	PCL-*b*-PEO-*b*-PCL, cross-linked [98]	5×10^{-4}	60
	PS-*b*-P(CL-*r*-TMC) [99]	5.0×10^{-6}	30
	P(BMA-*b*-TMC-*r*-CL) [100]	9.1×10^{-6}	30

[a] Reported Li-ion conductivity of the materials; [b] Temperature at which the Li-ion conductivity was recorded.

1.3. Ring-Opening Polymerisations and Ring-Opening Copolymerisations.

The ring-opening polymerization (ROP) of lactones produces aliphatic polyesters; the ring-opening co-polymerization (ROCOP) of epoxides with CO_2 or anhydride produces polycarbonates or polyesters respectively. Polyesters and polycarbonates are typically produced industrially from petrochemical monomers by condensation reactions. This requires precise monomer stoichiometries, and the resulting polymerization is slow and poorly controlled.[101] In contrast, ROP and ROCOP can use renewable feedstocks, have faster rates, are controllable, and can produce polymers with predictable molecular weights and narrow polydispersities.[102]

Homogenous metal catalysts are typically used for ROCOP and ROP, however there is little overlap between suitable catalysts.[103] Block co-polymers can be prepared which contain a polyester block made by ROP, and a different polyester or polycarbonate block made by ROCOP. This has been achieved by using a different catalyst for the ROCOP and ROP steps.[104-106] However, it is desirable to have a single catalyst which can operate both ROP and ROCOP cycles from a monomer mixture, with a high degree of control. There are examples of catalysts which can selectively form co-polymers in lactide, epoxide and CO_2 monomer

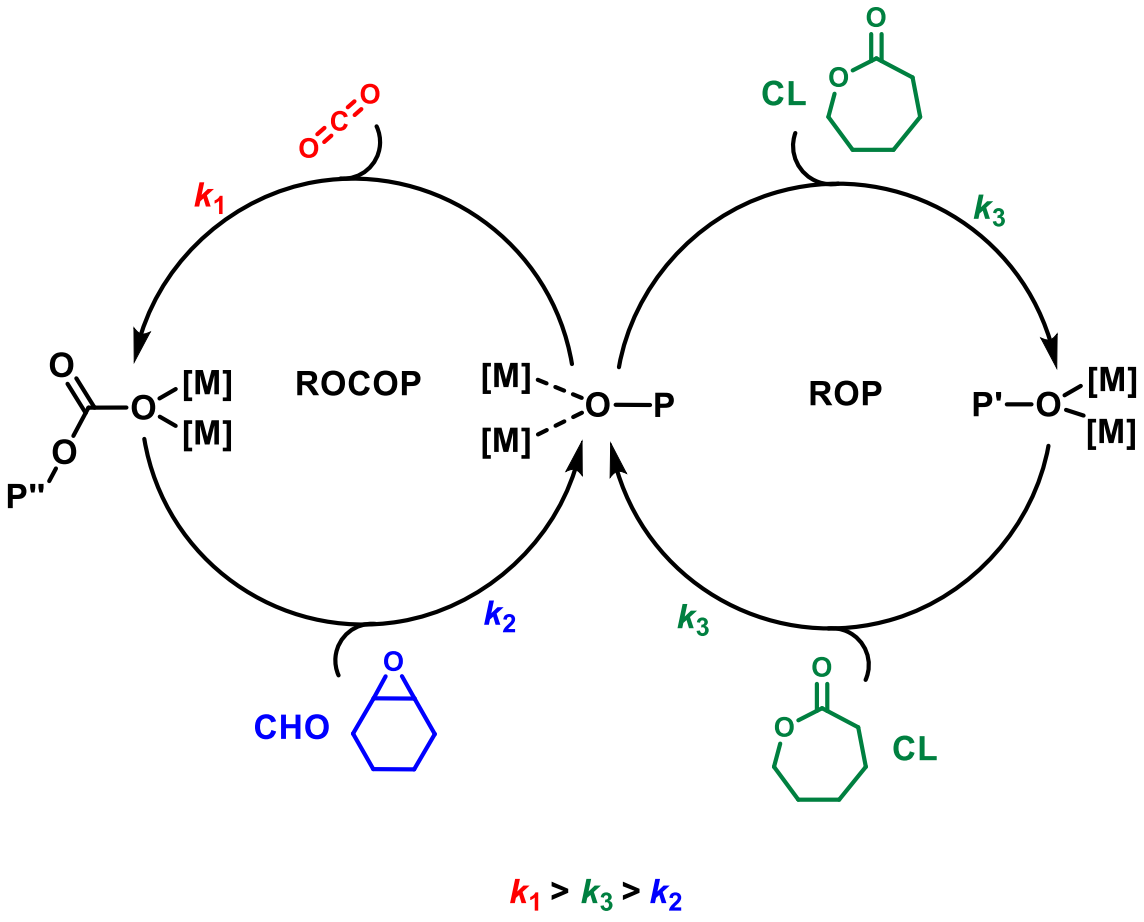
mixtures.[107, 108] There are also ROPs which can be switched on or off with a high degree of control, by changing the oxidation state of the metal catalyst,[109] changing the catalyst conformation by ion addition,[110] or by the addition and removal of CO_2 from the monomer mixture.[111] This idea of switching a catalytic cycle on and off is key for using a single catalyst to produce BCP via different polymerization cycles.

1.4. Switch Catalysis

A new approach to block co-polymer synthesis was reported by Williams and coworkers in 2014.[102] A single dizinc catalyst was used to selectively 'switch' between ring-opening polymerisation (ROP) and ring-opening copolymerisation (ROCOP), to produce poly(ester-*b*-carbonate)s. The catalyst was active and selective in both distinct polymerisation cycles and operated in a one-pot monomer mixture with control. It first demonstrated the ROP of CL and ROCOP of cyclohexene oxide (CHO) and CO_2 to produce ABA poly(cyclohexene carbonate-*b*-caprolactone-*b*-cyclohexene carbonate) (PCHC-*b*-PCL-*b*-PCHC) (Scheme 1.1).[102]

The bridging catalyst species was proposed to be the zinc alkoxide. In ROCOP, CO_2 inserts into the alkoxide to generate a zinc carbonate intermediate. CHO then inserts into the zinc carbonate to regenerate the alkoxide. In ROP, the putative zinc alkoxide is the sole catalyst species. The rate of lactone insertion into the alkoxide is proposed to be slower than CO_2 insertion; the zinc carbonate intermediate is more thermodynamically stable than the alkoxide and CO_2 insertion has a zeroth rate order.[112, 113] Therefore, if CO_2 or anhydride is present it rapidly inserts into the alkoxide to form the carbonate – which is ROP inactive, so ROCOP selectively proceeds. Only in the absence of CO_2 and anhydride is ROP able to proceed from

the zinc alkoxide. Hence, it is the nature of the zinc chain end-group (alkoxide or carbonate) which controls the catalytic selectivity.[102]



Scheme 1.1. CO_2/CHO ring-opening copolymerisation (ROCOP) and CL ring-opening polymerisation (ROP) cycles accessed by a single switchable catalyst to produce block copolymers, where [M] is the catalyst metal centre and k_1, k_2 and k_3 are the rate of CO_2, CHO and CL insertion, respectively.[102]

Switchable polymerisation catalysis has been shown to be applicable to a broad range of epoxides, anhydride, lactones and cyclic carbonates.[114, 115] Renewable feedstocks can be utilised and a wide range of polymer structures with different properties can be explored.[116, 117] Monomers with pendant vinyl groups, like vCHO, facilitate post-functionalisation to further tune polymer properties, such as adhesion.[97, 118] Sterically congested, bio-based tricyclic anhydrides (TCAs) are effective hard blocks and have a wide T_g range, spanning -60 (PCL) to 130 °C (poly(limonene carbonate)).[114, 115, 117, 119] As switch catalysis is a highly controlled and

selective approach for producing block polymers, it is useful to produce systematic series of polymers, where monomers, molar mass, block structure and composition can be varied to observe the effect on polymer properties.[120, 121]

Poly(cyclohexene carbonate-*b*-decalactone-*b*-cyclohexene carbonate) (PCHC-*b*-DL-*b*-PCHC) of various molar masses and compositions and molar masses were produced by the switch catalysis of cyclohexene oxide (CHO), decalactone (DL) and CO_2.[120] PCHC has a high T_g (105–115 °C) so provided rigidity and increased the tensile modulus, whilst PDL was a soft block (T_g = -60 °C). Materials with 20 wt% PCHC were used as pressure sensitive adhesives; 28 wt% PCHC was used as an elastin mimic; and 50 wt% PCHC was used as a toughened plastic. Similarly, poly(cyclohexene-*alt*-phthalate-*b*-decalactone-*b*-cyclohexene-*alt*-phthalate)s were studied to find the optimum elastomer composition; the lead polymers possessed superior mechanical properties to widely-used commercial elastomers whilst being recyclable and degradable.[121]

1.5. Aims and Objectives

This thesis aims to use switchable polymerisation catalysis to systematically produce poly(ester-*b*-carbonate)s for use in battery applications. The goal is to demonstrate the highly controlled and selective nature of switch catalysis as a method to make new block copolymer electrolytes and binders. The catalysis will be used to systematically vary the polymer molar mass, composition, block structure and sidechain substituents, to identify lead polymers (Figure 1.13). Chapters 2−4 present research inspired by recent developments in polyester, polycarbonate and block copolymer electrolytes and binders. This thesis examines the following questions:

1. What is the optimum block structure, molar mass and composition for a series of poly(ester-*b*-carbonate)s, where the polycarbonate is PvCHC and the polyester is P(CL-*r*-TMC)? Can such copolymers be used to improve battery performance?

2. Can switch catalysis be used to produce poly(carbonate-*b*-ester-*b*-carbonate)s with Li-ion conducting functional groups? What are the best side chain substituents for Li-ion conductivity?

3. Can switch catalysis be used to produce 'ABA-type' poly(carbonate-*b*-ester-*b*-carbonate)s from a mixture of anhydride/epoxide/cyclic carbonate? What is the optimum molar mass and composition of the resulting copolymer, for Li-ion conductivity? How will post-polymerisation modifications affect the polymer properties in battery applications?

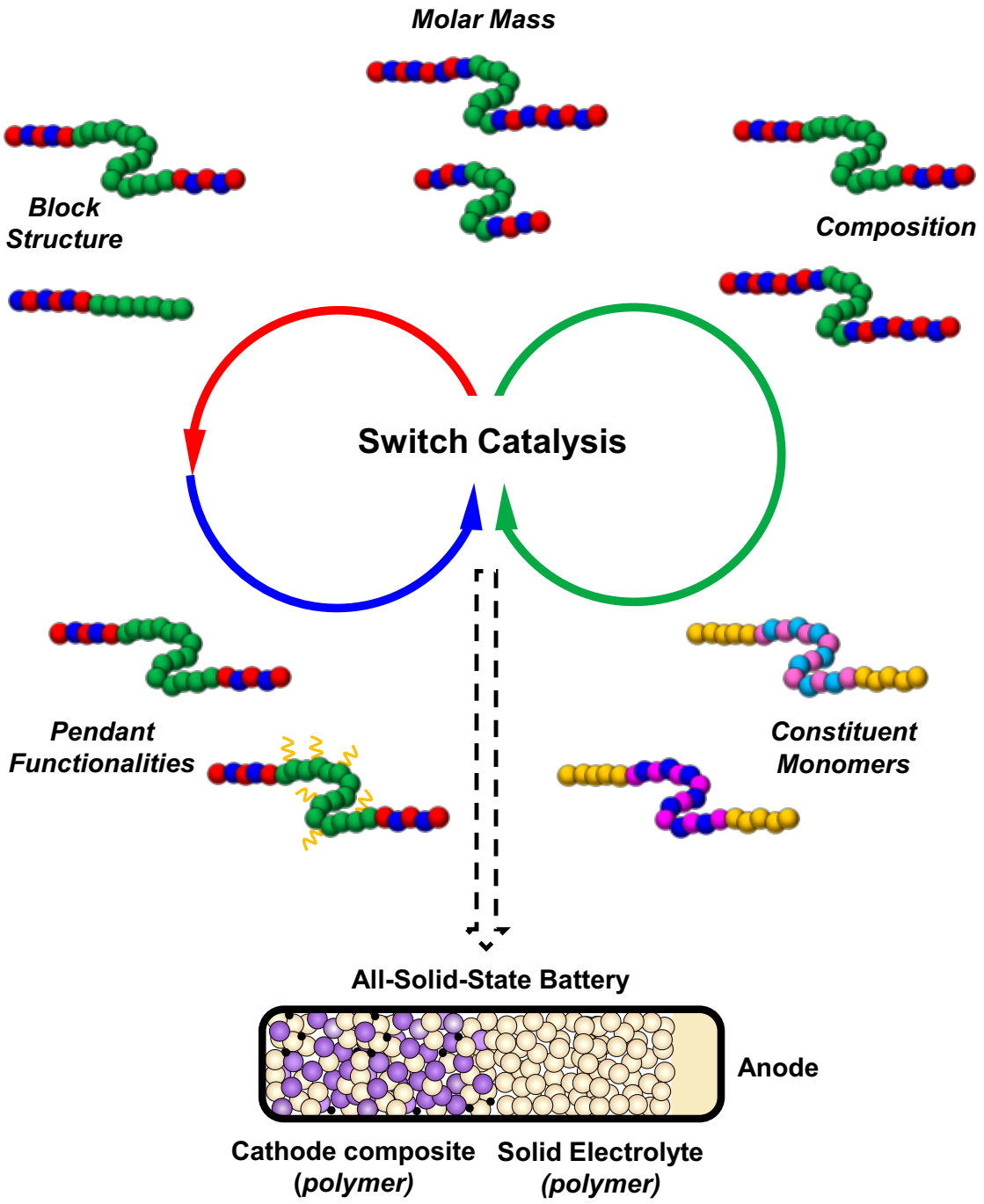


Figure 1.13. Illustration of the aims of this thesis: using switchable polymerisation catalysis to systematically vary poly(ester-*b*-carbonate) block structure, molar mass, composition, constituent monomers and pendant functionalities to produce polymers for use in all-solid-state Li-ion batteries, as either a cathode binder or an electrolyte.

1.6. References

1. K. J. Mizushima, P. C.; Wiseman, P. J.; Goodenough, J. B., *Mater. Res. Bull*., 1980, **15**, 783-789.
2. J. B. Goodenough and K.-S. Park, *J. Am. Chem. Soc.*, 2013, **135**, 1167-1176.
3. L. Long, S. Wang, M. Xiao and Y. Meng, *J. Mater. Chem. A*, 2016, **4**, 10038-10069.
4. K. Xi, X. Min, J. Xiao, M. Fang, W. Wang, Y. Zhao, Y.-g. Liu, A. Abdelkader, R. V. Kumar and Z. Huang, *Energy Environ. Sci.*, 2021, **14**, 2186-2243.
5. Y. Tian, G. Zeng, A. Rutt, T. Shi, H. Kim, J. Wang, J. Koettgen, Y. Sun, B. Ouyang, T. Chen, Z. Lun, Z. Rong, K. Persson and G. Ceder, *Chem. Rev.*, 2020, **121**, 1623-1669.
6. Official Journal of the European Union: Amending Regulation (EU) 2019/631 as regards strengthening the CO2 emission performance standards for new passenger cars and new light commercial vehicles in line with the Union's increased climate ambition, https://eur-lex.europa.eu/legal-content/EN/TXT/?uri=CELEX%3A52021PC0556, (accessed October 2023).
7. J. G. Rogelj, O; Cowie, A; Reising, A., *Nature*, 2021, **591**, 365-368.
8. P. Albertus, V. Anandan, C. Ban, N. Balsara, I. Belharouak, J. Buettner-Garrett, Z. Chen, C. Daniel, M. Doeff, N. J. Dudney, B. Dunn, S. J. Harris, S. Herle, E. Herbert, S. Kalnaus, J. A. Libera, D. Lu, S. Martin, B. D. McCloskey, M. T. McDowell, Y. S. Meng, J. Nanda, J. Sakamoto, E. C. Self, S. Tepavcevic, E. Wachsman, C. Wang, A. S. Westover, J. Xiao and T. Yersak, *ACS Energy Lett.*, 2021, **6**, 1399-1404.
9. D.-H. Liu, Z. Bai, M. Li, A. Yu, D. Luo, W. Liu, L. Yang, J. Lu, K. Amine and Z. Chen, *Chem. Soc. Rev.*, 2020, **49**, 5407-5445.
10. Q. Zhao, S. Stalin, C.-Z. Zhao and L. A. Archer, *Nat. Rev. Mater.*, 2020, **5**, 229-252.
11. M. Pasta, D. Armstrong, Z. L. Brown, J. Bu, M. R. Castell, P. Chen, A. Cocks, S. A. Corr, E. J. Cussen, E. Darnbrough, V. Deshpande, C. Doerrer, M. S. Dyer, H. El-Shinawi, N. Fleck, P. Grant, G. L. Gregory, C. Grovenor, L. J. Hardwick, J. T. S. Irvine, H. J. Lee, G. Li, E. Liberti, I. McClelland, C. Monroe, P. D. Nellist, P. R. Shearing, E. Shoko, W. Song, D. S. Jolly, C. I. Thomas, S. J. Turrell, M. Vestli, C. K. Williams, Y. Zhou and P. G. Bruce, *J. Phys. Energy*, 2020, **2**, 032008.
12. T. Famprikis, P. Canepa, J. A. Dawson, M. S. Islam and C. Masquelier, *Nat. Mater.*, 2019, **18**, 1278-1291.
13. S. Sharma and A. Manthiram, *Energy Environ. Sci.*, 2020, **13**, 4087-4097.
14. L. de Biasi, A. O. Kondrakov, H. Geßwein, T. Brezesinski, P. Hartmann and J. Janek, *J. Phys. Chem. C*, 2017, **121**, 26163-26171.
15. Y. Shi, X. Zhou and G. Yu, *Acc. Chem. Res.*, 2017, **50**, 2642-2652.

16. H. Chen, M. Ling, L. Hencz, H. Y. Ling, G. Li, Z. Lin, G. Liu and S. Zhang, *Chem. Rev.*, 2018, **118**, 8936-8982.

17. R. V. Chebiam, A. M. Kannan, F. Prado and A. Manthiram, *Electrochem. Commun.*, 2001, **3**, 624-627.

18. K. Kimura, J. Motomatsu and Y. Tominaga, *J. Phys. Chem. C*, 2016, **120**, 12385-12391.

19. W. Dou, M. Zheng, W. Zhang, T. Liu, F. Wang, G. Wan, Y. Liu and X. Tao, *Adv. Funct. Mater*., 2023, 2305161.

20. J. Shim, R. Kostecki, T. Richardson, X. Song and K. A. Striebel, *J. Power Sources*, 2002, **112**, 222-230.

21. Z. Chen, L. Christensen and J. R. Dahn, *J. Appl. Polym. Sci.*, 2004, **91**, 2958-2965.

22. S.-B. Hong, Y.-J. Lee, U.-H. Kim, C. Bak, Y. M. Lee, W. Cho, H. J. Hah, Y.-K. Sun and D.-W. Kim, *ACS Energy Lett*., 2022, **7**, 1092-1100.

23. A. Rensmo, E. K. Savvidou, I. T. Cousins, X. Hu, S. Schellenberger and J. P. Benskin, *Environ. Sci.: Process. Impacts*, 2023, **25**, 1015-1030.

24. X. Lim, *Nature*, 2023, **620**, 24-27.

25. S. Sen, E. Trevisanello, E. Niemöller, B.-X. Shi, F. J. Simon and F. H. Richter, *J. Mater. Chem. A*, 2021, **9**, 18701-18732.

26. F. Zou and A. Manthiram, *Adv. Energy Mater.,* 2020, **10**, 2002508.

27. K. Lee, J. Lee, S. Choi, K. Char and J. W. Choi, *ACS Energy Lett.*, 2019, **4**, 94-101.

28. J. Lopez, Y. Sun, D. G. Mackanic, M. Lee, A. M. Foudeh, M.-S. Song, Y. Cui and Z. Bao, *Adv. Mater.*, 2018, **30**, 1804142.

29. S.-J. Zhang, Y.-P. Deng, Q.-H. Wu, Y. Zhou, J.-T. Li, Z.-Y. Wu, Z.-W. Yin, Y.-Q. Lu, C.-H. Shen, L. Huang and S.-G. Sun, *ChemElectroChem*, 2018, **5**, 1321-1329.

30. S. S. Jeong, N. Böckenfeld, A. Balducci, M. Winter and S. Passerini, *J. Power Sources,* 2012, **199**, 331-335.

31. K. Prasanna, T. Subburaj, Y. N. Jo, W. J. Lee and C. W. Lee, *ACS Appl. Mater. Interfaces*, 2015, **7**, 7884-7890.

32. T. Zhang, J.-t. Li, J. Liu, Y.-p. Deng, Z.-g. Wu, Z.-w. Yin, D. Guo, L. Huang and S.-g. Sun, *Chem. Commun.*, 2016, **52**, 4683-4686.

33. J. Sun, Y. Huang, W. Wang, Z. Yu, A. Wang and K. Yuan, *Electrochim. Acta*, 2008, **53**, 7084-7088.

34. A. F. Léonard and N. Job, *Mater. Today Energy*, 2019, **12**, 168-178.

35. M. Ling, J. Qiu, S. Li, C. Yan, M. J. Kiefel, G. Liu and S. Zhang, *Nano Lett.*, 2015, **15**, 4440-4447.

36. H. Q. Pham, J. Lee, H. M. Jung and S.-W. Song, *Electrochim. Acta*, 2019, **317**, 711-721.

37. Z. Zhang, T. Zeng, Y. Lai, M. Jia and J. Li, *J. Power Sources*, 2014, **247**, 1-8.

38. G. Liu, S. Xun, N. Vukmirovic, X. Song, P. Olalde-Velasco, H. Zheng, V. S. Battaglia, L. Wang and W. Yang, *Adv. Mater.,* 2011, **23**, 4679-4683.

39. L. Long, S. Wang, M. Xiao and Y. Meng, *J. Mater. Chem. A*, 2016, **4**, 10038-10069.

40. J. Lopez, D. G. Mackanic, Y. Cui and Z. Bao, *Nat. Rev. Mater.*, 2019, **4**, 312-330.

41. K. J. Kim, M. Balaish, M. Wadaguchi, L. Kong and J. L. M. Rupp, *Adv. Energy Mater.*, 2021, **11**, 2002689.

42. C. Wang, K. Adair and X. Sun, *Acc. Mater. Res.*, 2022, **3**, 21-32.

43. T. Shi, Y.-Q. Zhang, Q. Tu, Y. Wang, M. C. Scott and G. Ceder, *J. Mater. Chem. A*, 2020, **8**, 17399-17404.

44. D. E. Fenton, J. M. Parker and P. V. Wright, *Polymer*, 1973, **14**, 589.

45. M. Armand, *Solid State Ion.*, 1983, **9-10**, 745-754.

46. D. L. Bresser, S.; Iojoiu, C.; Picard, L.; Passerini, S., *Mol. Syst. Des. Eng.*, 2019, **4**, 779-792.

47. M. Armand, *Adv. Mater.*, 1990, **2**, 278-286.

48. Z. Geng, N. S. Schauser, J. Lee, R. P. Schmeller, S. M. Barbon, R. A. Segalman, N. A. Lynd and C. J. Hawker, *Macromolecules*, 2020, **53**, 4960-4967.

49. C. Vachon, C. Labreche, A. Vallee, S. Besner, M. Dumont and J. Prud'homme, *Macromolecules*, 1995, **28**, 5585-5594.

50. P. M. Blonsky, D. F. Shriver, P. Austin and H. R. Allcock, *Solid State Ion.*, 1986, **18-19**, 258-264.

51. Y. Zheng, F. Chia, G. Ungar, T. H. Richardson and P. V. Wright, *Electrochim. Acta*, 2001, **46**, 1397-1405.

52. S. Guhathakurta and K. Min, *Polymer*, 2010, **51**, 211-221.

53. J. Zhang, J. Yang, T. Dong, M. Zhang, J. Chai, S. Dong, T. Wu, X. Zhou and G. Cui, *Small*, 2018, **14**, 1800821.

54. K. Xu, *Chem. Rev.,* 2014, **114**, 11503-11618.

55. H. Xu, J. Xie, Z. Liu, J. Wang and Y. Deng, *MRS Energy Sustain*., 2020, **7**, E2.

56. D. Mecerreyes, L. Porcarelli and N. Casado, *Macromol. Chem. Phys.*, 2020, **221**, 1900490.

57. X. Wei and D. F. Shriver, *Chem. Mater.*, 1998, **10**, 2307-2308.

58. T. Itoh, K. Fujita, K. Inoue, H. Iwama, K. Kondoh, T. Uno and M. Kubo, *Electrochim. Acta*, 2013, **112**, 221-229.

59. K. Kimura, J. Hassoun, S. Panero, B. Scrosati and Y. Tominaga, *Ionics*, 2015, **21**, 895-900.

60. Y. Tominaga, V. Nanthana and D. Tohyama, *Polym. J.*, 2012, **44**, 1155-1158.

61. Y. Tominaga, *Polym. J.*, 2017, **49**, 291-299.

62. M. Nakamura and Y. Tominaga, *Electrochim. Acta*, 2011, **57**, 36-39.

63. Y. Tominaga, T. Shimomura and M. Nakamura, *Polymer*, 2010, **51**, 4295-4298.

64. X. Yu, M. Xiao, S. Wang, D. Han and Y. Meng, *J. Appl. Polym. Sci.*, 2010, **118**, 2078-2083.

65. X.-Y. Yu, M. Xiao, S.-J. Wang, Q.-Q. Zhao and Y.-Z. Meng, *J. Appl. Polym. Sci.,* 2010, **115**, 2718-2722.

66. X. Huang, J. Huang, J. Wu, X. Yu, Q. Gao, Y. Luo and H. Hu, *RSC Adv.,* 2015, **5**, 52978-52984.

67. J. Zhang, J. Zhao, L. Yue, Q. Wang, J. Chai, Z. Liu, X. Zhou, H. Li, Y. Guo, G. Cui and L. Chen, *Adv. Energy Mater.,* 2015, **5**, 1501082.

68. K. Deng, S. Wang, S. Ren, D. Han, M. Xiao and Y. Meng, *ACS Appl. Mater. Interfaces*, 2016, **8**, 33642-33648.

69. J. Mindemark, M. J. Lacey, T. Bowden and D. Brandell, *Prog. Polym. Sci.*, 2018, **81**, 114-143.

70. J. Mindemark, E. Törmä, B. Sun and D. Brandell, *Polymer*, 2015, **63**, 91-98.

71. J. Mindemark, L. Imholt, J. Montero and D. Brandell, *J. Polym. Sci. Polym. Chem*., 2016, **54**, 2128-2135.

72. J. Mindemark, L. Imholt and D. Brandell, *Electrochim. Acta*, 2015, **175**, 247-253.

73. M. Ebadi, T. Eriksson, P. Mandal, L. T. Costa, C. M. Araujo, J. Mindemark and D. Brandell, *Macromolecules*, 2020, **53**, 764-774.

74. I. D. Wu and F.-C. Chang, *Polymer*, 2007, **48**, 989-996.

75. C. P. Fonseca, D. S. Rosa, F. Gaboardi and S. Neves, *J. Power Sources*, 2006, **155**, 381-384.

76. M. Ravi, S. H. Song, K. M. Gu, J. N. Tang and Z. Y. Zhang, *Ionics*, 2015, **21**, 2171-2183.

77. D. Zhang, L. Zhang, K. Yang, H. Wang, C. Yu, D. Xu, B. Xu and L.-M. Wang, *ACS Appl. Mater. Interfaces*, 2017, **9**, 36886-36896.

78. J. Mindemark, B. Sun, E. Törmä and D. Brandell, *J. Power Sources*, 2015, **298**, 166-170.

79. C.-K. Lin and I. D. Wu, *Polymer*, 2011, **52**, 4106-4113.

80. M. Watanabe, M. Rikukawa, K. Sanui and N. Ogata, *Macromolecules*, 1986, **19**, 188-192.

81. M. A. Webb, Y. Jung, D. M. Pesko, B. M. Savoie, U. Yamamoto, G. W. Coates, N. P. Balsara, Z.-G. Wang and T. F. Miller, *ACS Cent. Sci.*, 2015, **1**, 198-205.

82. D. M. Pesko, Y. Jung, A. L. Hasan, M. A. Webb, G. W. Coates, T. F. Miller and N. P. Balsara, *Solid State Ion.,* 2016, **289**, 118-124.

83. H.-C. Kim, S.-M. Park and W. D. Hinsberg, *Chem. Rev.*, 2010, **110**, 146-177.

84. M. W. Matsen and F. S. Bates*, Macromolecules*, 1996, **29**, 7641-7644.

85. C. M. Bates and F. S. Bates, *Macromolecules*, 2017, **50**, 3-22.

86. F. S. Bates and G. H. Fredrickson, *Phys. Today*, 1999, **52**, 32-38.

87. M. Singh, O. Odusanya, G. M. Wilmes, H. B. Eitouni, E. D. Gomez, A. J. Patel, V. L. Chen, M. J. Park, P. Fragouli, H. Iatrou, N. Hadjichristidis, D. Cookson and N. P. Balsara, *Macromolecules*, 2007, **40**, 4578-4585.

88. W.-S. Young, W.-F. Kuan and I. Epps, Thomas H., *J. Polym. Sci., Part B: Polym. Phys.*, 2014, **52**, 1-16.

89. Y. Zhao, Y. Bai, W. Li, M. An, Y. Bai and G. Chen, *Chem. Mater.*, 2020, **32**, 6811-6830.

90. M. D. Galluzzo, W. S. Loo, E. Schaible, C. Zhu and N. P. Balsara, *ACS Appl. Mater. Interfaces*, 2020, **12**, 57421-57430.

91. T. N. Phan, S. Issa and D. Gigmes, *Polym. Int.*, 2019, **68**, 7-13.

92. V. Ganesan, V. Pyramitsyn, C. Bertoni and M. Shah, *ACS Macro. Lett.*, 2012, **1**, 513-518.

93. R. Bouchet, T. N. T. Phan, E. Beaudoin, D. Devaux, P. Davidson, D. Bertin and R. Denoyel, *Macromolecules*, 2014, **47**, 2659-2665.

94. R. Yuan, A. A. Teran, I. Gurevitch, S. A. Mullin, N. S. Wanakule and N. P. Balsara, *Macromolecules*, 2013, **46**, 914-921.

95. R. Bouchet, S. Maria, R. Meziane, A. Aboulaich, L. Lienafa, J.-P. Bonnet, T. N. T. Phan, D. Bertin, D. Gigmes, D. Devaux, R. Denoyel and M. Armand, *Nat. Mater.*, 2013, **12**, 452-457.

96. M. Melchiors, H. Keul and H. Höcker, *Polymer*, 1996, **37**, 1519-1527.

97. G. L. Gregory, H. Gao, B. Liu, X. Gao, G. J. Rees, M. Pasta, P. G. Bruce and C. K. Williams, *J. Am. Chem. Soc.*, 2022, **144**, 17477-17486.

98. P.-M. Jalbert, B. Commarieu, J.-C. Daigle, J. P. Claverie and K. Zaghib, *J. Electrochem. Soc*., 2020, **167**, 080527.

99. A. Bergfelt, M. J. Lacey, J. Hedman, C. Sångeland, D. Brandell and T. Bowden, *RSC Adv.*, 2018, **8**, 16716-16725.

100. A. Bergfelt, G. Hernández, R. Mogensen, M. J. Lacey, J. Mindemark, D. Brandell and T. M. Bowden, *ACS Appl. Polym. Mater.*, 2020, **2**, 939-948.

101. M. Okada, *Prog. Polym. Sci.*, 2002, **27**, 87-133.

102. C. Romain and C. K. Williams, *Angew. Chem. Int*., 2014, **53**, 1607-1610.

103. T. Stößer, T. T. D. Chen, Y. Zhu and C. K. Williams, *Phil. Trans. A*, 2018, **376**, 20170066.

104. M. R. Kember, J. Copley, A. Buchard and C. K. Williams, *Polym. Chem*., 2012, **3**, 1196-1201.

105. G.-P. Wu, D. J. Darensbourg and X.-B. Lu, *J. Am. Chem. Soc.*, 2012, **134**, 17739-17745.

106. Y. Li, J. Hong, R. Wei, Y. Zhang, Z. Tong, X. Zhang, B. Du, J. Xu and Z. Fan, *Chem. Sci.*, 2015, **6**, 1530-1536.

107. M. Kröger, C. Folli, O. Walter and M. Döring, *Adv. Synth. Catal.*, 2006, **348**, 1908-1918.

108. P. Song, H. Xu, X. Mao, X. Liu and L. Wang, *Polym. Advan. Technol.*, 2017, **28**, 736-741.

109. H. J. Yoon, J. Kuwabara, J.-H. Kim and C. A. Mirkin, *Science*, 2010, **330**, 66-69.

110. X. Wang, A. Thevenon, J. L. Brosmer, I. Yu, S. I. Khan, P. Mehrkhodavandi and P. L. Diaconescu, *J. Am. Chem. Soc.*, 2014, **136**, 11264-11267.

111. O. Coulembier, S. Moins, R. Todd and P. Dubois, *Macromolecules*, 2014, **47**, 486-491.

112. C. Romain, Y. Zhu, P. Dingwall, S. Paul, H. S. Rzepa, A. Buchard and C. K. Williams, *J. Amer. Chem. Soc.*, 2016, **138**, 4120-4131.

113. T. T. D. Chen, Y. Zhu and C. K. Williams, *Macromolecules*, 2018, **51**, 5346-5351.

114. Y. Zhu, M. R. Radlauer, D. K. Schneiderman, M. S. P. Shaffer, M. A. Hillmyer and C. K. Williams, *Macromolecules*, 2018, **51**, 2466-2475.

115. T. Stößer and C. K. Williams, *Angew. Chem. Int. Ed.*, 2018, **57**, 6337-6341.

116. T. T. D. Chen, L. P. Carrodeguas, G. S. Sulley, G. L. Gregory, G. S. Sulley and C. K. Williams *Angew. Chem. Int. Ed.*, 2020, **59**, 23450-23455.

117. P. K. Saini, G. Fiorani, R. T. Mathers and C. K. Williams, *Chem. Eur. J.*, 2017, **23**, 4260-4265.

118. G. L. Gregory, G. S. Sulley, J. Kimpel, M. Łagodzińska, L. Häfele, L. P. Carrodeguas and C. K. Williams, *Angew. Chem. Int. Ed.*, 2022, **61**, e202210748.

119. L. P. Carrodeguas, T. T. D. Chen, G. L. Gregory, G. S. Sulley and C. K. Williams, *Green Chem.*, 2020, **22**, 8298-8307.

120. G. S. Sulley, G. L. Gregory, T. T. D. Chen, L. Peña Carrodeguas, G. Trott, A. Santmarti, K.-Y. Lee, N. J. Terrill and C. K. Williams, *J. Am. Chem. Soc.*, 2020, **142**, 4367-4378.

121. G. L. Gregory, G. S. Sulley, L. P. Carrodeguas, T. T. D. Chen, A. Santmarti, N. J. Terrill, K.-Y. Lee and C. K. Williams, *Chem. Sci.*, 2020, **11**, 4367-4378.

CHAPTER 2

Structural Optimisation of Poly(carbonate-*b*-ester) Electrolytes and their Application as Cathode Binders

2.1. Introduction

In an all-solid-state battery, solid composite cathodes typically comprise a mixture of cathode particles, solid electrolyte, carbon and a polymer binder. The latter holds the solid phases together and enables large-scale electrode processability.[1, 2] Elastomeric polymers can also mitigate cathode volume changes during battery operation.[3] So far, traditional rubber binders (nitrile butadiene, NBR and styrene butadiene, SBR), require modification with polar functionalities to impart adhesiveness for appreciable cycling stability.[4] Polytetrafluoroethylene (PTFE) is the prevalent binder for producing cathode composites, but alongside also commonly used polyvinylidene fluoride (PVDF), fluorinated polymers pose significant environmental concerns.[5, 6] Consequently, many fluorinated substances are proposed to be banned by the EU following a recommendation by the European Chemicals Agency.[7] Besides, given that providing effective pathways for ions is fundamental for maximising cathode capacity, the inherent non-conductive nature of these and most binders is also limiting.[8, 9] Recent work demonstrates that chemically modifying PTFE with ionomers to impart even modest ionic conductivities (1.6×10^{-5} S cm^{-1} at 25 °C) results in a 20% capacity gain over PTFE.[10]

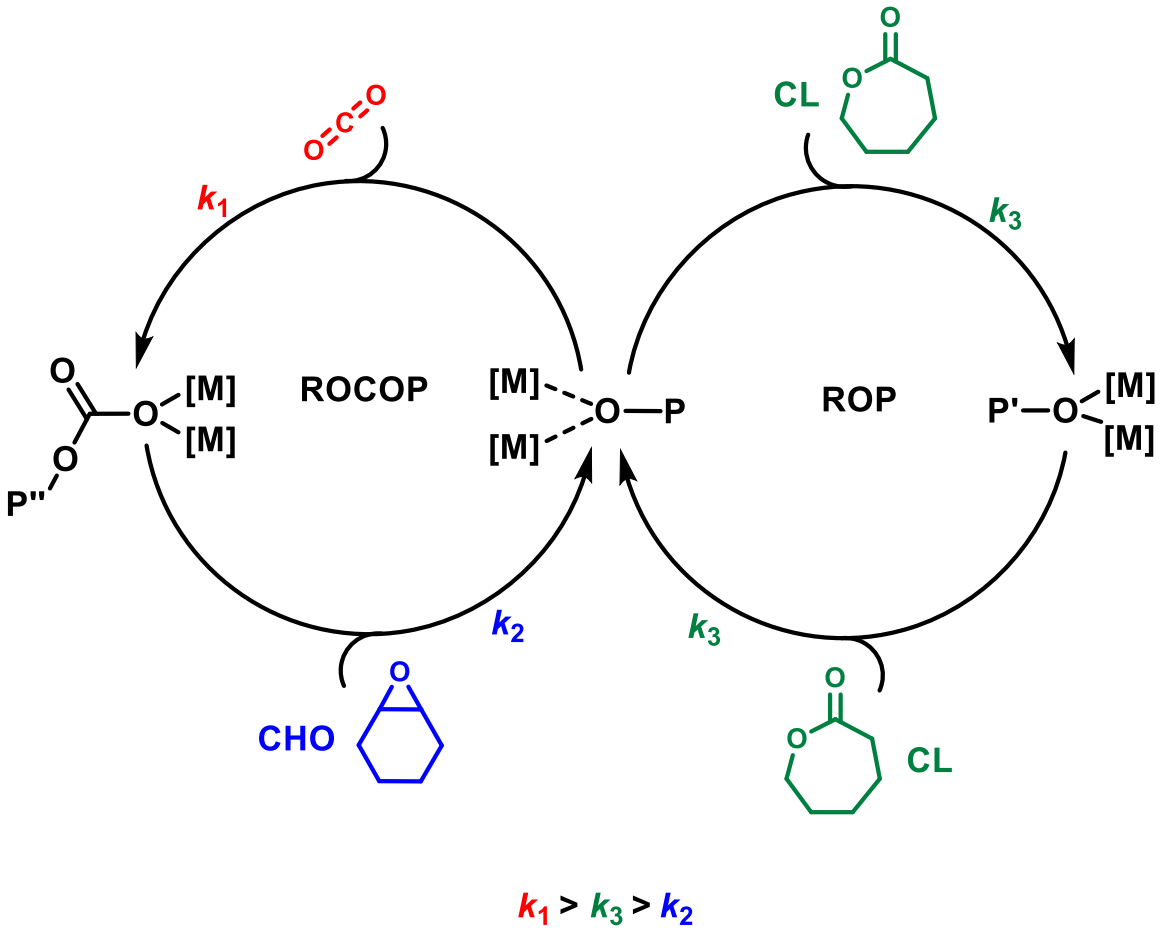
Poly(ethylene oxide) (PEO) is one of the best-known polymeric ionic conductors ($\sigma = 10^{-4} – 10^{-3}$ S cm^{-1} at 80 °C). However, for application in high voltage and high capacity composite cathodes, its low oxidative stability (< 3.9 V vs Li^+/Li) is not ideal and it does not offer the right mechanical properties for mitigating volume change.[11, 12] On the other hand, polycarbonate- and polyester-based ion conductors are known to show good oxidative stability (> 4.5 – 5 V), placing them in the right range for use with the popular high capacity nickel-rich

manganese-cobalt oxide (NMC) cathodes.[13] Indeed, introducing polycarbonate end-blocks either side of PEO has helped to mitigate some of its instabilities.[3]

Poly(trimethylene carbonate) (PTMC) and poly(caprolactone) (PCL) are aliphatic polycarbonates and polyesters, respectively, that have attracted significant attention as polymer electrolytes for high voltage batteries. Of particular note are random copolymers of TMC and CL, P(CL-*r*-TMC) first reported by Mindemark and co-workers whereby a 1/4 ratio of TMC/CL (20 mol% TMC) delivered optimal ionic conductivity (4.1×10^{-5} S cm^{-1} at 25 °C) due to TMC disrupting PCL's crystallinity.[14] P(CL-*r*-TMC) has been utilised in diblock copolymers with a poly(styrene) (PS) or poly(benzyl methacrylate) (PBMA) block to impart mechanical strength, but with a concomitant reduction of Li-ion conductivity.[15, 16]

Preparing AB or ABA-type block polymers, where the 'A' block is hard (T_g > ambient temperature) and the 'B' block is soft (T_g < ambient temperature), is an effective strategy where block phase separation leads to predictable microstructures which correlate with particular mechanical behaviours.[17] This approach has proved widely effective for conductive PEO in conjunction with non-conductive PS blocks, but is less well-studied for polyester and polycarbonate electrolytes.[18, 19] Block copolymers can be produced in a selective and controlled manner by switch catalysis.[20] From a lactone and epoxide monomer mixture, the sequence of lactone/cyclic carbonate ROP or epoxide/CO_2 ROCOP is controlled by the presence or absence of CO_2. The reaction involves connecting different catalytic cycles and the common catalyst species is a metal alkoxide. The first report of switch catalysis was from a CL/cyclohexene oxide (CHO) monomer mixture: in the absence of CO_2, CL ROP selectively occurs. CL inserts into the common catalyst intermediate, regenerating the metal alkoxide.[20] When the

atmosphere is changed to CO_2, CO_2 rapidly inserts into the metal alkoxide to form a metal carbonate intermediate, which only CHO can insert into, thus ROCOP selectively occurs (Scheme 2.1).[20] By varying the duration of the ROP and ROCOP steps, polymer composition and molar mass were controlled. Additionally, by varying the types of initiators that the polymer chains grow from (here, monofunctional or bifunctional alcohol), the polymer block structure was controlled (diblock or triblock).[21]



Scheme 2.1. CO_2/CHO ring-opening copolymerisation (ROCOP) and CL ring-opening polymerisation (ROP) cycles accessed by a single switchable catalyst to produce block copolymers, where [M] is the catalyst metal centre and k_1, k_2 and k_3 are the rate of CO_2, CHO and CL insertion, respectively.

2.2. Aims

This project aims to produce ABA- and AB-block copolymers, where the 'A' block is hard (T_g > ambient temperature) and the 'B' block is soft (T_g < ambient temperature), by switch catalysis. Systematic variation of polymer molar mass, composition and block structure will identify trends relating these features to Li-ion conductivity. These trends will be rationalised with respect to T_g and block copolymer phase morphology. The lead polymer will be identified; its thermomechanical and electrochemical properties measured; and finally it will be applied in an all-solid-state battery to improve its performance.

P(CL-*r*-TMC) will be used as the soft (B) block, with a 1/4 TMC/CL molar ratio; this was identified as the optimum for ionic conductivity by Mindemark and co-workers.[14] Poly(4-vinyl cyclohexene carbonate) (PvCHC) will be used as the hard (A) block: it is rigid and amorphous whilst also being polar and ion coordinating, thus lessening the detrimental impact of an inactive hard block component, such as PS. Both blocks are carbonyl-coordinating; this is known to improve oxidative stability compared to PEO and it has precedent for Li-ion conductivity.[13]

The polymers will be produced by switchable polymerisation catalysis to effectively deliver Li-ion conducting polyester/carbonates from commercial monomers (TMC, CL, vCHO and CO_2) in one-pot. The sequestering of CO_2 is particularly relevant for sustainability considerations. Because of the controlled nature of CL/TMC ROP and CO_2/vCHO ROCOP, this is an effective polymerisation method to investigate systematic series of well-defined ABA- and AB- polymers: block polymer structures (di vs triblock), molar mass (M_n) and

polymer composition (A/B ratio) can be systematically varied. These parameters are expected to influence successful polymer binder function. The lead polymer electrolyte will then be applied as a polymer binder for composite cathodes. Elastomeric and ionically conductive binders are thought to improve cell cycling; the lead polymer will be compared to widely used commercial binders to evaluate its success.

2.3. Polymer Optimisation

2.3.1. Polymer Synthesis

Three systematic series of polymers were targeted: Series I are AB (diblock) polymers with fixed A-block content expressed as a weight fraction (w_{PC} = 0.5) but variable overall molar masses, M_n (26 – 69 kg mol^{-1}); Series II are ABA (triblock) copolymers with similarly fixed A-block content (w_{PC} = 0.5) and variable molar masses, M_n (35 – 66 kg mol^{-1}); Series III feature ABA polymers with a fixed molar mass (50 kg mol^{-1}) but variable A-block content (w_{PC} 0.26 – 0.62) (Figure 2.1, Table 2.1). Henceforth, the polymers are labelled as ABA/AB(M_n, w_{PC}).

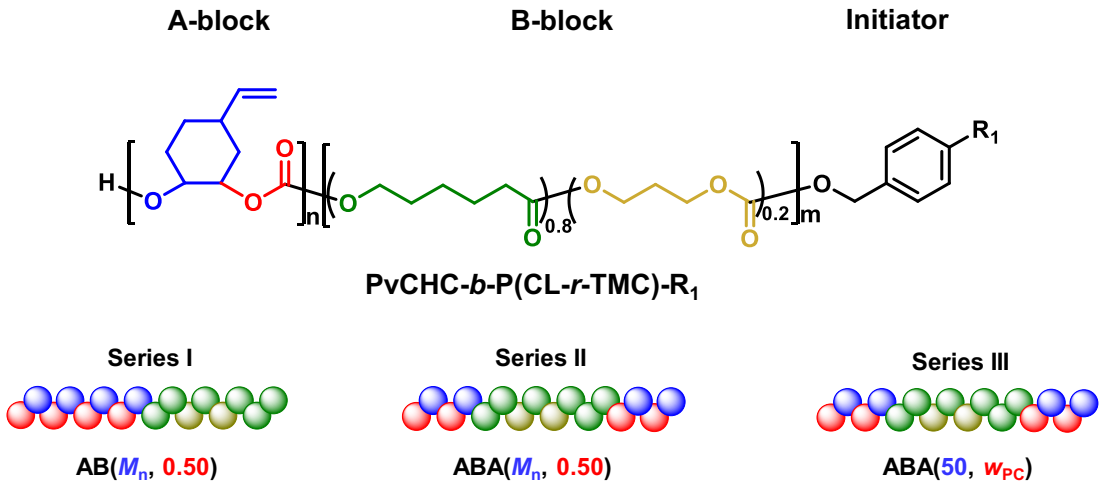


Figure 2.1. Structure of PvCHC-*b*-P(CL-*r*-TMC)-R_1, the polymer investigated in this project, and depiction of the three systematic series of polymers targeted. *n* and *m* correspond to the DP of the A and B blocks, respectively, and are detailed in Table 6.1; R_1 corresponds to -CH_3 for the diblock

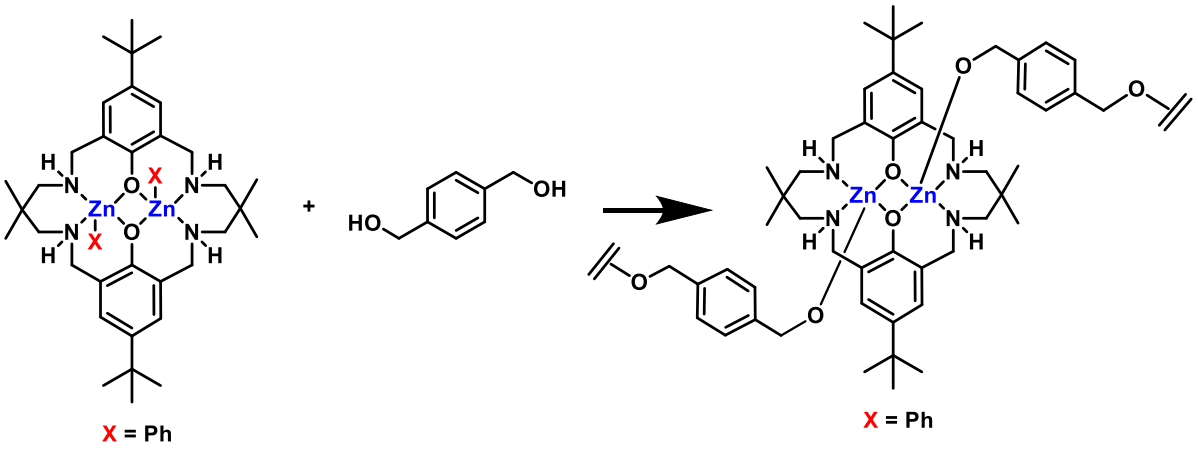
polymers of Series I; R_1 corresponds to CH_2-O-P(CL-*r*-TMC-*b*-vCHC) for the triblock copolymers of series II and III.

Table 2.1. Poly(ester-*b*-carbonate)s and their compositions.

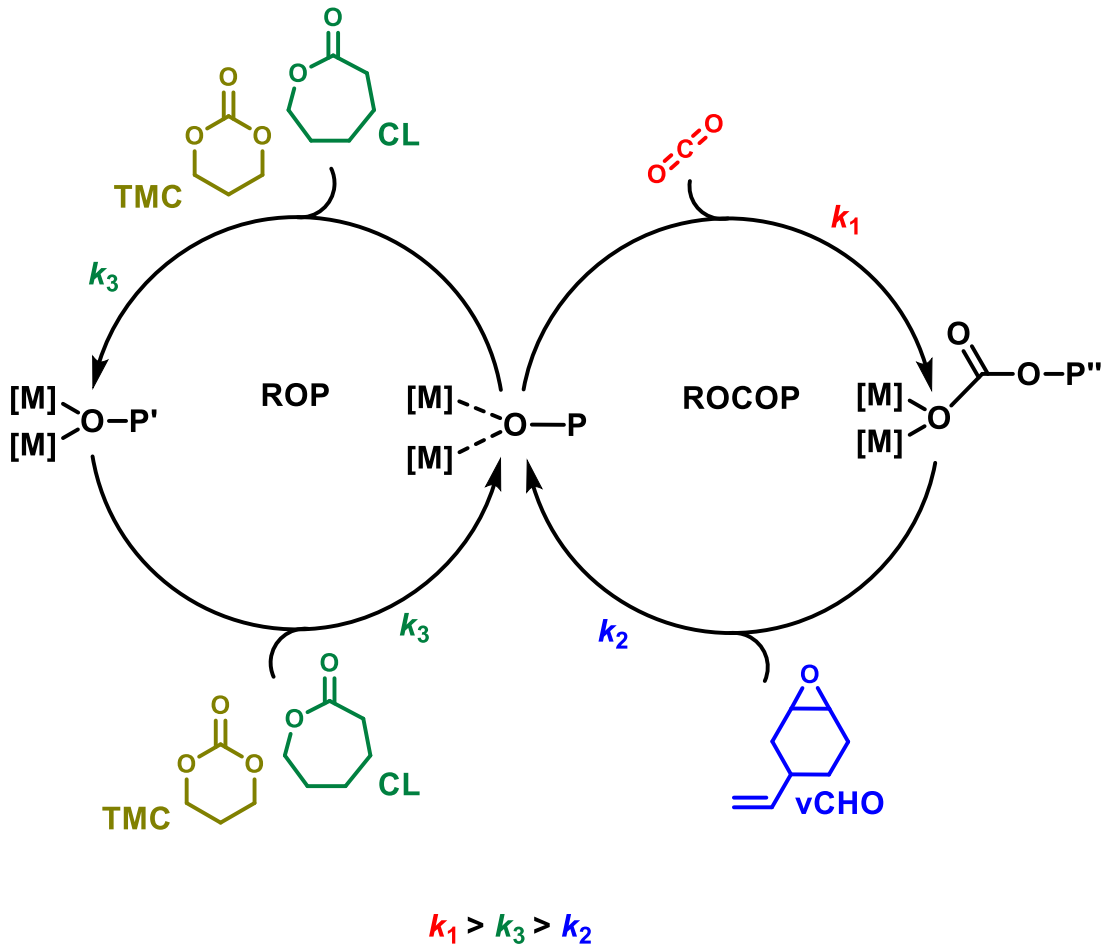
Series [a]	Entry [b]	M_n (kg mol^{-1}) [c]	w_{PC} [c]
I	AB(26, 0.45)	28	0.45
I	AB(32, 0.51)	32	0.51
I	AB(45, 0.47)	45	0.47
I	AB(69, 0.58)	69	0. 58
II	ABA(35, 0.52)	35	0.52
II	ABA(44, 0.53)	44	0.53
II	ABA(50, 0.47)	50	0.47
II	ABA(66, 0.52)	66	0.52
III	ABA(51, 0.26)	52	0.26
III	ABA(47, 0.30)	47	0.30
III	ABA(50, 0.35)	50	0.35
III	ABA(50, 0.47)	50	0.47
III	ABA(50, 0.62)	50	0.62

[a] Series I are AB (diblock) polymers with fixed A-block content (w_{PC} = 0.5) but variable molar masses, M_n (26 – 69 kg mol^{-1}); Series II are AB (diblock) copolymers with similarly fixed A-block content (w_{PC} = 0.5) but variable molar masses, M_n (35 – 66 kg mol^{-1}); Series III are ABA polymers with fixed molar mass (50 kg mol^{-1}) but variable A-block content (w_{PC} = 0.26 – 0.62). [b] Polymers labelled as ABA/AB (M_n, w_{PC}) where M_n = overall molar mass in kg mol^{-1} and w_{PC} = weight fraction of PvCHC. [c] Determined from the ^{1}H NMR spectra of the purified polymer by integration of the aromatic initiator resonance (7.34 ppm for 1,4-BDM, 7.17 ppm for Me-BnOH) against those of PvCHC (5.76 ppm) and P(CL-*r*-TMC) (2.00, 1.38 ppm).

All polymers were synthesised using an organometallic di-Zn(II) catalyst, referred to as [LZn_2Ph_2].[22] This catalyst is highly active for lactone ROP and epoxide/CO_2 ROCOP; it is also a switchable catalyst able to selectively form block polymers from monomer mixtures.[22, 23] It has phenyl co-ligands which do not initiate polymerisation but rather react rapidly and irreversibly with an added alcohol to produce the true catalyst in situ (Scheme 2.2).[22] According to switch catalysis theory, from a CL/TMC/vCHO monomer mixture, under an N_2 atmosphere, only CL/TMC can insert into the metal alkoxide, thus CL/TMC ROP occurs. When the atmosphere is changed to CO_2, the CO_2 rapidly inserts into the metal alkoxide to form a metal-carbonate intermediate, which only the vCHO can insert into, regenerating the metal alkoxide (Scheme 2.3). vCHO/CO_2 ROCOP now occurs, even if lactone remains in the reaction mixture, because CO_2 insertion into the metal alkoxide is more rapid than CL or TMC insertion. Hence, the polymerisation cycle accessed can be controlled by the presence of CO_2 in the atmosphere.



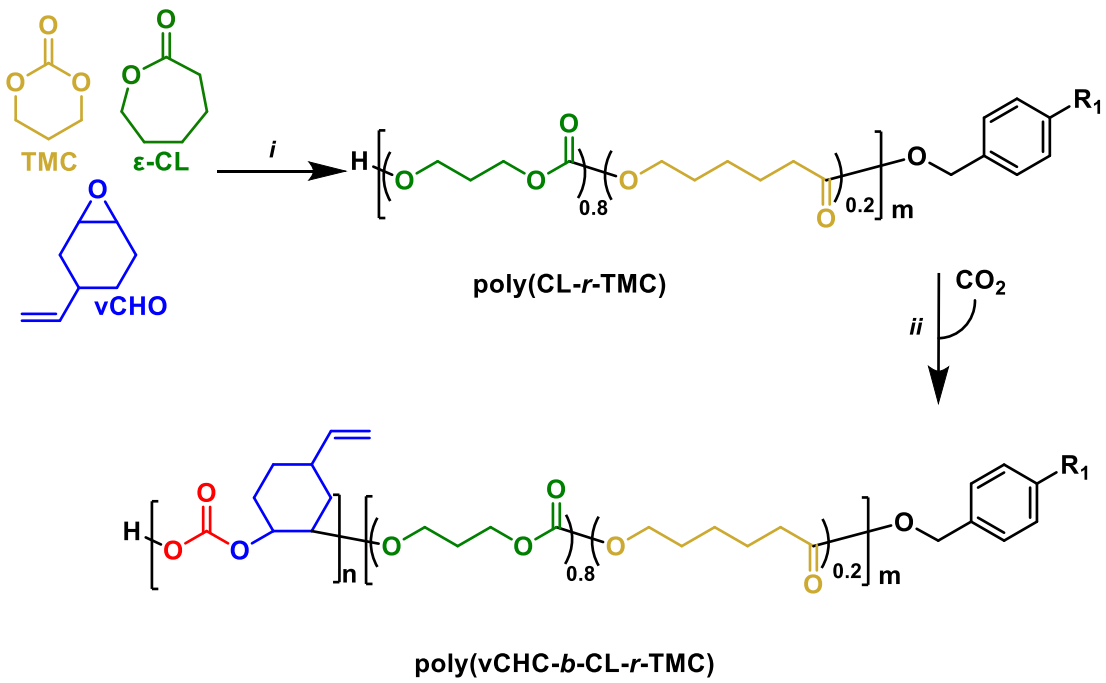
Scheme 2.2. The structure of the catalyst used in polymerisations, [LZn_2Ph_2], and its initiation with the bifunctional alcohol BDM. Alcohol reacts with the catalyst in situ to form the alkoxide initiator essential for ROP and ROCOP. Initiation occurs analogously with the monofunctional alcohol Me-BnOH. BDM is used to make triblock (ABA) polymers; Me-BnOH is used to make diblock (AB) polymers.



Scheme 2.3. CL/TMC ring-opening polymerisation (ROP) and vCHO/CO_2 ring-opening copolymerisation (ROCOP) cycles accessed by a single switchable catalyst to produce triblock (ABA)

or diblock (AB) block copolymers, where [M] is the catalyst metal centre and k_1, k_2 and k_3 are the rate of CO_2, vCHO and CL/TMC insertion, respectively.

When applied with bifunctional alcohol, 1,4-benzene dimethanol (BDM), the catalyst produces only hydroxy-telechelic polymers and, hence, in switchable polymerisations, yields ABA triblock polymers. When applied with monofunctional alcohol, 4-methyl benzyl alcohol (Me-BnOH), it delivers AB diblock polymers (Scheme 2.4).[24, 25]



Scheme 2.4. Switchable polymerisation from a TMC/CL/vCHO monomer mixture to produce block copolymer poly(vCHC-*b*-CL-*r*-TMC). [LZn_2Ph_2] = 0.8 mM, [vCHO] = 2.8 M, [TMC + CL]$_0$ = 0.9 M. Exemplar ratio: [LZn_2Ph_2]/[*initiator*]/[TMC]/[CL]/[vCHO] = 1/4/200/800/3500, where [*initiator*], [CL] and [TMC + CL]$_0$ were adjusted to achieve the desired composition and M_n. (i) ROP at 100 °C for 1 h, under an N_2 atmosphere in a 15 mL toluene solution; (ii) ROCOP at 100 °C for 16 – 44 h, under a CO_2 atmosphere. To produce the AB polymers (Series I), the initiator was monofunctional alcohol Me-BnOH, $R_1 = CH_3$; to produce the ABA polymers (Series II and III), the initiator was bifunctional alcohol BDM, $R_1 = CH_2$-O-P(CL-*r*-TMC-*b*-vCHC).

A typical polymerisation was conducted using a relative ratio of 1/4/200/800/3500 [LZn_2Ph_2]/[initiator]/[TMC]/[CL]/[vCHO]; this catalyst/initiator ratio was optimal for end-group control (Table 6.1).[25] The reaction mixture was 26 mL: by volume, 40% vCHO and 60% toluene. The optimal catalyst concentration was 0.8 mM; the initial (TMC + CL) and vCHO concentrations were 0.9 and 3.0 M, respectively. Experiments were stirred at 1600 rpm and heated to 100 °C. To control molar mass and w_{PC}, the vCHO conversion was varied and the ratio of $[CL+TMC]_0$ was adjusted with respect to the initiator (Table 6.1).

From the monomer mixture, CL and TMC ROP always proceeded selectively to produce poly(CL-*r*-TMC) (Scheme 2.4). An aliquot removed from the polymerisation after 1 hour shows, by ^{1}H NMR spectroscopy, 90% CL conversion (Figure 2.2). The reactivity ratios of TMC and CL have been previously reported and evidences the random copolymerisation of these monomers in ROP.[26] At this point, the reaction atmosphere was switched from N_2 to CO_2, by partial removal of N_2 under vacuum and refilling with 1 bar CO_2, which immediately switched the polymerisation to vCHO/CO_2 ROCOP. Following the addition of CO_2, the polycarbonate blocks were propagated for a further 16 – 44 h, producing either ABA PvCHC-*b*-P(CL-*r*-TMC)-*b*-PvCHC, or AB PvCHC-*b*-P(CL-*r*-TMC) (Scheme 2.4). The polymerisation catalyses were quenched with benzoic acid (0.1 mL, 1 M in $CHCl_3$) and crude polymer samples were retained. These were analysed by ^{1}H NMR spectroscopy, to determine CL and vCHO conversions by comparisons of the normalised monomer (δ = 2.70, 3.20 ppm) and polymer (δ = 4.14, 4.87 ppm) integrals (Figure 2.2). The crude polymers were purified by precipitation three times from methanol (3 × 200 mL) to yield a white gummy solid. The material was dried under a vacuum of 10^{-1} mbar at 60 °C; isolated in good yield (> 75%); and characterised using ^{1}H and ^{13}C{^{1}H} NMR spectroscopy, chain end-group analysis, size-exclusion chromatography (SEC) and differential scanning calorimetry (DSC).

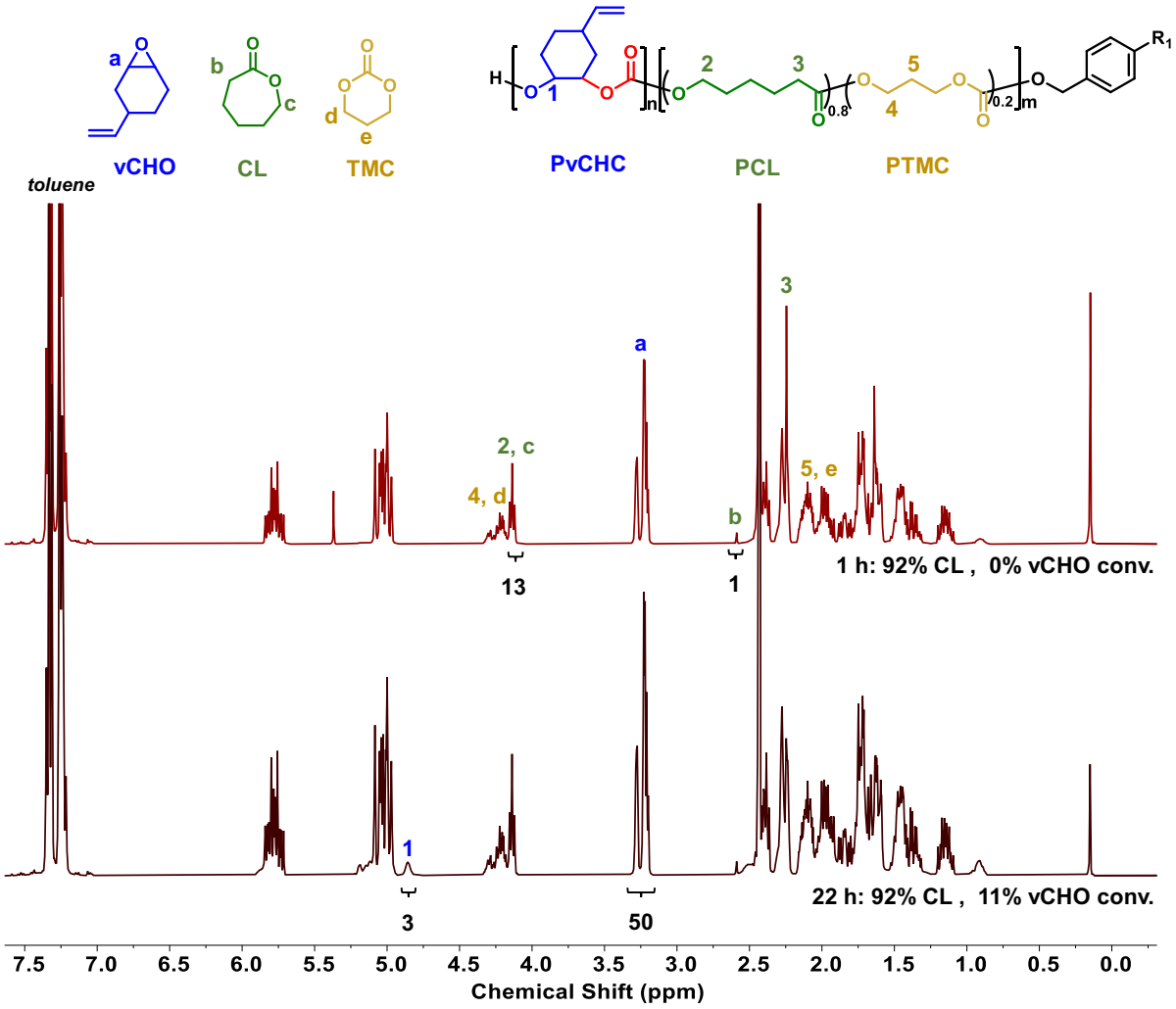


Figure 2.2. Crude ^{1}H NMR spectra ($CDCl_3$) of the polymerisation process, identifying the signals used to calculate monomer conversions (labelled). Top: Product after 1 hour of stirring, at 100 °C, under N_2. Bottom: Product after a further 22 h of stirring at 100 °C, under CO_2 (1 bar).

2.3.2. Polymer Characterisation

The ^{1}H NMR spectra of the purified polymers all showed the expected signals for the PvCHC and P(CL-*r*-TMC) blocks, with the relative integrals determining the polymer composition (Figure 2.3). The polymerisation is highly selective and no ether linkages were observed (3.30 – 3.60 ppm). Due to the high polymer molar masses, junction signals were not detectable. Polymer molar masses were determined by ^{1}H NMR spectroscopy, by integrating the signal corresponding to the aromatic initiator (7.34 ppm for 1,4-BDM, 7.17 ppm for Me-

BnOH) against those of the polymer (5.75, 4.12, 4.03 ppm) (Figure 2.3). These values were compared against theoretical masses based on monomer conversions and the monomer to initiator ratio. There was good agreement between $M_{n,calc}$ and $M_{n,NMR}$, consistent with a controlled polymerisation (Table 6.2).

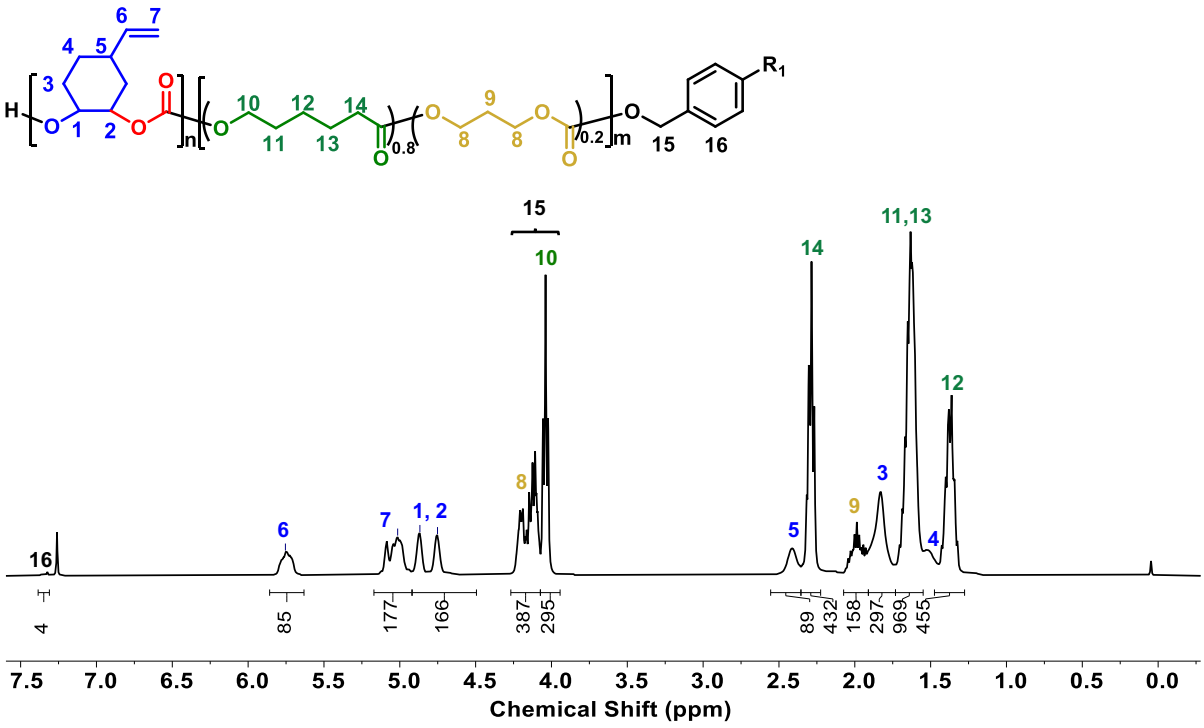


Figure 2.3. Assigned ^{1}H NMR spectrum ($CDCl_3$) of the purified polymer ABA(47, 0.30), poly(vCHC-*b*-CL-*r*-TMC-*b*-vCHC), where R_1 = CH_2-O-P(CL-*r*-TMC-*b*-vCHC).

The $^{13}C\{^{1}H\}$ NMR spectra showed the expected signals (Figure 2.4). Also, it provided evidence to support the random incorporation of CL and TMC units in the midblock. The carbonyl group is sensitive to the distribution of repeating units around it thus distinct signals can be observed corresponding to different triad sequences, as studied by Brandell and co-workers.[27] In the CL carbonyl region, signals were observed for CCC, CCT and TCT triads; in the TMC carbonyl region, signals were observed for CTC, CTT and TTT triads, where T is a TMC unit and C is a CL unit (Figure 2.5).

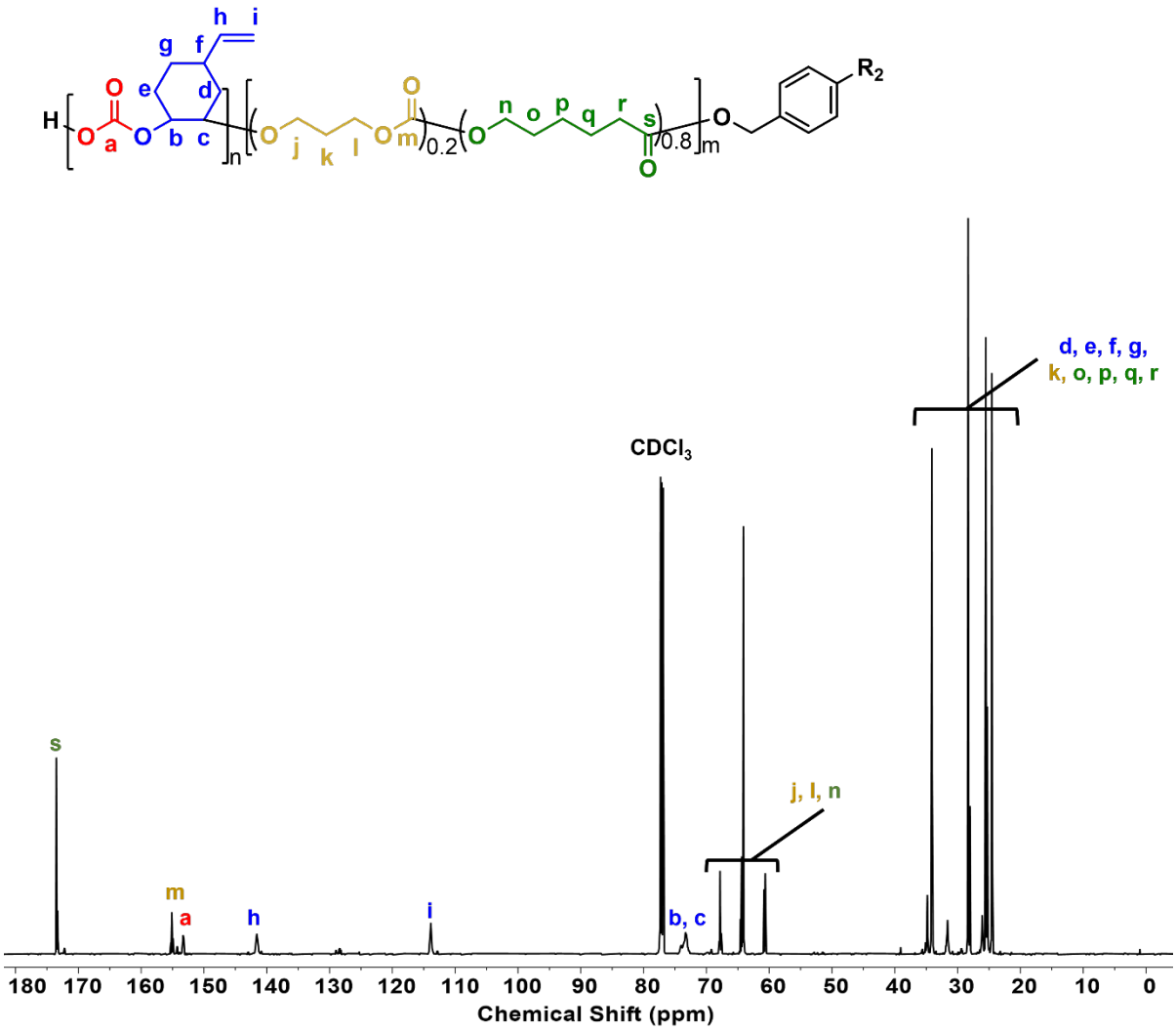


Figure 2.4. $^{13}C\{^{1}H\}$ NMR spectrum ($CDCl_3$) of poly(vCHC-*b*-CL-*r*-TMC-*b*-vCHC), ABA(47, 0.30).

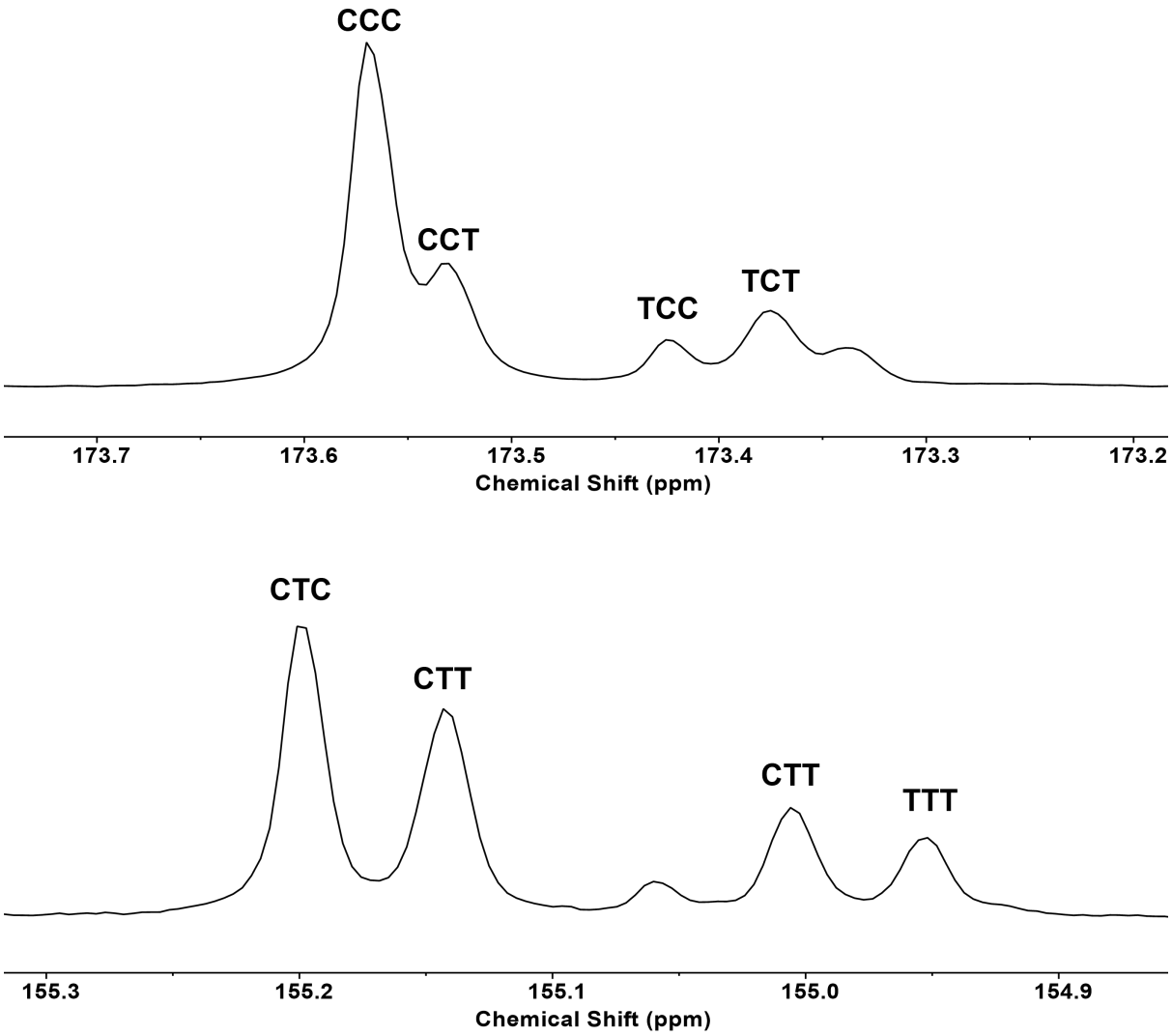


Figure 2.5. $^{13}C\{H\}$ NMR spectrum ($CDCl_3$) of the CL (top) and TMC (bottom) carbonyl regions of poly(vCHC-*b*-CL-*r*-TMC-*b*-vCHC) with the triads labelled; C refers to the repeating CL units and T refers to TMC units, with the centre unit in each triad giving rise to the observed signal.

Chain end-group analysis was conducted by capping the terminal hydroxyl chain end groups with dioxaphospholane via a condensation reaction with 2-chloro-4,4,5,5,-tetramethyl-1,3,2-dioxaphospholane. The end group signals were then identified by $^{31}P\{H\}$ NMR spectroscopy: for the block copolymer, this showed signals for vinyl cyclohexenol end groups (146.6 ppm) without any residual P(CL-*r*-TMC) signals (147.9, 148.1 ppm), indicative of selective block polymer formation (Figure 2.6). The block structures were further evidenced

by DOSY NMR spectroscopy where a single diffusion coefficient was observed for all signals (PvCHC and P(CL-*r*-TMC)) (Figure 2.7).[28]

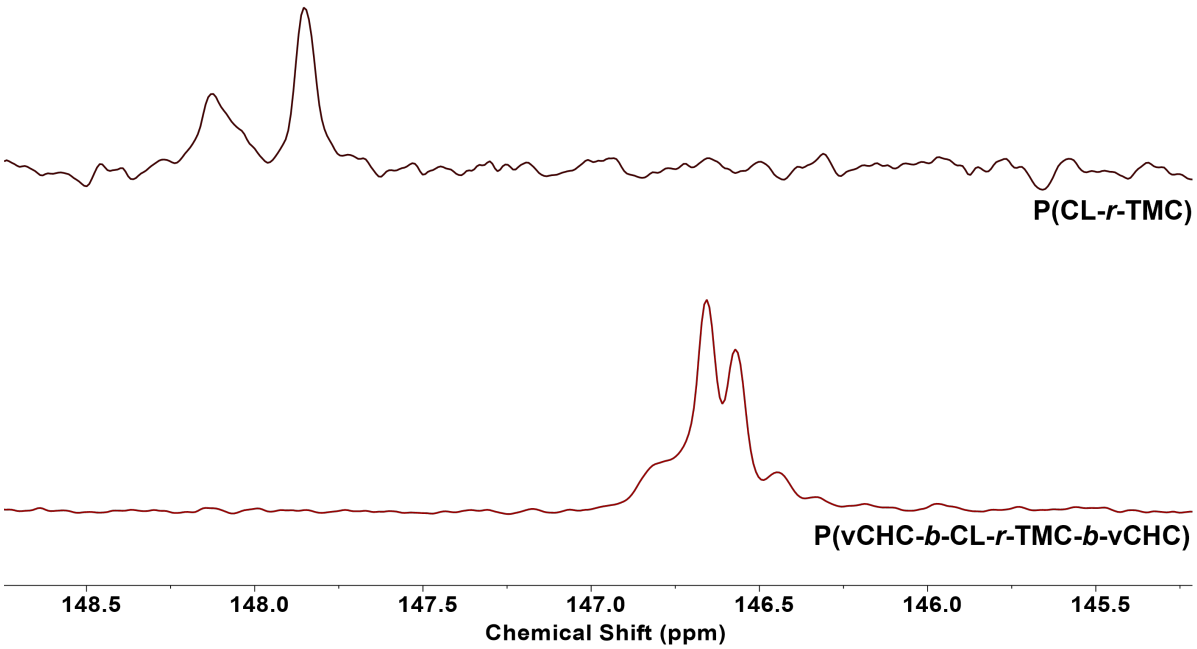


Figure 2.6. Exemplar $^{31}P\{^{1}H\}$ NMR spectra ($CDCl_3$) after reaction of the polymer hydroxyl end groups with 2-chloro-4,4,5,5-tetramethyldioxaphospholone. Top: poly(CL-*r*-TMC), displaying poly(CL)-OH and poly(TMC)-OH end groups. Bottom: poly(vCHC-*b*-CL-*r*-TMC-*b*-vCHC), ABA(47, 0.30) displaying poly(vCHC)-OH end groups.

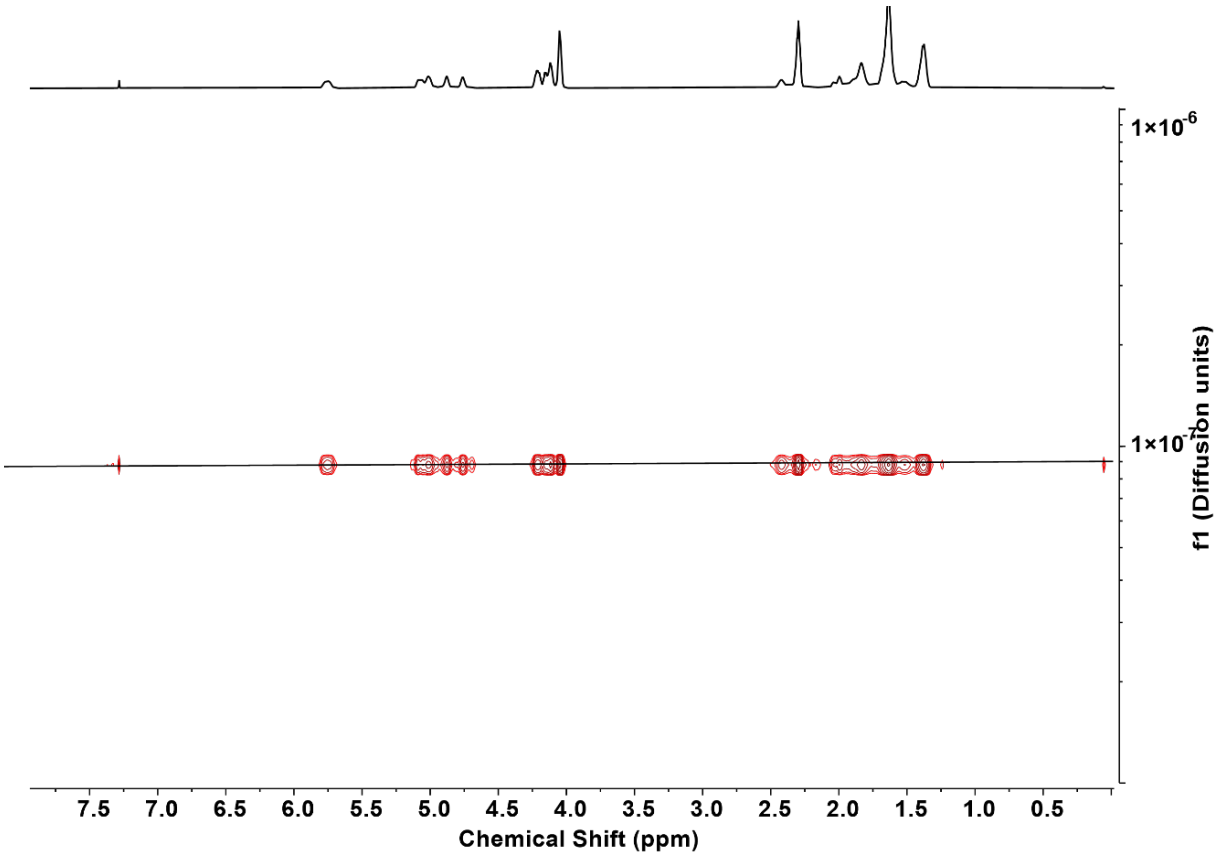


Figure 2.7. Exemplar DOSY NMR spectrum of ABA(47, 0.30), showing a single diffusion coefficient.

SEC measurements, conducted in THF, confirmed monomodal mass distributions at molar mass values close to the expected values (Table 6.2). An increase in molar mass was observed after ROCOP, supporting polycarbonate chain growth from the polyester chain ends to selectively form block copolymers (Figure 2.8).

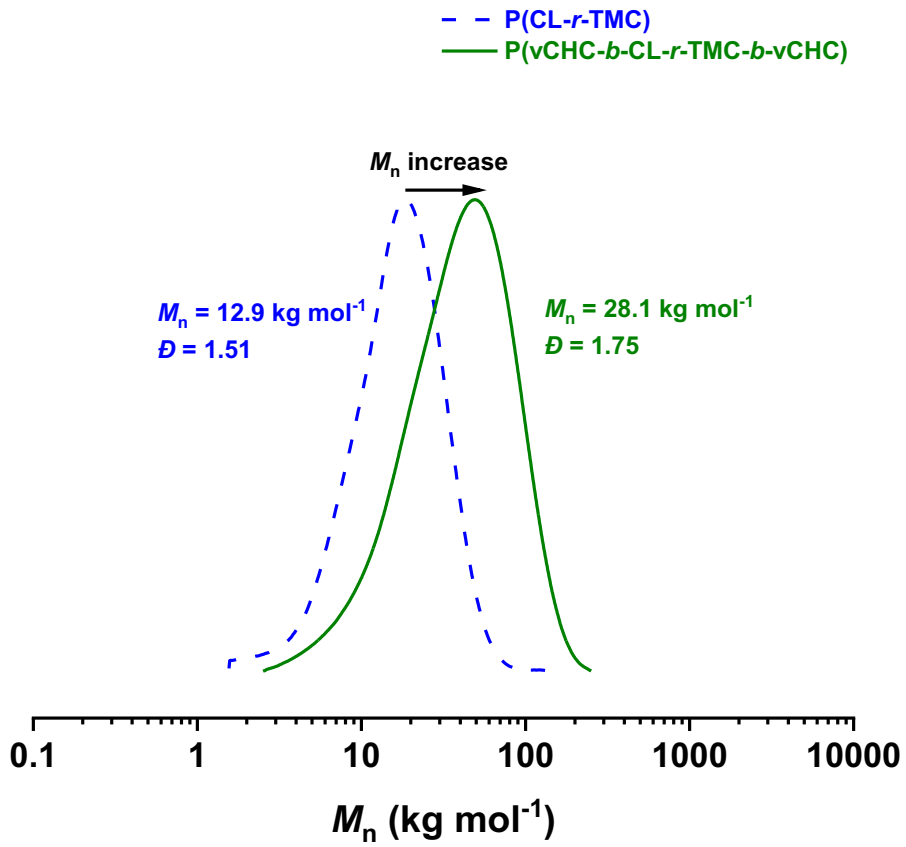


Figure 2.8. SEC traces from aliquots of the switch polymerisation of CL, TMC and vCHO, showing the growth in polymer molar mass after CL/TMC ROP (P(CL-*r*-TMC)) and after the subsequent vCHO/CO_2 ROCOP (P(vCHC-*b*-CL-*r*-TMC-*b*-vCHC)), measured in THF eluent with an RI detector vs narrow PS standards.

2.3.3. Thermal Properties

Thermal data was obtained by DSC, dynamic mechanical thermal analysis (DMA) and thermal gravimetric analysis (TGA). DSC showed that the polymers were fully amorphous and had two glass transition temperatures, consistent with phase separated microstructures. For ABA(50, 0.35), the lower T_g ($T_{g,B}$ = -49 °C) was consistent with the soft B-block phase P(CL-*r*-TMC) (-56 °C) and the upper T_g ($T_{g,A}$ = 89 °C) was associated with the hard PvCHC A-block phase (106 °C) (Figure 2.9, Table 7.1).[14, 29] Further evidence of phase separation was provided

by applying the Fox equation, used for determining the $T_{g,mix}$ of miscible polymer blocks based on the relative block weight fractions.[30] For ABA(50, 0.35), $T_{g,mix}$ was calculated to be -18 °C. This is significantly higher than the observed $T_{g,B}$ thus is supportive of phase separation.

The polymers' thermal properties were also investigated after mixing with LiTFSI to produce an electrolyte. This lithium salt is widely used in polymer electrolyte investigations and 17 wt% of LiTFSI was added in all cases (relative to the overall polymer mass) after optimisation with respect to ionic conductivity, to be discussed in section 2.3.5.[16] Polymer electrolyte films of ~250 μm thickness were prepared by mixing a stirred solution of the polymer and LiTFSI in THF, transferring to a Teflon mould and allowing the solvent to evaporate. Solvent was first removed at ambient temperature and pressure, and then under a vacuum of 10^{-1} mbar at 60 °C for a further 5 days.

DSC characterisation confirmed that the polymer electrolytes remained amorphous but exhibited increased T_g values (Figure 2.9). For example, $T_{g,B}$ of ABA(50, 0.35) increased from -48 to -40 °C after salt addition; this was attributed to lithium coordination resulting in transient soft-block crosslinking and concomitant stiffening. The increase to $T_{g,A}$ (89 to 100 °C) indicated that there are stiffening interactions between the lithium ions and the polymer carbonate groups.[31]

DMA of the ABA(50, 0.35) electrolyte was undertaken to further observe polymer electrolyte phase separation. A rectangular sample of dimensions 35×12.5×1 mm was prepared and an oscillation temperature sweep experiment was conducted between 35 and 115 °C, at a ramp rate of 3 °C min^{-1}, with an amplitude of 20 μm and a frequency of 1 Hz. The sample yielded at 115 °C thus data at higher temperatures were not obtained. The experiment clearly revealed two T_g values via peaks in the tan(δ) at -13 and 114 °C (Figure 2.10). These correspond to the T_g values of the P(CL-*r*-TMC) and PvCHC blocks, respectively.

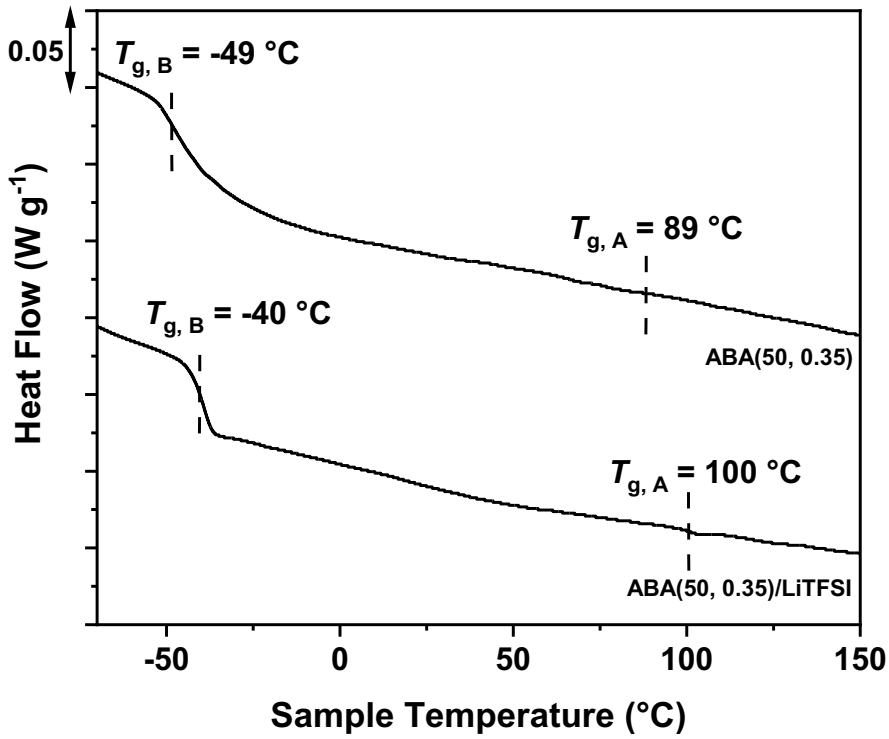


Figure 2.9. DSC traces of ABA(50, 0.35), without (top) and with (bottom) 17 wt% LiTFSI, upper and lower T_g values labelled. Data presented from the second heating cycle; scan rate 10 °C min^{-1}.

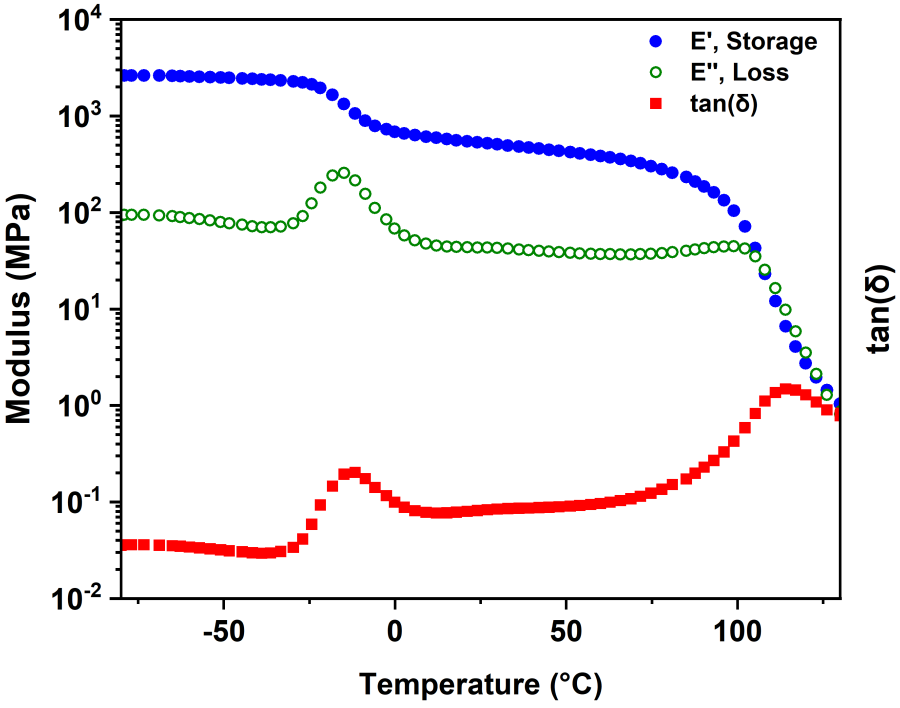


Figure 2.10. Dynamic mechanical temperature analysis (DMA) temperature sweep experiment for ABA(50, 0.35)/LiTFSI.

The polymer electrolytes' thermal stability, $T_{d,5\%}$, was above 200 °C in all cases, as determined by TGA (Figure 2.11, Table 7.1). For example, ABA(50, 0.35)/LiTFSI had a $T_{d,5\%}$ value of 241 °C. Such stability is sufficient for most battery applications and leaves a wide window for processing before degradation. The TGA trace showed three different regions: 200 – 270 °C corresponded to decomposition of the poly(CL-*r*-TMC) block; 270 – 385 °C corresponded to the decomposition of the poly(vCHC) block; and > 385 °C corresponded to LiTFSI. This was deduced by comparing the mass loss of the different temperature regions with the composition of the polymer electrolyte.

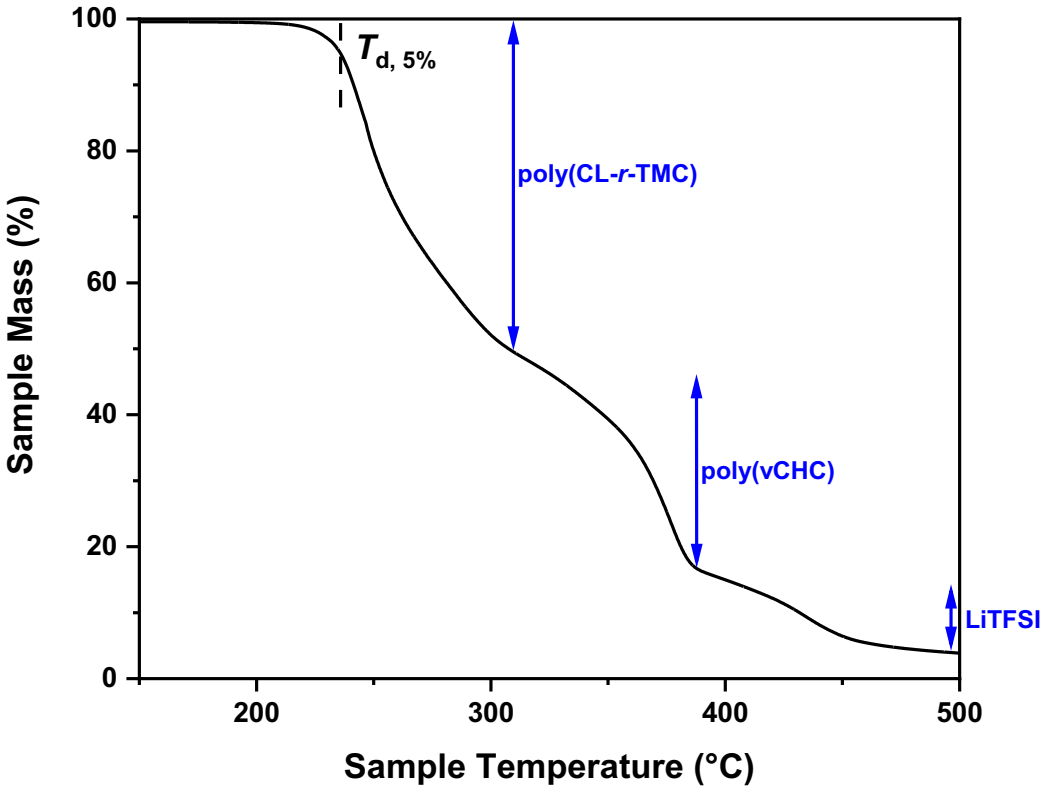


Figure 2.11. TGA trace for ABA(50, 0.35) polymer electrolyte with 17 wt.% LiTFSI.

2.3.4. Small Angle X-Ray Scattering

The phase-separated structures of the triblock copolymer electrolytes in Series II and III have been studied using small angle X-ray scattering (SAXS): this technique was used to identify morphologies through the observation of Bragg reflections.[32] 1D SAXS patterns were plotted as scattering intensity (I(q)) against the scattering vector (q) (Figure 2.12). For many of the polymers, higher order scattering peaks were not observed thus morphology was not determined. Nevertheless, the position of the principal scattering peak (q*) allowed for the domain spacing (*d*) to be calculated: $d = 2\pi/q^*$. Values ranged from 12.6 to 55.1 nm, however, no relationship between *d* and polymer composition was identified (Figure 2.12, Table 7.2).

Some of the polymer electrolytes exhibited higher order scattering peaks. These were indexed relative to q* and phase-separated morphologies were assigned. Of series II, ABA(35, 0.52) exhibited peaks at $q/q^* = 2, 3, 4$, so a lamellar morphology (LAM) was assigned. In series III, ABA(47, 0.30) showed $q/q^* = 1, \sqrt{3}, \sqrt{7}$; ABA(50, 0.35) showed $q/q^* = 1, \sqrt{3}$. Body-centered cubic (BCC) and BCC or hexagonal (HEX) morphologies were thus assigned, respectively.

The absence of higher-order scattering peaks observed in most of these electrolyte samples suggested that the samples exhibited weak long-range order. This is typical for low χ (Flory-Huggins interaction parameter) block copolymers: the blocks are highly compatible as they are both carbonyl-coordinating and can complex Li^+.[33] All polymers with a $DP_{n,hard} > 126$ only exhibited q* and did not show long range order; this could be due to the hard block forming entanglements above this DP which inhibited the equilibrium formation of morphologies. The polymer with the lowest molar mass, AB(26, 0.45) also did not exhibit higher order peaks: its molar mass could be too low for a phase morphology to emerge. Bowden and co-workers did not observe scattering peaks in the small-angle neutron scattering (SANS)

data of their polyester-*b*-carbonate electrolytes; they proposed that LiTFSI affected the resolution of the technique, rather than finding this to be symptomatic of a lack of order in the polymer.[16]

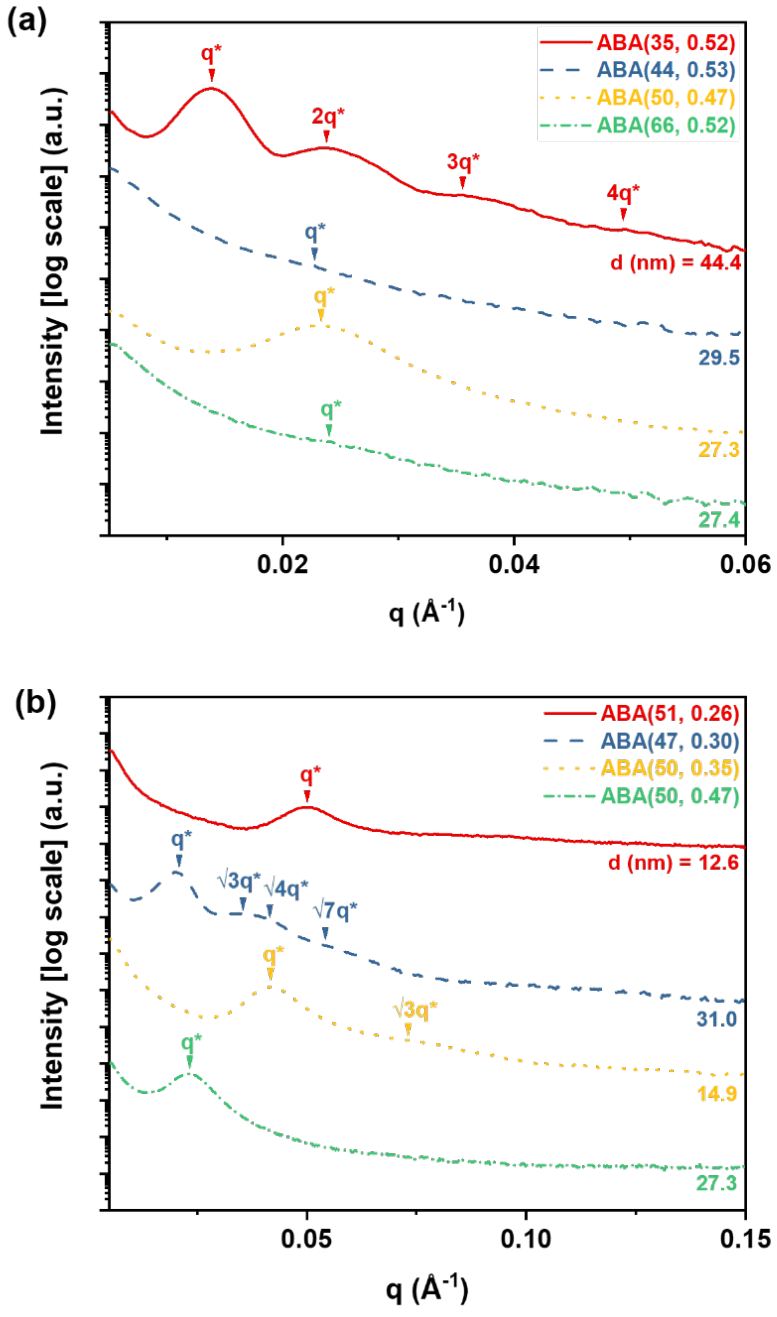


Figure 2.12. SAXS data for (a) Series **II** ABA(M_n, 0.50) and (b) Series **III** ABA(50, w_{PC}) polymer electrolytes. ABA(47, 0.30) and ABA(50, 0.35) were assigned to hexagonally packed spheres (HEX)

or body-centered cubic (BCC) morphology. q^* and the expected Bragg maxima/allowed higher order SAXS reflections for microphase separated cylinders arranged on a hexagonal lattice are labelled.

2.3.5. Li-ion conductivity

Li-ion conductivity was determined by electrochemical impedance spectroscopy (EIS), in a symmetric cell between two gold electrodes. To determine the optimum LiTFSI loading, the ionic conductivity of ABA(50, 0.28) was tested with 17, 20, 30, 40 and 50 wt% LiTFSI (vs the total polymer mass) (Figure 2.13). Samples with 17 wt% LiTFSI were the most conductive, in agreement with investigations by Bowden and co-workers. Too little salt results in too few free charge carriers, whereas too much results in transient crosslinking of the polymer chains.[16, 34] This was observed in the DSC data: as the Li-ion loading increased, the $T_{g,\,B}$ also increased (Figure 2.14). Samples with 40 and 50 wt% LiTFSI had similar T_g values (-22 and -25 °C): this could indicate a saturation of transient crosslinking at these salt concentrations.

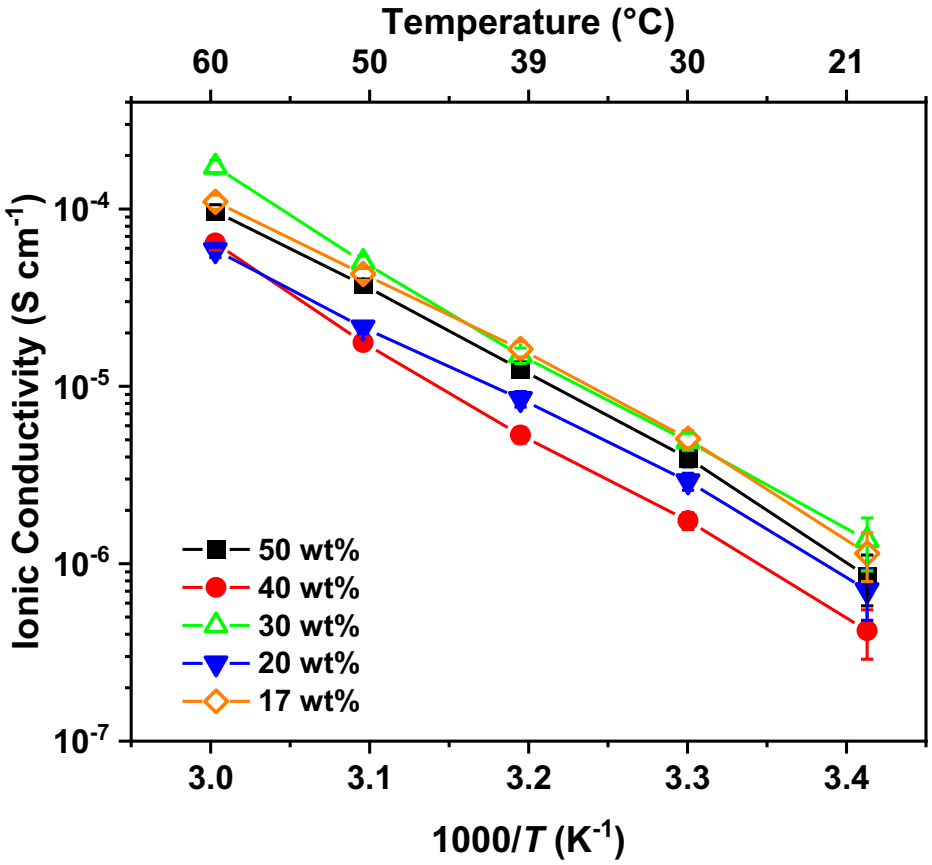


Figure 2.13. Li-ion conductivity as a function of temperature, with varying LiTFSI concentrations.

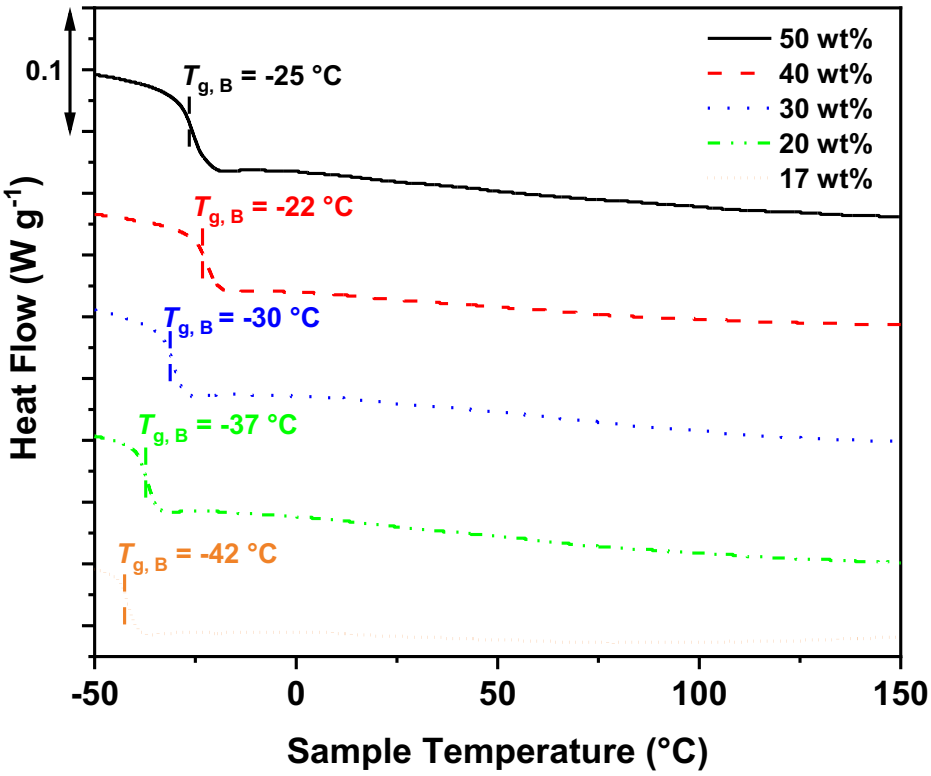


Figure 2.14. DSC traces for ABA(50, 0.28) electrolytes with different LiTFSI contents.

Li-ion conductivity was measured for all polymer electrolytes at 10 °C intervals, from 20 to 70 °C (Table 7.3, Figure 7.1). Nyquist curves were plotted and modelled to the equivalent circuit Q1 + Q2/R2 (Figure 2.15). The curves showed a single semi-circle, indicative of a single interface (in this case, polymer electrolyte|gold electrode). The intercept of the semi-circle with the x-axis is the resistance; the semi-circles were smaller at higher temperatures as the polymer electrolytes had lower resistance. From this, Li-ion conductivity was calculated using the relationship

$$\sigma = \frac{t}{R_{bulk} \times A} \quad \text{(Equation 2.1)}$$

where t = electrolyte thickness, R = resistance and A = electrolyte area.

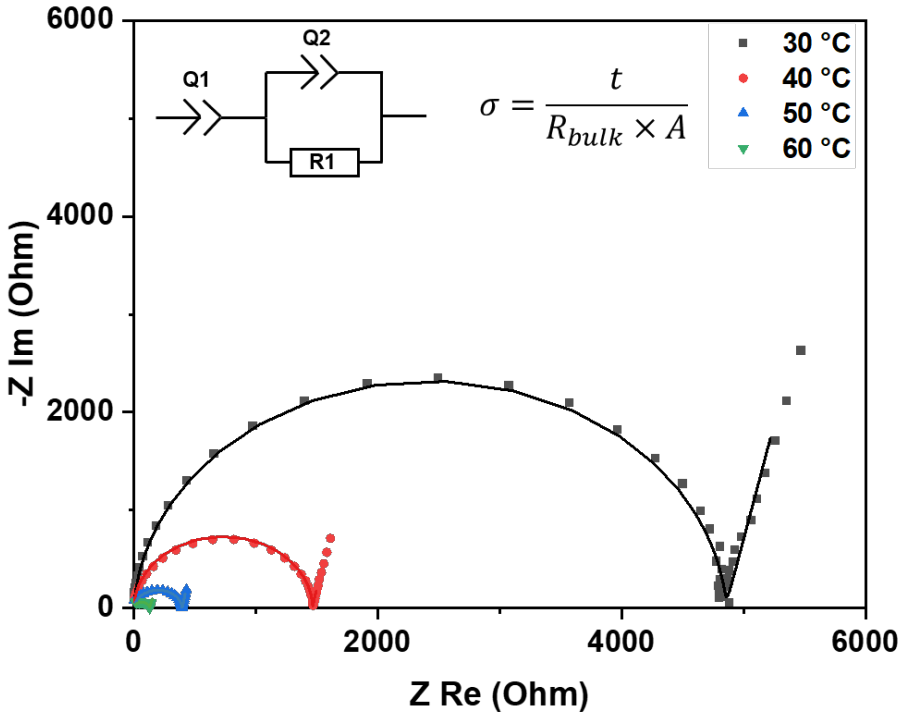


Figure 2.15. Representative Nyquist curves, where points are the collected data and lines represent the fits to the data (Inset: equivalent circuit; model used to determine *R*, then used to estimate σ where *t* = electrolyte thickness, *A* = electrolyte area).

The ABA(50, 0.35)/LiTFSI electrolyte showed the highest ionic conductivity at 30 °C (5.9×10^{-6} S cm^{-1}); this is superior to PEO at 30 °C ($10^{-6} - 10^{-8}$ S cm^{-1}).[11] Its conductivity increased to 2.2×10^{-4} S cm^{-1} at 60 °C (Figure 2.16). This value is highly competitive with other polyester block copolymer electrolytes; PS-*b*-P(CL-*r*-TMC) had a conductivity of 5×10^{-5} S cm^{-1} at 60 °C and PBMA-*b*-P(CL-*r*-TMC) had a conductivity of 7×10^{-5} S cm^{-1} at 60 °C. ABA(50, 0.35) showed a superior conductivity which could be due to the hard block being able to coordinate Li-ions and even facilitating some Li-ion conductivity.

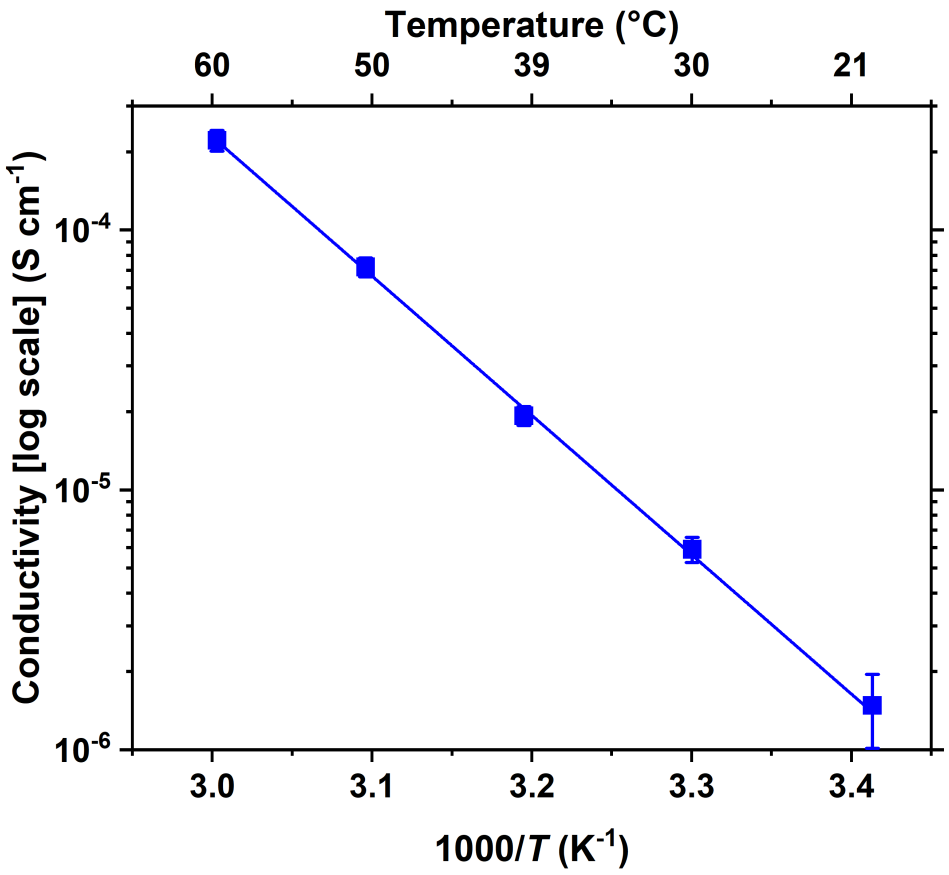


Figure 2.16. Li-ion conductivity as a function of temperature for ABA(50, 0.35)/LiTFSI, obtained by electrochemical impedance spectroscopy.

The temperature dependence of ionic conductivity was modelled using a Vogel-Fulcher-Tammann (VFT) fit:

$$\sigma = AT^{-1/2}\exp\left[-E_a/(T - T_0)\right] \quad \text{(Equation 2.2)}$$

where A is a constant that is proportional to the number of Li-ions; E_a is the Li-ion transport activation energy; and T_0 is the temperature where configurational entropy is zero ($T_0 \approx T_g - 50$ K). All of the polymer electrolytes in the series fit the VTF model. This is consistent with ionic conductivity governed by polymer chain segmental motion, as is common for polymer electrolytes.[35] The gradient indicated the ion transport activation energy; ABA(50, 0.35) had a relatively low E_a of 17.0 (± 0.7) kJ mol^{-1} (Figure 2.17).

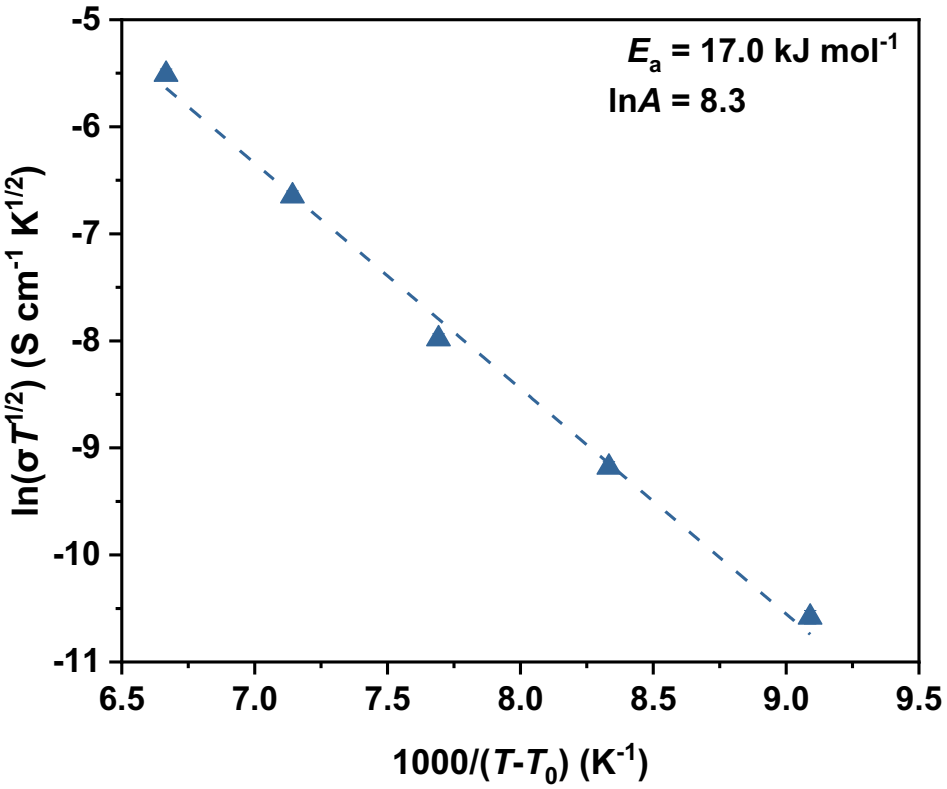


Figure 2.17. VTF fit for ABA(50, 0.35)/LiTFSI.

The relationships between the ionic conductivity and block structure, M_n and w_{PC} were explored. Comparing polymers in Series I (AB) and Series II (AB), both with w_{PC} fixed at 0.5, facilitated understanding of the optimum structure and molar mass. The block structure had a major impact, with overall trends being quite different for AB vs ABA type polymers of similar overall molar mass and compositions. For polymers in Series I, the ionic conductivity decreased with increasing molar mass. For, AB(26, 0.45), $\sigma = 1.5 \times 10^{-6}$ S cm^{-1} at 30 °C; whereas for AB(69, 0.58), $\sigma = 2.1 \times 10^{-8}$ S cm^{-1} (Figure 2.17, Table 7.3). The decreased conductivity (vs molar mass) is linked to the soft block $T_{g,B}$, which increased from -52 °C for AB(26, 0.45) to 0 °C for AB(69, 0.58). A good fit of the temperature dependence of ionic conductivity to the VFT model supported ionic conductivity being assisted by polymer chain segmental motion, related to $T_{g,\,B}$.

For the ABA polymers in Series II, the reverse relationship was observed: conductivity increased with molar mass despite constant or increased $T_{g,B}$. For ABA(35, 0.52), $\sigma = 6.6 \times 10^{-7}$ S cm^{-1} at 30 °C; whereas for ABA(66, 0.52), $\sigma = 5.5 \times 10^{-6}$ S cm^{-1} (Figure 2.18). This is attributed to slower dynamics of mobility from pinning at both ends by the rigid PvCHC blocks. This restricted segmental motion at the PvCHC/P(CL-*r*-TMC) interfaces is expected to be less influential at higher molar masses where the fraction of these interfaces is lower.[19]

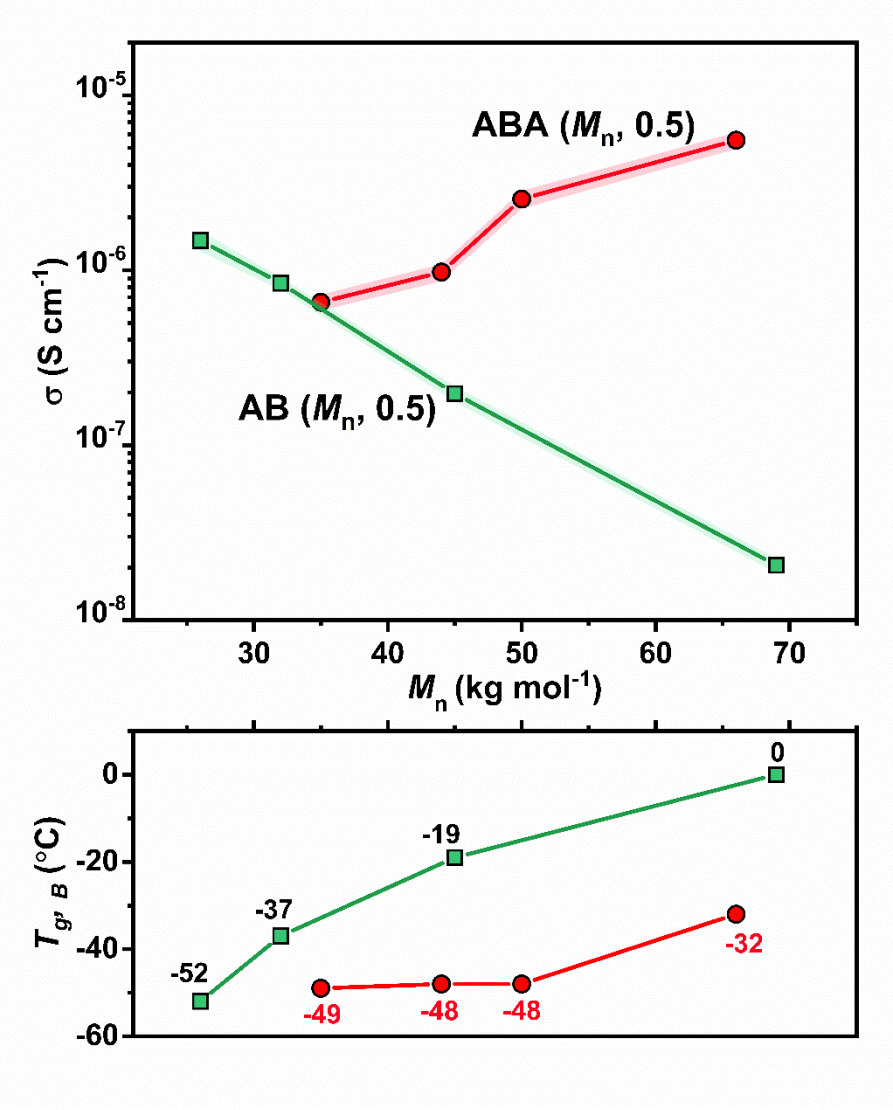


Figure 2.18. Top: M_n-dependence of ionic conductivity (σ) at T = 30 °C for AB vs ABA polymers/LiTFSI at fixed w_{PC} ~0.5. Bottom: Corresponding DSC $T_{g,B}$ values.

Since the ABA polymers showed the most promising conductivity values, the influence of w_{PC} for these polymers was then investigated (Series III). Keeping the overall molar mass

constant at 50 kg mol^{-1} and changing only w_{PC}, higher conductivity was achieved for w_{PC} 0.3 – 0.35 (Figure 2.19). It is proposed that at these compositions, the block polymers formed a common microstructure which maximised ion transport. SAXS confirmed this hypothesis since ABA(50, 0.30) and ABA(50, 0.35) formed weakly-ordered microstructures; either body-centered cubic or hexagonal (Figure 2.19). It is feasible that these microstructures provided channels that accelerated ion transport; this is consistent with previous reports of weakly ordered morphologies improving conductivity.[36, 37]

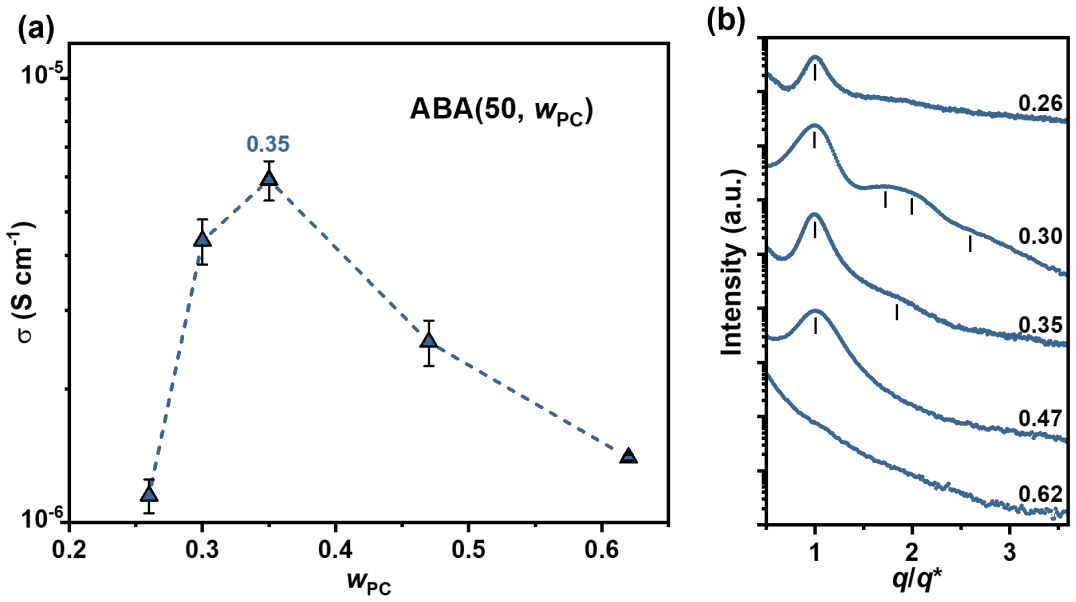


Figure 2.19. (a) Hard weight content (w_{PC}) dependence of Li-ion conductivity (σ) at 30 °C, for ABA polymers/LiTFSI, with M_n fixed at 50 kg mol^{-1}. (b) Corresponding SAXS data for the polymer electrolytes.

2.4. Polymer Electrolyte Properties

2.4.1. Electrochemical Properties

2.4.1.1. Oxidative Stability

A goal of this work is to improve upon the oxidative stability of PEO based systems (< 3.9 V).[13] To assess the electrochemical stability of the new block polymers, linear sweep voltammetry (LSV) was conducted using the lead electrolyte sample, ABA(50, 0.35)/LiTFSI. Oxidative stability was measured versus lithium metal with a stainless-steel counter electrode. The stability was assessed from the open-cell voltage (OCV = 2.51 V) to 6 V, at 60 °C, at a sweep rate of 0.1 mV s^{-1}. This is a slow scan rate compared to many literature reports; this is recommended for polymer electrolytes, as compared to liquid electrolytes, some solid-state reactions are slower.[38]

The electrolyte was stable to 5.2 V (vs Li/Li^+) which is important for any application using high voltage cathodes (such as Ni- and Mn-rich oxides).[12] A PEO electrolyte tested in the same experimental conditions achieved an oxidative stability < 3.9 V (Figure 2.20). Additionally, cyclic voltammetry (CV) experiments were conducted from 3 to 4.5 V, using the same cell configuration, at a scan rate of 0.5 mV s^{-1} with the electrolyte showing consistently high stability throughout 35 cycles (Figure 2.21). Its stability was comparable and superior to other polyester/carbonate-based electrolytes, e.g. P(CL-*r*-TMC) (5 V) or PS-*b*-P(CL-*r*-TMC) (5 V).[14, 15]

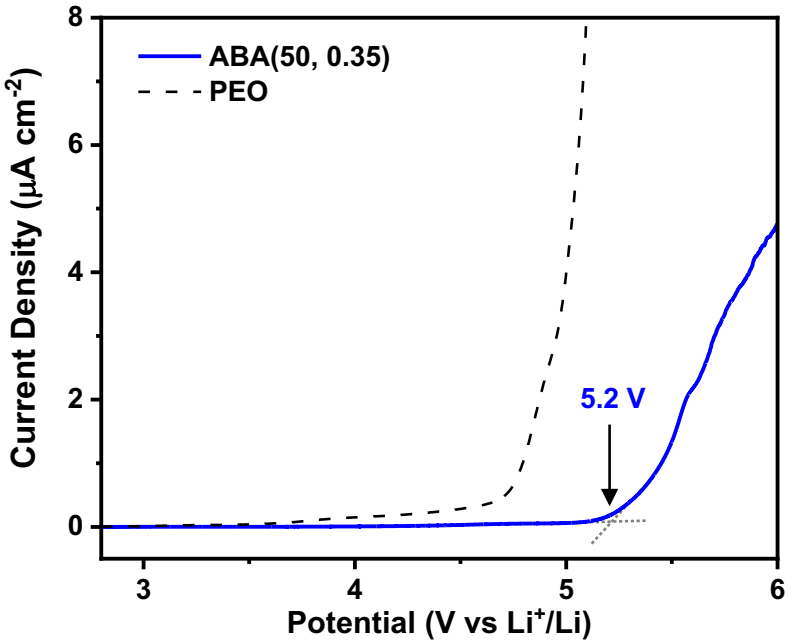


Figure 2.20. Oxidative stability vs Li metal and stainless-steel counter electrode, measured by LSV at 60 °C, 0.1 mV s^{-1} scan rate, for ABA(50, 0.35) and PEO.

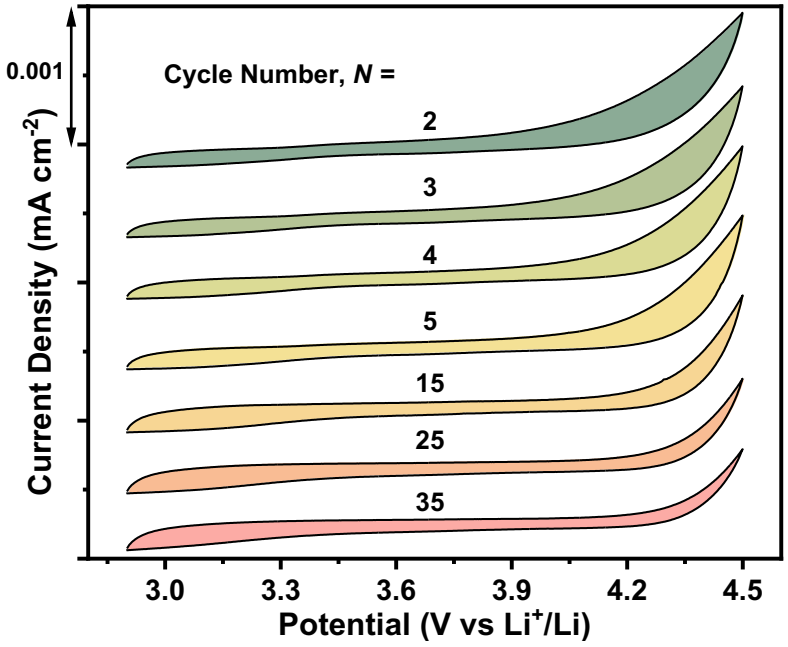


Figure 2.21. Oxidative stability vs Li metal and stainless-steel counter electrode, measured by CV at 0.5 mV s^{-1} scan rate, recorded over 35 cycles.

2.4.1.2. Li-ion Transference Number

The Li-ion transference number (t_{Li+}) is the ratio of Li-ion mobility to the total ion migration in the electrolyte:

$$t_{Li^+} = \frac{\mu_{Li^+}}{\mu_{Li^+} + \mu_{TFSI^-}} \quad \text{(Equation 2.3)}$$

where μ = ion migration. Ideally, the transference number would approach unity, i.e. ion migration is solely due to Li-ion movement and the counter anion does not contribute. Carbonyl-coordinating solid polymer electrolytes commonly have lithium transference numbers superior to PEO (> 0.4 vs 0.1 – 0.3).[19, 39, 40] This is in part due to strong Li-ion complexation by the ether oxygen in PEO, making Li^+ less able to move and thus the anion has a greater contribution to the overall ion transport.[41] Transference number is commonly measured by potentiostatic polarisation (Bruce-Vincent method) or by pulsed-field gradient (PFG) NMR spectroscopy.[39, 42, 43] Potentiostatic polarisation is often favoured due to its simplicity, speed and low cost; however, it is designed for binary and ideal solid electrolytes.[44] PFG NMR spectroscopy is less widespread but allows for the study of non-binary and multicomponent systems.[43] This is of interest for block copolymer electrolytes as different dynamics may be observed in the different domains.[45] Both methods have been used to obtain t_{Li+} of the lead polymer electrolyte, ABA(50, 0.35)/LiTFSI.

The transference number of the electrolyte was first found by solid-state PFG NMR spectroscopy. Solid state ^{7}Li NMR spectroscopy of the ABA(50, 0.35) electrolyte revealed a broad asymmetrical peak (0.89 ppm) which was modelled and deconvoluted into a broader peak at 2.73 ppm and a sharper peak at 0.85 ppm. These were assigned by studying the NMR spectra of the constituent homopolymers: PvCHC showed broad peak at 0.53 ppm and P(CL-*r*-TMC) showed a sharp peak at 0.81 ppm. Thus, in the spectra of ABA(50, 0.35), 2.73 ppm corresponded to the PvCHC-rich domain and 0.85 ppm to the P(CL-*r*-TMC)-rich domain

(Figure 2.22). The same study was conducted using ^{19}F NMR spectroscopy: a broad asymmetrical peak was observed which was deconstructed into peaks corresponding to PvCHC- (-78.2 ppm) and P(CL-*r*-TMC)-rich domains (-77.0 ppm) (Figure 2.23). This evidenced that both blocks are able to coordinate Li-ions. Note that the shifts of the block-copolymers do not perfectly align with that of the homopolymers. This can be attributed to the block copolymer showing some degree of phase mixing; nevertheless, a broad peak corresponding to PvCHC and a sharp speak corresponding to P(CL-*r*-TMC) was observed.

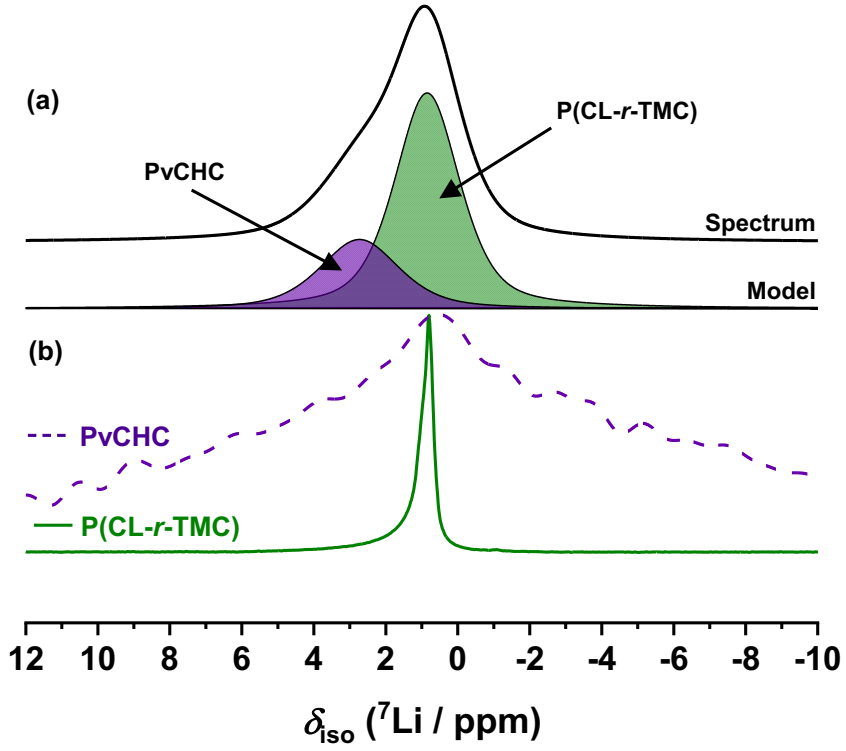


Figure 2.22. (a) ^{7}Li NMR spectrum of ABA(50, 0.35)/LiTFSI, showing the spectrum deconvoluted into two distinct peaks; (b) ^{7}Li NMR spectrum of PvCHC and P(CL-*r*-TMC) homopolymer electrolytes.

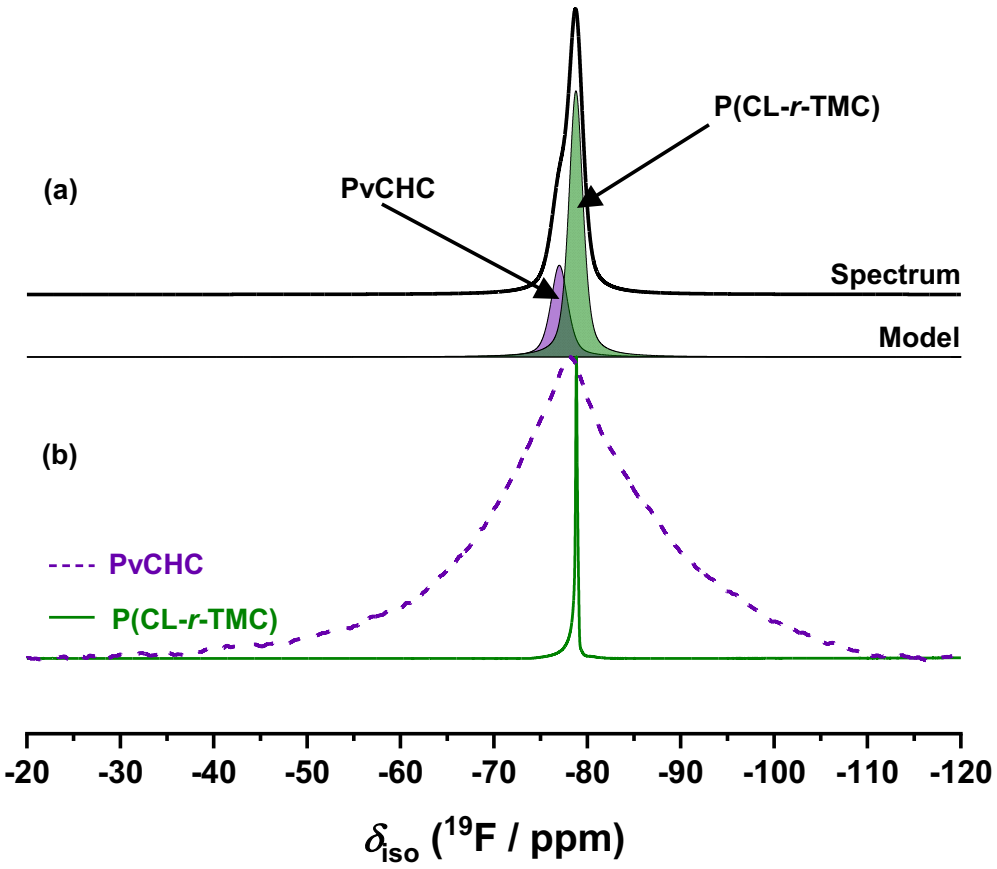


Figure 2.23. (a) ^{19}F NMR spectrum of ABA(50, 0.35)/LiTFSI, showing the spectrum deconvoluted into two distinct peaks; (b) ^{19}F NMR spectrum of PvCHC and P(CL-*r*-TMC) homopolymer electrolytes.

The diffusion of Li^+ was observed by ^{7}Li NMR spectroscopy; the diffusion of $TFSI^-$ ions was observed by ^{19}F NMR spectroscopy (Figures 2.24, 2.25). This assumed a fully dissociated LiTFSI salt, likely at this low salt content, thus the measured diffusion coefficients for Li- and F-containing species correlated to Li^+ and $TFSI^-$.[44] Two distinct diffusion coefficients were observed in the spectra, corresponding to the hard and soft domains (Table 7.4). From the diffusion coefficients of the Li and F species in the hard and soft domains, two t_{Li+} were estimated: the hard domain had a t_{Li+} of 0.52; the soft domain had a t_{Li+} of 0.44. To find the overall Li-ion transference number, these values were averaged, considering the proportion of each block in the polymer, i.e. (0.435 × 0.65) + (0.522 × 0.35) = 0.47.

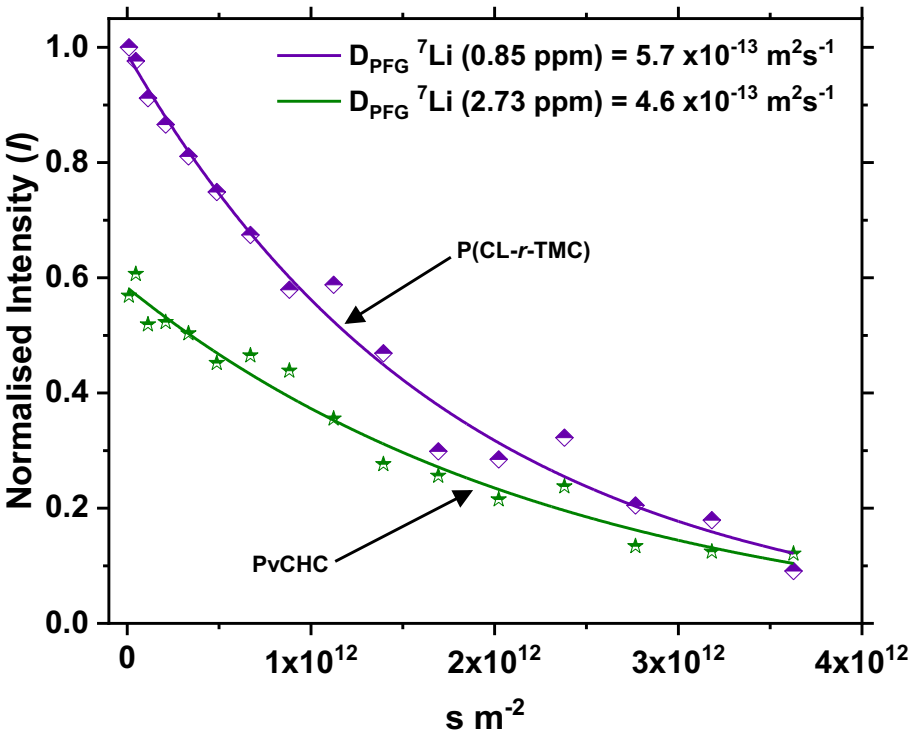


Figure 2.24. Diffusion coefficients of ABA(50, 0.35)/LiTFSI by ^{7}Li PFG NMR spectroscopy.

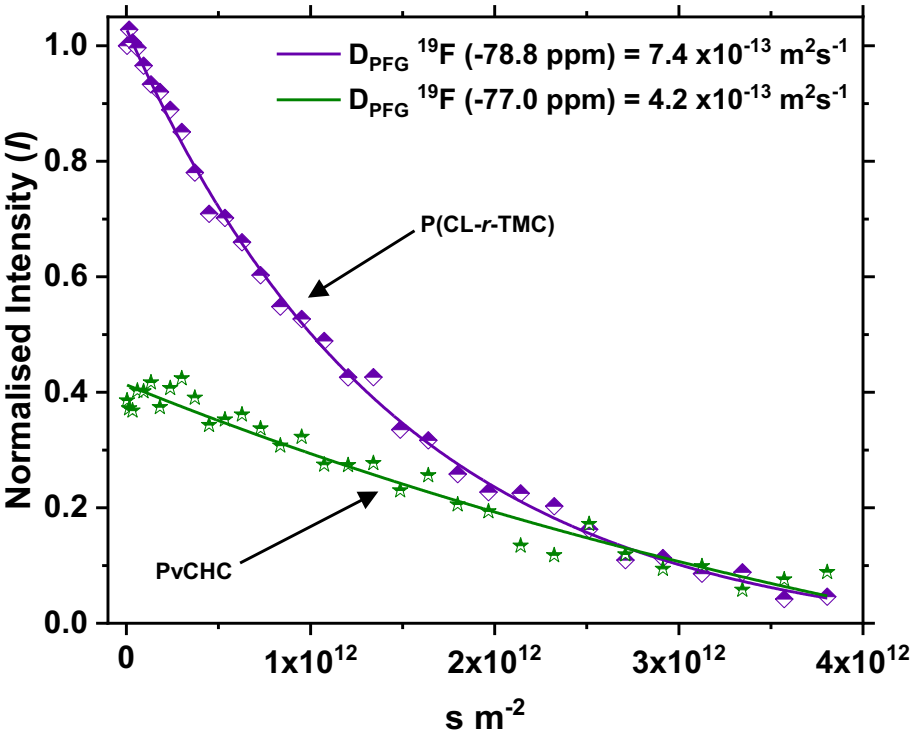


Figure 2.25. Diffusion coefficients of ABA(50, 0.35)/LiTFSI by ^{19}F PFG NMR spectroscopy.

The Bruce-Vincent method was also used to calculate t_{Li+}. Symmetric steel|ABA(50, 0.35)/LiTFSI|steel cells were polarised with a 50 mV potential. This induced a concentration gradient and the time taken to reach a steady-state current was observed. Using the equation

$$t_{Li^+} = \frac{I^S(\Delta V - I^0 R^0)}{I^0(\Delta V - I^S R^S)} \quad \text{(Equation 2.4)}$$

where *I* is current, *V* is potential, *R* is resistance and superscripts *0* and *S* correspond to the time when the potential is applied and the time at which steady-state current is reached, a lithium-transference number of 0.57 was calculated (Table 7.4). This is comparable to values obtained for similar block copolymer electrolytes by this method in the literature.[16]

2.4.2. Mechanical Properties

2.4.2.1. Elastic Recovery

In a battery, polymer electrolytes experience both stress and strain during charge/discharge cycles, therefore it is important that polymers are sufficiently elastomeric and robust. The elastic recovery of the ABA(50, 0.35) electrolyte was determined by subjecting samples to 10 hysteresis cycles at 20% strain, at an extension rate of 10 mm min^{-1}. The samples were dumbbell-shaped with uniform thickness (~ 250 μm) and the remaining dimensions conformed to ISO 527-2 type 5B. 20% strain was used as it is a little above the volume change experienced by high-capacity cathode particles.[2] The first elastic cycle differs to those subsequent due to the initial disentangling of polymer chains. Overall, the electrolyte showed a good elastic recovery of 68%. This value is lower than for an ideal elastomer but could be sufficient in terms of electrolyte cell performance (Figure 2.26).

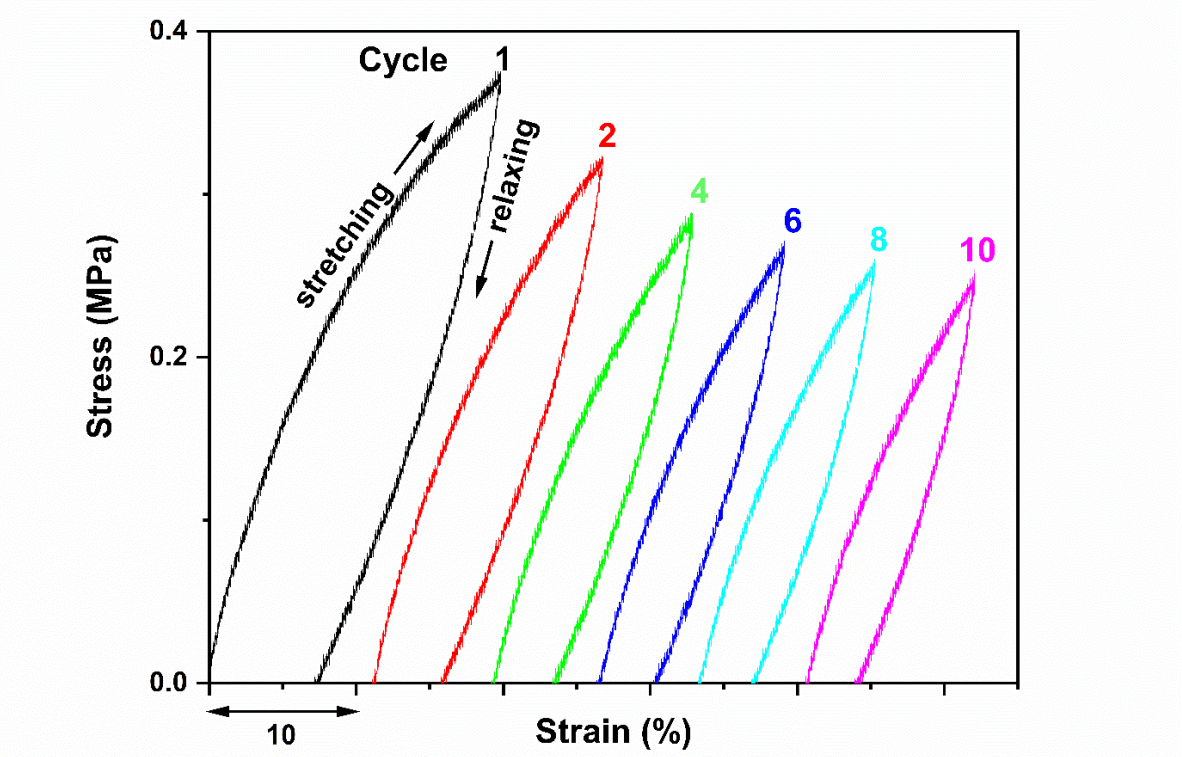


Figure 2.26. Elastic behaviour of ABA(50, 0.35)/LiTFSI. Cyclic tensile testing (20% strain, 10 mm min^{-1} extension rate). Alternate cycles, horizontally shifted, showed for clarity.

2.4.2.2. Rheology

Rheology was conducted to investigate the viscoelastic properties of the ABA(50, 0.35) electrolyte. In dynamic oscillatory rheology, a sinusoidal stress is applied to a sample at a defined frequency, resulting in strain deformation. The stress required to produce this deformation is measured thus modulus can be calculated using the relationship

$$G = \frac{\sigma}{\gamma} = \frac{M}{\theta} \times K \quad \text{(Equation 2.5)}$$

where G = modulus, σ = stress, γ = shear strain, M = torque, θ = angular displacement, K = geometric constants (relating to initial sample dimensions).

Temperature sweep experiments show how the mechanical properties change in response to temperature. The sample was subjected to an oscillation frequency of 1 Hz at 1% strain. This was in the material's linear viscoelastic region; it is where viscoelastic parameters

are strain independent and exhibit a linear, Hookean stress-strain relationship. The storage and loss moduli (*G*', *G*'') were then measured with increasing temperature, from 30 to 120 °C. The electrolyte exhibited a crossover point (*G*'=*G*'') at 73 °C (Figure 2.27). Below this temperature, the Li-ion conducting binder behaved as an elastic solid with a low *G*' (2 – 0.2 MPa), resulting in a soft, more resilient polymer. Above this temperature the material became viscous and processable.

The frequency dependence of modulus was then measured. At a constant temperature and strain (1%), the sample was subjected to oscillation frequencies from 100 to 0.1 Hz and its storage and loss moduli were measured. This experiment was repeated at 10 °C temperature intervals between 30 and 130 °C; a time-temperature superposition graph was then generated by applying shift factors (a_T) to the frequency sweep data obtained at each temperature, from a reference temperature of 60 °C. The shift factors were derived using the Williams-Landel-Ferry (WLF) equation

$$\log(a_T) = {-c_1(T - T_0)}\Big/{c_2 + (T - T_0)} \quad \text{(Equation 2.6)}$$

where a_T = shift factor. T = temperature, T_0 = reference temperature, c = constants from curve fitting.[46] For ABA(50, 0.35), the WLF fit had an R^2 value of 0.999 (Figure 7.2). This enabled observation of the frequency response of the material beyond the instrument's range. The moduli of the polymer electrolytes increased with frequency, as observed in the literature: between 0.002 and 3 rad s^{-1}, G'' > G' thus viscous behaviour was observed; between 3 and 200,000 rad s^{-1} G' > G'' so elastic behaviour was observed (Figure 2.27).[15]

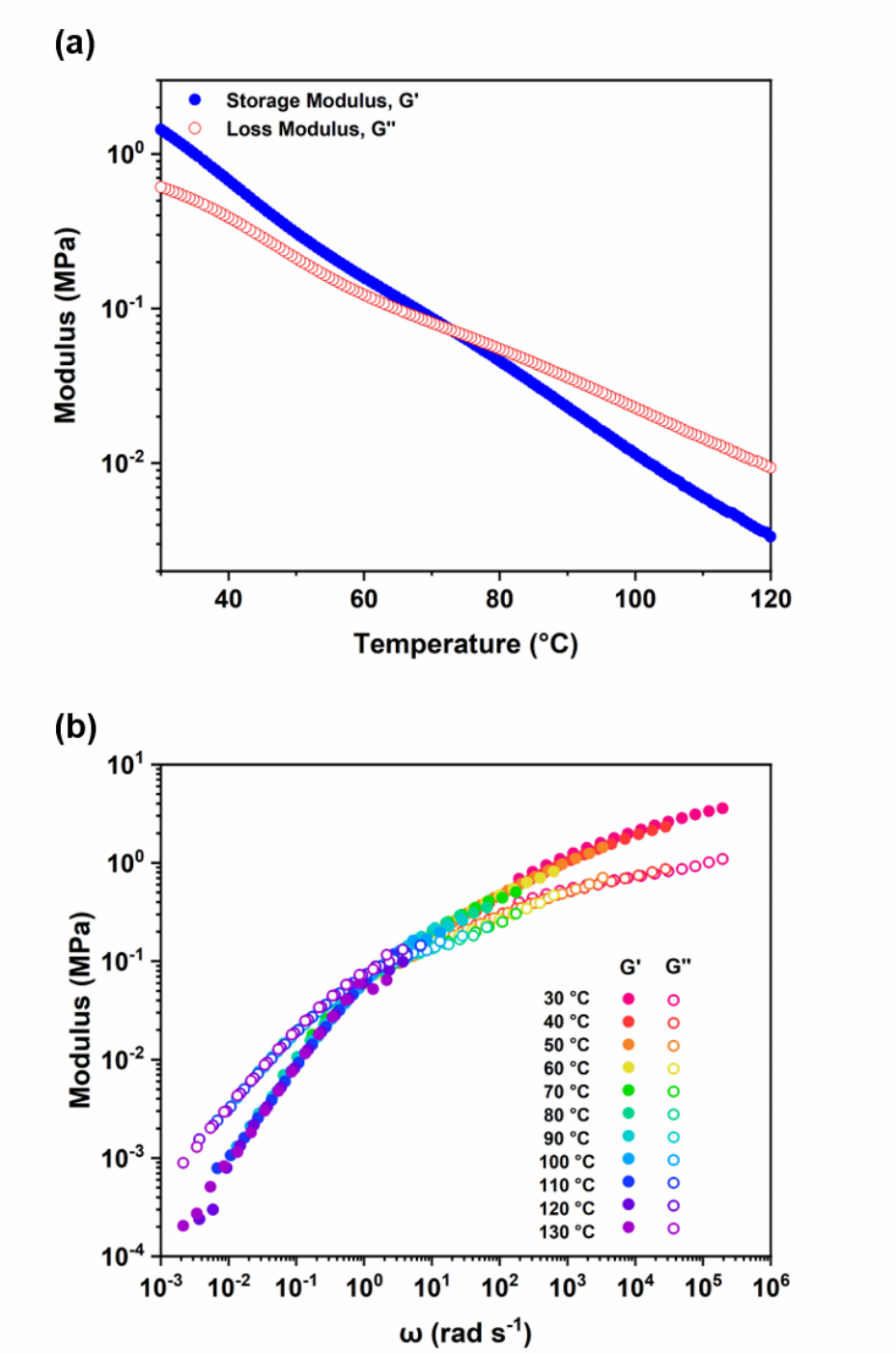


Figure 2.27. Rheological data obtained for ABA(50, 0.35)/LiTFSI. (a) Storage and loss moduli as a function of temperature, conducted at a frequency of 1 Hz and a strain of 1%. (b) Time-temperature superposition (TTS) graph collated by measuring the storage and loss moduli as a function of oscillation frequency and repeating this at 10 °C intervals between 30 and 130 °C.

2.5. Cell Performance

2.5.1. Chemical Stability

The chemical stability of ABA(50, 0.35)/LiTFSI was tested with Li_6PS_5Cl, an extensively studied inorganic solid-state electrolyte. This was to test the feasibility of using the polymer in conjunction with Li_6PS_5Cl in an all-solid-state battery. A cell was assembled with the structure Ni|polymer|Li_6PS_5Cl|polymer|Ni and its electrochemical impedance spectrum was recorded 150 times, once per hour, at 60 °C. The shape of the spectrum remained the same for each run; this was supportive of the polymer having good chemical stability with Li_6PS_5Cl (Figure 2.28). A change in the shape, size, or number of semi-circular loops would be indicative of a chemical reaction which produced a new phase in the cell.

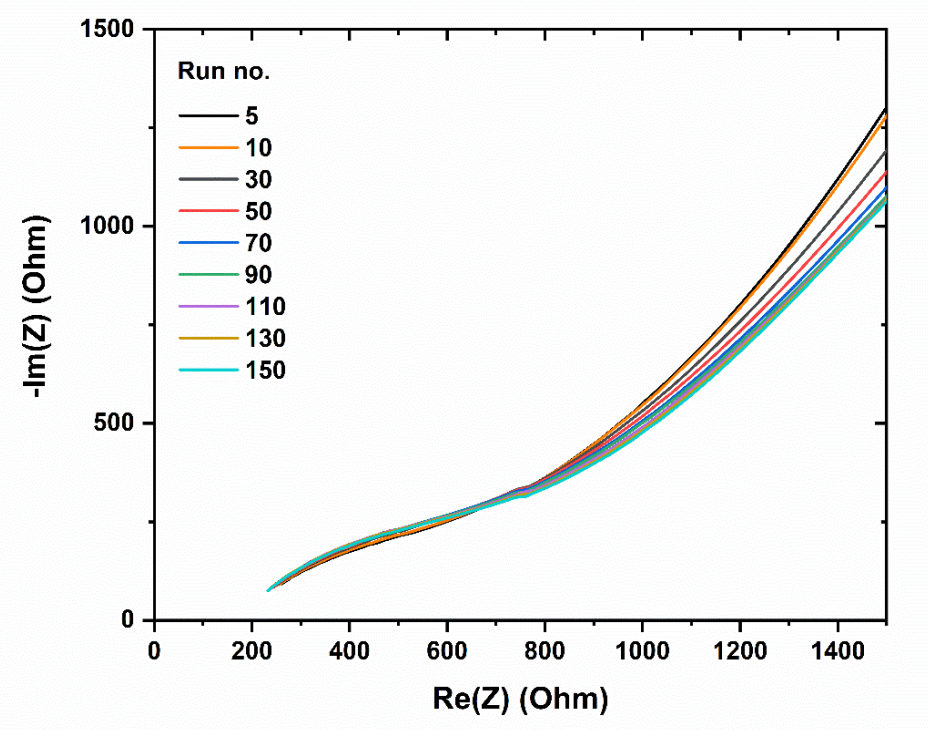


Figure 2.28. EIS plots of a Ni|PE|Li_6PS_5Cl|PE|Ni cell, at 60 °C, with one measurement recorded per hour and where PE is ABA(50, 0.35)/LiTFSI.

2.5.2. Cell Cycling

Due to its good ionic conductivity, excellent oxidative stability and viscoelasticity, ABA(50, 0.35)/LiTFSI was tested as a cathode binder for use in an all-solid-state battery. The ABA(50, 0.35) electrolyte film was cryo ball-milled to produce a fine powder and dry-mixed into a free-standing composite cathode. The polymer was integrated in 5 wt% with high-performance cathode material sc-NMC811, ceramic electrolyte Li_6PS_5Cl and carbon nanofibre (CNF), in a 70/23/2 wt% ratio (Figure 2.29). The resulting cathode composite was then densified at 250 MPa before being assembled into a full solid-state cell with a $Li_4Ti_5O_{12}$ (LTO) anode and Li_6PS_5Cl solid electrolyte.

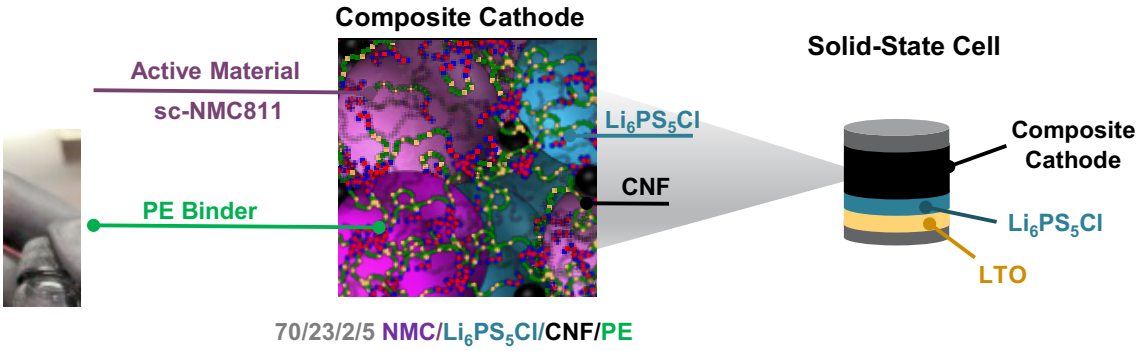


Figure 2.29. Fabrication of composite cathode and solid-state cell configuration, LTO| Li_6PS_5Cl |NMC-PE composite.

The cell was cycled at 60 °C with a low applied pressure (1 MPa). A high initial discharge capacity of 189 mAh g^{-1} was observed, compared to 177 mA h g^{-1} with analogous cells prepared with PTFE binder (Figures 2.30, 2.31). The ABA(50, 0.35) binder was investigated separately with LiTFSI and LiFSI salt. Whereas the capacity with the TFSI anion declined with the number of charge/discharge cycles (73% capacity retention after 200 cycles), this was not observed with FSI (96.7% capacity retention after 200 cycles), with only a small reduction in initial discharge capacity (186 mAh g^{-1}). (Figures 2.30, 2.31). This could be

attributed to the TFSI anion forming unstable interfaces with the cathode.[47, 48] ABA(50, 0.35)/LiFSI also outperformed the PTFE binder, which retained 86.4% capacity over 200 cycles starting at 177 mA h g^{-1} (Figures 2.30 – 31). Furthermore, the composite cathode also showed excellent coulombic efficiency of > 99.7%.

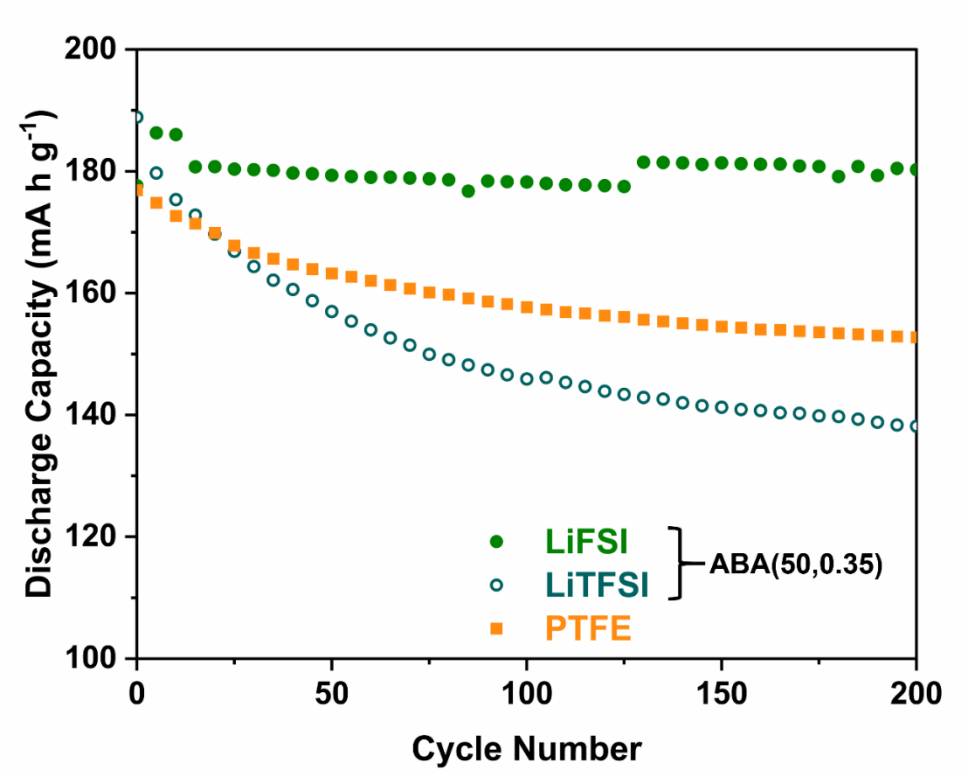


Figure 2.30. Specific discharge capacity vs cycle number at T = 60 °C, 1 MPa stack pressure.

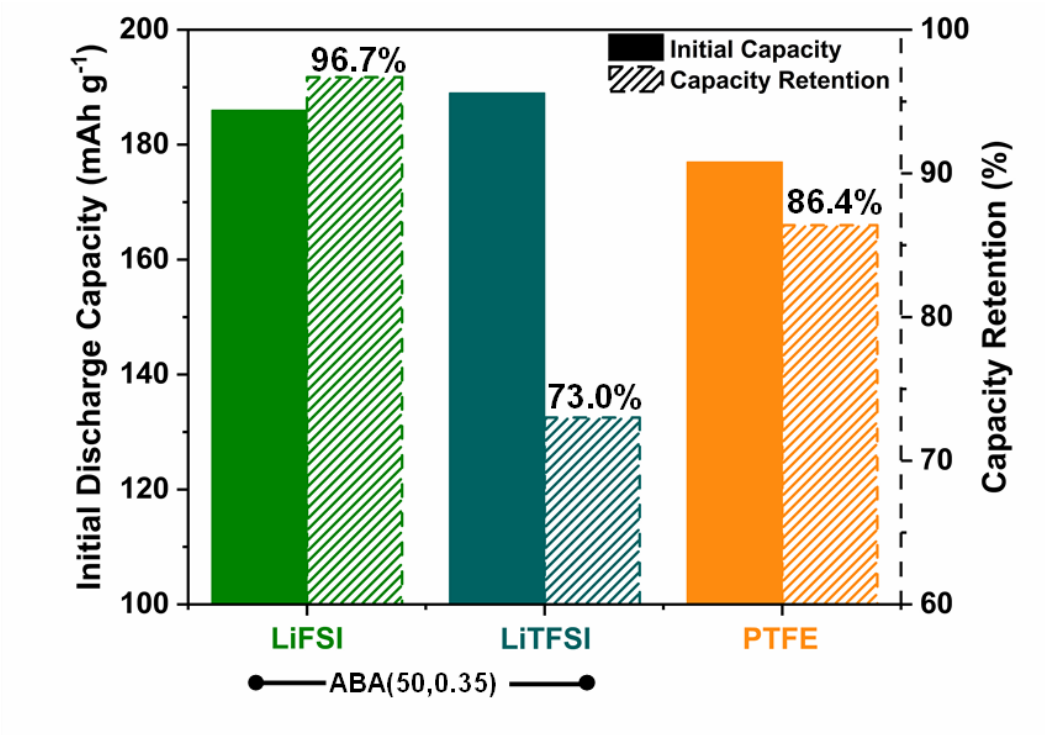


Figure 2.31. Initial discharge capacity and capacity retention after 200 cycles (labelled).

Potential vs capacity profiles were observed for cycles 1, 50, 100, 150 and 200 for cells with the ABA(50, 0.35)/LiFSI binder. The capacity clearly decreased with cycle number; from 186 mAh g^{-1} after cycle 1 to 180 mAh g^{-1} after cycle 200 (Figure 2.32); the mirrored charge/discharge cycles indicated high coulombic efficiency. The potential vs capacity profile for cycle 1 has been compared for cells utilising ABA(50, 0.35)/LiFSI, ABA(50, 0.35)/LiTFSI

and PTFE cathode binders (Figure 2.33). ABA(50, 0.35) had the largest discharge capacity (185 mAh g^{-1} with LiTFSI; 183 mAh g^{-1} with LiFSI) compared to 177 mAh g^{-1} for PTFE.

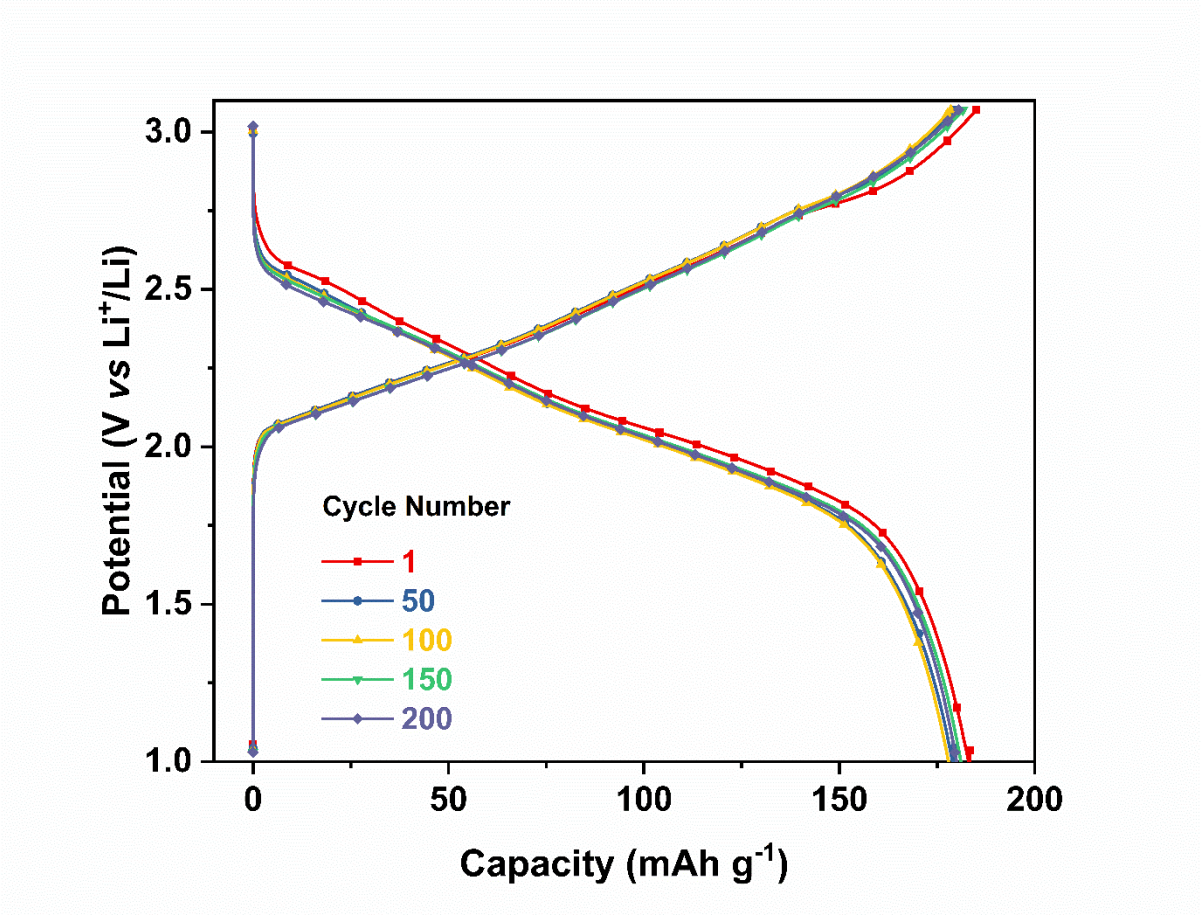


Figure 2.32. Charge-discharge profiles for the LTO|Li_6PS_5Cl|NMC-PE cell where PE is ABA(50, 0.35)/LiFSI, at cycle numbers 1, 50, 100, 150 and 200.

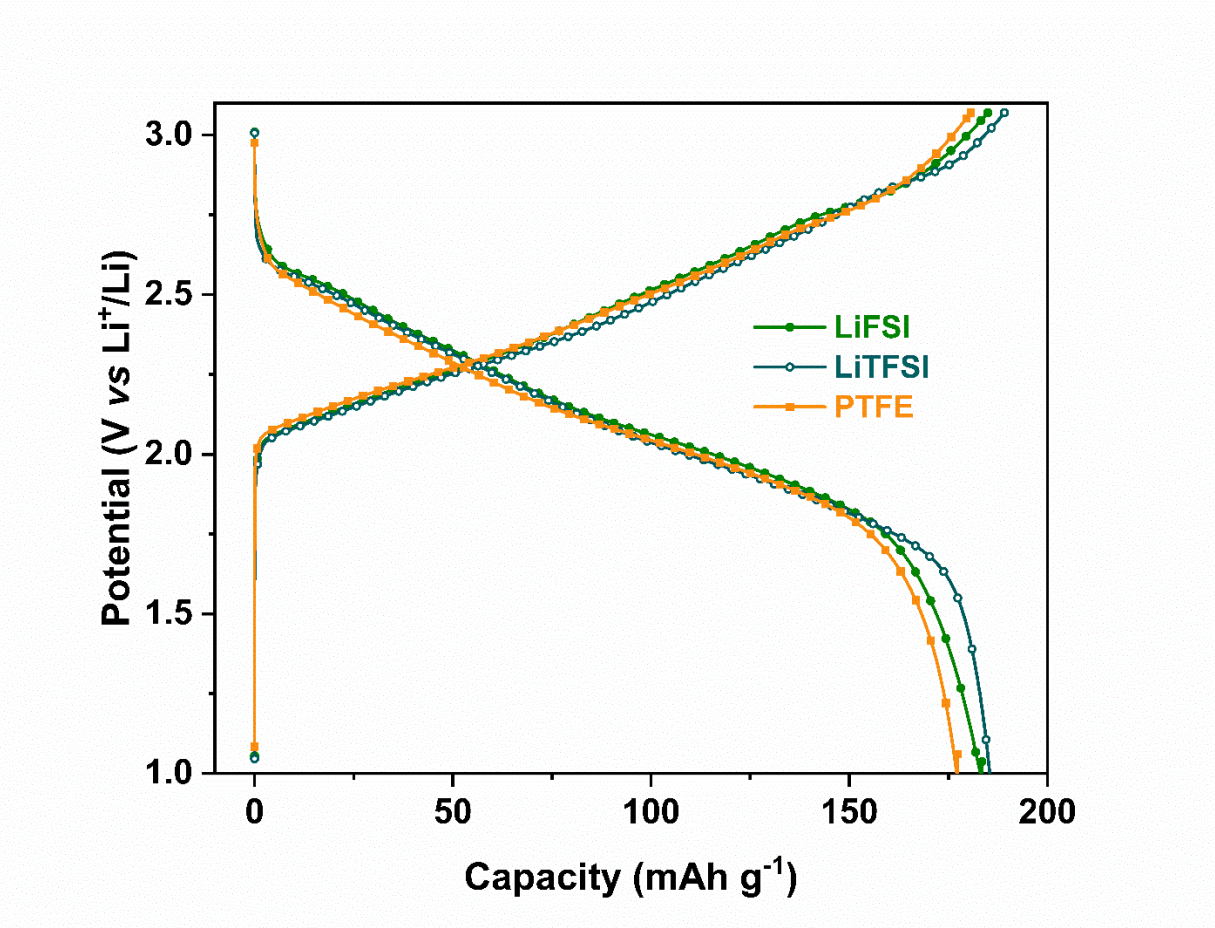


Figure 2.33. Potential vs capacity at cycle 1 for the LTO| Li_6PS_5Cl |NMC-PE cell, where PE is either ABA(50, 0.35)/LiFSI, ABA(50, 0.35)/LiTFSI or PTFE.

2.7. Conclusions and Future Work

A series of ABA- and AB-block polymers, where A = poly(vinyl cyclohexene carbonate) (PvCHC), and B = poly(caprolactone-*r*-trimethylene carbonate) (P(CL-*r*-TMC)) were studied for application in all-solid-state batteries. The polymers were prepared using a one-pot, di-Zn(II) catalysed switchable polymerisation process, allowing for control over the block structure (AB vs ABA), molar mass ($26 < M_n < 69$ kg mol^{-1}) and the composition ($0.26 < w_{PC} < 0.62$).

Trends relating ionic conductivity to polymer structure were observed. For AB polymers, conductivity decreased with increasing molar mass due to the corresponding

increase in T_g; for ABA polymers, conductivity increased with increasing molar mass, likely due to a lower proportion of A/B interfaces which impede ion transport. The best performing electrolyte was ABA (50, 0.35): this w_{PC} formed a weakly-ordered phase-separated morphology that was beneficial for ion transport. It showed high oxidative stability (5.2 V), good Li-ion conductivity (2.2×10^{-4} S cm^{-1} at 60 °C), thermal stability ($T_{d,5\%}$ = 241 °C), viscoelasticity and elastic recovery.

As such, the polymer was tested as a binder with a leading cathode (sc-NMC811) and an inorganic solid electrolyte (Li_6PS_5Cl). The resulting full solid-state cell capacities were high, measuring 186 mAh g^{-1}, and showed impressive capacity retention of 96.7% over 200 cycles. These results outperformed PTFE, which is the leading binder for dry-processed solid-state composites; it had an inferior initial discharge capacity of 177 mAh g^{-1} and 86.4% capacity retention over 200 cycles.

The cell's capacity retention improved when the LiTFSI salt was replaced with LiFSI. It would therefore be prudent to test more salts to see if further improvements can be made: $LiBF_4$, $LiCF_3SO_3$, $LiB(C_2O_4)_2$ (LiBOB) and $LiClO_4$ should be investigated.[49, 50] These salts may plasticise or rigidify the polymer to different extents and form different interfaces, thus affecting battery performance. The soft block of the lead polymer composition should be further optimised: the molar ratio of 4/1 CL/TMC was optimum for ionic conductivity in the poly(CL-*r*-TMC) homopolymer but perhaps less TMC is required in the block copolymer electrolyte.[14] This could improve ionic conductivity.

The polymer synthesis method described is generally applicable to many other epoxides, cyclic esters/carbonates and to anhydrides – thus analogous materials should be produced and tested. There should be an epoxide and lactone scope: CHO, allyl glycidyl ether (AGE), butylene oxide (BO) and limonene oxide (LO) could be tested.[51] The different T_g values

of these polycarbonates will impart different thermal and mechanical properties onto the polymer electrolyte; the effect of this on ionic conductivity is of interest. Alternative lactone ROPs can also be studied; poly(propiolactone) and poly(ethylene adipate) have both been reported as polyester electrolytes with good Li-ion conductivity and can be produced by ROP.[13, 52, 53]

The vinyl functionality on the polycarbonate block allows for easy functionalisation of the polymer. This should be used to incorporate adhesive groups, such as alcohols and carboxylic acids, to improve interfacial contact thus cycling performance.[2] Furthermore, a lithium salt could be tethered to the polymer backbone to produce a single lithium-ion conductor (SLIC). This renders the backbone anionic, leaving only the lithium cation to move and thus improves the lithium ion transference number.[54]

The conductivity of the lead polymer is too low to be used as a standalone polymer electrolyte. However, it could be used in a composite material, for example with the inorganic solid-state electrolyte $Li_7La_3Zr_2O_{12}$ (LLZO). Inorganic solid-state electrolytes have high Li-ion conductivities (10^{-4} – 10^{-2} S cm^{-1} at 25 °C) but have poor interfacial contact and are challenging to process.[55] By forming a composite material, the beneficial properties of the polymer and inorganic solid-state electrolytes can be combined: high Li-ion conductivity whilst being processable and having good interfacial contact.

2.8. References

1. H. Chen, M. Ling, L. Hencz, H. Y. Ling, G. Li, Z. Lin, G. Liu and S. Zhang, *Chem. Rev.*, 2018, **118**, 8936-8982.
2. Y. Shi, X. Zhou and G. Yu, *Acc. Chem. Res.*, 2017, **50**, 2642-2652.
3. G. L. Gregory, H. Gao, B. Liu, X. Gao, G. J. Rees, M. Pasta, P. G. Bruce and C. K. Williams, *J. Am. Chem. Soc.*, 2022, **144**, 17477-17486.
4. L. Rao, X. Jiao, C.-Y. Yu, A. Schmidt, C. O'Meara, J. Seidt, J. R. Sayre, Y. M. Khalifa and J.-H. Kim, *ACS Appl. Mater. Interfaces*, 2022, **14**, 861-872.

5. W. Dou, M. Zheng, W. Zhang, T. Liu, F. Wang, G. Wan, Y. Liu and X. Tao, *Adv. Funct. Mater.*, 2023, 2305161.
6. A. Rensmo, E. K. Savvidou, I. T. Cousins, X. Hu, S. Schellenberger and J. P. Benskin, *Environ. Sci.: Process. Impacts*, 2023, **25**, 1015-1030.
7. X. Lim, *Nature*, 2023, **620**, 24-27.
8. A. Bielefeld, D. A. Weber and J. Janek, *ACS Appl. Mater. Interfaces*, 2020, **12**, 12821-12833.
9. X. Gao, B. Liu, B. Hu, Z. Ning, D. S. Jolly, S. Zhang, J. Perera, J. Bu, J. Liu, C. Doerrer, E. Darnbrough, D. Armstrong, P. S. Grant and P. G. Bruce, *Joule*, 2022, **6**, 636-646.
10. S.-B. Hong, Y.-J. Lee, U.-H. Kim, C. Bak, Y. M. Lee, W. Cho, H. J. Hah, Y.-K. Sun and D.-W. Kim, *ACS Energy Lett.*, 2022, **7**, 1092-1100.
11. Z. Xue, D. He and X. Xie, *J. Mater. Chem. A*, 2015, **3**, 19218-19253.
12. P. K. Nayak, E. M. Erickson, F. Schipper, T. R. Penki, N. Munichandraiah, P. Adelhelm, H. Sclar, F. Amalraj, B. Markovsky and D. Aurbach, *Adv. Energy Mater.*, 2018, **8**, 1702397.
13. H. Xu, J. Xie, Z. Liu, J. Wang and Y. Deng, *MRS Energy Sustain.*, 2020, **7**, E2.
14. J. Mindemark, B. Sun, E. Törmä and D. Brandell, *J. Power Sources*, 2015, **298**, 166-170.
15. A. Bergfelt, M. J. Lacey, J. Hedman, C. Sångeland, D. Brandell and T. Bowden, *RSC Adv.*, 2018, **8**, 16716-16725.
16. A. Bergfelt, G. Hernández, R. Mogensen, M. J. Lacey, J. Mindemark, D. Brandell and T. M. Bowden, *ACS Appl. Polym. Mater.*, 2020, **2**, 939-948.
17. F. S. Bates, M. A. Hillmyer, T. P. Lodge, C. M. Bates, K. T. Delaney and G. H. Fredrickson, *Science*, 2012, **336**, 434.
18. A. Panday, S. Mullin, E. D. Gomez, N. Wanakule, V. L. Chen, A. Hexemer, J. Pople and N. P. Balsara, *Macromolecules*, 2009, **42**, 4632-4637.
19. K. Timachova, H. Watanabe and N. P. Balsara, *Macromolecules*, 2015, **48**, 7882-7888.
20. C. Romain and C. K. Williams, *Angew. Chem. Int. Ed.*, 2014, **53**, 1607-1610.
21. A. C. Deacy, G. L. Gregory, G. S. Sulley, T. T. D. Chen and C. K. Williams, *J. Am. Chem. Soc.*, 2021, **143**, 10021-10040.
22. C. Romain, J. A. Garden, G. Trott, A. Buchard, A. J. P. White and C. K. Williams, *Chem. Eur. J.*, 2017, **23**, 7367-7376.
23. M. R. Kember, J. Copley, A. Buchard and C. K. Williams, *Polym. Chem.*, 2012, **3**, 1196-1201.
24. G. L. Gregory, G. S. Sulley, L. P. Carrodeguas, T. T. D. Chen, A. Santmarti, N. J. Terrill, K.-Y. Lee and C. K. Williams, *Chem. Sci.*, 2020, **11**, 4367-4378.
25. G. S. Sulley, G. L. Gregory, T. T. D. Chen, L. Peña Carrodeguas, G. Trott, A. Santmarti, K.-Y. Lee, N. J. Terrill and C. K. Williams, *J. Am. Chem. Soc.*, 2020, **142**, 4367-4378.
26. J. M. Contreras-Ramírez and M. Monsalve, *Int. J. Polym. Anal. Charact.*, 2022, **27**, 16-31.
27. J. Mindemark, E. Törmä, B. Sun and D. Brandell, *Polymer*, 2015, **63**, 91-98.

28. T. Stößer, T. T. D. Chen, Y. Zhu and C. K. Williams, *Phil. Trans. A*, 2018, **376**, 20170066.
29. H. Zhang, B. Liu, H. Ding, J. Chen and Z. Duan, *Polymer*, 2017, **129**, 5-11.
30. G. Fox, *Bull. Am. Phys. Soc.*, 1952, **1**, 123.
31. K. Kimura, J. Motomatsu and Y. Tominaga, *J. Phys. Chem. C*, 2016, **120**, 12385-12391.
32. I. W. Hamley and V. Castelletto, *Prog. Polym. Sci.*, 2004, **29**, 909-948.
33. C. Sinturel, F. S. Bates and M. A. Hillmyer, *ACS Macro. Lett.*, 2015, **4**, 1044-1050.
34. M. A. Ratner and D. F. Shriver, *Chem. Rev.*, 1988, **88**, 109-124.
35. R. C. Agrawal and G. P. Pandey, *J. Phys. D: Appl. Phys.*, 2008, **41**, 223001.
36. B.-K. Cho, A. Jain, S. M. Gruner and U. Wiesner, *Science*, 2004, **305**, 1598-1601.
37. J. Park, A. Staiger, S. Mecking and K. I. Winey, *Macromolecules*, 2021, **54**, 4269-4279.
38. M. P. S. Mousavi, A. J. Dittmer, B. E. Wilson, J. Hu, A. Stein and P. Bühlmann, *J. Electrochem. Soc.*, 2015, **162**, A2250-A2258.
39. J. Evans, C. A. Vincent and P. G. Bruce, *Polymer*, 1987, **28**, 2324-2328.
40. B. Sun, J. Mindemark, E. V. Morozov, L. T. Costa, M. Bergman, P. Johansson, Y. Fang, I. Furó and D. Brandell, *Phys. Chem. Chem. Phys.*, 2016, **18**, 9504-9513.
41. M. A. Ratner, P. Johansson and D. F. Shriver, *MRS Bull.*, 2000, **25**, 31-37.
42. S. Bhattacharja, S. W. Smoot and D. H. Whitmore, *Solid State Ion.*, 1986, **18-19**, 306-314.
43. K. S. Han, J. D. Bazak, Y. Chen, T. R. Graham, N. M. Washton, J. Z. Hu, V. Murugesan and K. T. Mueller, *Chem. Mater.*, 2021, **33**, 8562-8590.
44. S. Zugmann, M. Fleischmann, M. Amereller, R. M. Gschwind, H. D. Wiemhöfer and H. J. Gores, *Electrochim. Acta*, 2011, **56**, 3926-3933.
45. T. V. Huynh, R. J. Messinger, V. Sarou-Kanian, F. Fayon, R. Bouchet and M. Deschamps, *The Journal of Chemical Physics*, 2017, **147**.
46. M. L. Williams, R. F. Landel and J. D. Ferry, *J. Am. Chem. Soc.*, 1955, **77**, 3701-3707.
47. E. R. Logan, A. Eldesoky, E. Eastwood, H. Hebecker, C. P. Aiken, M. Metzger and J. R. Dahn, *J. Electrochem. Soc.*, 2022, **169**, 040560.
48. I. L. Johansson, C. Sångeland, T. Uemiya, F. Iwasaki, M. Yoshizawa-Fujita, D. Brandell and J. Mindemark, *ACS Appl. Energy Mater.*, 2022, **5**, 10002-10012.
49. C. Liu, X. Tang, Y. Wang, R. L. Sacci, W. Bras, J. K. Keum and X. C. Chen, *ACS Macro. Lett.*, 2022, **11**, 595-602.
50. Y. Zhao, Y. Bai, W. Li, M. An, Y. Bai and G. Chen, *Chem. Mater.*, 2020, **32**, 6811-6830.
51. S. Paul, Y. Zhu, C. Romain, R. Brooks, P. K. Saini and C. K. Williams, *Chem. Commun.*, 2015, **51**, 6459-6479.
52. M. Watanabe, M. Togo, K. Sanui, N. Ogata, T. Kobayashi and Z. Ohtaki, *Macromolecules*, 1984, **17**, 2908-2912.
53. M. Lu, X. Zhu, X.-H. Li, X.-M. Yang and Y.-F. Tu, *Chinese J. Polym. Sci.*, 2017, **35**, 1051-1060.

54. X. Wang, R. Kerr, F. Chen, N. Goujon, J. M. Pringle, D. Mecerreyes, M. Forsyth and P. C. Howlett, *Adv. Mater.*, 2020, **32**, 1905219.

55. F. P. Nkosi, M. Valvo, J. Mindemark, N. A. Dzulkurnain, G. Hernández, A. Mahun, S. Abbrent, J. Brus, L. Kobera and K. Edström, *ACS Appl. Energy Mater.*, 2021, **4**, 2531-2542.

CHAPTER 3

Investigation of Block Copolymers with Fluorinated and PEG-ylated Functionalities.

3.1. Introduction

Poly(ethylene oxide) (PEO) is a successful and extensively studied polymer electrolyte: it excels at solvating and transporting Li-ions and can achieve a Li-ion conductivity of 10^{-4} to 10^{-3} S cm^{-1} at 80 °C.[1, 2] PEO has a low T_g (-60 °C) but is semicrystalline. Consequently, it has low conductivity at ambient temperature, 10^{-8} to 10^{-6} S cm^{-1}, at 30 °C.[3] Its electrochemical performance is also limited by its oxidative stability (< 3.9 V vs Li^+/Li): this obstructs use with new, high-capacity cathodes such as NMC, which requires a potential of 4.3 V.[4]

PEO's structure can be modified to improve its properties. To inhibit PEO's crystallinity, polyethylene glycol (PEG) side chains can be incorporated onto other polymer backbones. Itoh and co-workers copolymerised vinylene carbonate and vinyl ethers, with ethylene oxide unit lengths from 2 to 23.5. The PEO crystallinity was inhibited, with the highest conductivity achieved with the longest side chain.[5] PEO-based block copolymers can impart favourable mechanical properties and improved oxidative stability. Polystyrene (PS) hard blocks with a PEO soft block are well studied, in both diblock and triblock structures, and can achieve conductivities of 10^{-5} S cm^{-1} at 30 °C.[6-8] Incorporating hard blocks which are polar and oxygenated is posited to improve performance further, with enhanced inorganic surface adhesion and conductivity; PvCHC-*b*-PEO-*b*-PvCHC showed a Li-ion conductivity of 10^{-4} S cm^{-1} at 30 °C and an oxidative stability > 4 V.[9]

Fluorinated polymers are also successful in battery applications. They are widely used as polymeric cathode binders: poly(vinylidene fluoride) (PVDF) and poly(tetrafluoroethylene) (PTFE) are favoured due to their good electrochemical stability and high salt dissociation

ability.[10] However, these polymers are non-conductive so can inhibit battery performance; they have low flexibility thus contact loss can occur during the expansion and contraction of the cathode material on cycling.[11] Recently, fluorinated polymers have been rendered conductive by the inclusion of ionomeric groups; their conductivity was modest (1.6×10^{-5} S cm^{-1} at 25 °C) yet cell capacity was improved by 20%.[12] Despite their popularity, fluorinated polymers pose environmental concerns: they are 'forever chemicals' that cannot be naturally degraded and cause persistent pollution. In February 2023, the European Chemicals Agency recommended that around 10,000 of these fluorinated chemicals are restricted.[13] It is therefore important to justify the use of fluorinated polymers by comparing their performance to non-fluorinated alternatives, and to find effective non-fluorinated polymers for battery applications.

Monomers with these functionalities of interest are known to homopolymerise: the fluorinated anhydride 2,2,3,3,4,4-hexafluoropentanedioic anhydride (HFA) was copolymerised with ethyl glycidyl ether;[14] glycidyl ethers have been copolymerised with ethylene oxide.[15] As previously described in this thesis, switch catalysis from an anhydride/epoxide/cyclic carbonate mixture enables poly(carbonate-*b*-esters) to be selectively formed, by the sequential occurrence of anhydride/epoxide ROCOP and cyclic carbonate ROP. A wealth of monomers can be applied; monomers with aromatic and vinyl functionalities, such as PA, CHO and vCHO are well-known, as well as tricyclic anhydrides.[16, 17] Polymers can be post-functionalised to introduce further functionalities, such as carboxylic acids, sulfones and lithium salts.[18-20] It would be more elegant, however, to directly use functionalised monomers in the switchable polymerisation procedure. It is proposed that HFA and glycidyl ethers, with pendant PEG chains, can be used in switchable polymerisation catalysis, in combination with a cyclic carbonate, to selectively yield poly(ester-*b*-carbonate)s with fluorinated and ether functionalities.

3.2. Aims

This Chapter aims to produce a systematic series of polyester electrolytes with different functionalities: featuring a fluorinated or non-fluorinated backbone; and with PEG side chains of varying lengths. The corresponding block copolymers will then be studied, with a hard-soft-hard (A-B-A) block structure, where the 'A' block is a polycarbonate and the 'B' block is the polyester. The effect of these structural differences on Li-ion conductivity will be investigated in order to identify new polymer electrolytes warranting further study for battery applications.

To achieve this, anhydride/epoxide ring-opening copolymerisation will be conducted to produce polyesters. To study the effect of a fluorinated polymer backbone, the anhydride will be diglycolic anhydride (DGA) or 2,2,3,3,4,4-hexafluoropentanedioic anhydride (HFA) (Figure 3.1). HFA has been previously reported for epoxide/anhydride ROCOP and had the highest rate of polymerisation of the anhydrides studied.[14] To study the effect of the PEG side chain, epoxides featuring oligoether units of varying lengths will be explored (Figure 3.1). 2-[(2-(2-(2-Meth-oxyethoxy)ethoxy)ethoxy)methyl]oxirane (ME_3MO) features a side chain with three ether units: this can reduce the T_g and provide additional Li-ion solvation sites to improve Li-ion conductivity. This will be compared to epoxides with longer oligoether side chains with five or twelve ether repeat units: poly(ethylene glycol)-α-methoxy-ω-glycidyl ether (MGE-$(PEG)_5$ and MGE-$(PEG)_{12}$). Itoh and co-workers observed that longer polyether units lowered the T_g and improved Li-ion conductivity.[5] Poly(dimethyltrimethylene carbonate) (P(DTC)) will be used as the hard block in the block copolymer: it can be produced by DTC ROP and it has a T_m of 109 °C so should provide mechanical integrity.

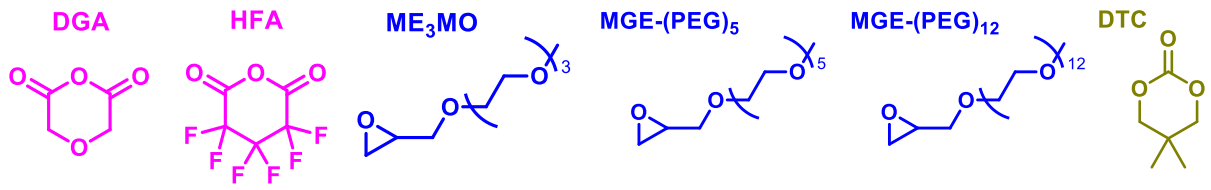


Figure 3.1. The epoxides, anhydrides and cyclic carbonate to be polymerised in this study.

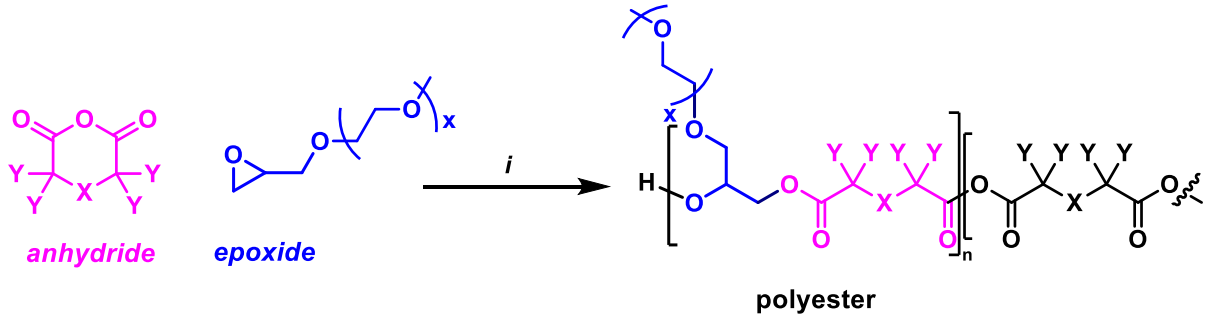
Firstly, the polyesters will be synthesised by anhydride/epoxide ROCOP and characterised. Polymer electrolytes will then be produced and their thermal properties and Li-ion conductivity will be measured. Then, the corresponding block copolymers will be produced by switch catalysis. The polymerisations will be monitored to observe if the catalysis is selective and block copolymers will be characterised to ensure successful block formation. Their thermal properties and Li-ion conductivity will be determined; the effect of the fluorinated backbone, PEG side chain length and poly(DTC) hard block will then be studied.

3.3. Anhydride/Epoxide ROCOP to Produce Fluorinated and PEG-ylated Polyesters

3.3.1. Polymer Synthesis and Characterisation

The catalyst must perform a range of anhydride/epoxide ROCOPs, where the anhydride is DGA or HFA and the epoxide is ME_3MO, MGE-$(PEG)_5$ or MGE-$(PEG)_{12}$; and DTC ROP. Furthermore, it must selectively perform epoxide/anhydride ROCOP and cyclic carbonate ROP sequentially from a monomer mixture to produce block copolymers of the right block sequence, i.e. poly(carbonate-*b*-ester-*b*-carbonate). A non-initiating catalyst is sought to maximise the resulting polymer molar mass. First, the phosphazene base P_2-*t*-Bu was used as an organocatalyst. It has been reported for the epoxide/anhydride ROCOP of a variety of epoxides and anhydrides; and for selective switchable polymerisation from anhydride/epoxide/lactide monomer mixtures.[21-23] In this work, its ability to perform the required anhydride/epoxide ROCOP was first studied.

For molar mass control, a bifunctional chain transfer agent (CTA) was used which ensured a majority of dihydroxy telechelic chains. For polymerisations using DGA, diglycolic acid was used as the CTA; for polymerisations using HFA, hexafluoroglutaric acid was used as the CTA. These were chosen to match any remaining acid impurities in the anhydride and to prevent competition between different CTAs, which could broaden the molar mass distribution. A series of polymers were produced using either DGA or HFA as the anhydride; and ME_3MO, MGE-$(PEG)_5$ or MGE-$(PEG)_{12}$ as the epoxide (Scheme 3.1, Tables 3.1, 7.7). Polymerisations were conducted at 100 °C, under an anaerobic atmosphere with 1600 rpm stirring, using a 1/8/240/250 ratio of catalyst/CTA/anhydride/epoxide, with the P_2-*t*-Bu catalyst in toluene to maintain a catalyst concentration of 2 mM (Table 6.3). Polymerisations were halted by the addition of 5 equivalents of acetic acid with respect to the catalyst and the polymer was purified in good yield (70%) by precipitation from hexane and drying under vacuum (10^{-1} mbar at 80 °C) for 12 hours. In all cases, 100% anhydride conversion was achieved.



Scheme 3.1. Anhydride/epoxide ROCOP, conducted at 100 °C under an anaerobic atmosphere. (i) [P_2-*t*-Bu]/[CTA]/[anhydride]/[epoxide]/ = 1/8/240/250, [cat] = 2 mM, in toluene, n = 30. When anhydride = DGA, *Y* = H and *X* = O; when anhydride = HFA, *Y* = F and *X* – CF_2. When the epoxide = ME_3MO, *x* = 3; when the epoxide = MGE-$(PEG)_5$, *x* = 5; when epoxide = MGE-$(PEG)_{12}$, *x* = 12.

Table 3.1. Polyester Characterisation Data.

Entry [a]	Anhydride	Epoxide	$M_{n,th}$ (kg mol^{-1}) [b]	$M_{n,NMR}$ (kg mol^{-1}) [c]	$M_{n,SEC,THF}$ (kg mol^{-1}) [d]	T_g (°C) [e]
1	DGA	ME_3MO	10.0	5.0	3.0 [1.42]	-34
2	HFA	ME_3MO	13.3	5.7	1.2 [1.34]	-53
3	DGA	MGE-$(PEG)_5$	12.5	10.8	1.5 [1.25]	-43
4	HFA	MGE-$(PEG)_5$	15.7	7.8	1.6 [1.77]	-58
5	DGA	MGE-$(PEG)_{12}$	21.5	18.6	2.5 [1.34]	-53 (T_c = -13)
6	HFA	MGE-$(PEG)_{12}$	24.7	12.3	2.5 [1.58]	-62 (T_c = -35)

[a] All polymerisations conducted at 100 °C under an anaerobic atmosphere, using a catalyst/CTA/anhydride/epoxide ratio of 1/8/240/250 and P_2-*t*-Bu catalyst of 2 mM concentration in toluene in all cases; the CTA was diglycolic acid for entries 1, 3, and 5; the CTA was hexafluoroglutaric acid for entries 2, 4, and 6; [b] M_n as estimated by the initial reagent ratios and monomer conversions, where DGA conversion was monitored by comparing the monomeric signal at 4.41 ppm to the polymeric signal at 4.21 ppm, epoxide conversion was determined by comparing the monomeric signal at 3.21 ppm to the polymeric signal at 5.36 ppm; [c] DP_n as determined from the ^{1}H NMR spectra of the purified polymer by integration of the polymeric end group resonance at 3.98 ppm against those of the polyester (5.28 – 4.24 ppm); [d] Determined by SEC using THF eluent and calibrated against narrow PS standards; [e] Determined by DSC (10 °C min^{-1} heating rate), second heating curve.

Polymerisations were monitored by ^{1}H NMR spectroscopy and SEC, by taking aliquots of the reaction mixtures. For entry 1, the ^{1}H NMR spectra shows DGA consumption, by the depletion of the anhydride signal at 4.41 ppm, and the growth of the polyester signal at 4.21 ppm. ME_3MO consumption was monitored by depletion of the signal at 3.21 ppm and growth of the signal at 5.36 ppm (Figure 3.2). The polymer molar mass was monitored throughout the polymerisation process by SEC; a linear increase in molar mass was observed with DGA conversion and the dispersity was reasonably narrow throughout the reaction (Figures 3.3, 3.4).

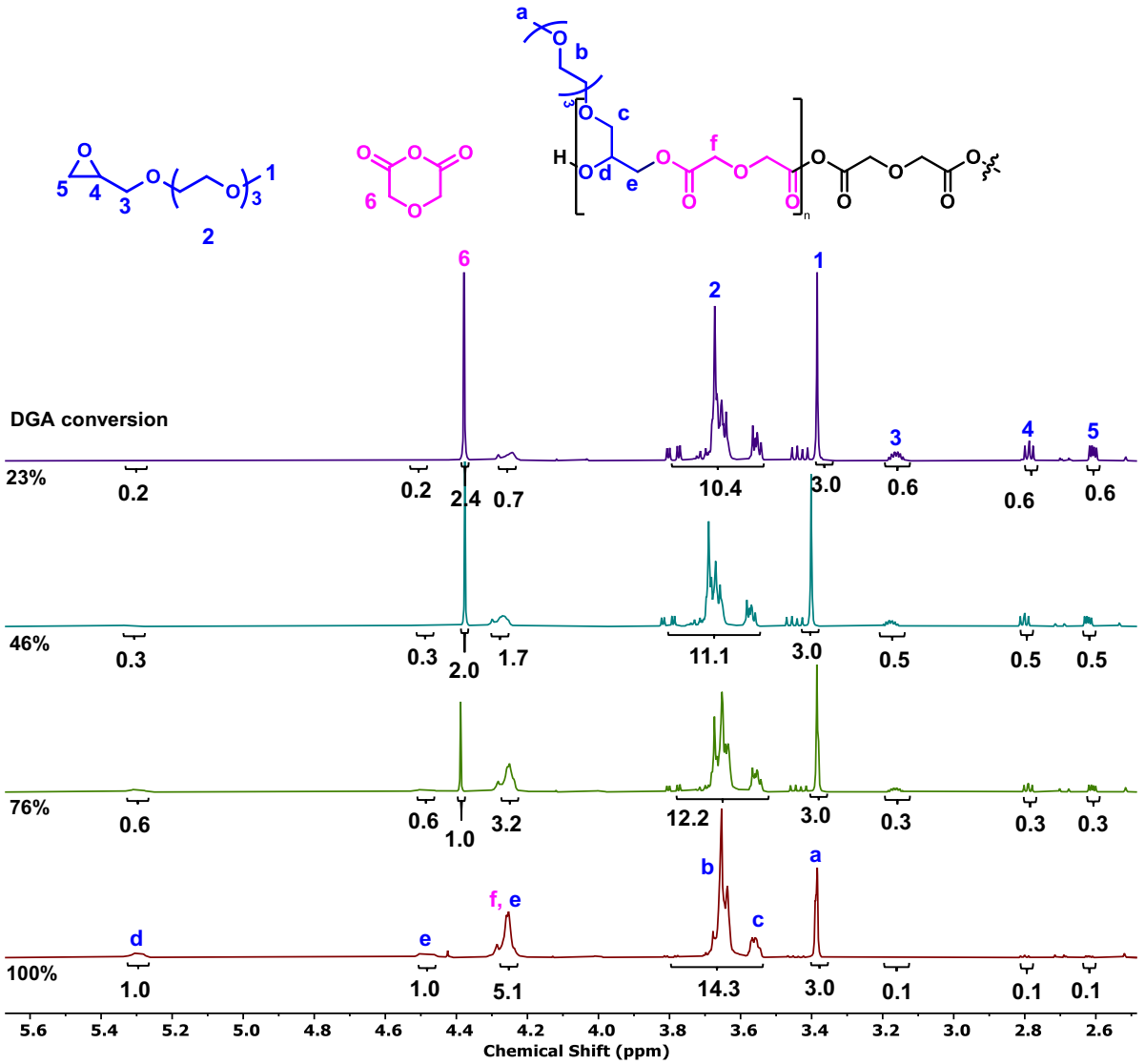


Figure 3.2. ^{1}H NMR spectra ($CDCl_3$, 500 MHz) from aliquots from DGA/ME_3MO ROCOP at 23%, 46%, 76% and 100% DGA consumption, depicting the consumption of DGA and ME_3MO monomer and formation of poly(DGA-*alt*-ME_3MO). See Figure 7.3 for spectra spanning 0.0 – 7.5 ppm and zoomed so all 'd' signals at 5.29 ppm are observable.

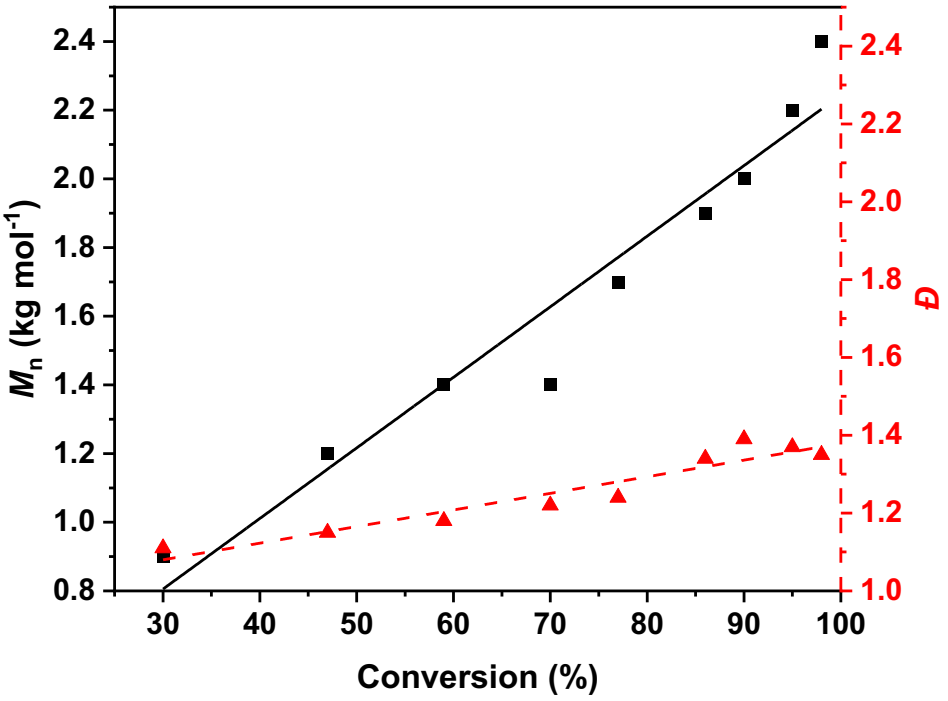


Figure 3.3. SEC data from aliquots of DGA/ME$_3$MO ROCOP, showing the growth in polymer molar mass.

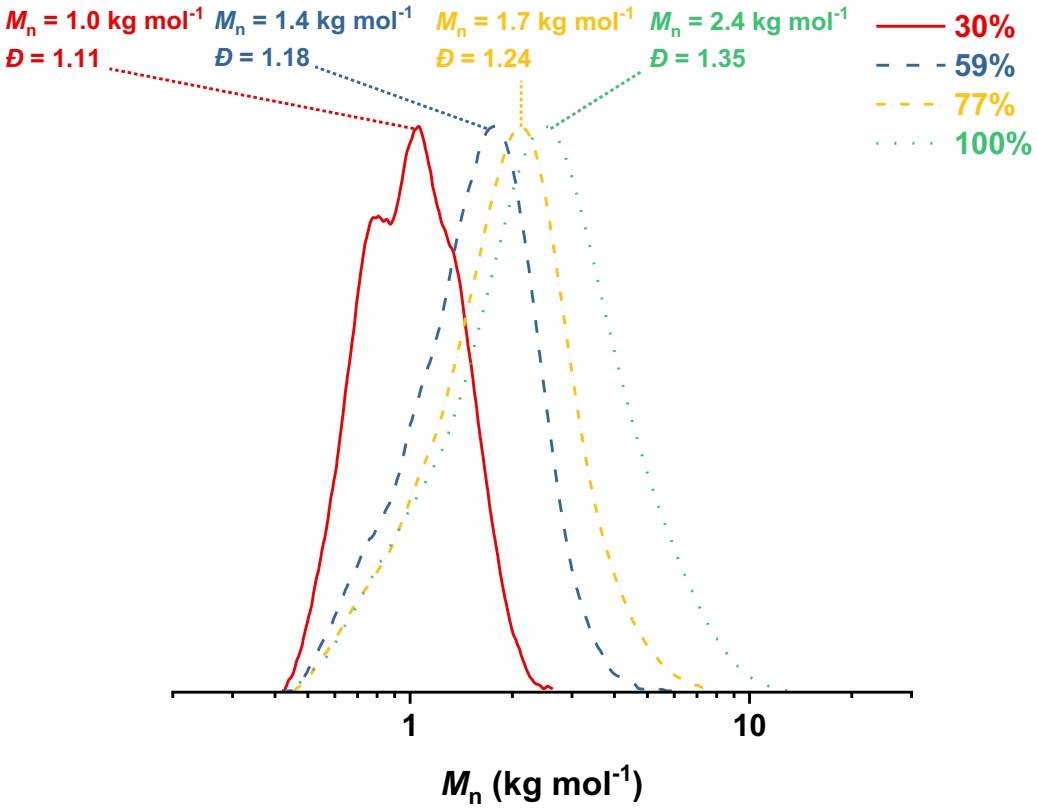


Figure 3.4. Growth in polymer molar mass and change in dispersity index *Đ*, recorded by SEC, with increasing DGA conversion.

^{1}H NMR spectroscopy of the purified polymers showed the expected signals corresponding to the polymer (Figures 3.5, 7.4 – 7.8). The molar mass of the polymers were determined using ^{1}H NMR spectroscopy, from the relative integrals of the signals corresponding to the polyester end group (3.98 ppm, d_{end}) and of the main-chain signal (5.28 ppm, d).

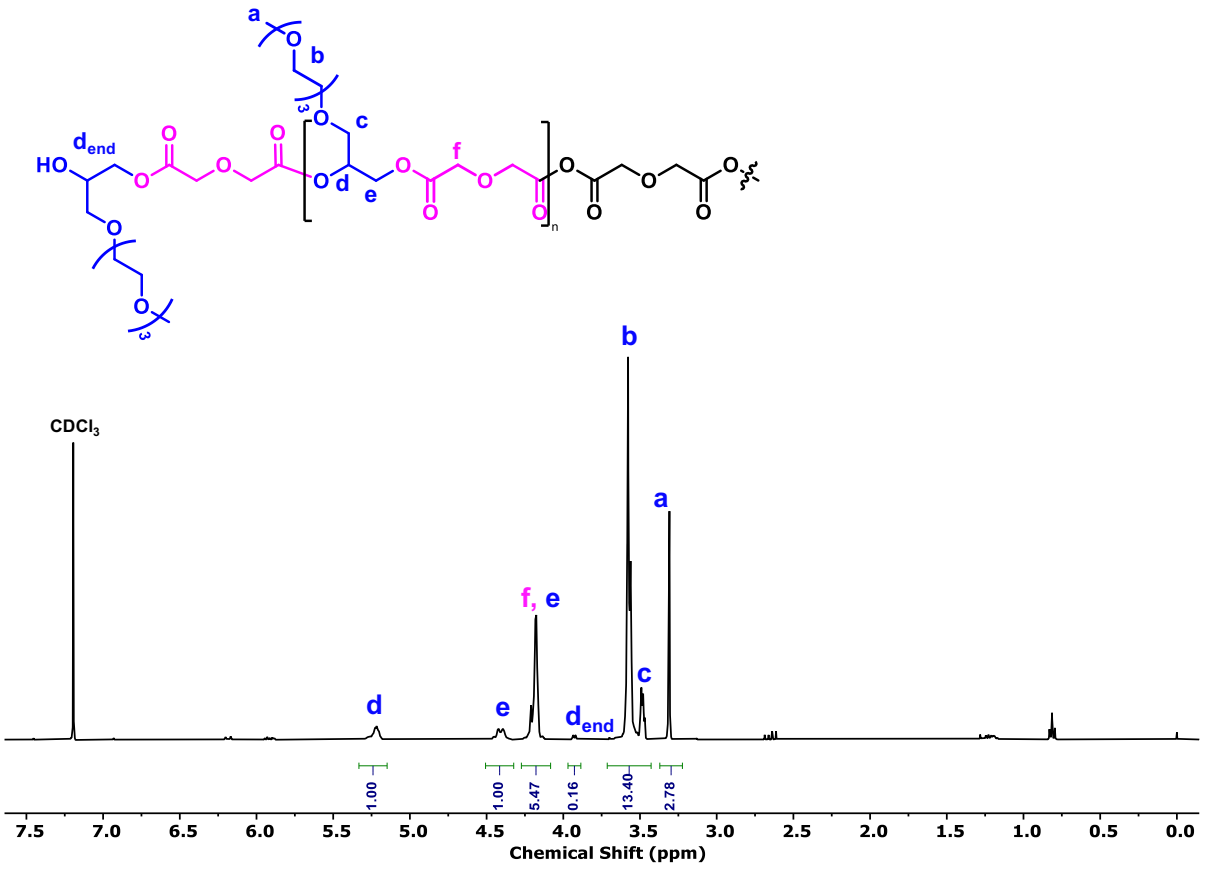


Figure 3.5. Assigned ^{1}H NMR spectrum ($CDCl_3$, 500 MHz) of the purified polymer, poly(DGA-*alt*-ME_3MO).

SEC data for all purified polymers had a monomodal, reasonably narrow trace (Figure 3.6, 7.9). The molar mass measured by SEC differed from the theoretical mass and the mass calculated by ^{1}H NMR spectroscopy (Table 3.1 and 6.4). It is proposed that the highly

oxygenated oligomers behave differently in solution compared to high molar mass polystyrene calibrants. Other calibrants (e.g. PMMA and PEG) were also investigated but this did not improve the alignment.

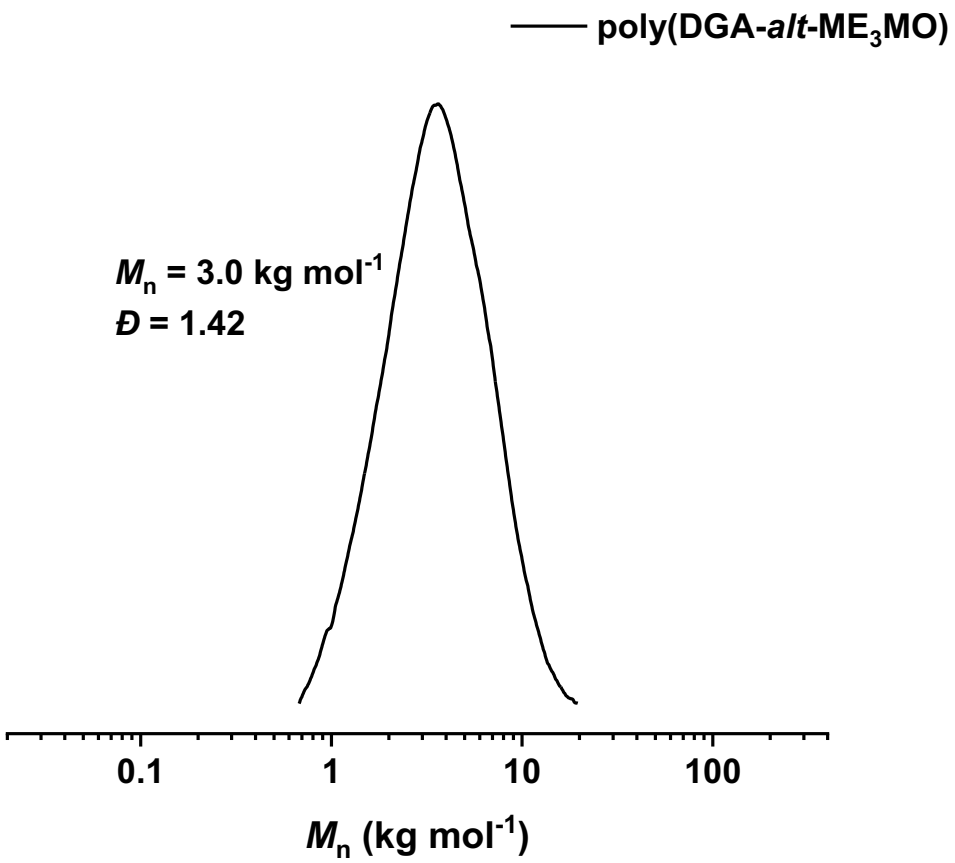


Figure 3.6. SEC trace for the purified polymer poly(DGA-*alt*-ME$_3$MO), measured in THF with an RI detector vs. narrow PS standards.

For entry 2, HFA consumption was also observed by ^{19}F NMR spectroscopy: the sharp monomer signals at -118.9 and -124.1 ppm depleted and broad signals at -118.3 and -123.8 ppm appeared (Figure 3.7). Epoxide conversion was also studied by ^{1}H NMR spectroscopy, using the same approach as entry 1. Entries 3 to 6 were monitored analogously. Increasing length of the PEG side chain was observed by the increase in relative signal intensity at 3.65 – 3.55 ppm, in the ^{1}H NMR spectra (Figures 7.4 – 7.8).

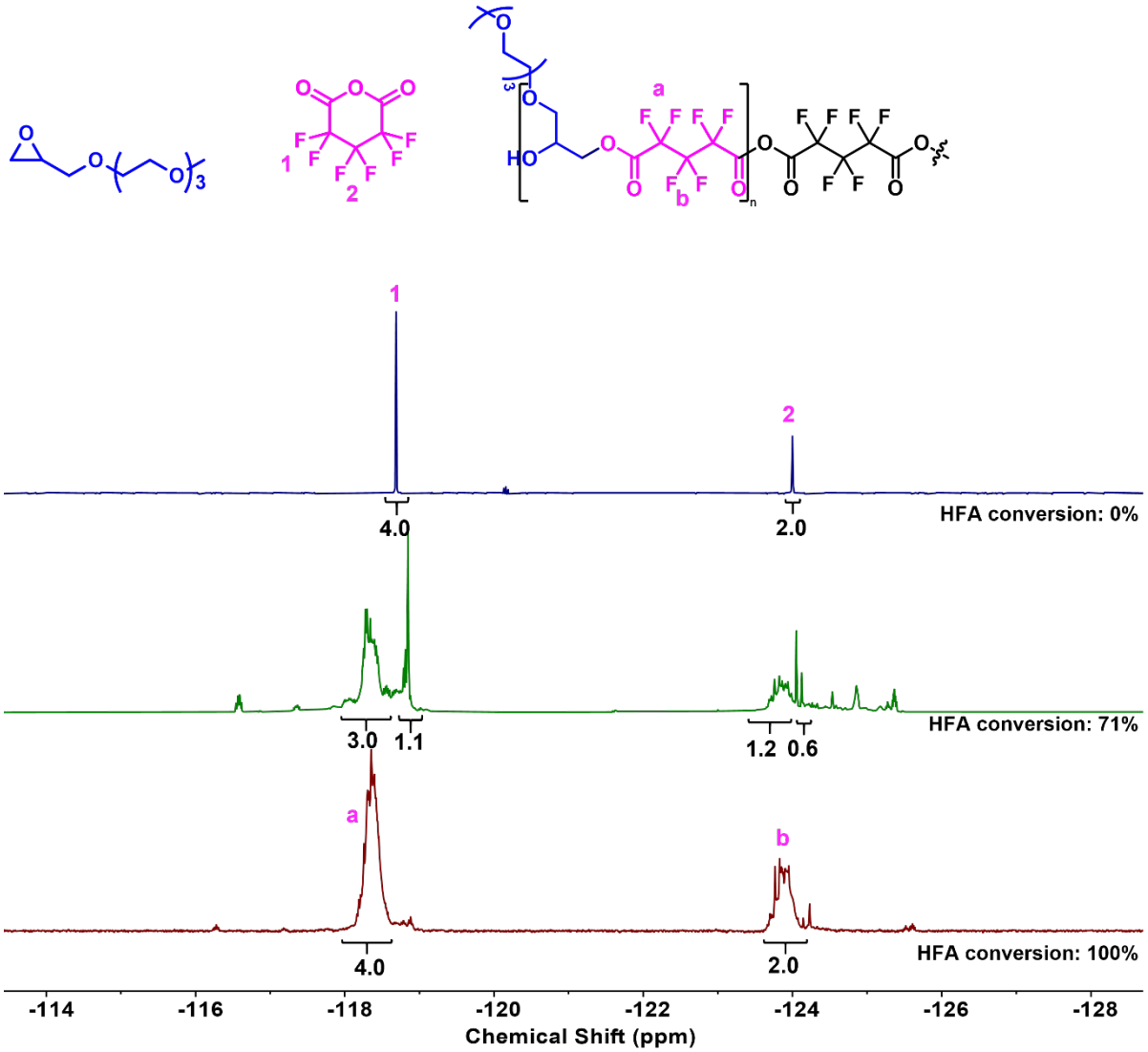


Figure 3.7. ^{19}F NMR spectra ($CDCl_3$, 500 MHz) from aliquots of HFA/ME_3MO ROCOP at 0%, 71%, and 100% HFA consumption, depicting the consumption of HFA monomer and formation of poly(HFA-*alt*-ME_3MO).

The thermal properties of the polyesters were analysed by DSC. Data was obtained from the second scan, with the first scan removing thermal history. All showed a single T_g between -62 and -34 °C; entries 5 and 6 also showed a T_c and T_m corresponding to the PEG side chain at -34 to 4 °C (Table 3.1, Figure 3.8). At this $(PEG)_n$ chain length, n = 12, the oligoether side chains crystallise.

Two trends were observed. Firstly, longer PEG chains corresponded to a lower T_g. This is consistent with work by Kubo and coworkers; polyether side chains are highly flexible thus aid segmental motion.[5] Secondly, the fluorinated polymers had lower T_g values than the unfluorinated; the incorporation of C-F bonds into the polymer backbone improved chain mobility. The highly electronegative fluorines could increase chain free volume by electrostatic repulsion and thus improve chain mobility. Both MGE-$(PEG)_{12}$-based polyesters had T_g values similar to or lower than PEG (-50 to -60 °C); this demonstrated the plasticising effect of longer side chains.[5] For all of the polyesters studied, the T_g values were very low thus they are promising midblocks for block copolymer electrolytes.

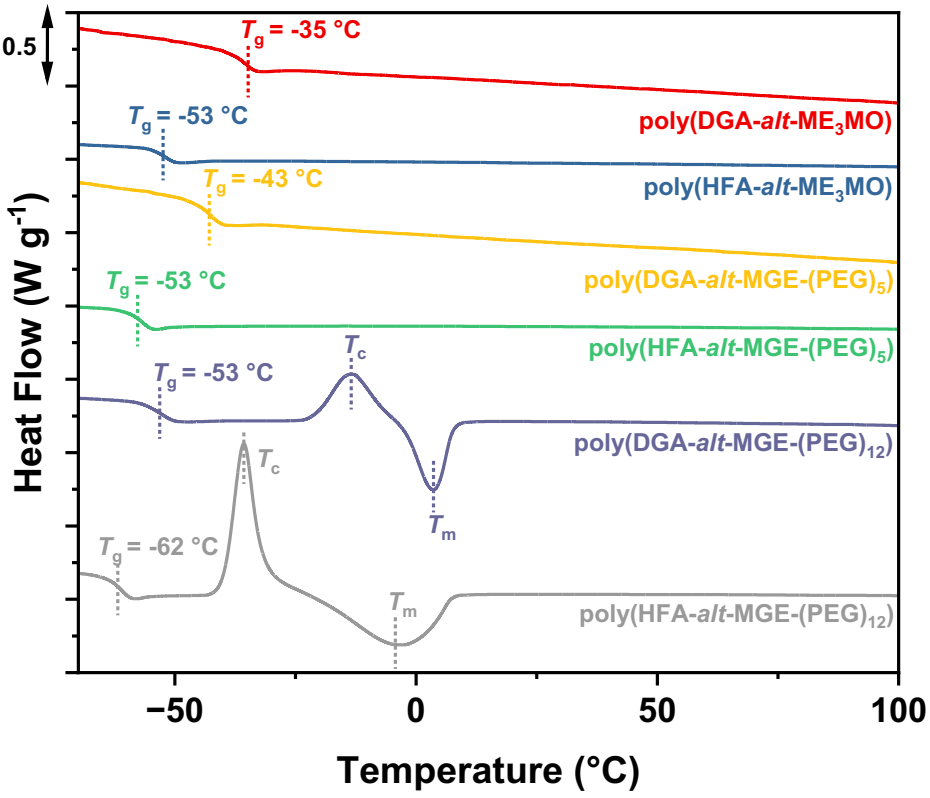


Figure 3.8. DSC data for polyesters as listed in Table 3.1, at a scan rate of 10 °C min^{-1}. Data from the second heating curve displayed.

3.3.2. Polyester Electrolyte Properties

Polymer electrolytes were prepared by mixing a stirred solution of the polyesters with LiTFSI, in THF, and allowing the solvent to evaporate. The solvent was removed first at ambient temperature and pressure, and then under a vacuum, of 10^{-1} mbar, at 60 °C. The salt concentration was defined as the molar ratio of lithium ions to coordinating oxygen atoms, $\rho = [Li^+]/[O]$. A value of $\rho = 0.037$ was used for all materials since this loading was found to be the best in prior work investigating poly(DGA-*alt*-AGE). Using less salt reduces the Li-ion conductivity as there are fewer charge carriers, but using more salt also decreases conductivity as it increases the interchain interactions and stiffens the polymer electrolyte, impeding charge transport.[24]

DSC data showed a single T_g for all polyester electrolytes which increased with respect to the polyester without salt. For example, poly(DGA-*alt*-ME_3MO) showed a T_g that increased from -35 to -12 °C after salt addition (Figure 3.9, Table 3.2). This was attributed to LiTFSI forming transient crosslinks between the polymer chains, stiffening the material. The crystallinity of the $(PEG)_{12}$ side chain in poly(DGA-*alt*-MGE-$(PEG)_{12}$) and poly(HFA-*alt*-MGE-$(PEG)_{12}$) was supressed by salt addition, as observed by the disappearance of the T_m from -4 to 4 °C. The effect is likely due to salt coordination to the ether oxygens which prevents the formation of crystalline domains.

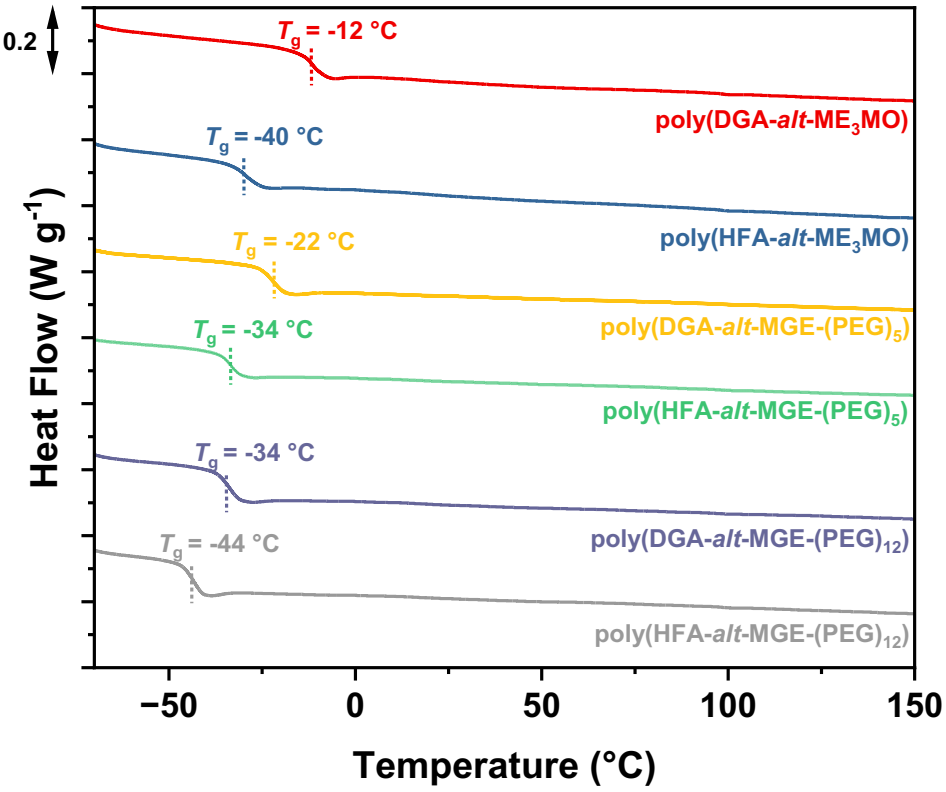


Figure 3.9. DSC data for polyester electrolytes as listed in Table 3.1, at a scan rate of 10 °C min^{-1}. Second heating curve data is displayed.

Table 3.2. Polyester Electrolyte VFT Parameters and Thermal Data.

Polymer [a]	T_g (°C) [b]	E_a (kJ mol^{-1}) [c]	ln$A$ [d]
Poly(DGA-*alt*-ME_3MO)	-12	12.9	5.3
Poly(HFA-*alt*-ME_3MO)	-40	15.0	5.3
Poly(DGA-*alt*-MGE-$(PEG)_5$)	-22	14.2	6.6
Poly(HFA-*alt*-MGE-$(PEG)_5$)	-34	14.1	6.0
Poly(DGA-*alt*-MGE-$(PEG)_{12}$)	-34	14.1	7.3
Poly(HFA-*alt*-MGE-$(PEG)_{12}$)	-44	12.6	5.1

[a] All polymers with ρ = 0.037 LiTFSI; [b] Determined by DSC, second heating curve; [c] Activation energy of Li-ion transfer, obtained from the VFT fit; [d] Relative free charge carrier concentration of the polymer electrolyte, obtained from the VFT fit.

Li-ion conductivity was measured by electrochemical impedance spectroscopy (EIS) at 10 °C temperature intervals between 30 and 80 °C (Table 3.3). A coin cell was used to contain the polymer electrolyte, which was sandwiched between two steel discs. The lead polyester electrolyte, poly(HFA-*alt*-MGE-$(PEG)_{12}$), showed a Li-ion conductivity of 4.7×10^{-5} S cm^{-1} at 30 °C and 8.7×10^{-4} S cm^{-1} at 80 °C. These values are high for a polymer electrolyte and are comparable to PEO at high temperatures. They are superior to PEO at 30 °C as the new polymer is fully amorphous.[2]

Li-ion conductivity increased with increasing length of the ether side chain. For example, at 40 °C, the Li-ion conductivity was 2.8×10^{-6} S cm^{-1} for poly(DGA-*alt*-ME_3MO), 6.3×10^{-6} S cm^{-1} for poly(DGA-*alt*-MGE-$(PEG)_5$) and 1.0×10^{-4} S cm^{-1} for poly(DGA-*alt*-MGE-$(PEG)_{12}$) (Figure 3.10, Table 3.3). These values correlate with the T_g values decreasing with increasing ether side chain length – -12, -22 and -34 °C, respectively (Figure 3.9, Table 3.2). The longer PEG side chains are highly mobile thus facilitate Li^+ transport. Polyethers are proposed to conduct Li-ions by a rapid intrachain hopping mechanism, compared to polyesters and polycarbonates which transport by slower interchain hopping. Therefore, the longer PEG side chains also enable higher Li-ion conductivity due to the faster Li-ion transport mechanism.[24, 25]

For the polymers with shorter PEG side chains (ME_3MO and MGE-$(PEG)_5$), the fluorinated polyester showed modestly improved Li-ion conductivity. For the ME_3MO-based polyester, the Li-ion conductivity was 3.2×10^{-5} S cm^{-1} with DGA and 7.4×10^{-5} S cm^{-1} with HFA. For the MGE-$(PEG)_5$-based polyesters, the Li-ion conductivity was higher at 1.1×10^{-4} S cm^{-1} with DGA and 1.9×10^{-4} S cm^{-1} with HFA, at 60 °C (Table 3.2, Figure 3.10). The

fluorinated polyesters have lower T_g values and thus more mobile polymer chains for transporting Li^+. Also, the fluorinated polymers have enhanced salt dissociation which facilitates ion transport.[10] For the MGE-$(PEG)_{12}$-based polymers, there was no significant difference between the DGA- and HFA-based polyesters, despite poly(DGA-*alt*-MGE-$(PEG)_{12}$) having a T_g of -34 °C and poly(HFA-*alt*-MGE-$(PEG)_{12}$) having a T_g of -44 °C. The PEG side-chains constitute the majority of the polymer structure, rather than the polyester backbone. The conductivity is thus proposed to be dominated by PEG and the main polymer backbone appears to be rather inaccessible and does not significantly affect the conductivity.

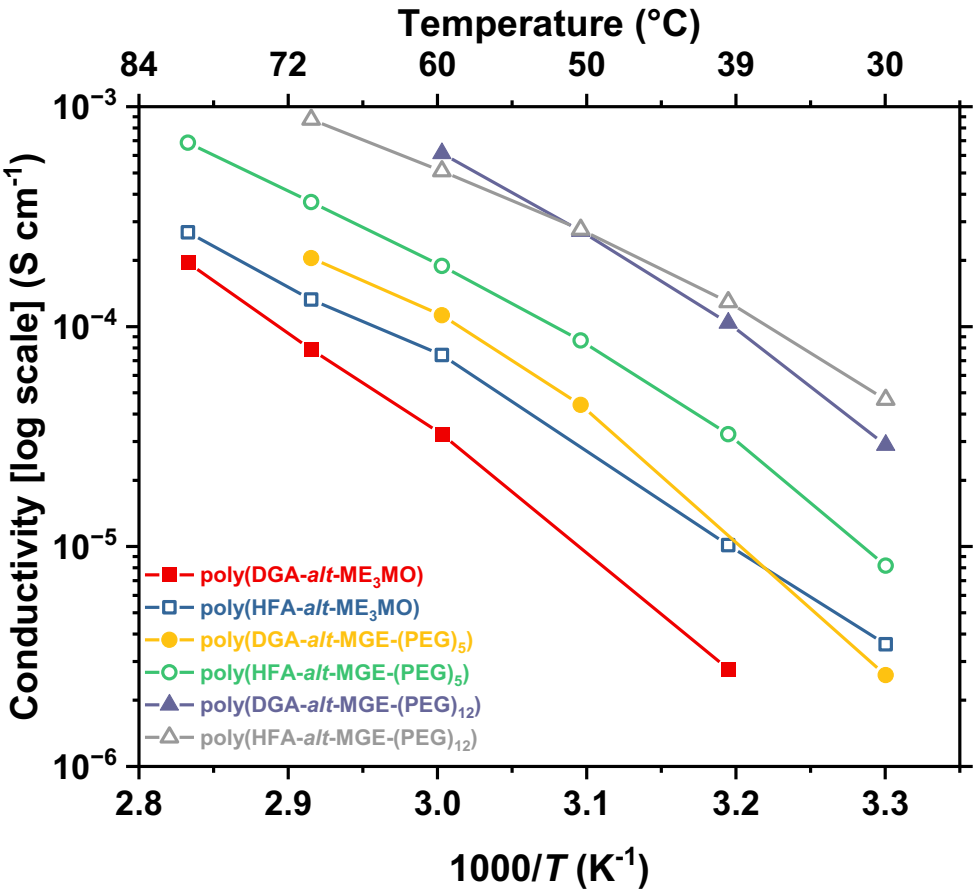


Figure 3.10. Li-ion conductivity as a function of temperature for the polyester electrolytes, with LiTFSI concentration $\rho = 0.037$.

Table 3.3. Polyester Electrolyte Li-ion Conductivity.

Polymer [a]	σ (S cm^{-1}) [b]					
	30 °C	40 °C	50 °C	60 °C	70 °C	80 °C
Poly(DGA-*alt*-ME$_3$MO)	-	2.8×10^{-6}	-	3.2×10^{-5}	7.9×10^{-5}	1.9×10^{-4}
Poly(HFA-*alt*-ME$_3$MO)	3.6×10^{-6}	1.0×10^{-5}	-	7.4×10^{-5}	1.3×10^{-4}	2.7×10^{-4}
Poly(DGA-*alt*-MGE-(PEG)$_5$)	2.6×10^{-6}	6.3×10^{-6}	4.4×10^{-5}	1.1×10^{-4}	2.1×10^{-4}	-
Poly(HFA-*alt*-MGE-(PEG)$_5$)	8.2×10^{-6}	3.2×10^{-5}	8.7×10^{-5}	1.9×10^{-4}	3.7×10^{-4}	6.9×10^{-4}
Poly(DGA-*alt*-MGE-(PEG)$_{12}$)	2.9×10^{-5}	1.0×10^{-4}	2.7×10^{-4}	6.1×10^{-4}	-	-
Poly(HFA-*alt*-MGE-(PEG)$_{12}$)	4.7×10^{-5}	1.3×10^{-4}	2.8×10^{-4}	5.0×10^{-4}	8.7×10^{-4}	-

[a] All polymers with ρ = 0.037 LiTFSI; [b] Measured using electrochemical impedance spectroscopy, with ionic conductivity being calculated from the resistance obtained by fitting the data to the equivalent circuit Q1+Q2/R2. Error values were determined from the standard deviation from three experiments and corresponded to ± 23%, 14%, 11%, 9%, 3% and 9% at 30, 40 °C, 50 °C, 60 °C, 70 °C and 80 °C, respectively.

For all polymers, the Li-ion conductivity increased at high temperatures. The temperature dependence of Li-ion conductivity was modelled using the VFT relationship,

$$\sigma = AT^{-1/2}\exp\left[-E_a/(T - T_0)\right] \quad \text{Equation 3.1}$$

where A is a constant proportional to the number of Li-ions; E_a is the Li-ion transport activation energy; and T_0 is the temperature where configurational entropy is zero. All polymers conformed to the VFT model, as evidenced by the linear VFT plots (Table 3.2, Figure 3.11). This indicated that Li-ion conductivity was coupled to the segmental motion of the polymer chain. The ion transport activation energy was obtained from the gradient of the fit. Values

ranged from 12.6 to 15.0 kJ mol^{-1} for these polyesters, which is typical for polymer electrolytes (Table 3.2, Figure 3.11).

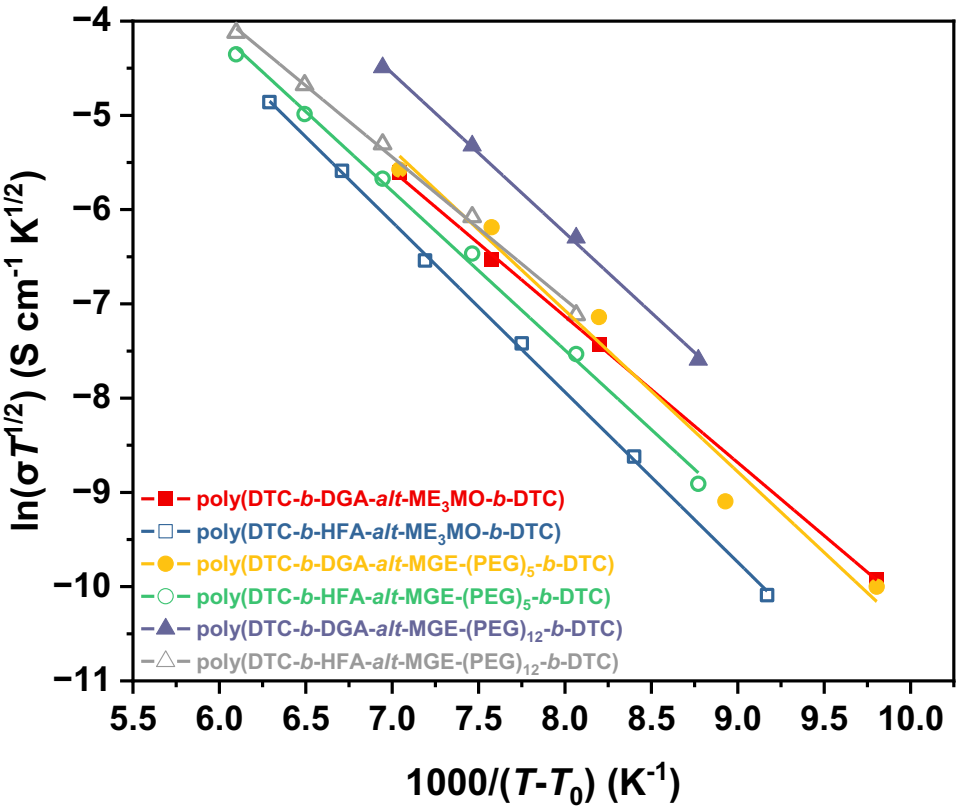


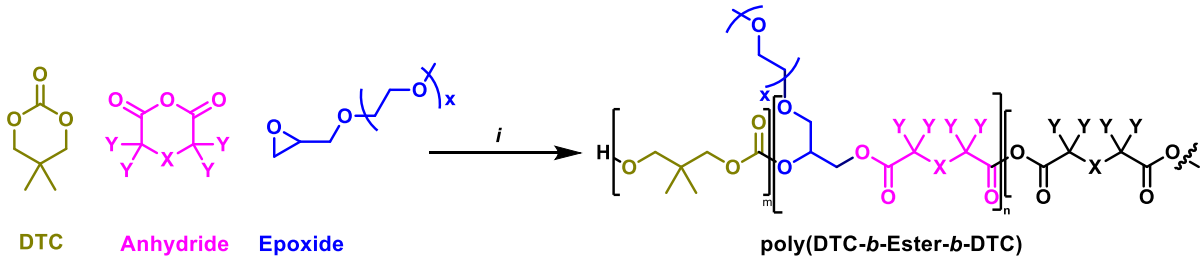
Figure 3.11. VFT fits for the polyester electrolytes. R^2 = 0.999, 0.999, 0.970, 0.997, 0.998, 0.997

3.4. Switchable Polymerisation of Anhydride/Epoxide/Cyclic Carbonate to Produce Fluorinated and PEG-lyated Block Copolymers

3.4.1. Synthesis and Characterisation

Block copolymers were produced by switchable polymerisation catalysis using analogous conditions used to produce polyesters. The polymerisations were conducted at 100 °C, under an anaerobic atmosphere, with 1600 rpm stirring, using a 1/8/240/250/(231 to

570) ratio of catalyst/CTA/anhydride/epoxide/DTC which should target a hard block (P(DTC)) weight fraction of 0.2. The P_2-*t*-Bu catalyst was used in toluene at a catalyst concentration of 2 mM (Scheme 3.2, Table 6.5). Polymerisations were halted by the addition of 5 equivalents of acetic acid, with respect to the catalyst, and the polymer was purified in good yield (75%) by precipitation of the crude mixture from hexane, followed by drying, under a 0.1 mbar vacuum, at 80 °C for 12 hours. In all cases, 100% anhydride conversion and 72 to 75% DTC conversion was achieved.



Scheme 3.2. Polymerisation of anhydride, epoxide, and DTC via switch catalysis, conducted at 100 °C under an anaerobic atmosphere. (i) [P_2-*t*-Bu]/[CTA]/[anhydride]/[epoxide]/[DTC] = 1/8/240/250/(231 – 570), [P_2-*t*-Bu] = 2 mM, in toluene. n = 30, m = 30 – 70 When anhydride = DGA, Y = H and X = O; when anhydride = HFA, Y = F and X – CF_2. When the epoxide = ME_3MO, x = 3; when the epoxide = MGE-$(PEG)_5$, x = 5; when epoxide = MGE-$(PEG)_{12}$, x = 12.

A series of polymers were produced; the soft, central polyester block was prepared from either DGA or HFA as the anhydride and ME_3MO, MGE-$(PEG)_5$ or MGE-$(PEG)_{12}$ as the epoxide. The hard, outer polycarbonate blocks were prepared from the cyclic carbonate DTC (Table 3.4 and 6.6). As with the polyester syntheses, bifunctional CTAs were used to produce triblock copolymers – diglycolic acid for the DGA-based block copolymers and hexafluoroglutaric acid for the HFA-based block copolymers. A hard block (P(DTC)) weight fraction of 0.2 was targeted in all cases. For poly(vCHC-*b*-CL-*r*-TMC-*b*-vCHC), studied in Chapter 2, a higher hard weight fraction (0.35) was optimum for Li-ion conductivity. However, in that case the block copolymer was phase separated and had a greater molar mass (50 kg mol-

[1]) than those studied in this Chapter. Thus, the structure-property trends should be different. Indeed, a lower hard block weight fraction of 0.20 will be shown to be optimum for a similar low molar mass (< 20 kg mol^{-1}) block copolymer in Chapter 4.

Table 3.4. Block Copolymer Characterisation Data

Entry [a]	Anhydride	Epoxide	Cyclic carbonate	$M_{n,th}$ (kg mol^{-1}) [b]	$M_{n,NMR}$ (kg mol^{-1}) [c]	$M_{n,SEC,\ THF}$ (kg mol^{-1}) [d]	Hard wt fraction [c]	T_g (°C) [e]
1	DGA	ME_3MO	DTC	12.5	9.3	3.5 [1.36]	0.22	-46
2	HFA	ME_3MO	DTC	16.6	7.8	2.9 [1.89]	0.18	-45
3	DGA	MGE-$(PEG)_5$	DTC	15.5	9.9	2.5 [1.46]	0.16	-45
4	HFA	MGE-$(PEG)_5$	DTC	19.5	17.5	3.5 [1.52]	0.17	-55
5	DGA	MGE-$(PEG)_{12}$	DTC	27.0	6.5	3.8 [1.26]	0.24	-58 (T_m = 0)
6	HFA	MGE-$(PEG)_{12}$	DTC	31.0	6.8	2.1 [1.41]	0.26	-58 (T_m = -6)

[a] All polymerisations conducted at 100 °C under an anaerobic atmosphere, using a catalyst/CTA/anhydride/epoxide/DTC ratio of 1/8/240/250/X, where X is varied between 231 and 570 to target 0.20 hard weight block (P(DTC)) fraction. P_2-*t*-Bu catalyst was used at 2 mM concentration in toluene in all cases; diglycolic acid CTA used for entries 1, 3, and 5; hexafluroglutaric acid CTA used for entries 2, 4, and 6; [b] M_n as estimated by the initial reagent ratios and monomer conversions, where DGA conversion was monitored by comparing the monomeric signal at 4.41 ppm to the polymeric signal at 4.21 ppm, epoxide conversion was determined by comparing the monomeric signal at 3.21 ppm to the polymeric signal at 5.45 ppm, and DTC conversion was monitored by comparing the monomeric signal at 1.10 ppm to the polymeric signal at 0.97 ppm; [c] Determined from the ^{1}H NMR spectra of the purified polymers by integration of the polycarbonate end group signal (0.92 ppm) against those of the polyester (5.28, 4.46, 4.25, 3.64 – 3.37 ppm) and polycarbonate (3.96, 0.99 ppm); [d] Determined by SEC, using THF eluent and calibrated against narrow PS standards; [e] Determined by DSC (10 °C min^{-1} heating rate), second heating curve.

For all six entries, switchable catalysis and sequential monomer consumption was observed by ^{1}H NMR spectroscopy. From a one-pot monomer mixture of anhydride, epoxide and cyclic carbonate, switch catalysis theory predicts that firstly, anhydride/epoxide ROCOP selectively occurs, with cyclic carbonate ROP only proceeding once all of the anhydride has been consumed. For entry 1, DGA/ME_3MO ROCOP indeed proceeded first, as observed by the consumption of DGA (4.31 ppm) and ME_3MO (3.09, 2.71, 2.53 ppm) and the formation of new signals corresponding to the polyester in the ^{1}H NMR spectra (5.21, 4.19 ppm). DTC ROP only occurred once all of the DGA was consumed, as observed by the depletion of DTC monomer signals (4.07 and 1.10 ppm) and formation of new polycarbonate signals (3.96 and 0.97 ppm, Figure 3.12). Indeed, switch catalysis and sequential anhydride/epoxide ROCOP followed by DTC ROP was observed for all entries.

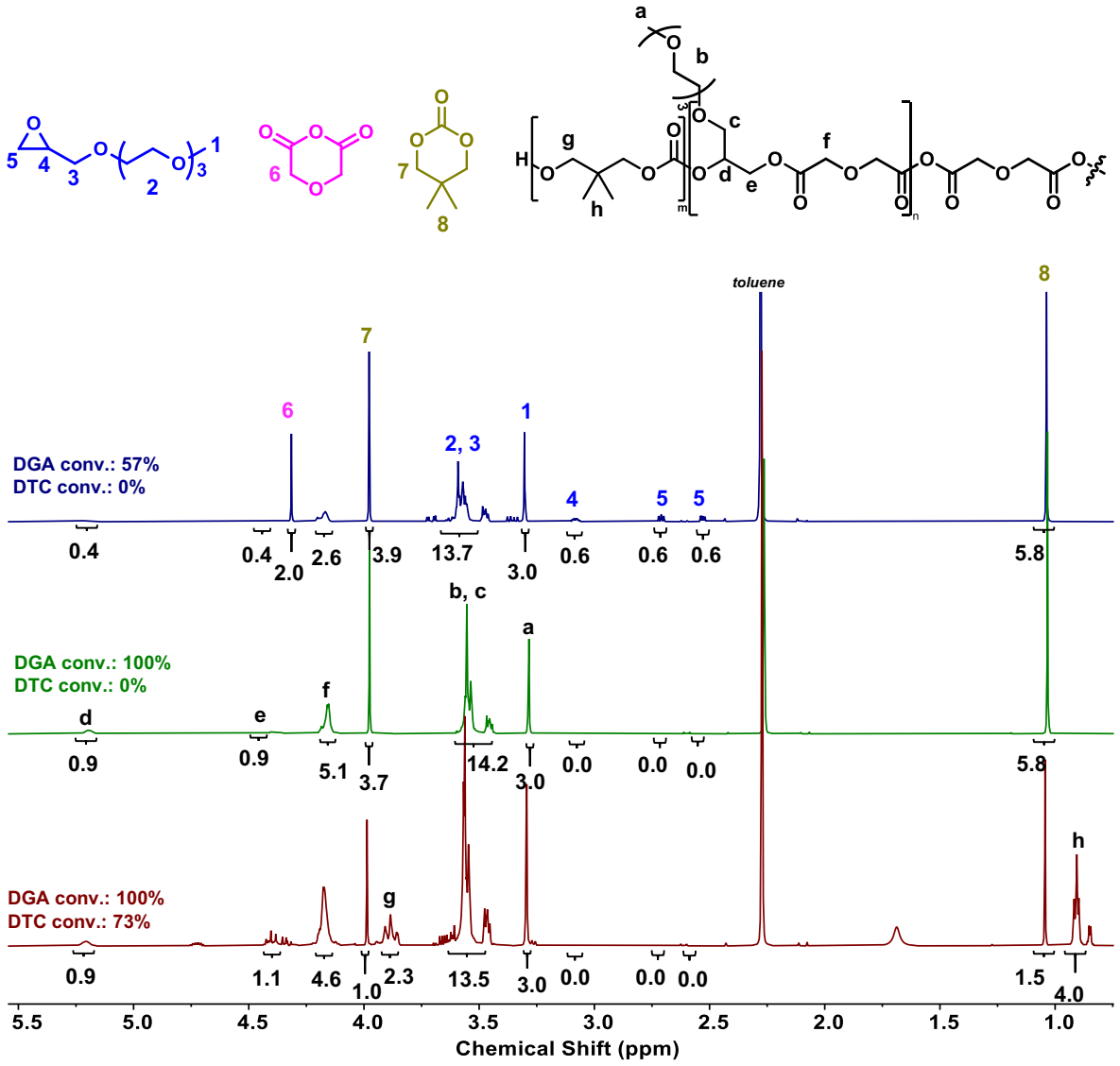


Figure 3.12. ^{1}H NMR spectra ($CDCl_3$, 500 MHz) of DGA/ME_3MO/DTC ROCOP at 57% DGA, 0% DTC; 100% DGA, 0% DTC; and 100% DGA, 73% DTC conversion, depicting the consumption of DGA, ME_3MO and DTC monomer and formation of poly(DTC-*b*-DGA-*alt*-ME_3MO-*b*-DTC). See Figure 7.10 for spectra spanning 0.0 – 7.5 ppm and zoomed so all 'd' signals at 5.29 ppm are observable.

Entry 2 was monitored by ^{1}H and ^{31}F NMR spectroscopy. During the first 10 minutes, HFA/ME_3MO ROCOP proceeded, as observed by the depletion of the ME_3MO signals in the ^{1}H NMR spectra (3.21 to 5.45 ppm, Figure 3.13) and the shifting and broadening of the HFA signals in the ^{31}F NMR spectra (-118.8 to -118.3 ppm, Figure 3.14). Only once all of the HFA was consumed, did DTC ROP proceed, as observed by the depletion of DTC monomer signals

at 4.07 and 1.10 ppm and the appearance of new polycarbonate signals at 3.96 and 0.97 ppm (Figure 3.13).

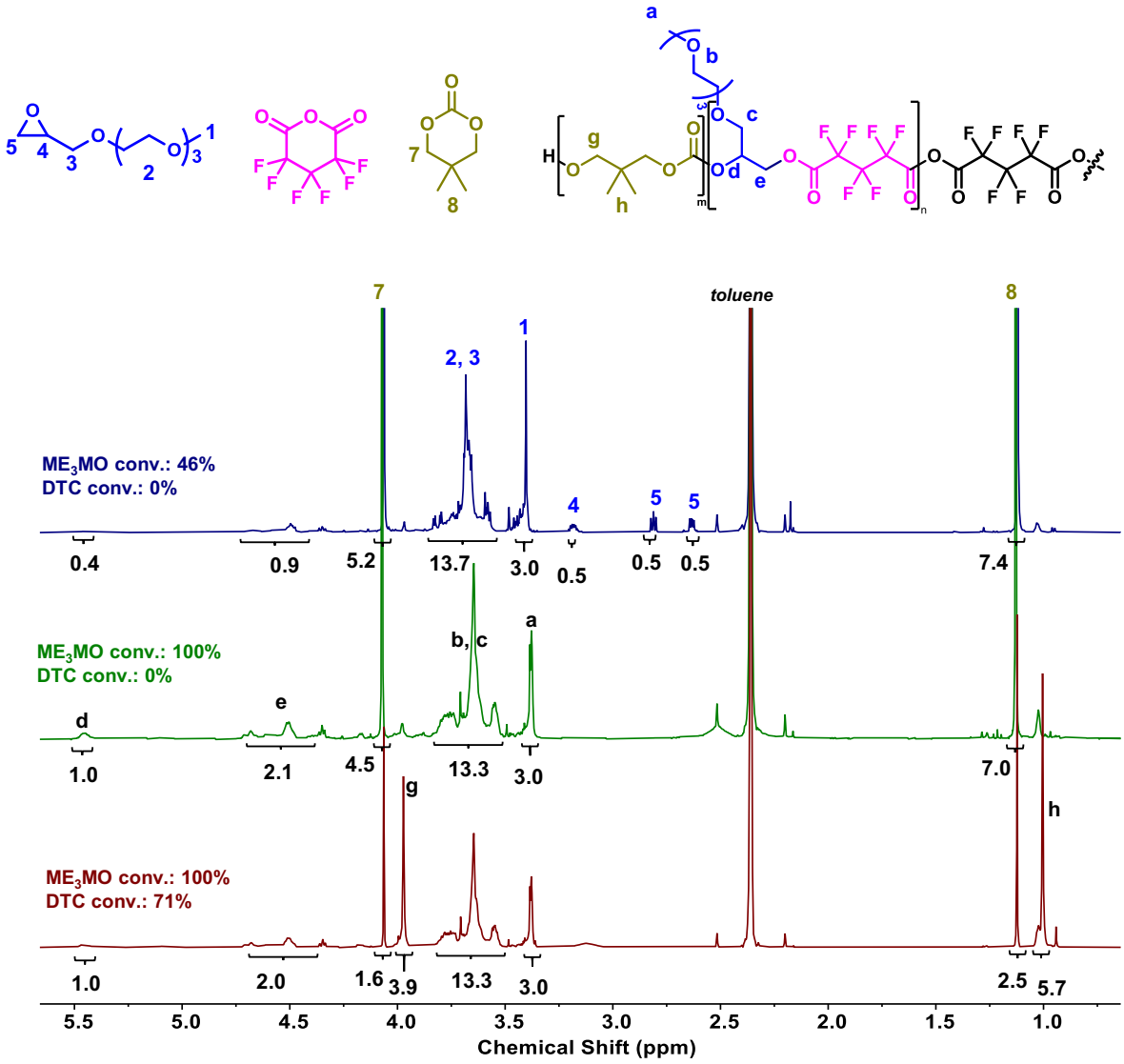


Figure 3.13. ^{1}H NMR spectra ($CDCl_3$, 500 MHz) of HFA/ME_3MO/DTC ROCOP at 46% ME_3MO, 0% DTC; 100% ME_3MO, 0% DTC; and 100% ME_3MO, 71% DTC conversion, depicting the consumption of ME_3MO and DTC monomer and formation of poly(DTC-*b*-HFA-*alt*-ME_3MO-*b*-DTC). See Figure 7.11 for spectra spanning 0.0 – 7.5 ppm and zoomed so all 'd' signals at 5.29 ppm are observable.

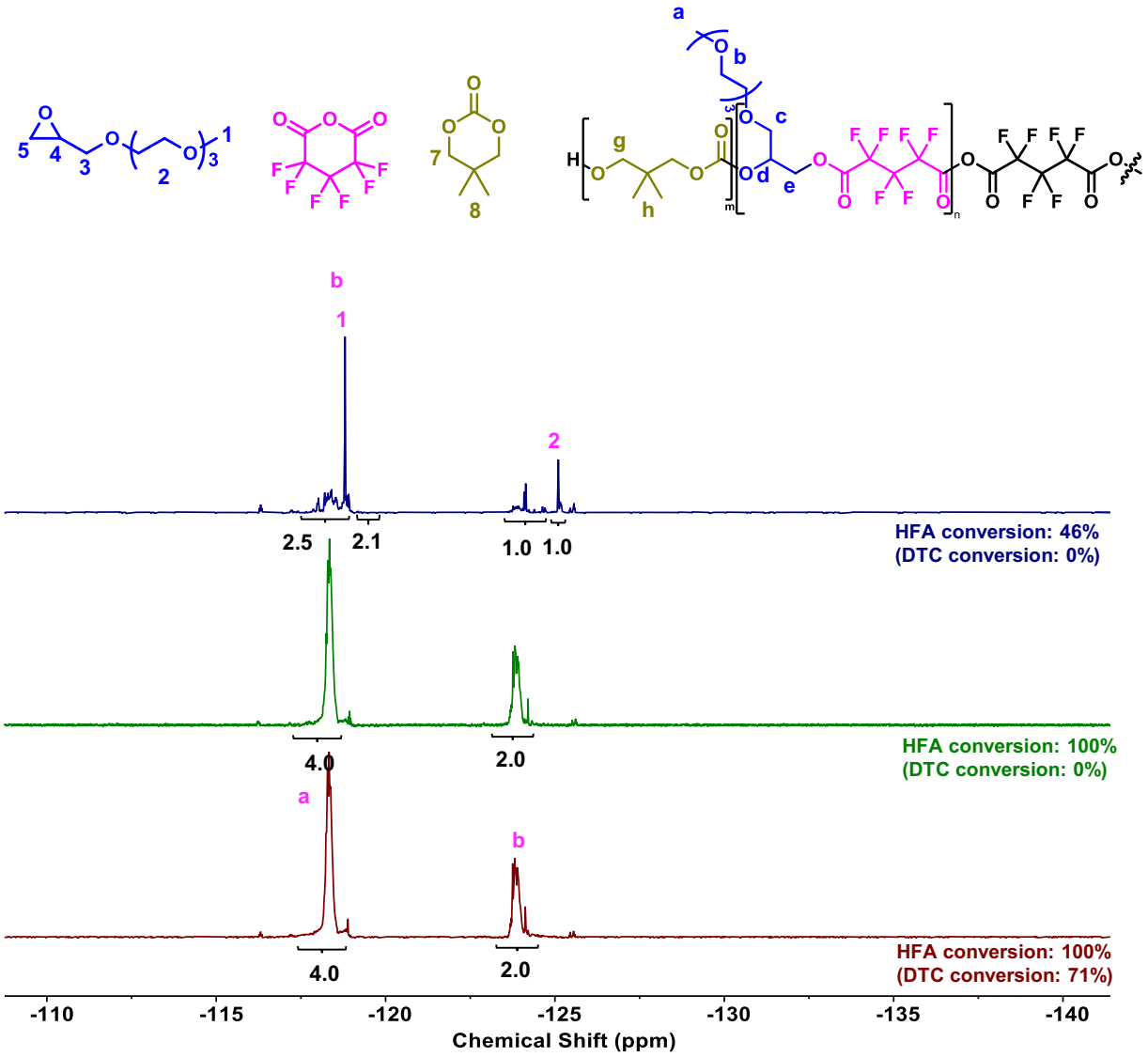


Figure 3.14. ^{19}F NMR spectra ($CDCl_3$, 500 MHz) from aliquots of HFA/ME_3MO/DTC copolymerisation at 46% HFA, 0% DTC; 100% HFA, 0% DTC; and 100% HFA, 71% DTC conversion, depicting the consumption of HFA monomer and formation of poly(DTC-*b*-HFA-*alt*-ME_3MO-*b*-DTC).

For entry 2, in-situ IR spectroscopy was used to establish the order of monomer enchainment. During the first hour of the polymerisation, the signal corresponding to HFA (1868 cm^{-1}) decreased and the signal corresponding to poly(HFA-*alt*-ME_3MO) increased (1785 cm^{-1}). Once HFA was fully consumed, the DTC (1113 cm^{-1}) was consumed and polycarbonate (1236 cm^{-1}) was produced (Figure 3.15, 3.16). The reaction was quenched when 50% DTC conversion was reached. This order of enchainment was as expected from the theory

of switch catalysis: from the alkoxide intermediate, anhydride insertion was fastest and formed the most stable linkage. The carboxylate intermediate can only react with the epoxide, thus the ROCOP cycle continued until all anhydride was consumed. Only then did DTC insert into the alkoxide and DTC ROP commenced (Scheme 3.3).

The rate law for HFA/ME_3MO copolymerisation is

$$rate = k_p[cat.]^x[ME_3MO]^y[HFA]^z \quad \text{Equation 3.2}$$

where

$$rate = \frac{d[polymer]}{dt} = -\frac{d[HFA]}{dt} \quad \text{Equation 3.3}$$

The polymerisation was conducted in excess epoxide thus [cat.] and [ME_3MO] were constant, and ROCOPs are typically zeroth order in anhydride, thus simplifying the rate law to

$$\frac{d[HFA]}{dt} = -k_{obs} \quad \text{Equation 3.4}$$

Rearranging this gives a differential equation which can be solved,

$$\int_{[HFA]_0}^{[HFA]_t} d[HFA] = -k_{obs} \int_0^t dt \quad \text{Equation 3.5}$$

$$[HFA]_t = -k_{obs}t + [HFA]_0 \quad \text{Equation 3.6}$$

Therefore, plotting [HFA] vs time gives a linear plot if HFA/ME_3MO ROCOP is pseudo-zeroth order, where the gradient is -k_{obs}: this was indeed observed and $k_{obs} = 3.78 \times 10^{-4}$ s^{-1} for HFA/ME_3MO ROCOP (Figure 7.12).

A similar process can be followed for DTC ROP, where the rate law for DTC ROP is

$$rate = k_p[cat.]^x[DTC]^y \quad \text{Equation 3.7}$$

As [cat.] is constant and ROPs are typically first order in cyclic carbonate, the rate law can be simplified to

$$\frac{d[DTC]}{dt} = -k_{obs}[DTC] \quad \text{Equation 3.8}$$

Rearranging this gives a differential equation which can be solved,

$$\int_{[DTC]_0}^{[DTC]_t} \frac{d[DTC]}{[DTC]} = -k_{obs} \int_0^t dt \quad \text{Equation 3.9}$$

$$ln[DTC]_t = -k_{obs}t + [DTC]_0 \quad \text{Equation 3.10}$$

Therefore, plotting ln[DTC] vs time yields a linear plot if DTC ROP is first order, where the gradient is -k_{obs}: this was observed and k_{obs} = = 1.15 × 10^{-5} s^{-1} (Figure 7.13).

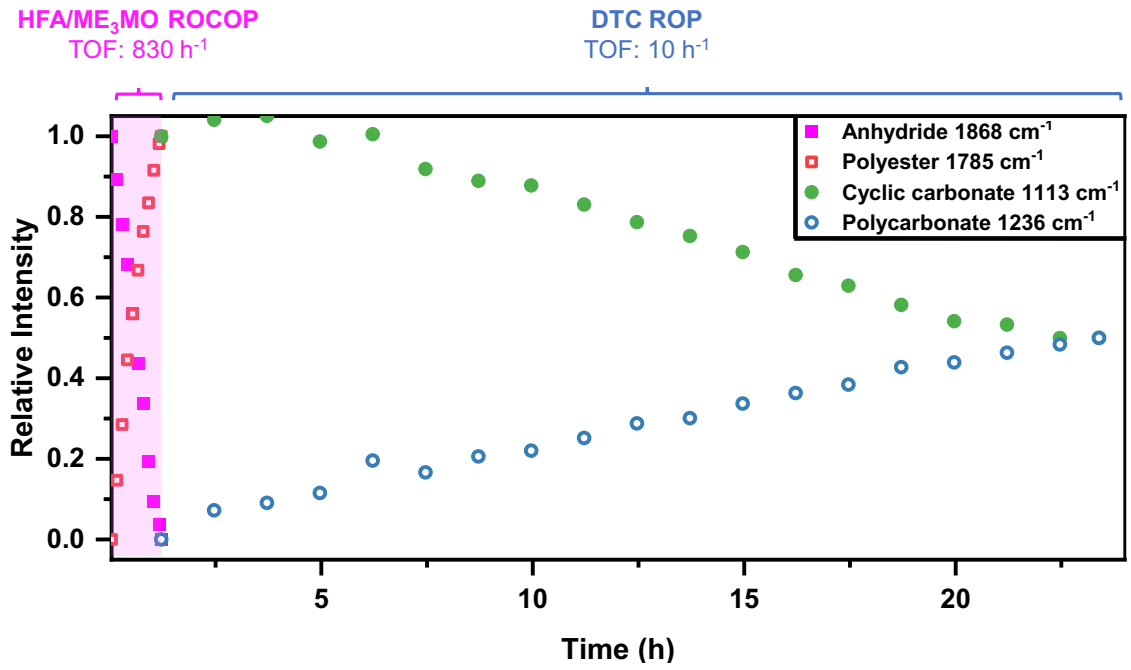


Figure 3.15.i. In-situ ATR-IR spectroscopy monitoring the switchable polymerisation catalysis of HFA, ME_3MO and DTC, catalysed by P_2-*t*-Bu, illustrating firstly HFA/ME_3MO ROCOP, followed by DTC ROP after 1 h. Relative intensity calibrated using ^{1}H NMR spectroscopy.

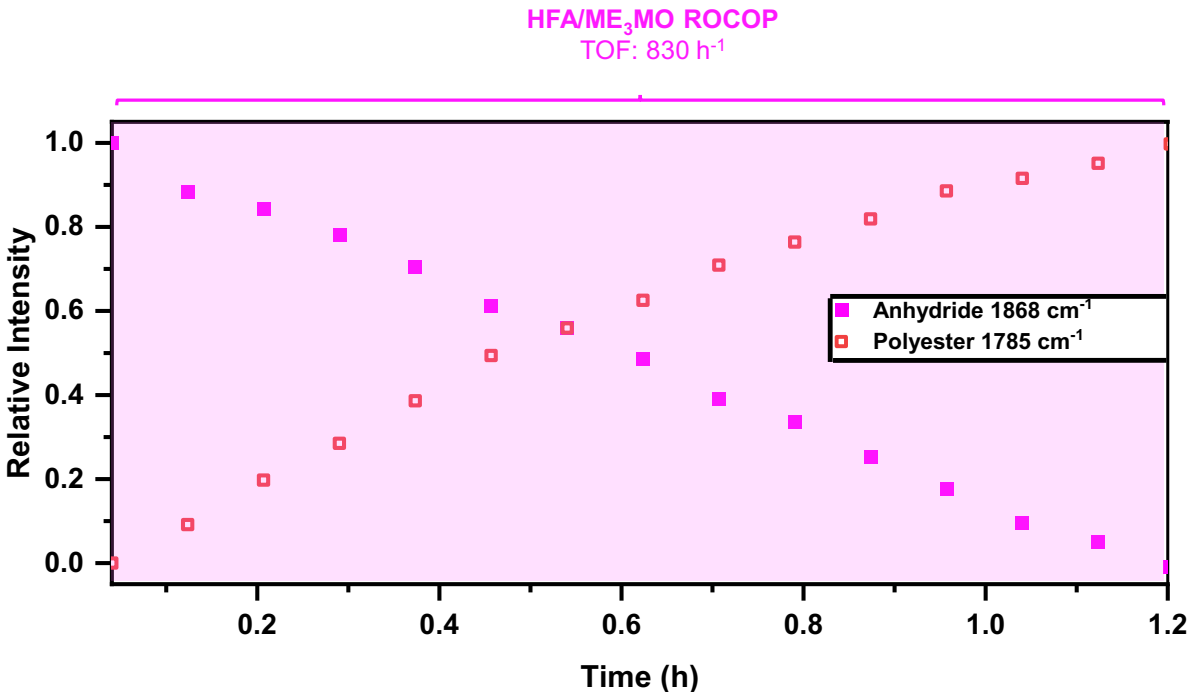
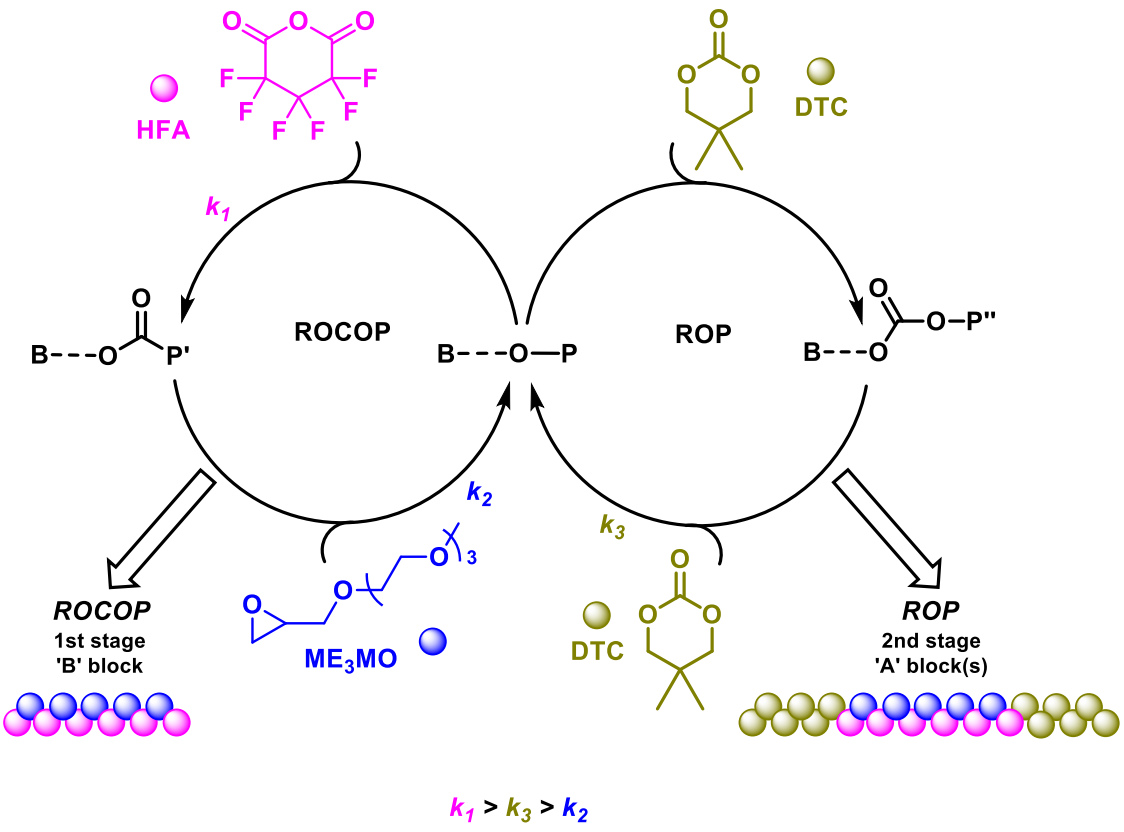


Figure 3.15.ii. In-situ ATR-IR spectroscopy monitoring the switchable polymerisation catalysis of HFA, ME_3MO and DTC, catalysed by P_2-*t*-Bu, magnified to illustrate only HFA/ME_3MO ROCOP. Relative intensity calibrated using ^1H NMR spectroscopy.



Scheme 3.3. Epoxide/anhydride ring-opening copolymerisation (ROCOP) and DTC ring-opening polymerisation (ROP) cycles accessed by a single switchable catalyst to produce block copolymers, where 'B' denotes the phosphazene base.

For entry 1, selective triblock copolymer formation was supported by SEC analyses. An increase in polymer molar mass was observed between the ROCOP and ROP stages, from 2.4 kg mol^{-1} to 3.5 kg mol^{-1}. This data may indicate the formation of the desired block copolymer. The dispersity of the traces were narrow and monomodal which is characteristic of a well-controlled polymerisation (Figure 3.17).

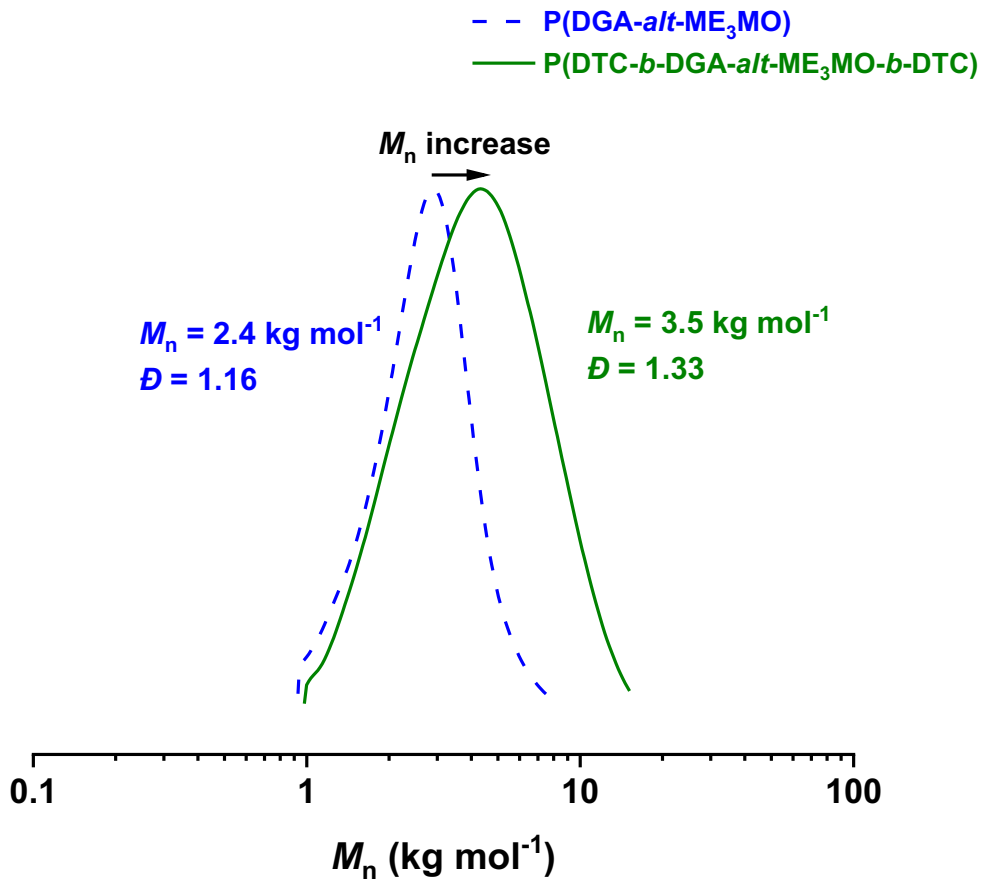


Figure 3.16. SEC traces from aliquots of the switch polymerisation of DGA, ME_3MO and DTC, showing the growth in polymer molar mass after DGA/ME_3MO ROCOP (P(DGA-*alt*-ME_3MO)), and after the subsequent DTC ROP P(DTC-*b*-DGA-*alt*-ME_3MO-*b*-DTC)).

The ^{1}H NMR spectra of all entries showed the expected signals for the polycarbonate and polyester blocks (Figures 3.18, 7.14 – 7.18). There was no indication of ME_3MO ROP (no signals at 2.5 to 3.1 ppm). The signal corresponding to the polyester chain end (d_{end}, Figure 3.5) disappeared, consistent with DTC ROP proceeding from the polyester chain ends. A new signal corresponding to the polycarbonate chain end (h_{end}) appeared. Integration of this signal allowed the polymer molar mass to be determined. Specifically, by integration of the signals corresponding to the polycarbonate chain end (0.92 ppm) against those of the polyester (5.28, 4.46, 4.25, 3.64 – 3.37 ppm) and polycarbonate (3.96, 0.99 ppm). The ^{13}C NMR spectrum for entry 1 showed the expected signals, there were just two types of carbonyl environment present

(P(DTC) and P(DGA-*alt*-ME$_3$MO)) which indicated block copolymer formation and an absence of detectable transesterification (Figure 3.19).

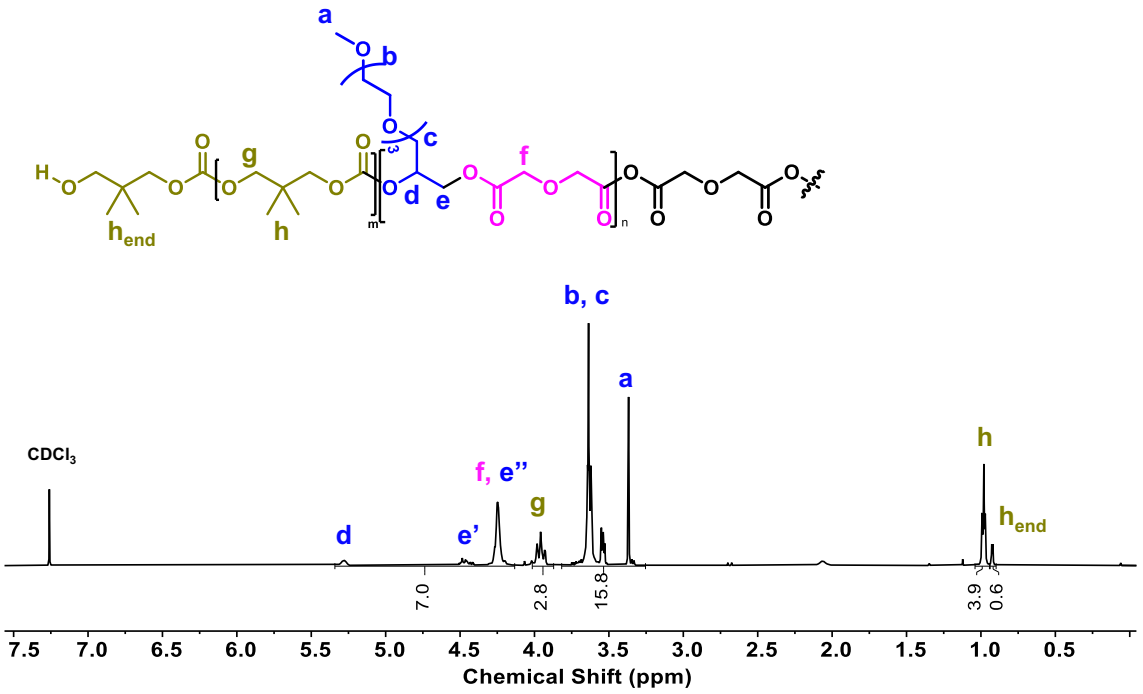


Figure 3.17. ^{1}H NMR spectrum (CDCl$_3$, 500 MHz) of poly(DTC-*b*-DGA-*alt*-ME$_3$MO-*b*-DTC).

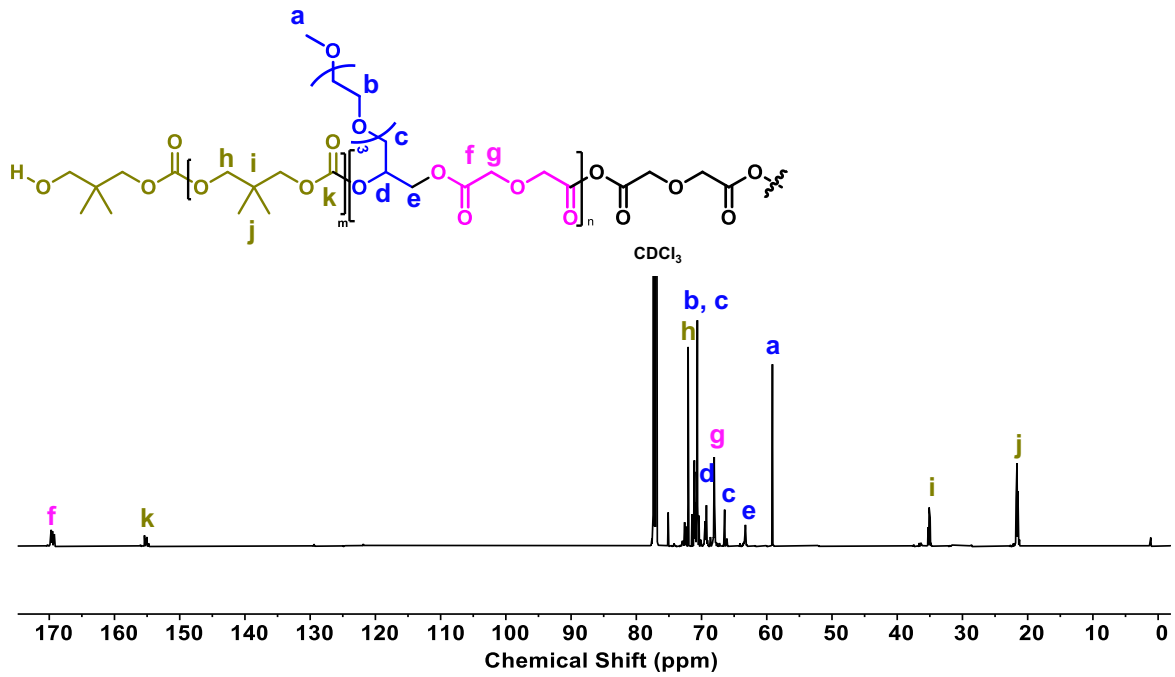


Figure 3.18. ^{13}C{H} NMR spectrum (CDCl3, 500 MHz) of poly(DTC-*b*-DGA-*alt*-ME$_3$MO-*b*-DTC).

SEC analyses revealed lower molar mass values with narrow, monomodal distributions, indicative of a well-controlled polymerisation (Figure 3.20, 7.19). The molar mass estimated by SEC was less than that determined by ^{1}H NMR spectroscopy. These highly oxygenated and fluorinated polymers are proposed to behave differently in solution than the PS calibration standards, thus their retention times to not reflect the true molar masses (Table 3.4 and 6.6).

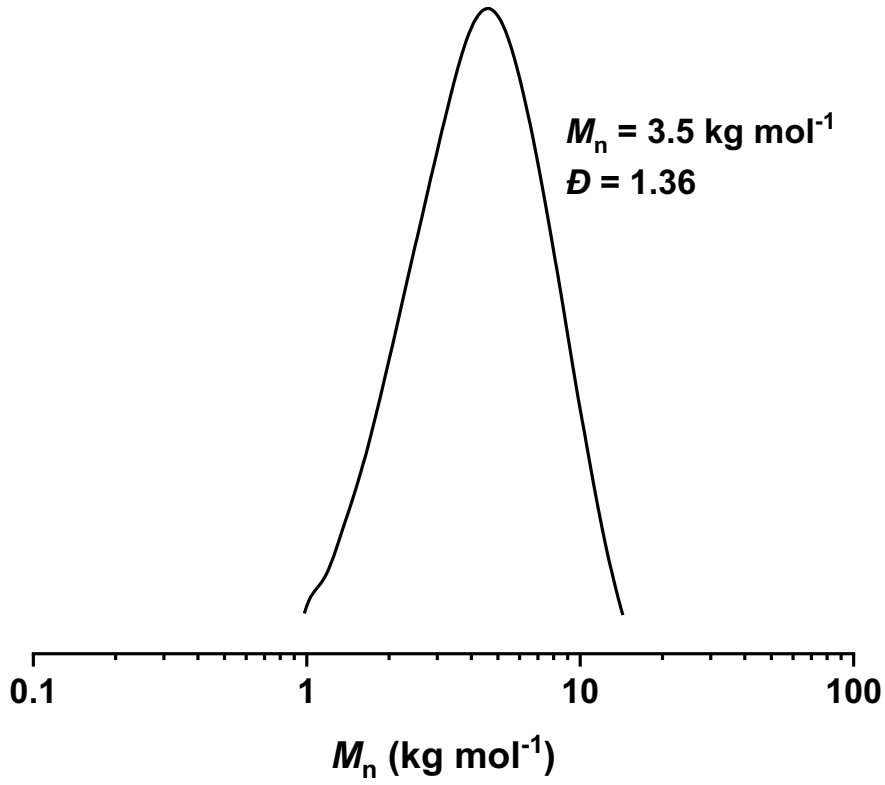


Figure 3.19. SEC trace for the purified polymer poly(DTC-*b*-DGA-*alt*-ME$_3$MO-*b*-DTC), measured in THF with an RI detector vs. narrow PS standards.

DOSY NMR spectroscopy showed a single diffusion coefficient, indicating that the polymer blocks were connected (Figure 3.21). Polymer chain end-group analysis was conducted by reaction of the hydroxyl chain ends with 2-chloro-4,4,5,5-tetramethyldioxaphospholone followed by identification of the end groups by ^{31}P NMR

spectroscopy. The poly(DGA-*alt*-ME$_3$MO) and poly(DTC) polymers were compared to poly(DTC-*b*-DGA-*alt*-ME$_3$MO-*b*-DTC). Only polycarbonate chain ends (148.47 ppm) were observed for the block copolymer without any residual polyester (147.14 ppm), which provided further evidence of DTC ROP proceeding from the polyester chain ends to produce a block copolymer, rather than a mixture of homopolymers (Figure 3.22).

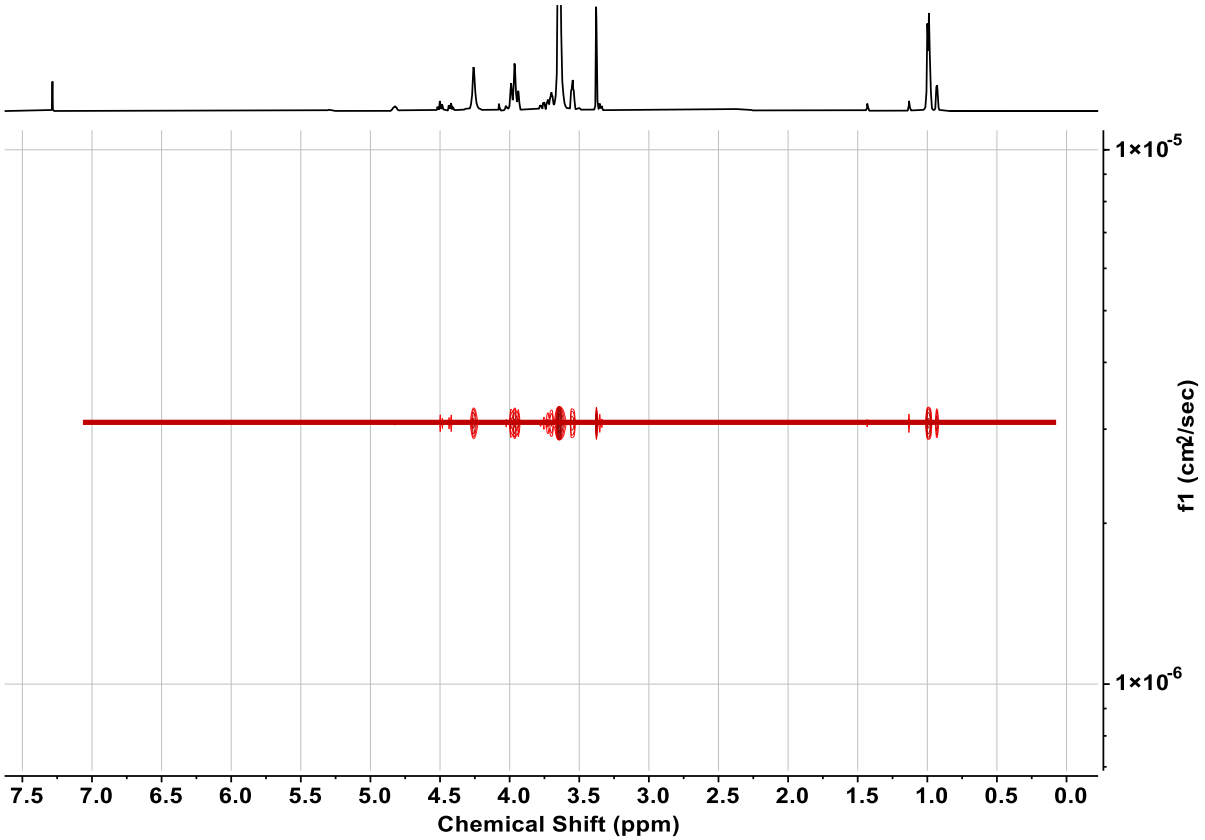


Figure 3.20. ^{1}H DOSY NMR spectrum of poly(DTC-*b*-DGA-*alt*-ME$_3$MO-*b*-DTC)

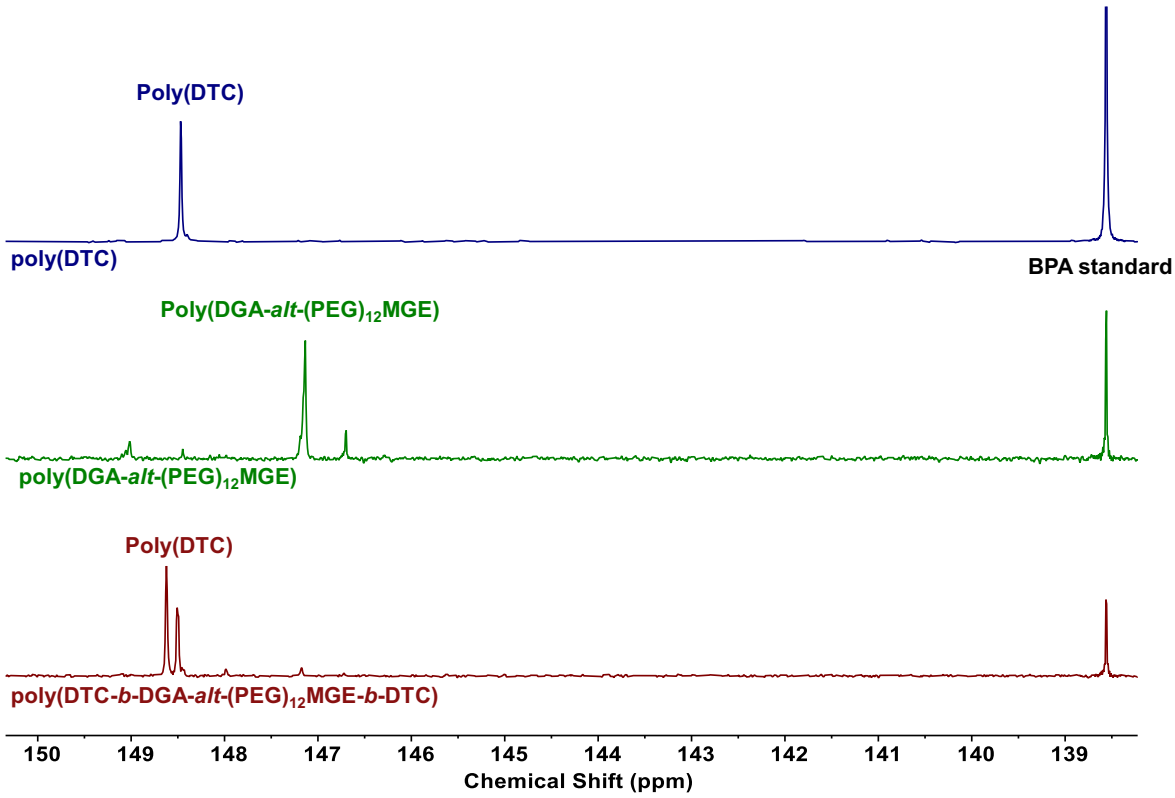


Figure 3.21. $^{31}P\{H\}$ NMR spectra ($CDCl_3$) after reaction of the polymer hydroxyl end groups with 2-chloro-4,4,5,5-tetramethyldioxaphospholone. Top: poly(DTC), displaying poly(DTC)-OH end groups. Middle: poly(DGA-*alt*-ME_3MO), displaying poly(DGA-*alt*-ME_3MO)-OH end groups. Bottom: Poly(DTC-*b*-DGA-alt-ME_3MO-*b*-DTC), displaying poly(DTC-*b*-DGA-alt-ME_3MO-*b*-DTC)-OH end groups.

Thermal data was acquired by DSC, from the second heating scan. All of the block polymers showed a single T_g value between -64 and -46 °C, attributed to the polyester block (Table 3.4, Figure 3.23). As observed with the polyesters, the two polymers with the longest PEG side chains, poly(DTC-*b*-DGA-*alt*-MGE-$(PEG)_{12}$-*b*-DTC) and poly(DTC-*b*-HFA-*alt*-MGE-$(PEG)_{12}$-*b*-DTC), were semicrystalline, as observed by a T_c at -20 °C and -28 °C and a T_m at 0 °C and -5 °C, respectively (Table 3.4, Figure 3.23). PEG is known to be semicrystalline thus in these polymers, the PEG side chain is long enough for ordered domains to emerge. With the exception of the ME_3MO-based polymers, the block copolymers showed a small decrease in T_g compared to their respective polyesters. For example, poly(DGA-*alt*-AGE) and

poly(DTC-*b*-DGA-*alt*-AGE-*b*-DTC) had T_g values of -43 and -45 °C, respectively. This could be due to small amounts of DTC impurities in the polymer, unobservable by NMR, which are acting as plasticisers and enhance chain mobility. The trends relating T_g to PEG side-chain length and backbone fluorination mirror what was observed with the polyesters: increasing PEG side-chain length decreased T_g and fluorinated backbones decreased T_g.

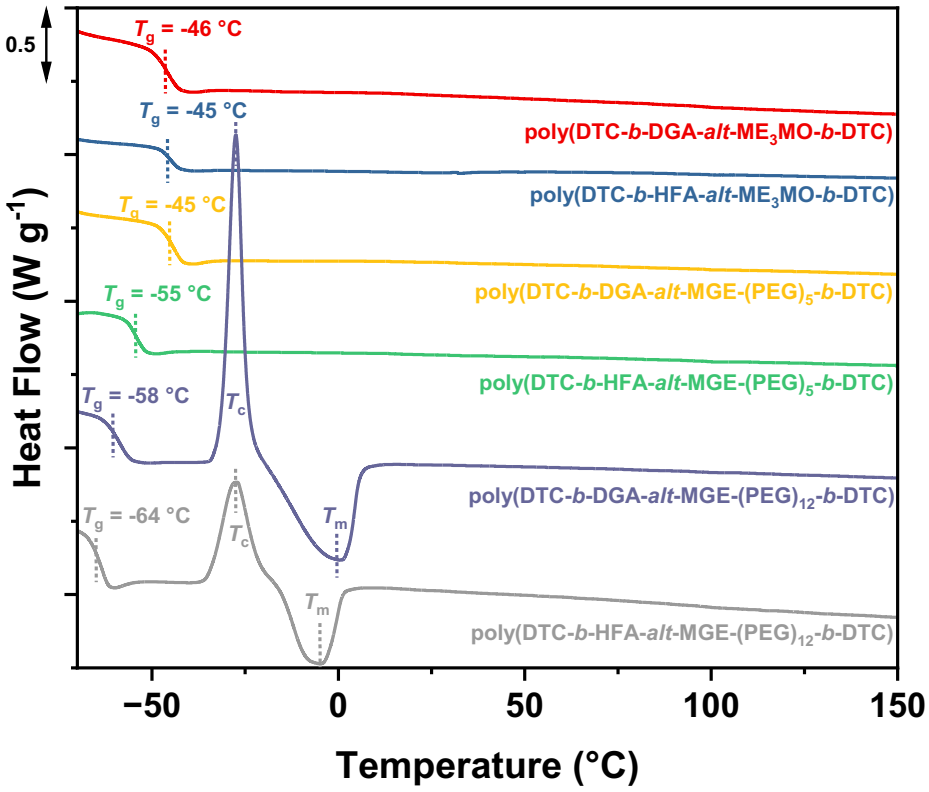


Figure 3.22. DSC data for block copolymers as listed in Table 3.2, at a scan rate of 10 °C min^{-1}. Second heating curve displayed.

3.4.2. Block Copolymer Electrolyte Properties

Polymer electrolytes were prepared by mixing a stirred solution of the polymer with LiTFSI, in THF, and allowing the solvent to evaporate. The solvent was removed first at ambient temperature and pressure, and then under a vacuum of 10^{-1} mbar at 60 °C. The salt loading was defined as the molar ratio of lithium ions to coordinating oxygen atoms, $\rho = [Li^+]/[O]$. A value of $\rho = 0.037$ was used for all materials, since this loading was found to be the best in prior work investigating poly(DGA-*alt*-AGE).[24]

Polymer thermal characterisation data was obtained by DSC. In all cases, the T_g of the polymer electrolyte is higher than the corresponding polymers, e.g. for poly(DTC-*b*-DGA-*alt*-ME_3MO-*b*-DTC), the T_g increased from -46 to -21 °C (Figure 3.24, Table 3.5). This was likely due to the salt causing transient interchain crosslinks which stiffen the material. The MGE-$(PEG)_{12}$-based block copolymer electrolytes no longer exhibited any crystallinity (Figure 3.24). This suppression of crystallinity is generally beneficial for Li-ion conductivity, as segmental motion of the polymer chains generally aids Li-ion transport.

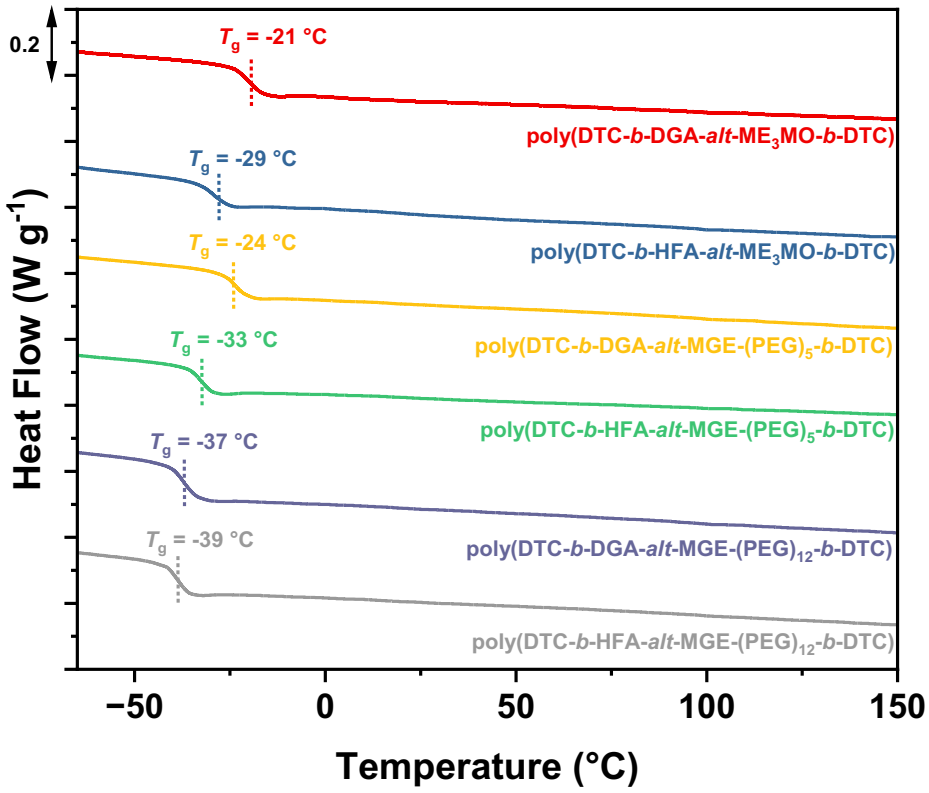


Figure 3.23. DSC data for block copolymers electrolytes as listed in Table 3.3, at a scan rate of 10 °C min^{-1}.

Table 3.5. Block Copolymer Electrolyte VFT Parameters and Thermal Data

Polymer [a]	T_g (°C) [b]	E_a (kJ mol^{-1}) [c]	lnA [d]
Poly(DTC-*b*-DGA-*alt*-ME$_3$MO-*b*-DTC)	-21	13.0	5.0
Poly(DTC-*b*-HFA-*alt*-ME$_3$MO-*b*-DTC)	-29	14.1	5.1
Poly(DTC-*b*-DGA-*alt*-MGE-(PEG)$_5$-*b*-DTC)	-24	12.7	4.8
Poly(DTC-*b*-HFA-*alt*-MGE-(PEG)$_5$-*b*-DTC)	-33	15.0	6.6
Poly(DTC-*b*-DGA-*alt*-MGE-(PEG)$_{12}$-*b*-DTC)	-37	11.5	3.7
Poly(DTC-*b*-HFA-*alt*-MGE-(PEG)$_{12}$-*b*-DTC)	-39	12.1	3.8

[a] All polymers with $\rho = 0.037$ LiTFSI; [b] Determined by DSC, second heating curve; [c] Activation energy of Li-ion transfer, obtained from the VFT fit; [d] Relative free charge carrier concentration of the polymer electrolyte, obtained from the VFT fit.

Li-ion conductivity was determined by EIS at 10 °C temperature intervals between 30 and 80 °C (Table 3.6). A coin cell was used to contain the polymer electrolyte, which was sandwiched between two steel discs. In all cases, semi-circular Nyquist curves were obtained and fitted to the equivalent circuit Q1+(Q2/R2) (Figure 3.25). All the polymers had conductivities greater than 10^{-6} S cm^{-1} at 30 °C and 10^{-4} S cm^{-1} at 80 °C.

Table 3.6. Li-ion conductivity and VTF parameter data for the block copolymer electrolytes.

Polymer [a]	σ (S cm^{-1}) [b]					
	30 °C	**40 °C**	**50 °C**	**60 °C**	**70 °C**	**80 °C**
Poly(DTC-*b*-DGA-*alt*-ME_3MO-*b*-DTC)	1.4×10^{-6}	7.8×10^{-6}	2.8×10^{-5}	7.1×10^{-5}	1.3×10^{-4}	2.1×10^{-4}
Poly(DTC-*b*-HFA-*alt*-ME_3MO-*b*-DTC)	1.5×10^{-6}	6.5×10^{-6}	2.0×10^{-5}	4.7×10^{-5}	9.6×10^{-5}	2.0×10^{-4}
Poly(DTC-*b*-DGA-*alt*-MGE-$(PEG)_5$-*b*-DTC)	2.6×10^{-6}	1.1×10^{-5}	3.2×10^{-5}	6.7×10^{-5}	1.6×10^{-4}	3.1×10^{-4}
Poly(DTC-*b*-HFA-*alt*-MGE-$(PEG)_5$-*b*-DTC)	4.0×10^{-6}	2.0×10^{-5}	5.9×10^{-5}	1.3×10^{-4}	3.0×10^{-4}	5.4×10^{-4}
Poly(DTC-*b*-DGA-*alt*-MGE-$(PEG)_{12}$-*b*-DTC)	1.8×10^{-5}	4.7×10^{-5}	1.0×10^{-4}	1.9×10^{-4}	3.4×10^{-4}	5.6×10^{-4}
Poly(DTC-*b*-HFA-*alt*-MGE-$(PEG)_{12}$-*b*-DTC)	1.2×10^{-5}	3.2×10^{-5}	7.0×10^{-5}	1.4×10^{-4}	2.5×10^{-4}	4.2×10^{-4}

[a] All polymers with $\rho = 0.037$ LiTFSI; [b] Measured using impedance spectroscopy, with ionic conductivity being calculated from the resistance obtained by fitting the data to the equivalent circuit Q1+Q2/R2. Error values were determined from the standard deviation of three repeated experiments and corresponded to ± 23%, 14%, 11%, 9%, 3% and 9% at 30 °C, 40 °C, 50 °C, 60 °C, 70 °C and 80 °C, respectively.

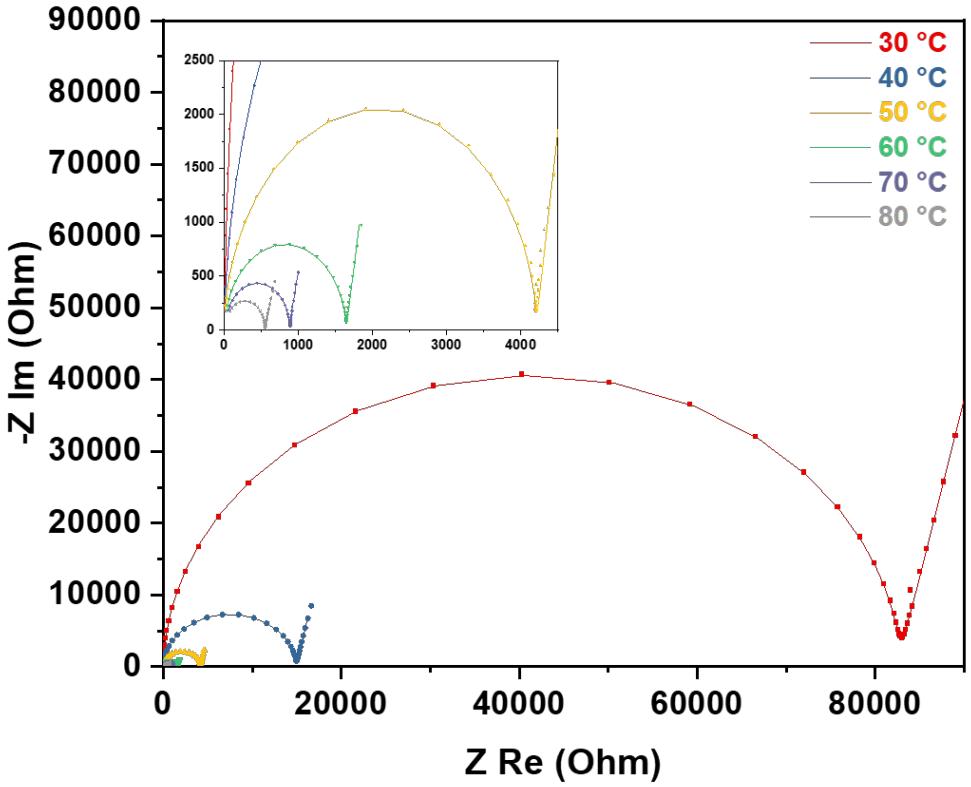


Figure 3.24. Nyquist curves generated from the electrochemical impedance spectroscopy of poly(DTC-*b*-DGA-*alt*-ME$_3$MO-*b*-DTC), with LiTFSI concentration ρ = 0.037, where points are the collected data and lines represent the fitted data.

The Li-ion conductivity increased with increasing length of the ether side chain: at 30 °C, Li-ion conductivity was 1.4 × 10^{-6} S cm^{-1} for poly(DTC-*b*-DGA-*alt*-ME$_3$MO-*b*-DTC), 2.6 × 10^{-6} S cm^{-1} for poly(DTC-*b*-DGA-*alt*-MGE-(PEG)$_5$-*b*-DTC) and 1.2 × 10^{-5} S cm^{-1} for poly(DTC-*b*-DGA-*alt*-MGE-(PEG)$_{12}$-*b*-DTC) (Table 3.6, Figure 3.26). This was analogous to the polyester electrolytes; as the PEG side chain length increased, the block copolymer electrolyte T_g decreased, thus the polymer chains are more mobile and show improved Li-ion transport. Polyethers transport Li-ions by a rapid intrachain transport mechanism whereas polycarbonates and polyesters transport Li-ions by interchain hopping, which is intrinsically slower.[24, 25]

Incorporating a fluorinated or non-fluorinated anhydride into the polymer backbone had an inconsistent effect on Li-ion conductivity. For the MGE-$(PEG)_5$-based block copolymers, the fluorinated polymer had a lower T_g value and thus higher Li-ion conductivity: poly(DTC-*b*-DGA-*alt*-MGE-(PEG_5)-*b*-DTC) had a T_g of -24 °C and a Li-ion conductivity of 2.6×10^{-6} S cm^{-1} at 30 °C, but poly(DTC-*b*-HFA-*alt*-MGE-(PEG_5)-*b*-DTC) had a T_g of -33 °C and a Li-ion conductivity of 4.0×10^{-6} S cm^{-1} at 30 °C (Table 3.5, 3.6). The fluorinated polymer could also be aiding salt dissociation, thus enhancing ion mobility.

For the MGE-$(PEG)_{12}$-based block copolymer electrolytes, there was an insignificant difference between the Li-ion conductivity of the unfluorinated and fluorinated polymer. For example, poly(DTC-*b*-DGA-*alt*-MGE-(PEG_{12})-*b*-DTC) had a T_g of -37 °C and a Li-ion conductivity of 1.8×10^{-5} S cm^{-1} at 30 °C, whilst poly(DTC-*b*-HFA-*alt*-MGE-(PEG_{12})-*b*-DTC) had a T_g of -39 °C and a Li-ion conductivity of 1.2×10^{-5} S cm^{-1} at 30 °C (Table 3.5, 3.6). The difference between the T_g values is small (2 °C) so chain mobility differences should have a negligible impact on Li-ion conductivity. Perhaps Li-ion conductivity was dominated by $(PEG)_n$ at this side chain length (n = 12). Generally, polyethers conduct by a faster ion transport mechanism than polyesters and the pendant side chains are more accessible than the polyester backbone.

For the ME_3MO-based block copolymers, a fluorinated polyester backbone had an insignificant effect on Li-ion conductivity. This was contrary to the conductivity differences observed in the polyester counterparts and any T_g differences. This was rationalised by considering the compositional differences of these block copolymers: they have the same polyester DP_n (30) and poly(DTC) weight fractions (0.2), however, as HFA has a greater molar

mass than DGA, they have different polycarbonate DP_n values (19 for poly(DTC-*b*-HFA-*alt*-ME_3MO-*b*-DTC), 26 for poly(DTC-*b*-HFA-*alt*-ME_3MO-*b*-DTC). Poly(DTC-*b*-HFA-*alt*-ME_3MO-*b*-DTC) thus has a lower proportion of ether and ester groups and a higher proportion of carbonate groups; ethers are known to facilitate more rapid Li-ion transport thus fewer ethers could hinder conductivity. This may not affect the MGE-$(PEG)_5$ and MGE-$(PEG)_{12}$-based block copolymers because as the pendant PEG chain length increases, the relative difference in poly(DTC) DP_n becomes smaller.

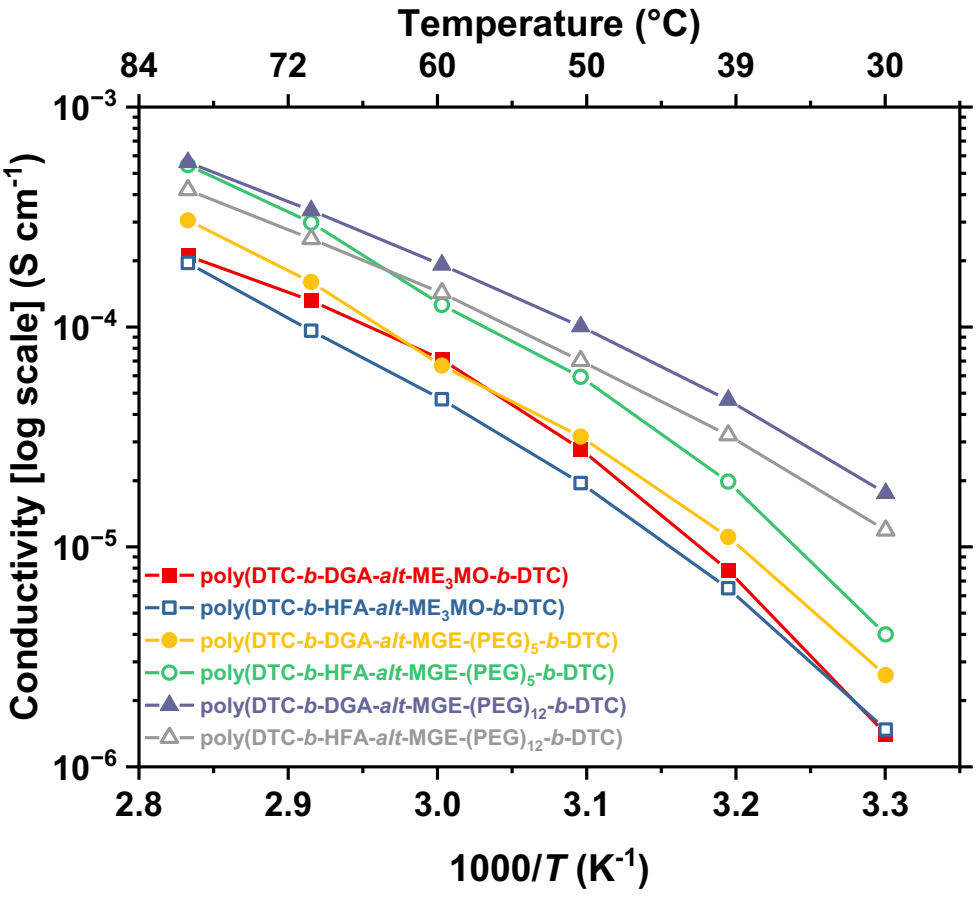


Figure 3.25. Li-ion conductivity as a function of temperature for the block copolymer electrolytes, with LiTFSI concentration $\rho = 0.037$.

The most conductive block copolymer was poly(DTC-*b*-DGA-*alt*-MGE-(PEG_{12})-*b*-DTC): it performed well at ambient and at high temperatures, with a Li-ion conductivity of 1.8×10^{-5} S cm^{-1} at 30 °C and 5.6×10^{-4} S cm^{-1} at 80 °C. The temperature dependence of Li-ion conductivity was modelled using the VFT relationship,

$$\sigma = AT^{-1/2}\exp\left[-E_a/(T - T_0)\right] \quad \text{Equation 3.11}$$

where A is a constant proportional to the number of Li-ions; E_a is the Li-ion transport activation energy; and T_0 is the temperature where configurational entropy is zero. The Li-ion conductivity of all polymers conformed to the VFT model, as evidenced by the linear VFT plots (Table 3.5, Figure 3.27). This indicated that Li-ion conductivity was coupled to the segmental motion of the polymer chain, which is common and well-known for polymer electrolytes.[26] For all polymers, the Li-ion conductivity increased at high temperatures, e.g. for poly(DTC-*b*-DGA-*alt*-ME_3MO-*b*-DTC), Li-ion conductivity increased from 1.4×10^{-6} S cm^{-1} at 30 °C, to 2.1×10^{-4} S cm^{-1} at 80 °C. As the temperature increased above the T_g, the polymer chains are increasingly mobile and thus able to transport Li^+.

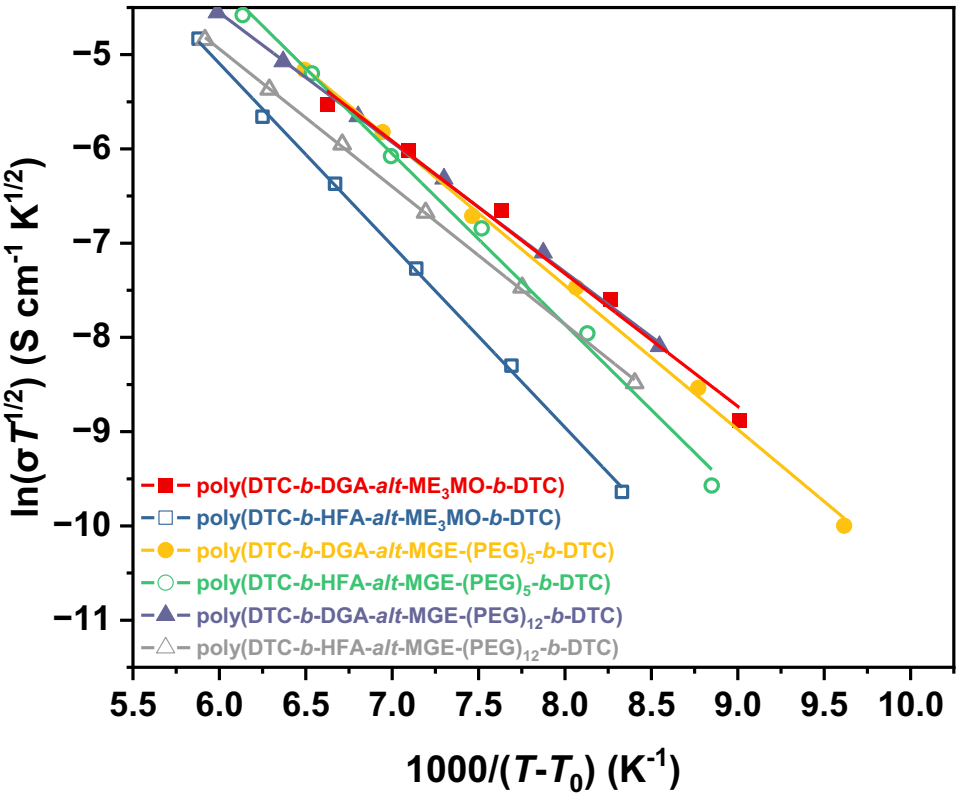


Figure 3.26. VFT fit of the temperature dependence of Li-ion conductivity for the block copolymer electrolytes. R^2 = 0.985, 0.994, 0.998, 0.999, 0.999, 0.999.

Finally, the oxidative stability of the two block copolymer electrolytes with the highest Li-ion conductivity was determined: poly(DTC-*b*-DGA-*alt*-MGE-$(PEG)_{12}$-*b*-DTC) and poly(DTC-*b*-HFA-*alt*-MGE-$(PEG)_{12}$-*b*-DTC). Linear sweep voltammetry (LSV) was measured vs lithium metal with a stainless-steel counter electrode. The stability was assessed from the open-circuit voltage (2.39 V for poly(DTC-*b*-DGA-*alt*-MGE-$(PEG)_{12}$-*b*-DTC), 2.65 V for poly(DTC-*b*-HFA-*alt*-MGE-$(PEG)_{12}$-*b*-DTC)) to 6 V, at a sweep rate of 0.1 mV s^{-1}. The DGA-based polymer had an oxidative stability of 5.1 V, whereas the HFA-based polymer had a lower oxidative stability of 5.0 V (Figure 3.28). This is perhaps contrary to expectations as fluorinated polymers are renowned for having superior oxidative stability, with the highly

fluorinated polymers PTFE and PVDF being popular cathode binders for this reason.[27] Perhaps the common pendant PEG groups are dominating the observed performance rather than the polyester backbones. The polymers with shorter pendant PEG groups should be tested in future as perhaps then the backbone will have a greater effect on oxidative stability.

Nevertheless, these polymers both have good oxidative stability which encourages their future application as polymer cathode binders or electrolytes. The stability of 5 V is competitive with other high performance polymer electrolytes in the literature, e.g. poly(CL-*r*-TMC) (5 V), and it exceeds a PEG-containing polymer electrolyte, PvCHC-*b*-PEO-*b*-PvCHC (4.2 V).[9, 28] The data suggests that the new polymers would be stable using high-voltage cathodes, such as Ni- and Mn-rich oxides (e.g. NMC-811 requires 4.2 V).[4] It is particularly relevant that the non-fluorinated polymer performs similarly, indeed is slightly superior to, the fluorinated polymer. Fluorinated chemicals have a detrimental environmental impact and may be restricted thus competitive alternatives are required.

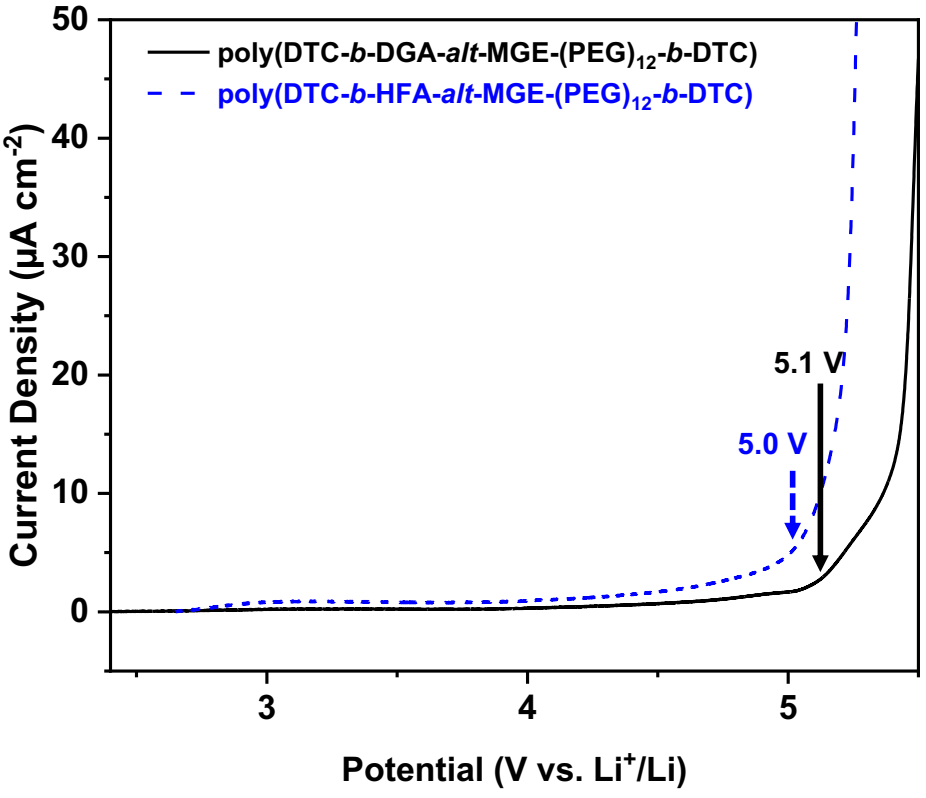


Figure 3.27. Oxidative stability vs Li metal and stainless-steel counter electrode measured at 60 °C, 0.1 mV s^{-1} scan rate.

3.5. Conclusions and Further Work

In this work, a series of polyester and poly(carbonate-*b*-ester) electrolytes were systematically produced and studied to observe the influence of altering the polymer backbone and side chain chemistry on the Li-ion conductivity. Firstly, a series of polyesters were produced by epoxide/anhydride ring-opening copolymerisation (ROCOP using an organocatalyst). These polymers were characterised by NMR spectroscopy and size-exclusion chromatography (SEC). Then, electrolytes with LiTFSI salts were formed. Polyesters with longer poly(ethylene glycol) (PEG) side chains and a fluorinated backbone showed higher Li-ion conductivity which correlated with lower T_g values for these polymers. Next, successful

switch catalysis using anhydride/epoxide/dimethyltrimethylene carbonate (DTC) was used to produce a series of block copolymers. The sequential and selective monomer consumption was observed by ^{1}H NMR spectroscopy and in-situ ATR-IR spectroscopy. The successful block copolymer formation was observed by SEC, chain end-group titration and DOSY NMR spectroscopy. The Li-ion conductivity of the block copolymer electrolytes revealed similar trends to the polyesters. Conductivity increased with increasing PEG chain length, with poly(DTC-*b*-DGA-*alt*-MGE-$(PEG)_{12}$-*b*-DTC) achieving the highest Li-ion conductivity of 5.6 × 10^{-4} S cm^{-1} at 80 °C. The oxidative stability of the two MGE-$(PEG)_{12}$-based block copolymers was measured. The non-fluorinated block polymer had a slightly higher oxidative stability (5 V) than the fluorinated analogue (4.9 V), thus poly(DTC-*b*-DGA-*alt*-MGE-$(PEG)_{12}$-*b*-DTC) was the lead polymer identified from this study.

Future work could involve further optimising the lead polymer's composition. It had the longest PEG side chains tested in the series; further increasing the side chain length could improve conductivity and thus the optimum ether side chain length should be identified. Above a certain side chain length, the oxidative stability could decrease (polyethers generally have an oxidative stability < 3.5 V) or the polyether could form crystalline regions, reducing conductivity.[26] Alternative polycarbonate hard blocks should also be explored: hexahydro-1,3-benzodioxolone could be ring-opened to produce poly(cyclohexene carbonate) (PCHC). This is more commonly produced by ring-opening copolymerisation of cyclohexene oxide (CHO) and CO_2 but forming this polymer from cyclic carbonate ROP may allow the whole process to be conducted in one-pot, under an N_2 atmosphere, obviating the need to switch the atmosphere to CO_2 for the polycarbonate formation. The hard block has a high T_g (115 °C) and the cyclohexene unit may reduce block miscibility and favour phase separation.[29, 30]

Block phase separation was not achieved in the current series, likely because the polymer molar masses were too low. One explanation is that monomer impurities were introducing additional protic compounds (CTAs) to the polymerisation and thereby reducing the molar mass. The most likely culprits for this are the epoxides: with the exception of ME_3MO, the epoxides' boiling temperature was too high to enable distillation. An alternative purification procedure could be used: reaction of the epoxide with methyl iodide prior to the polymerisation could cap any alcohol impurities to prevent them from initiating. The polymer molar mass could also be increased post-polymerisation by diisocyanate coupling reactions to form urethane links. This strategy may enable chain entanglement and thus impart mechanical strength to the polymer electrolyte.[31] The extent of coupling could be varied and the effect on the thermal and mechanical properties and Li-ion conductivity measured, in order to find the optimum extent of chain coupling.[32]

The lead polymer electrolyte studied here is a promising candidate for use in batteries, due to its processability and high Li-ion conductivity and oxidative stability. Composite electrolytes of garnet electrolyte (LLZO) and poly(CL-*r*-TMC) have been studied;[33] the lead polymer here has a greater Li-ion conductivity and similar oxidative stability so could achieve superior performance. Additionally, the polymer electrolyte with LiFSI salt could be tested as Chapter 2 demonstrated that this improved the capacity retention of cells with poly(vCHC-*b*-CL-*r*-TMC-*b*-vCHC) in the composite cathode.

3.6. References

1. D. E. Fenton, J. M. Parker and P. V. Wright, *Polymer*, 1973, **14**, 589.
2. D. L. Bresser, S.; Iojoiu, C.; Picard, L.; Passerini, S., *Mol. Syst. Des. Eng.*, 2019, **4**, 779-792.
3. Z. Xue, D. He and X. Xie, *J. Mater. Chem. A*, 2015, **3**, 19218-19253.

4. P. K. Nayak, E. M. Erickson, F. Schipper, T. R. Penki, N. Munichandraiah, P. Adelhelm, H. Sclar, F. Amalraj, B. Markovsky and D. Aurbach, *Adv. Energy Mater.*, 2018, **8**, 1702397.

5. T. Itoh, K. Fujita, K. Inoue, H. Iwama, K. Kondoh, T. Uno and M. Kubo, *Electrochim. Acta*, 2013, **112**, 221-229.

6. T. N. Phan, S. Issa and D. Gigmes, *Polym. Int.*, 2019, **68**, 7-13.

7. W. S. Loo and N. P. Balsara, *J. Polym. Sci., Part B: Polym. Phys.*, 2019, **57**, 1177-1187.

8. R. Bouchet, S. Maria, R. Meziane, A. Aboulaich, L. Lienafa, J.-P. Bonnet, T. N. T. Phan, D. Bertin, D. Gigmes, D. Devaux, R. Denoyel and M. Armand, *Nat. Mater.*, 2013, **12**, 452-457.

9. G. L. Gregory, H. Gao, B. Liu, X. Gao, G. J. Rees, M. Pasta, P. G. Bruce and C. K. Williams, *J. Am. Chem. Soc.*, 2022, **144**, 17477-17486.

10. Z. Zhang, T. Zeng, Y. Lai, M. Jia and J. Li, *J. Power Sources*, 2014, **247**, 1-8.

11. A. Guerfi, M. Kaneko, M. Petitclerc, M. Mori and K. Zaghib, *J. Power Sources*, 2007, **163**, 1047-1052.

12. S.-B. Hong, Y.-J. Lee, U.-H. Kim, C. Bak, Y. M. Lee, W. Cho, H. J. Hah, Y.-K. Sun and D.-W. Kim, *ACS Energy Lett.*, 2022, **7**, 1092-1100.

13. X. Lim, *Nature*, 2023, **620**, 24-27.

14. X. Xia, T. Gao, F. Li, R. Suzuki, T. Isono and T. Satoh, *Macromolecules*, 2023, **56**, 92-103.

15. Z. Geng, N. S. Schauser, J. Lee, R. P. Schmeller, S. M. Barbon, R. A. Segalman, N. A. Lynd and C. J. Hawker, *Macromolecules*, 2020, **53**, 4960-4967.

16. G. L. Gregory, G. S. Sulley, J. Kimpel, M. Łagodzińska, L. Häfele, L. P. Carrodeguas and C. K. Williams, *Angew. Chem. Int. Ed.*, 2022, **61**, e202210748.

17. G. Rosetto, A. C. Deacy and C. K. Williams, *Chem. Sci.*, 2021, **12**, 12315-12325.

18. G. L. Gregory and C. K. Williams, *Macromolecules*, 2022, **55**, 2290-2299.

19. M. Viviani, N. L. Meereboer, N. L. P. A. Saraswati, K. Loos and G. Portale, *Polym. Chem.*, 2020, **11**, 2070-2079.

20. K. Deng, S. Wang, S. Ren, D. Han, M. Xiao and Y. Meng, *ACS Appl. Mater. Interfaces*, 2016, **8**, 33642-33648.

21. H. Li, H. Luo, J. Zhao and G. Zhang, *Macromolecules*, 2018, **51**, 2247-2257.

22. H. Li, H. Luo, J. Zhao and G. Zhang, *ACS Macro Lett.*, 2018, **7**, 1420-1425.

23. H.-Y. Ji, B. Wang, L. Pan and Y.-S. Li, *Angew. Chem. Int. Ed.*, 2018, **57**, 16888-16892.

24. D. M. Pesko, Y. Jung, A. L. Hasan, M. A. Webb, G. W. Coates, T. F. Miller and N. P. Balsara, *Solid State Ion.*, 2016, **289**, 118-124.

25. M. A. Webb, Y. Jung, D. M. Pesko, B. M. Savoie, U. Yamamoto, G. W. Coates, N. P. Balsara, Z.-G. Wang and T. F. Miller, *ACS Cent. Sci.*, 2015, **1**, 198-205.

26. J. Mindemark, M. J. Lacey, T. Bowden and D. Brandell, *Prog. Polym. Sci.*, 2018, **81**, 114-143.

27. H. Q. Pham, G. Kim, H. M. Jung and S.-W. Song, *Adv. Funct. Mater.*, 2018, **28**, 1704690.

28. J. Mindemark, B. Sun, E. Törmä and D. Brandell, *J. Power Sources*, 2015, **298**, 166-170.

29. C. Koning, J. Wildeson, R. Parton, B. Plum, P. Steeman and D. J. Darensbourg, *Polymer*, 2001, **42**, 3995-4004.

30. G. S. Sulley, G. L. Gregory, T. T. D. Chen, L. Peña Carrodeguas, G. Trott, A. Santmarti, K.-Y. Lee, N. J. Terrill and C. K. Williams, *J. Am. Chem. Soc.*, 2020, **142**, 4367-4378.

31. D. G. Mackanic, X. Yan, Q. Zhang, N. Matsuhisa, Z. Yu, Y. Jiang, T. Manika, J. Lopez, H. Yan, K. Liu, X. Chen, Y. Cui and Z. Bao, *Nat. Commun.*, 2019, **10**, 5384.

32. L. Zhang, *Ionics*, 2021, **27**, 599-605.

33. F. P. Nkosi, M. Valvo, J. Mindemark, N. A. Dzulkurnain, G. Hernández, A. Mahun, S. Abbrent, J. Brus, L. Kobera and K. Edström, *ACS Appl. Energy Mater.*, 2021, **4**, 2531-2542.

CHAPTER 4

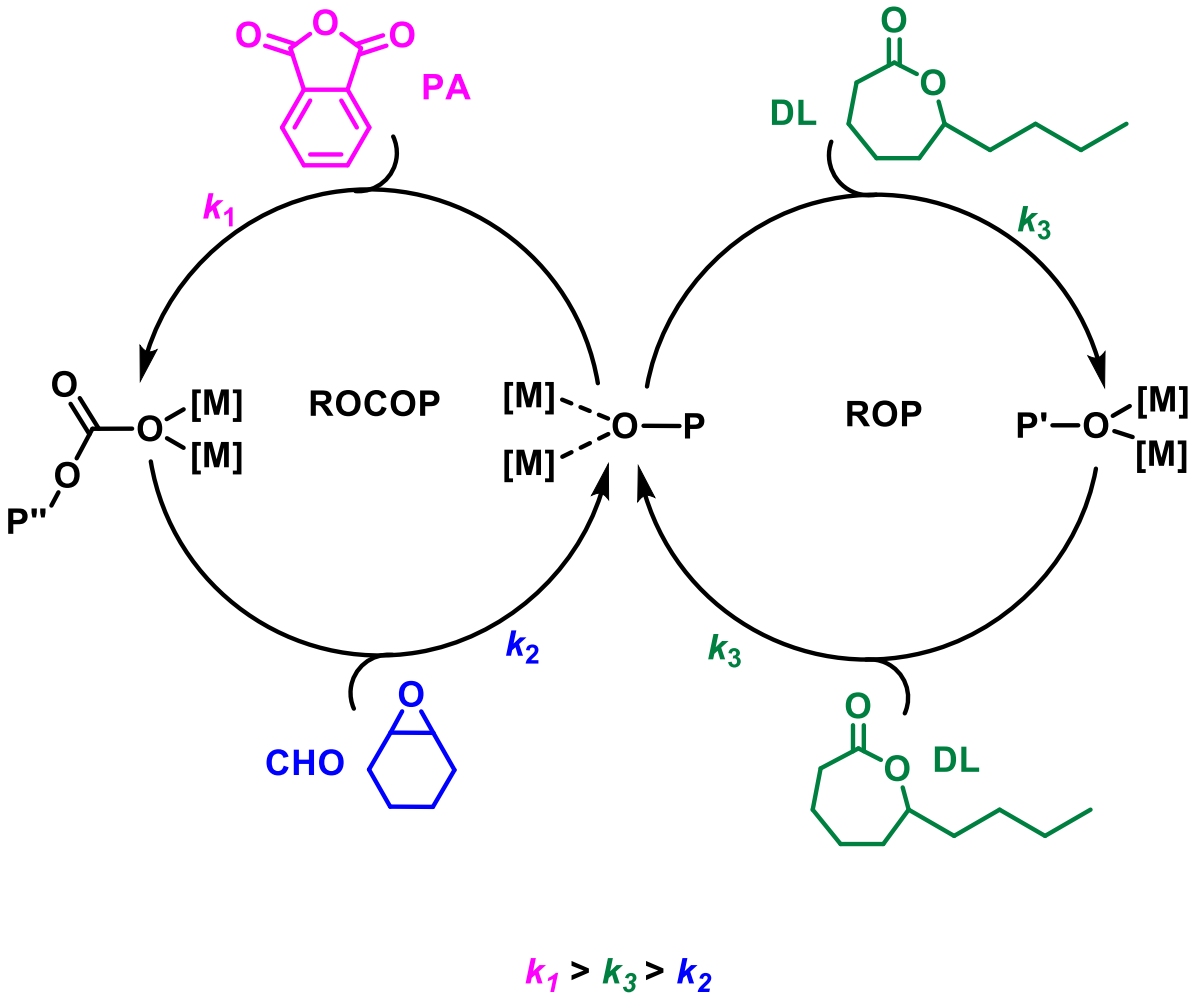
ABA Triblock Polymers from Anhydride, Epoxide and Cyclic Carbonate: Properties and Modifications for Battery Applications.

4.1. Introduction

Switchable polymerisations are an attractive approach to produce polymers for battery applications: it is a controlled, one-pot method which allows access to a wide library of oxygenated monomers to produce polymers with different compositions, molar masses and architectures. Polymer properties can thus be readily optimised: adjusting the ratio of hard (high T_g or T_m) block to soft (low T_g) block will affect the mechanical properties and Li-ion conductivity.

Switch catalysis is conducted from an anhydride (or CO_2)/epoxide/cyclic carbonate (or lactide) mixture.[1, 2] The bridging catalytic species is a metal alkoxide. Firstly, anhydride/epoxide ROCOP occurs: the anhydride rapidly inserts into the metal alkoxide to produce a metal carbonate intermediate, which only the epoxide can insert into, regenerating the metal alkoxide. Only once all of the anhydride is consumed can the cyclic carbonate (or lactide) insert into the metal alkoxide, so that ROP proceeds (Scheme 4.1).[3] In most reported switchable polymerisations, the block formed by anhydride/epoxide ROCOP has a rigid structure (high T_g, hard block) and the block formed by lactone/cyclic carbonate ROP has a flexible backbone (low T_g, soft block): for example, phthalic anhydride (PA)/cyclohexene oxide (CHO) ROCOP produces a polyester with a T_g between 133 and 146 °C; decalactone (DL) ROP produces a polyester with a T_g of -51 °C.[4] Thus, from an anhydride/epoxide/cyclic carbonate monomer mixture, BAB-type block copolymers are usually formed, where 'B' are the soft blocks, formed by ROCOP, and 'A' is the hard block, formed by ROP.[3] To achieve an ABA-type block copolymer, sequential monomer addition can be performed: work by Gregory and co-workers produced PCHPE-*b*-PDL-*b*-PCHPE by first conducting the homopolymerisation of DL and then adding PA and CHO to the crude reaction mixture to

initiate the mechanistic switch to PA/CHO ROCOP.[4] This produced an ABA block copolymer where $T_{g,A\text{-block}}$ = -51 – -41 °C and $T_{g,B\text{-block}}$ = 105 – 146 °C.



Scheme 4.1. PA/CHO ring-opening copolymerisation (ROCOP) and DL ring-opening polymerisation (ROP) cycles accessed by a single switchable catalyst to produce block copolymers.

Whilst sequential monomer addition is effective, a method where all monomers are added at the start might be preferable. This requires finding a ROCOP which produces a soft block polymer. Examples include butyl glycidyl ether/CO_2 ROCOP, producing a polycarbonate of T_g = -22 °C; and PO/allyl glycidyl ether (AGE)/CO_2 terpolymerisation,

producing a polymer of T_g = -14 °C.[5, 6] Balsara, Coates and co-workers studied a series of polyesters produced by epoxide/anhydride ROCOP, where the epoxides were propylene oxide (PO), AGE or 2-((2-(2-methoxyethoxy) ethoxy) methyl) oxirane, and the anhydrides were diglycolic anhydride (DGA) or glutaric anhydride (GA). Polymer T_g values ranged from -48 to 12 °C and poly(DGA-*alt*-AGE) was highlighted as an excellent polymer for battery applications due to its high Li-ion solvation site connectivity.[7, 8] It had a Li-ion conductivity of 2.5×10^{-4} S cm^{-1} at 90 °C. It is challenging to produce high molar mass polymers by ROCOP, largely due to residual protic impurities present in the monomers. Successful examples are limited: Diment and co-workers produced a polyester by PA/vCHO ROCOP with a molar mass of 91 kg mol^{-1}; Feng and co-workers produced polycarbonates by 1-octene oxide (OO)/CO_2 and AGE/CO_2 ROCOP with molar masses of 152 kg mol^{-1} and 45 kg mol^{-1}, respectively.[9, 10] The latter two polymers were achieved through rigorous drying of 99.995% purity CO_2 by passing it through triisobutylaluminium. A lactone or cyclic carbonate ROP that produces a hard polymer is also required: these often require rigid or aromatic lactones which are complicated to synthesise and many show poor polymerizability.[11-13] The ROP of the cyclic carbonate 2,2-dimethyltrimethylene carbonate (DTC) produces a semicrystalline polycarbonate with a T_m of 109 °C.[14]

When designing polymers for battery applications, different functionalities can be introduced to improve battery performance. Fluorinated groups can improve oxidative stability and Li-ion conductivity, by enhancing salt dissociation; nitrile and sulfone groups increase Li-ion transference number (t_{Li+}) and salt dissociation; and cross-linked polymers can enhance mechanical integrity.[15-19] An improvement in one performance parameter can mean a deterioration of another; the ideal balance of properties depends on the specific polymer application in the cell.[20]

4.2. Aims

This project aims to produce block copolymers by a one-pot switch catalysis with an ABA (hard-soft-hard) block structure, starting from an anhydride/epoxide/cyclic carbonate monomer mixture. The block copolymer is targeted for battery applications: it will need to be highly-oxygenated and the soft block should have a low T_g to facilitate Li-ion transport. Polymer modification will then be explored to improve its thermomechanical properties and Li-ion conductivity.

To deliver this, the novel triblock copolymer poly(DTC-*b*-DGA-*alt*-AGE-*b*-DTC) was targeted for use as a battery material. The polymer should combine high ionic conductivity, electrochemical stability and mechanical integrity. The central polyester block (T_g = -14 °C) is already known to give reasonable Li-ion conductivity, as studied by Balsara and co-workers; its combination with the hard DTC block (T_m = 109 °C) in an ABA structure should improve overall mechanical integrity.[7, 8, 14] Additionally, both blocks are carbonyl-coordinating which should improve the overall ionic conductivity. Switchable polymerisation catalysis of anhydride/epoxide/cyclic carbonate (or lactone) mixtures has not previously been used to produce such ABA (hard-soft-hard) block copolymers. Prior studies usually exploited low T_g blocks produced by ring-opening polymerisation (ROP) which flanked high T_g blocks produced by ROCOP. This work will 'invert' the structure and apply one-pot switch catalysis to access these polymers.

Firstly, a catalyst must be identified which is capable of both DGA/AGE ROCOP and DTC ROP. Switch catalysis, from a monomer mixture, must be able to produce the right block sequence, giving poly(DTC-*b*-DGA-*alt*-AGE-*b*-DTC). The optimum polymer composition for Li-ion conductivity will then be determined; a series of polymers with different molar masses and P(DTC) weight fractions will be used to identify the material showing the best Li-ion conductivity. The lead polymer will be cross-linked and functionalised to correlate structural features with thermomechanical properties and Li-ion conductivity.

4.3. Anhydride/Epoxide/Cyclic Carbonate-based Polymers: Synthesis and Characterisation.

4.3.1. Catalyst Testing for ROCOP and ROP

Monomers need to be purified to remove any contaminating protic species as these act as additional chain transfer agents (CTAs) thus reduce overall polymer molar mass. DGA was purified by two recrystallisations, from acetic anhydride, followed by two sublimations (80 °C, 0.1 mbar).[7] AGE was purified by a thorough triple distillation method (18 mbar, 60 °C); before the first distillation, the AGE was dried using CaH_2; before the second, it was dried using *n*-BuLi; and in the third distillation no drying agent was used. DTC was purified by recrystallisation from Et_2O, followed by a sublimation (60 °C, 0.1 mbar).

Catalysts were evaluated separately for DGA/AGE ROCOP and DTC ROP so that the fastest and most controlled catalyst could be used for switchable polymerisation. The catalyst must conduct both DGA/AGE ROCOP and DTC ROP. Five different catalysts were tested: two different organocatalysts, P_2-*t*-Bu and P_1-*t*-Bu; two metal salen catalysts,

[salcyAlCl]/PPNCl and [salcyCrCl]/PPNCl (where PPNCl is bis(triphenylphosphine)iminium chloride); and [L_{van}AlK(OAc)$_2$] (Figure 4.1). The first four catalysts are commercially available; the latter was synthesised according to a literature procedure.[21]

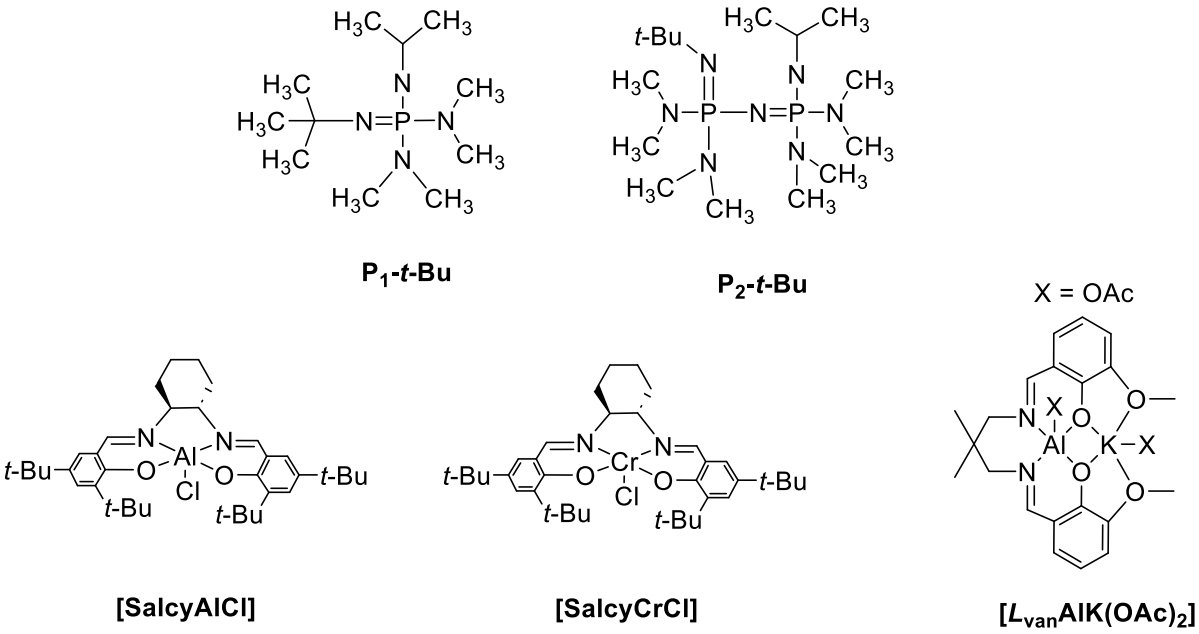


Figure 4.1. Catalysts tested for DGA/AGE ROCOP (all) and DTC ROP (P_1-*t*-Bu, P_2-*t*-Bu and [L_{van}AlK(OAc)$_2$].

Polymerizations were conducted at 100 °C, under anaerobic conditions, and using a 1/1 volume ratio of toluene/AGE as the solvent, in all cases. BDM was used as the CTA for all experiments; triblock copolymers were targeted as these were found to give improved ionic conductivity compared to diblocks for the series of polymers [poly(vCHC-*b*-CL-*r*-TMC-*b*-vCHC)] in Chapter 2. Catalyst/CTA was varied for each catalyst according to the range of conditions previously reported for each catalyst.[21]

All five catalysts successfully conducted DGA/AGE ROCOP (Table 4.1). The polymerisations were monitored by ^{1}H NMR spectroscopy: the DGA signal at 4.41 ppm decreased in intensity, as the corresponding polymeric peak at 4.21 ppm increased. The AGE

signals at 3.68 and 3.38 ppm decreased as the polymeric signal at 3.55 ppm increased (Figure 4.2). The relative integrals of these peaks were used to calculate the % monomer conversion to polymer. 100% DGA conversion was achieved for each entry. Turnover frequency (TOF) was then calculated by considering the amount of monomer the catalyst converts to polymer, per hour, using the following equation:

$$TOF = \frac{n_{mon.} \times conv.}{n_{cat.} \times t} \quad \text{(Equation 4.1)}$$

where $n_{cat.}$ is the moles of catalyst, $n_{mon.}$ is the total moles of DGA monomer that can be enchained (i.e. not including the excess AGE) and *conv.* is the % monomer conversion achieved in time period *t*. The productivity or turnover number (TON) is calculated as

$$TOF = \frac{n_{mon.} \times conv.}{n_{cat.}} \quad \text{(Equation 4.2).}$$

Comparing the different catalysts showed that $L_{van}AlK(OAc)_2$ had a moderate TOF (25 h^{-1}); the chromium salen catalyst system had a faster TOF (100 h^{-1}); and the aluminium salen catalyst system was slow with a TOF of 8 h^{-1}. Both organocatalysts showed good TOFs, with P_2-*t*-Bu being faster than P_1-*t*-Bu, at 100 h^{-1} compared to 50 h^{-1} (Table 4.1). Excluding Entry 2, these TOFs are in the upper range for anhydride/epoxide ROCOP.[22]

Table 4.1. Data for DGA/AGE ROCOP, Using 5 Different Catalysts.

Entry	Catalyst	Cat/BDM/DGA /AGE [a]	[cat] (mM)	Time (h)	TON [b]	TOF_{ROCOP} [c] (h^{-1})
1	$L_{van}AlK(OAc)_2$	1/4/200/528	8	8	200	25

2	SalcyAlCl/PPNCl	1/10/200/250	17	24	200	8
3	SalcyCrCl/PPNCl	1/10/200/250	17	2	200	100
4	P_2-*t*-Bu	1/2/800/1200	4	8	800	100
5	P_1-*t*-Bu	1/2/800/1200	4	16	800	50

[a] Relative molar ratio of catalyst, BDM, DGA and AGE; [b] Turnover number (TON) = (number of moles consumed)/(number of moles of catalyst); [c] TOF (turnover frequency) = TON per unit time, calculated by ^{1}H NMR spectroscopy using signals corresponding to DGA (4.41 ppm), AGE (3.68 ppm) and P(DGA-*alt*-AGE) (4.21, 3.55 ppm).

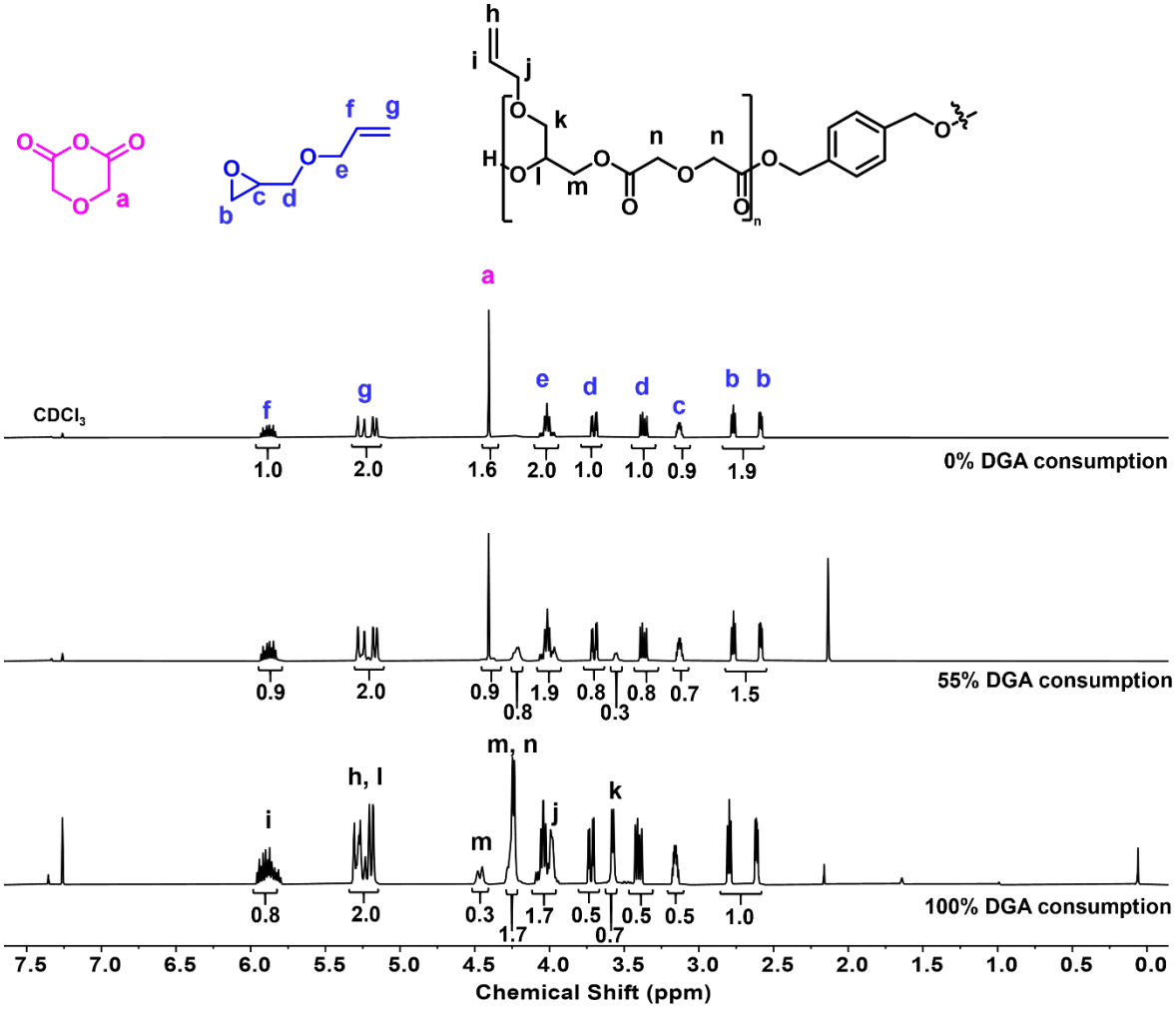


Figure 4.2. Assigned ^{1}H NMR spectra ($CDCl_3$, 500 MHz) from aliquots of DGA/AGE ROCOP at 0%, 55%, and 100% DGA conversion, depicting the consumption of AGE and DGA monomer and the

formation of P(DGA-*alt*-AGE); integrals labelled below the peaks; unlabelled peaks at 2.17 and 1.56 ppm correspond to acetone and water, respectively.

Next, DTC ROP was examined (Table 4.2). Reactions were again conducted at 100 °C, under an anaerobic atmosphere, using a 1/1 volume ratio of toluene to AGE as the solvent, in all cases. The metal salen catalysts were not tested for DTC ROP because the aluminium catalyst system was too slow during ROCOP and there were concerns that any residual chromium might be detrimental for battery applications, due to its redox activity. DTC conversion to P(DTC) was monitored by ^{1}H NMR spectroscopy: the DTC signal at 1.10 ppm decreased in intensity, as the corresponding polymeric signal at 0.97 ppm increased (Figure 4.3). Note the DTC signal at 4.06 ppm cannot be used to calculate conversion as it overlaps with an AGE signal. L_{van}AlK(OAc)$_2$ showed excellent DTC ROP performance, with a TOF of 1200 h^{-1}. The organocatalysts were slower: 100 h^{-1} for P$_2$-*t*-Bu and no activity for P$_1$-*t*-Bu (Table 4.2). Therefore, the L_{van}AlK(OAc)$_2$ complex was selected for further testing as a switch catalyst since it combined the best balance of rates in both DGA/AGE ROCOP and DTC ROP.

Table 4.2. Data for DTC ROP, Using 3 Different Catalysts.

Entry	Catalyst	Cat/BDM/DTC /AGE [a]	[cat] (mM)	Time (h)	TON [b]	TOF_{ROP} [c] (h^{-1})	DTC conv.
1	L_{van}AlK(OAc)$_2$	1/4/200/528	8	0.2	200	1200	76%
2	P$_2$-*t*-Bu	1/2/100/1200	4	1	100	100	77%
3	P$_1$-*t*-Bu	1/2/100/1200	4	1	0	0	74%

[a] Relative molar ratio of catalyst, BDM initiator, DTC and AGE; [b] Turnover number (TON) = (number of moles consumed)/(number of moles of catalyst); [c] TOF (turnover frequency) = TON per unit time, calculated by ^{1}H NMR spectroscopy using signals corresponding to DTC (1.10 ppm) to PDTC (0.97 ppm).

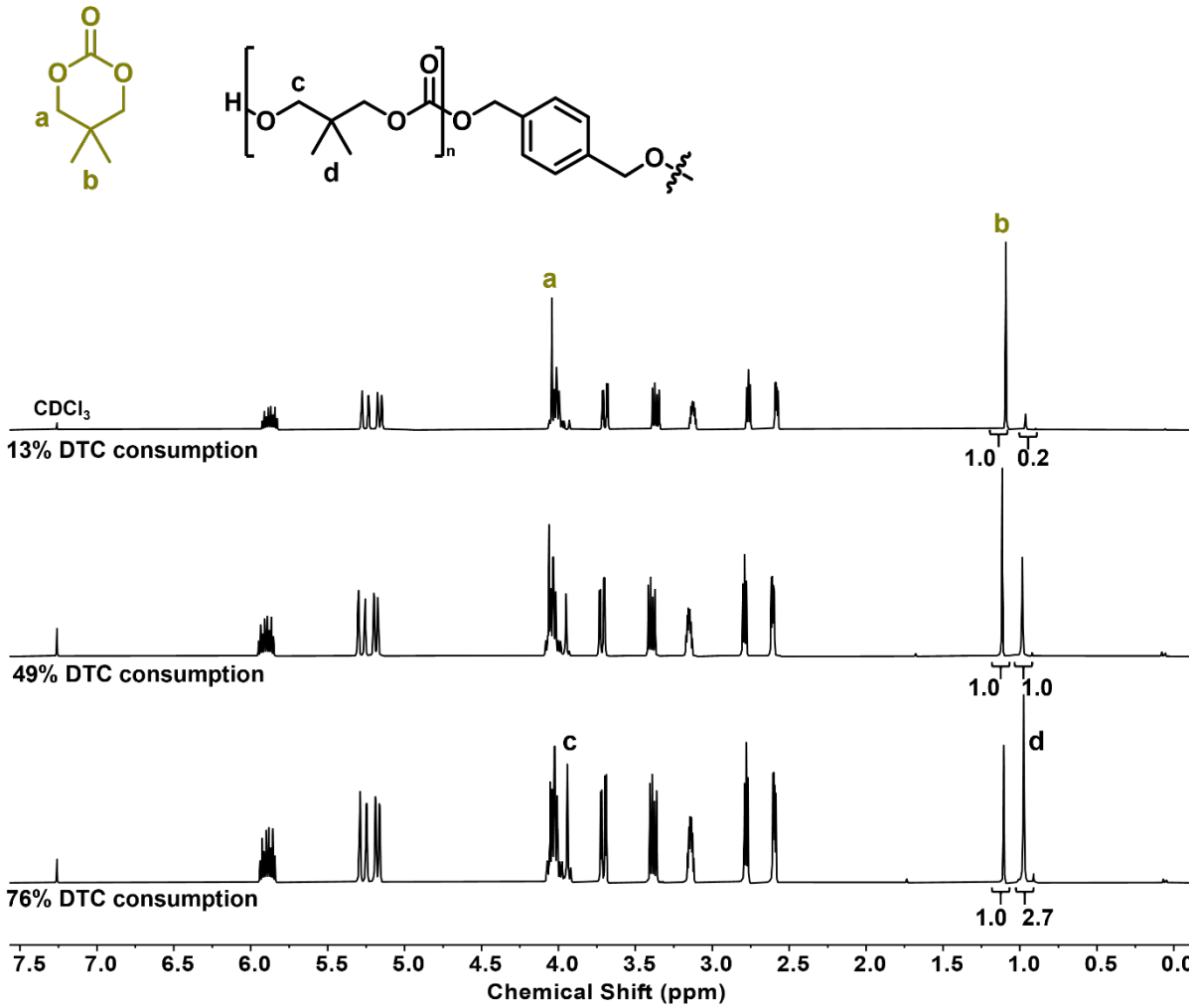
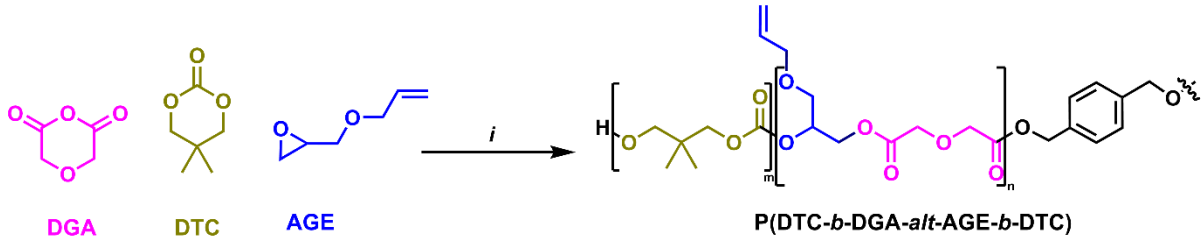


Figure 4.3. Assigned ^{1}H NMR spectra ($CDCl_3$, 500 MHz) from aliquots of DTC ROP at 13, 49 and 76% DTC conversion, depicting signals corresponding to the DTC monomer and P(DTC) polymer; integrals labelled below the peaks; unlabelled peaks correspond to AGE, as assigned in Figure 4.2.

4.3.2. Poly(DTC-*b*-DGA-*alt*-AGE-*b*-DTC) by Switch Catalysis.

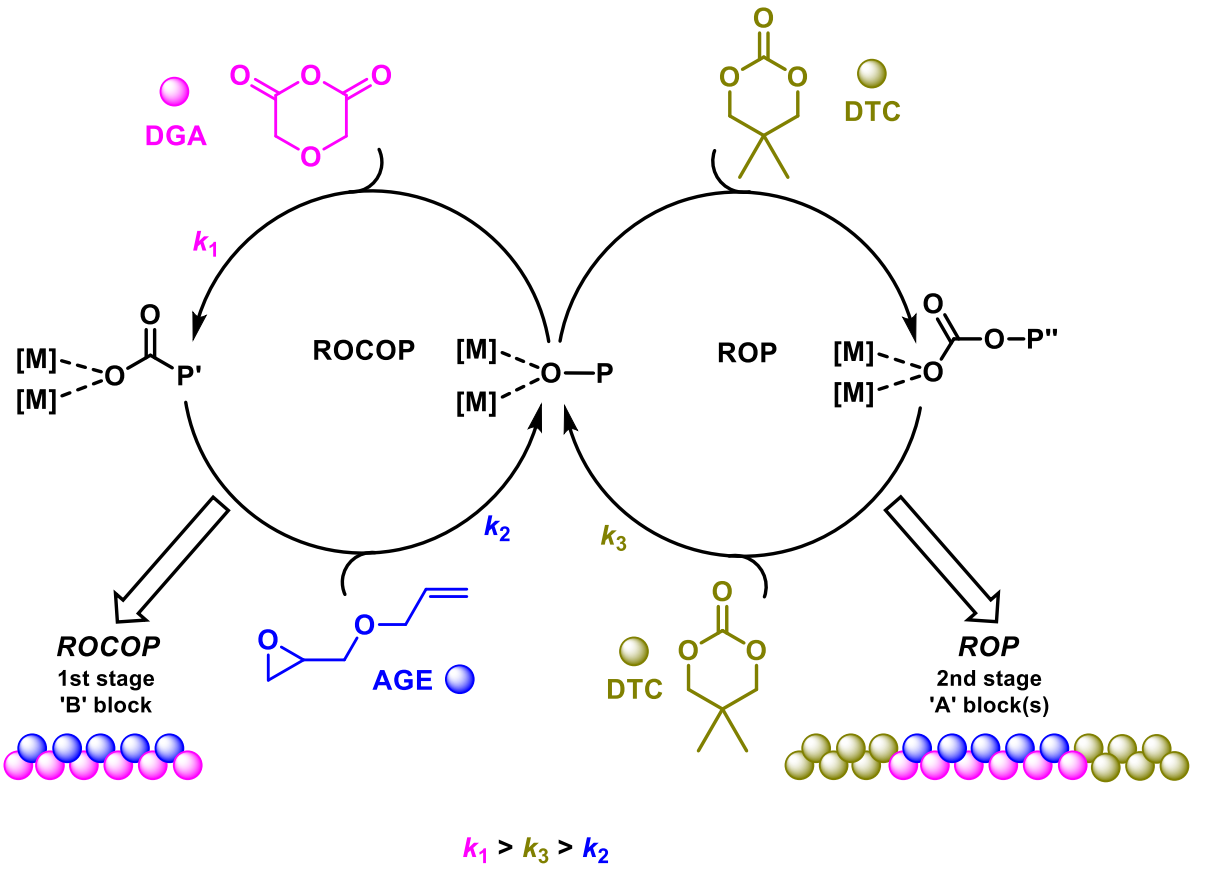
Poly(DTC-*b*-DGA-*alt*-AGE-*b*-DTC) was produced by switchable polymerisation catalysis from a DGA/DTC/AGE monomer mixture (Scheme 4.2). [L_{van}AlK(OAc)$_2$] was selected as the most suitable catalyst, but it features two acetate groups which could also initiate polymerisation thus may also form diblock poly(DTC-*b*-DGA-*alt*-AGE). To produce triblock copolymers, an excess of bifunctional chain transfer agent was used, in this work, 1,4-benzene

dimethanol (BDM). This ensured that the majority of chains are dihydroxy telechelic. In some cases, SEC shows a minor lower molar mass series assigned to acetate-hydroxy terminated polymers.[21] In this work, SEC showed a relatively narrow molecular weight distribution ($Đ$ = 1.45 – 1.67), consistent with suppressing acetate initiation.



Scheme 4.2. Polymerisation of DGA, AGE and DTC by switch catalysis, conducted at 100 °C under an anaerobic atmosphere. (i) [L_{van}AlK(OAc)$_2$]/[BDM]/[DGA]/[DTC]/[AGE] = 1/4/X/Y/528 where X = 90 – 440, Y = 60 – 462, [cat] = 8 mM, solvent mixture 50 vol.% toluene, 50 vol.% AGE. See Table 4.3 for *m* and *n* values, where *m* = DP_n of the P(DTC) block and *n* = DP_n of the P(DGA-*alt*-AGE) block.

From a monomer mixture, switch catalysis theory predicts that the ROCOP of DGA and AGE occurs first and selectively. When the DGA is fully consumed, there should be a mechanistic switch to DTC ROP (Scheme 4.3).[3] To test this hypothesis, the polymerisations were conducted and monitored from a L_{van}AlK(OAc)$_2$/BDM/DTC/DGA/AGE mixture of molar ratio 1/4/X/Y/528 with X = 90 – 440 and Y = 60 – 462 to affect molar mass and composition (Tables 4.3, 7.9). The catalyst concentration was kept constant (8 mM) and the reaction was conducted in a solvent mixture of 50% toluene and 50% AGE, by volume. Polymerisations were conducted at 100 °C, under an anaerobic atmosphere, at a stirring rate of 1600 rpm. Polymers were isolated pure in good yield (80%), by precipitation from diethyl ether followed by dialysis with THF to remove excess epoxide. Polymers were then dried under vacuum (1×10^{-1} mbar) at 80 °C and for 12 hours. The target triblock copolymers showed molar mass values in the range of 4 – 20 kg mol^{-1} and A-block PDTC weight fractions of 0.2 and 0.5.



Scheme 4.3. DGA/AGE ring-opening copolymerisation (ROCOP) and DTC ring-opening polymerisation (ROP) cycles accessed by a single switchable catalyst to produce block copolymers.

The polymerisation of DGA, AGE and DTC, catalysed by $L_{van}AlK(OAc)_2$, was monitored to establish the order of monomer enchainment. In-situ ATR-IR spectroscopy showed that DGA/AGE ROCOP occurred before DTC ROP. This was established over the first 9 h of the polymerisation when the signal corresponding to DGA (1860 cm^{-1}) decreased and the signal attributed to the ROCOP polyester (1695 cm^{-1}) increased until the DGA was fully consumed. After 9 h, DTC (1113 cm^{-1}) was consumed to form the polycarbonate (1236 cm^{-1}) (Figure 4.4). These results are absolutely consistent with the theory and predicted order of monomer enchainment in switch catalysis.[2] They may be rationalised by understanding that from the metal alkoxide intermediate common to both the ROCOP and ROP cycles, anhydride insertion is fastest and forms the most stable linkage to the catalyst. Since the formed

metal carboxylate does not react with cyclic carbonate it can then only react with epoxide, reforming the metal alkoxide species. This ROCOP cycle is favoured until all anhydride is consumed – only then does the DTC insert into the metal alkoxide so that DTC ROP occurs.[3] The rate laws for DGA/AGE copolymerisation and DTC polymerisation are

$$rate = k_p[cat.]^x[AGE]^y[DGA]^z \quad \text{Equation 4.3}$$

and

$$rate = k_p[cat.]^x[DTC]^y \quad \text{Equation 4.4}$$

respectively. Following the same procedure as described in chapter 3, the rate laws can be simplified and rearranged and plotted to obtain k_{obs}: 1.21×10^{-4} M s^{-1} for DGA/AGE ROCOP and 8.70×10^{-4} s^{-1} for DTC ROP (Figures 7.20, 7.21).

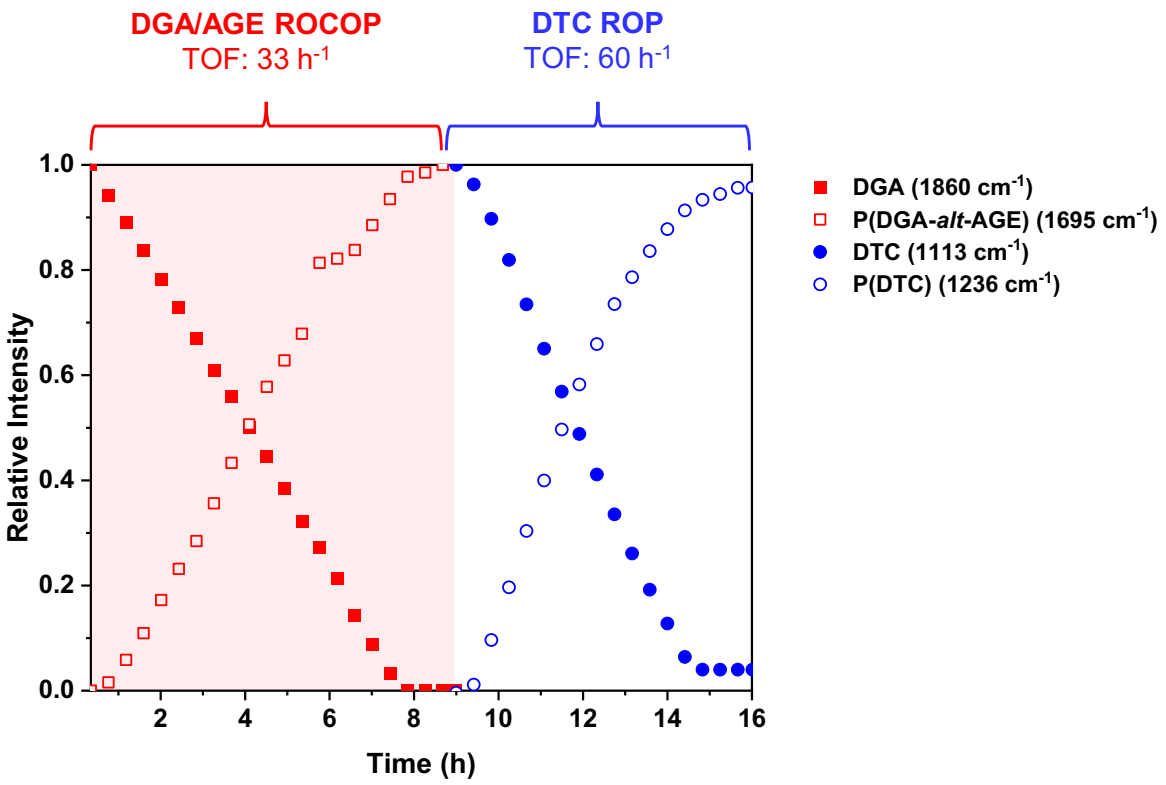


Figure 4.4. In-situ ATR-IR spectroscopy monitoring the switchable polymerisation catalysis of DGA, AGE and DTC, catalysed by L_{van}AlK(OAc)$_2$, illustrating firstly DGA/AGE ROCOP, followed by DTC ROP after 9 h. Relative intensity calibrated using ^{1}H NMR spectroscopy.

Similarly, the polymerisation was studied by ^{1}H NMR spectroscopy by taking aliquots of the reaction mixture. DGA and AGE were consumed first, as observed by the depletion of signals corresponding to DGA and AGE, at 4.41 and 3.67 ppm, respectively. This resulted in the formation of poly(DGA-*alt*-AGE), as shown by the growth in signals at 4.21 and 3.54 ppm, until 100% DGA conversion was reached (Figure 4.5). At this point, no DTC consumption was observed – there was no change in monomer peak intensity at 1.11 ppm, suggesting that DGA/AGE ROCOP selectively occurred. DTC ROP to form P(DTC) was then observed, as shown by the depletion of the signal at 1.11 ppm and the growth of a new peak at 0.97 ppm. Thus, DTC ROP occurred only once DGA/AGE ROCOP was completed and 100% DGA conversion was achieved. The DTC ROP proceeded until 71% DTC conversion, corresponding

to an equilibrium DTC concentration of 0.25 mol dm^{-3} at 373 K.[14] Solubility issues at lower temperatures and volatility issues at higher temperatures obstructed the calculation of thermodynamic parameters but this equilibrium behaviour is consistent with ring-opening polymerisation thermodynamics.[23]

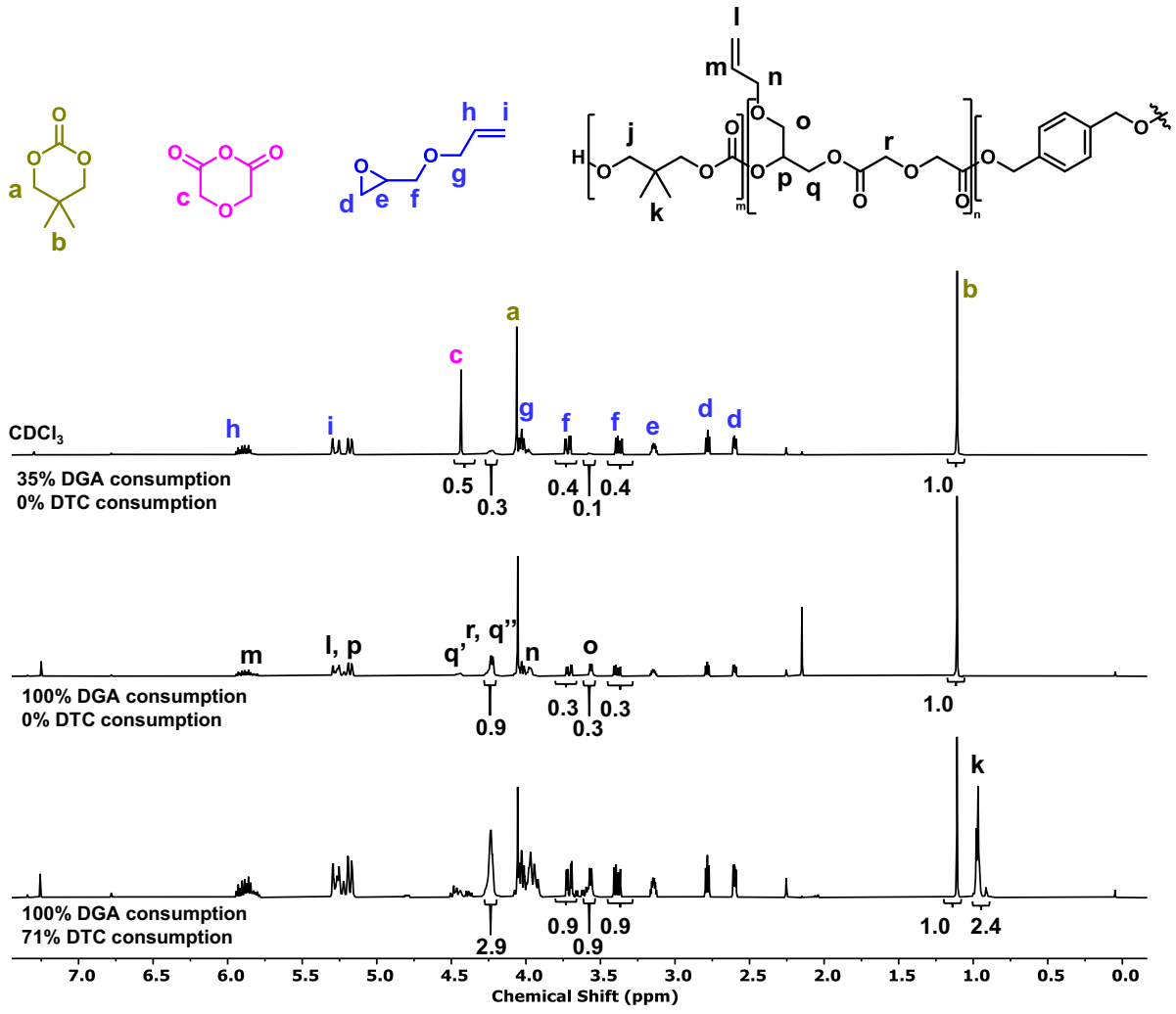


Figure 4.5. ^{1}H NMR spectra ($CDCl_3$, 500 MHz) from the copolymerisation of DGA, AGE and DTC, catalysed by $L_{van}AlK(OAc)_2$, illustrating firstly the ROCOP of DGA/AGE, followed by DTC ROP.

The selective formation of a triblock copolymer was supported by SEC, which showed an increase in the molar mass of the polymer between ROCOP and the ROP stages, from 4.5 to 7.1 kg mol^{-1} (Figure 4.6). A moderately narrow and monomodal distribution was observed;

the increase in molar mass was indicative of block connectivity and the formation of the desired ABA triblock copolymer.

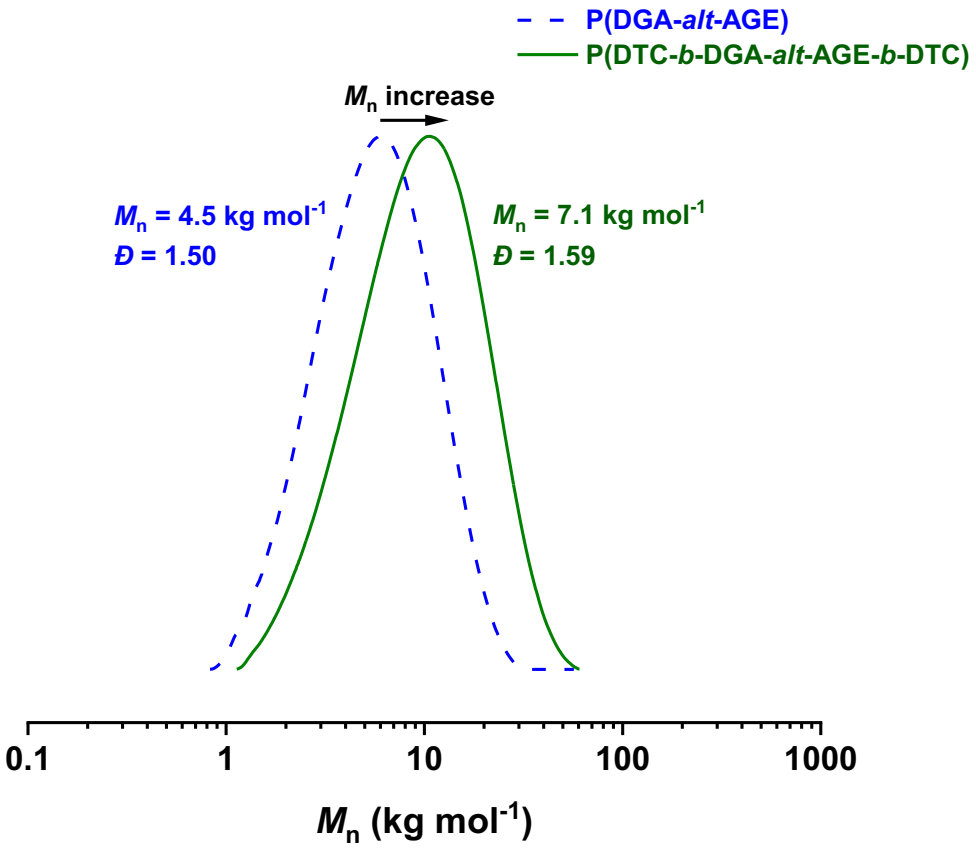


Figure 4.6. SEC traces from aliquots of the switch polymerisation of DGA, AGE and DTC, showing the growth in polymer molar mass after DGA/AGE ROCOP (P(DGA-*alt*-AGE)) and after the subsequent DTC ROP (P(DTC-*b*-DGA-*alt*-AGE-*b*-DTC)).

The triblock copolymer was characterised by ^{13}C NMR spectroscopy which showed the expected signals, especially in the carbonyl region (Figure 4.7). The presence of just two types of carbonyls – P(DTC) and P(AGE-*alt*-AGE) – was a clear indication of block copolymer formation and indicated lack of detectable transesterification. DOSY NMR spectroscopy showed a single diffusion coefficient, which indicated that the polymer blocks are connected (Figure 4.8). Polymer chain end-group analysis, by ^{31}P NMR spectroscopy, was not successful as the reagents degraded the polymer backbone. This was indicated by SEC analysis where the

starting polymer had a molar mass of 5.4 kg mol^{-1} and a dispersity index ($Đ$) of 1.58; but after the reaction, it had a molar mass of 0.6 kg mol^{-1} and a $Đ$ of 6.3. Thus, degradation occurred and the end group of the polymers could not be determined.

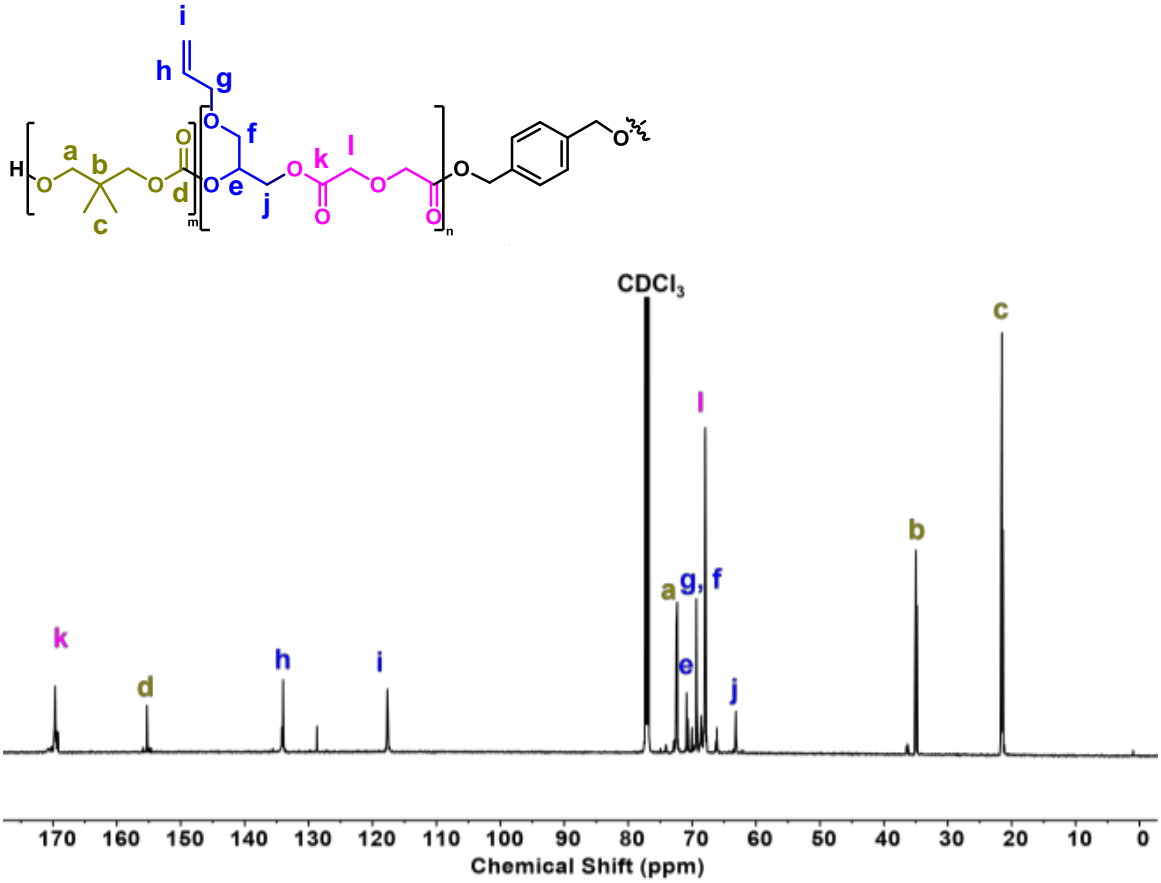


Figure 4.7. $^{13}C\{H\}$ NMR spectrum ($CDCl_3$, 500 MHz) of poly(DTC-*b*-AGE-*alt*-DGA-*b*-DTC).

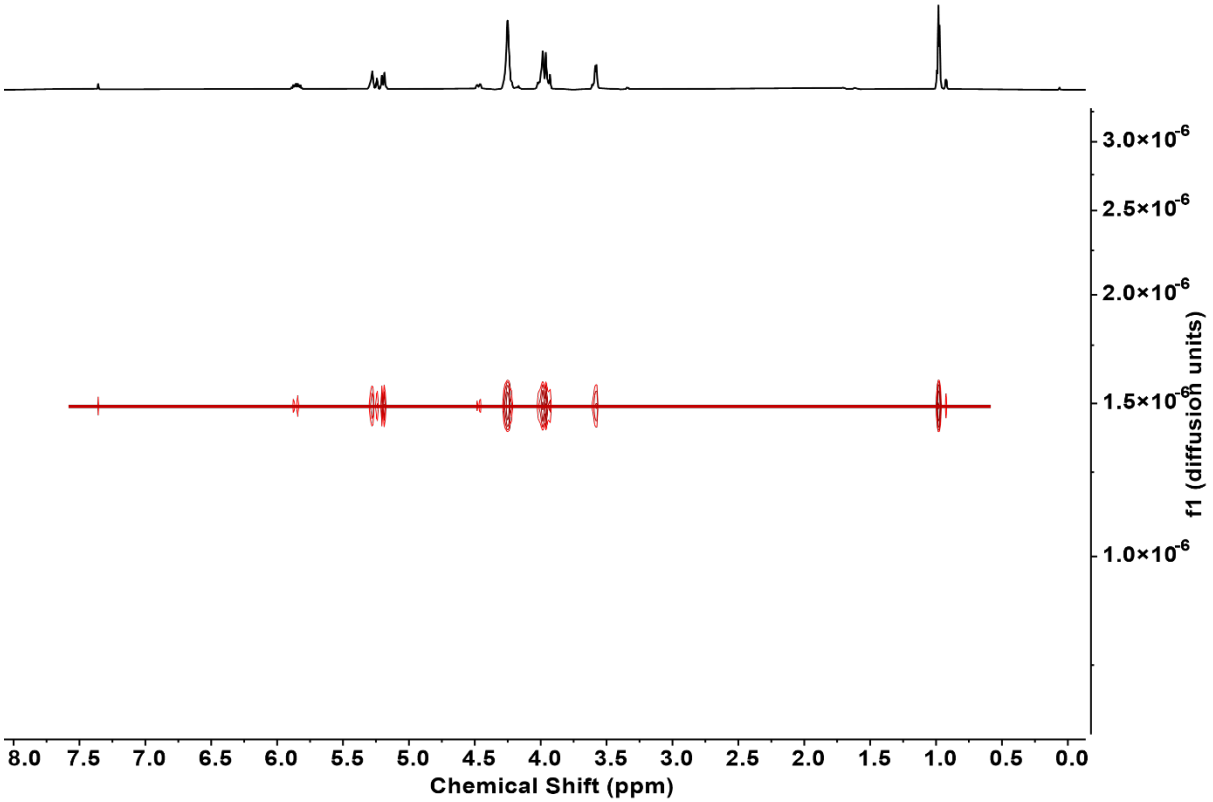


Figure 4.8. DOSY NMR spectrum of poly(DTC-*b*-DGA-*alt*-AGE-*b*-DTC).

4.4. Polymer Composition Optimisation

4.4.1. Synthesis and Characterisation

Following from the proof of triblock polymer formation by switch catalysis, a series of polymers were produced. The series was targeted to vary molar mass and hard weight fraction to identify the optimal composition with respect to Li-ion conductivity. Control over the molar mass and hard weight fraction was achieved by varying the BDM/DTC/DGA ratio (Table 4.3 and 6.7). Polymers are identified by ABA(XX, 0.YY) labelling, where ABA denotes triblock structure, XX is the molar mass (kg mol^{-1}) and 0.YY is the hard weight fraction, where the hard block is P(DTC) (Table 4.3).

Table 4.3. Overview of the Poly(DTC-*b*-DGA-*alt*-AGE-*b*-DTC) ABA(XX, 0.YY) Characterisation Data.

Entry	Cat./BDM/DTC/ DGA/AGE [a]	DP_n ABA (calc) [b]	DP_n ABA (NMR) [c]	Hard wt. fraction [c]	$M_{n,NMR}$ (kg mol^{-1}) [c]	$M_{n,SEC}$ [$Đ$] (kg mol^{-1}) [d]
ABA(4, 0.20)	1/4/60/90/528	4 – 15 – 4	3 – 13 – 3	0.20	3.8	3.5 [1.51]
ABA(9, 0.22)	1/4/110/220/528	8 – 37 – 8	7 – 30 – 7	0.22	8.7	4.8 [1.67]
ABA(18, 0.20)	1/4/220/440/528	16 – 73 – 16	14 – 62 – 14	0.20	17.9	6.7 [1.63]
ABA(9, 0.43)	1/4/240/150/528	17 – 25 – 17	15 – 22 – 15	0.43	9.0	5.7 [1.45]
ABA(19, 0.47)	1/4/462/330/528	28 – 55 – 28	27 – 53 – 27	0.47	19.2	6.5 [1.60]

[a] Relative molar ratios of catalyst, BDM initiator, DTC, DGA and AGE; [b] Degree of Polymerisation (DP_n) as calculated by the initial reagent ratios and monomer conversions, where DGA conversion was monitored by comparing the monomer signal at 4.41 ppm to the polymer signal at 4.21 ppm, AGE conversion was determined by comparing the monomer signal at 3.68 ppm to the polymer signal at 3.55 ppm and DTC conversion was determined by comparing the monomer signal at 1.10 ppm to the polymer signal at 0.97 ppm; [c] DP_n as determined from the ^{1}H NMR spectra of the purified polymer by integration of the aromatic initiator resonance (7.34 ppm for 1,4-BDM) against those of P(DGA-*alt*-AGE) (4.19, 3.52 ppm) and P(DTC) (0.92 ppm); [d] Determined by SEC, using THF eluent and calibrated against narrow PS standards.

Polymer molar mass was determined using ^{1}H NMR spectroscopy, from the relative integrals of the signals corresponding to the BDM initiator (7.34 ppm) and the polymer (4.23, 3.56, 0.96 ppm). The values take into consideration the initiation from the residual acetate ligands on the catalyst; these acetate ligands act as monofunctional initiators. ^{1}H NMR spectroscopy showed the expected signals corresponding to the polymer (Figure 4.9). SEC data

for all polymers showed distributions that are monomodal and reasonably narrow (Table 4.3 and 6.8, Figure 4.6). The $M_{n,NMR}$ is greater than the $M_{n,SEC}$ which is likely a consequence of SEC data being calibrated against polystyrene standards and hence is only an estimate. It is proposed that these highly oxygenated oligomers behave differently in solution compared to high molar mass polystyrene calibrants. Other calibrants were also investigated but this did not improve the alignment.

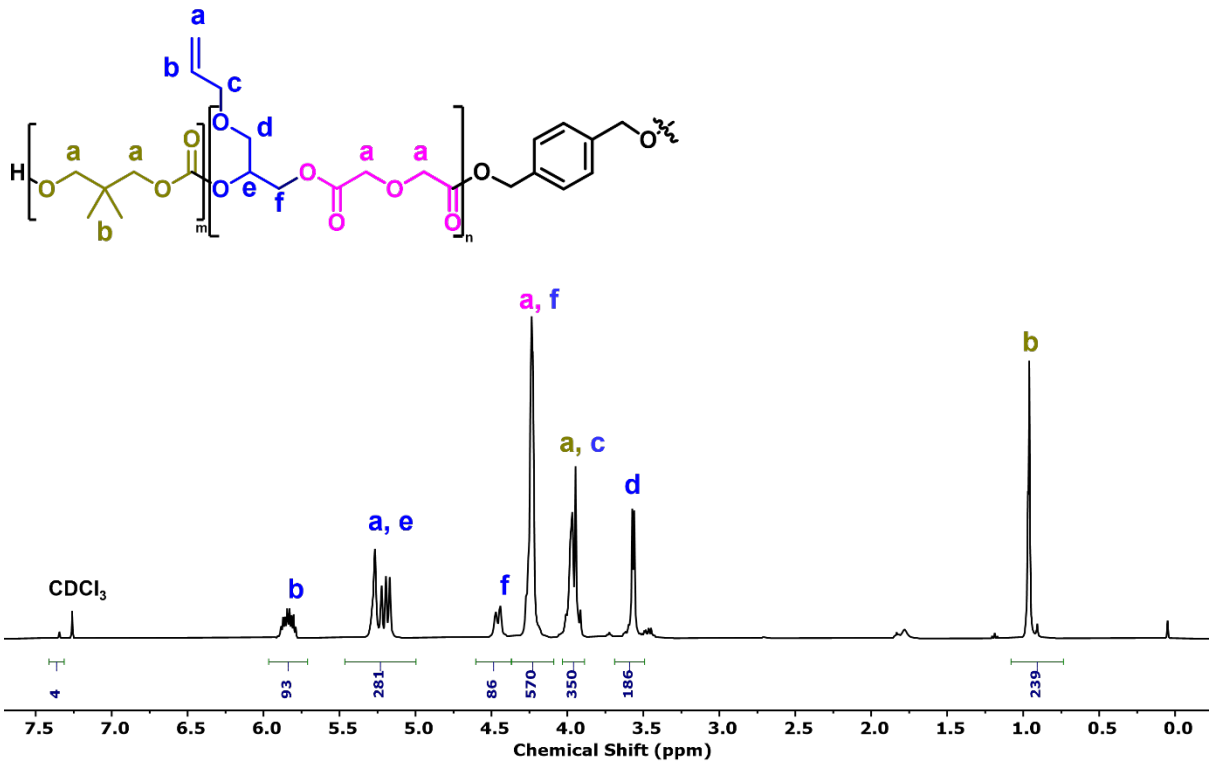


Figure 4.9. Exemplar assigned ^{1}H NMR spectrum of the purified polymer, poly(DTC-*b*-DGA-*alt*-AGE-*b*-DTC), ABA(18, 0.20).

4.4.2. Polymer Thermal Properties

Polymer electrolytes were prepared by mixing a stirred THF solution of the polymer with LiTFSI and allowing the solvent to evaporate. Solvent was removed first at ambient

temperature and pressure, and then under a vacuum (10^{-1} mbar) at 60 °C. The salt loading was defined as the molar ratio of lithium ions to monomer units, ρ = [Li^+]/[monomer]. A value of ρ = 0.22 was used for all materials since this loading was found to be the best in prior investigations of poly(DGA-*alt*-AGE).[7] The thermal properties of the polymers, and their electrolytes, were studied by DSC and TGA.

DSC data was obtained from the second scan, with the first scan removing thermal history. The polymers showed fully amorphous structures, with no crystallinity observed from the P(DTC) block. In all cases, a single T_g was observed at -11 to -18 °C (Table 4.4, Figure 4.10). The corresponding polymer electrolytes showed an increase in T_g. This occurred because of transient interchain crosslink formation by Li^+ which reduced chain segmental motion.[24] Thermal gravimetric analysis (TGA) showed a $T_{d,5\%}$ of above 200 °C for all samples (Table 4.4, Figure 4.11). Addition of LiTFSI salt resulted in a small reduction in the $T_{d,5\%}$ value. Still, the degradation temperature is sufficiently high for all polymer electrolytes studied (Table 4.4).

Table 4.4. Overview of the poly(DTC-*b*-DGA-*alt*-AGE-*b*-DTC) thermal data.

Entry [a]	T_g, polymer (°C) [a]	T_g, electrolyte (°C) [a]	$T_{d,5\%}$, polymer (°C) [b]	$T_{d,5\%}$, electrolyte (°C) [b]
ABA(4, 0.20)	-18	-4	304	271
ABA(9, 0.22)	-18	-5	293	268
ABA(18, 0.20)	-18	-5	292	264
ABA(9, 0.43)	-18	-4	266	264
ABA(19, 0.47)	-13	0	275	265

[a] Determined by DSC (10 °C min^{-1} heating rate), second heating curve; [b] The temperature at which 5% of mass loss of the polymer is recorded, measured by TGA (20 °C min^{-1} heating rate).

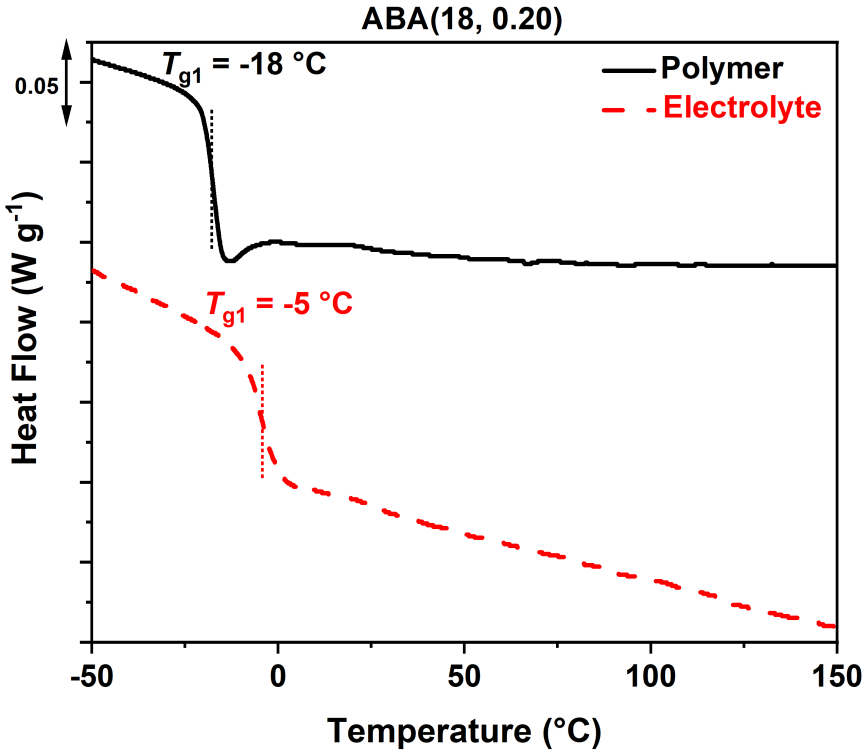


Figure 4.10. DSC data for ABA(18, 0.20) and its polymer electrolyte (ρ = 0.22), at a scan rate of 10 °C min^{-1}.

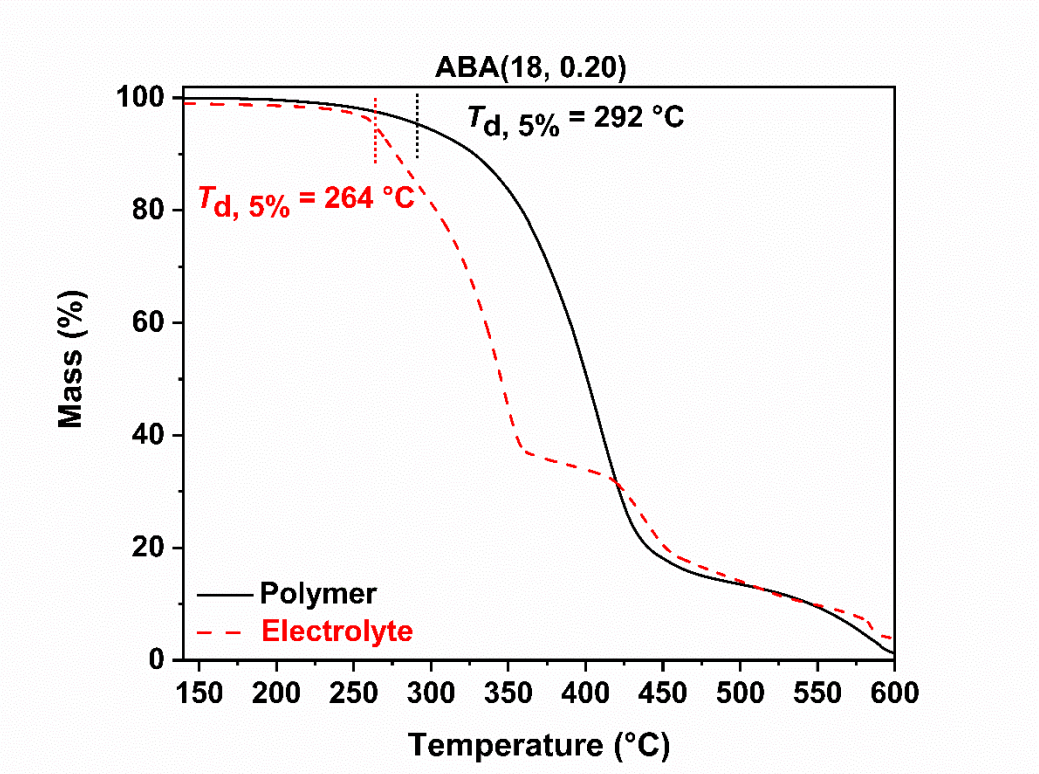


Figure 4.11. TGA data for ABA(18, 0.20) and its polymer electrolyte (ρ = 0.22).

4.4.3. Li-ion Conductivity

For each of the polymer electrolytes, Li-ion conductivity was measured, at 10 °C intervals between 30 and 70 °C, using electrochemical impedance spectroscopy (EIS) (Table 4.5, Figure 4.12). Trends relating ionic conductivity to molar mass and hard weight fraction were studied. All polymers having a hard weight fraction of ~0.2 – ABA(4, 0.20), ABA(9, 0.22) and ABA(18, 0.20) – showed very similar ionic conductivities of $\sigma = 2 \times 10^{-5}$ S cm^{-1} at 60 °C. Likewise, polymers with a hard weight fraction of ~0.5 – ABA(9, 0.43) and ABA(15, 0.47) – had a similar, but lower, conductivity of $\sigma = 6 \times 10^{-6}$ S cm^{-1} at 60 °C. The soft poly(DGA-*alt*-AGE) block is primarily responsible for the lithium-ion conductivity of these electrolytes hence a common hard weight fraction results in a similar conductivity. There were no obvious relationships between ionic conductivity and molar mass. This is likely to be because the overall mass values were very low and the range of values was quite narrow.[25]

The temperature dependence of Li-ion conductivity was modelled using the VFT relationship,

$$\sigma = AT^{-1/2}\exp\left[-E_a/(T - T_0)\right] \quad \text{(Equation 4.5)}$$

where A is a constant proportional to the number of Li-ions; E_a is the Li-ion transport activation energy; and T_0 is the temperature where configurational entropy is zero. All polymers tested conformed to the VFT model, as observed by the VFT plots (Figure 4.13). This finding indicated that ionic conductivity is governed by polymer chain segmental motion; such relationships are quite common for polymer electrolytes.[26] The ion transport activation energy

were obtained from the gradient of the linear fit; the values were between 10 and 15 kJ mol^{-1}, typical for polymer electrolytes (Table 4.5).[7]

Table 4.5. Ionic Conductivity Data for the Polymer Electrolytes.

Entry	Li-ion conductivity, σ (S cm^{-1}) [a]					E_a (kJ mol^{-1}) [b]	lnA [c]
	70 °C	60 °C	50 °C	40 °C	30 °C		
ABA(4, 0.20)	–	1.9×10^{-5}	6.4×10^{-6}	1.5×10^{-6}	–	10.6	3.7
ABA(9, 0.22)	3.3×10^{-5}	2.0×10^{-5}	5.6×10^{-6}	1.1×10^{-6}	1.1×10^{-7}	12.8	7.1
ABA(18, 0.20)	5.3×10^{-5}	2.3×10^{-5}	6.6×10^{-6}	1.1×10^{-6}	5.0×10^{-8}	11.9	5.1
ABA(9, 0.43)	1.2×10^{-5}	6.4×10^{-6}	1.5×10^{-6}	2.4×10^{-7}	1.4×10^{-8}	15.1	4.3
ABA(19, 0.47)	1.7×10^{-5}	5.8×10^{-6}	1.6×10^{-6}	3.0×10^{-7}	1.8×10^{-8}	12.2	12.2

[a] Measured using EIS, with ionic conductivity being calculated from the resistance obtained by fitting the data to the equivalent circuit Q1+Q2/R2. Error values were determined from the standard deviation from three experiments and corresponds to ± 34%, 21%, 16%, 11%, and 35%, at 30 °C, 40 °C, 50 °C, 60 °C, and 70 °C, respectively; [b] Activation energy of Li-ion transfer, obtained from the VFT fit; [c] Relative free charge carrier concentration of the polymer electrolyte, obtained from the VFT fit.

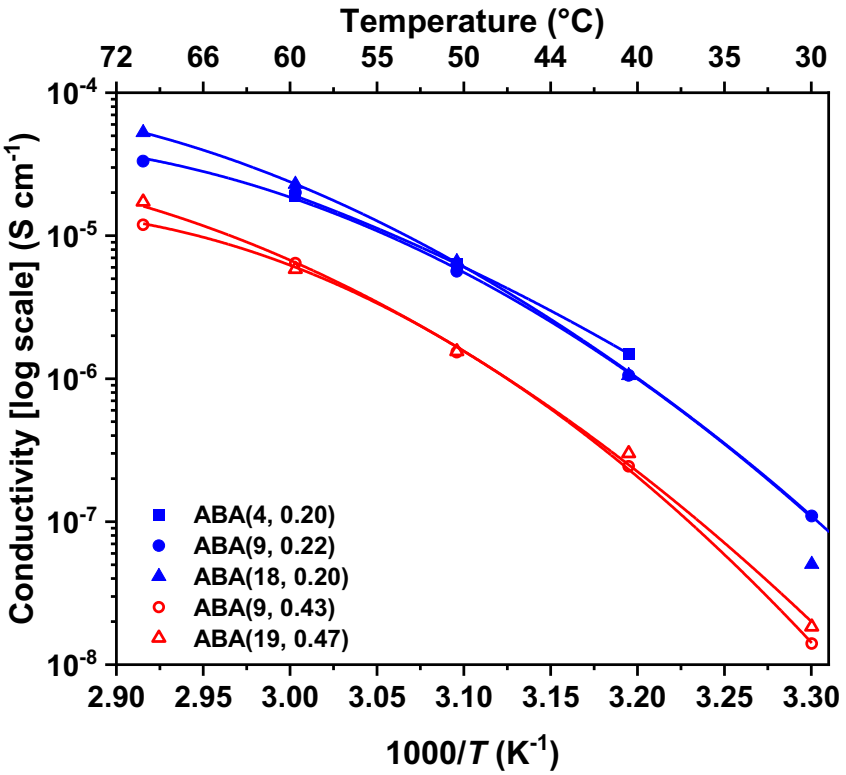


Figure 4.12. Li-ion conductivity as a function of temperature for the poly(DTC-*b*-DGA-*alt*-AGE-*b*-DTC) electrolytes, with LiTFSI concentration $\rho = 0.22$.

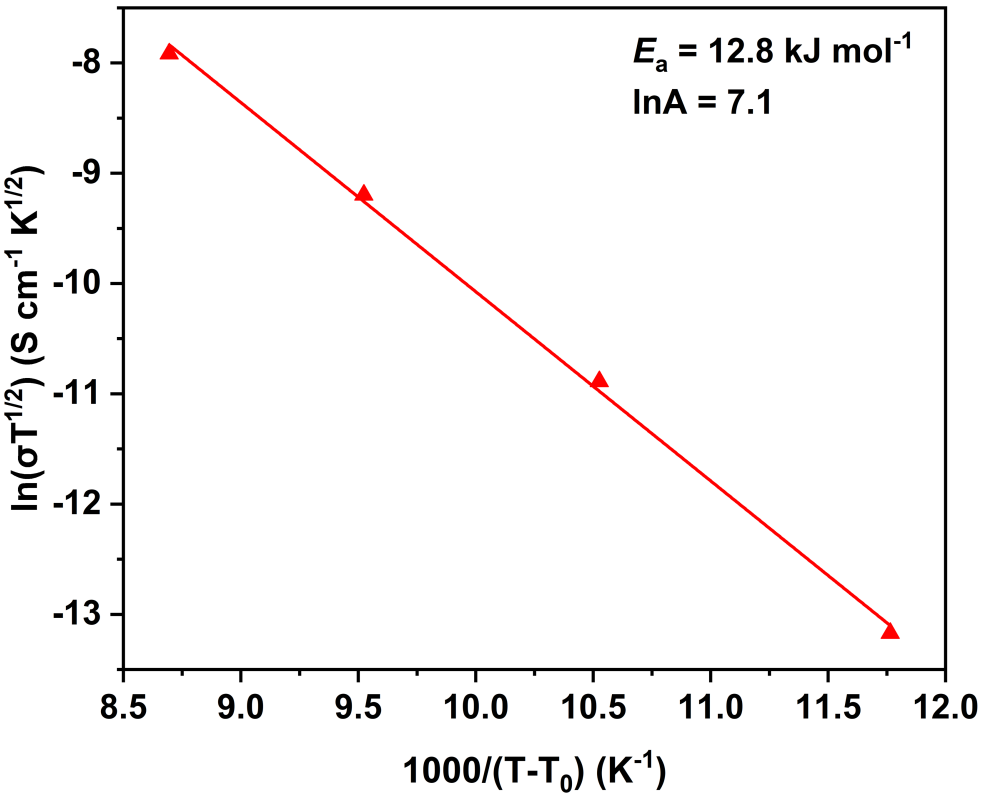


Figure 4.13. VFT fit for ABA(9, 0.22) polymer electrolyte. $R^2 = 0.998$.

4.5. Polymer Modification

4.5.1. Polymer Cross-Linking

Polymers with higher molar masses are sought to improve mechanical integrity; this was explored by chain extension via a diisocyanate coupling reaction (Scheme 4.4). The coupling procedure was adapted from a report by Bao and co-workers where coupling was performed to increase the mechanical strength of a polymer electrolyte.[27] Under an anaerobic atmosphere, poly(DTC-*b*-DGA-*alt*-AGE-*b*-DTC) with a molar mass of 18 kg mol^{-1} was dissolved in DMF and stirred at 85 °C. Three equivalents of isophorone diisocyanate and a catalytic quantity of dibutyltin dilaurate (DBTDL, 1 mg) were then added and the reaction

stirred, at 85 °C for 3 h. After which time, 2 equivalents of 1,6-hexanediol were added and the reaction was stirred for a further 3 h. The polymer solution was precipitated from diethyl ether. A visible change in polymer properties was observed: before coupling it was a viscous fluid and afterwards it was a free-standing gummy solid. The polymer would not dissolve in any of the solvents tested, so NMR and SEC characterisation were not conducted. This lack of solubility was indicative of extensive crosslinking.

The thermal properties of the polymers before and after coupling were observed by DSC and TGA. The polymer T_g increased from -18 to -9 °C, after coupling, due to the increased chain entanglement; additionally, there could be hydrogen bonding between the isocyanate linkers (Figure 4.14). The polymer thermal stability decreased after coupling ($T_{d,5\%}$ = 292 °C before, 225 °C after); however, it was still high enough for battery applications and provides a reasonable processing window (Figure 4.15).[28]

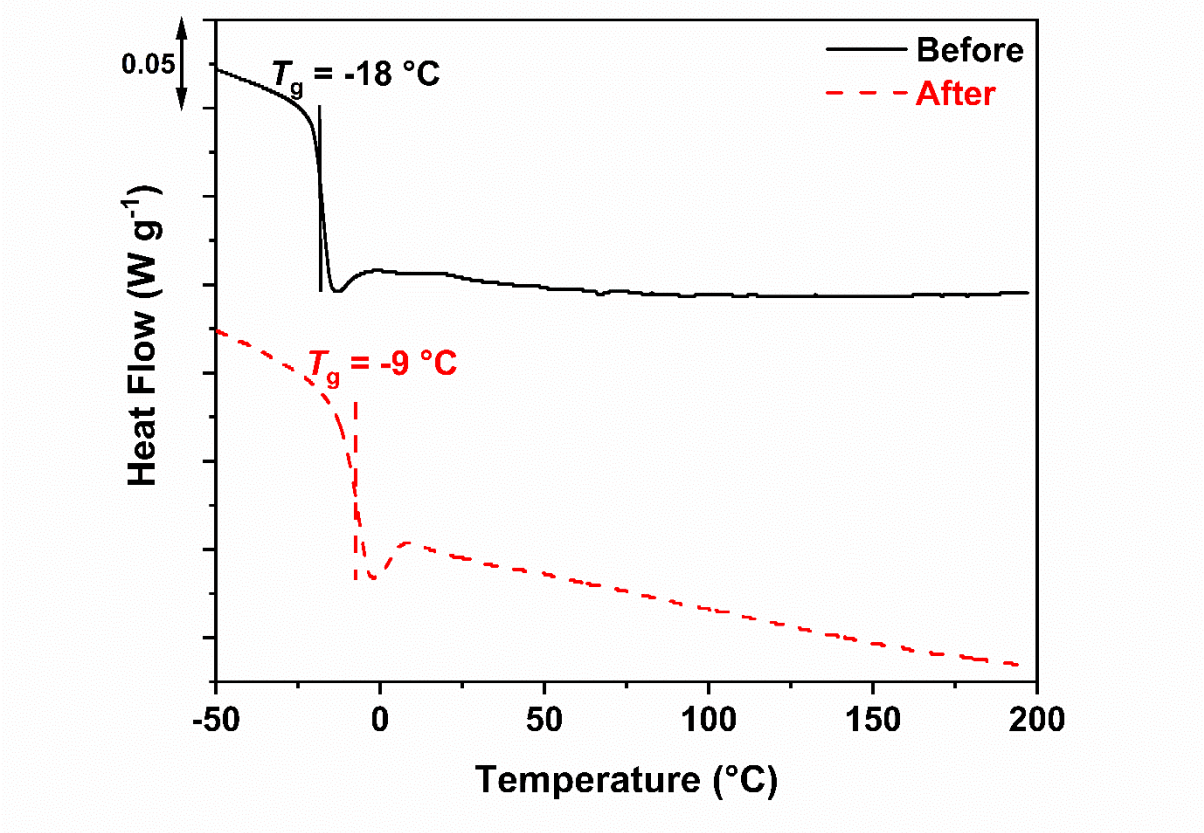


Figure 4.14. DSC data for poly(DTC-*b*-DGA-*alt*-AGE-*b*-DTC), before and after the diisocyanate coupling reaction. Scan rate = 10 °C min^{-1}, data obtained from the second heating cycle.

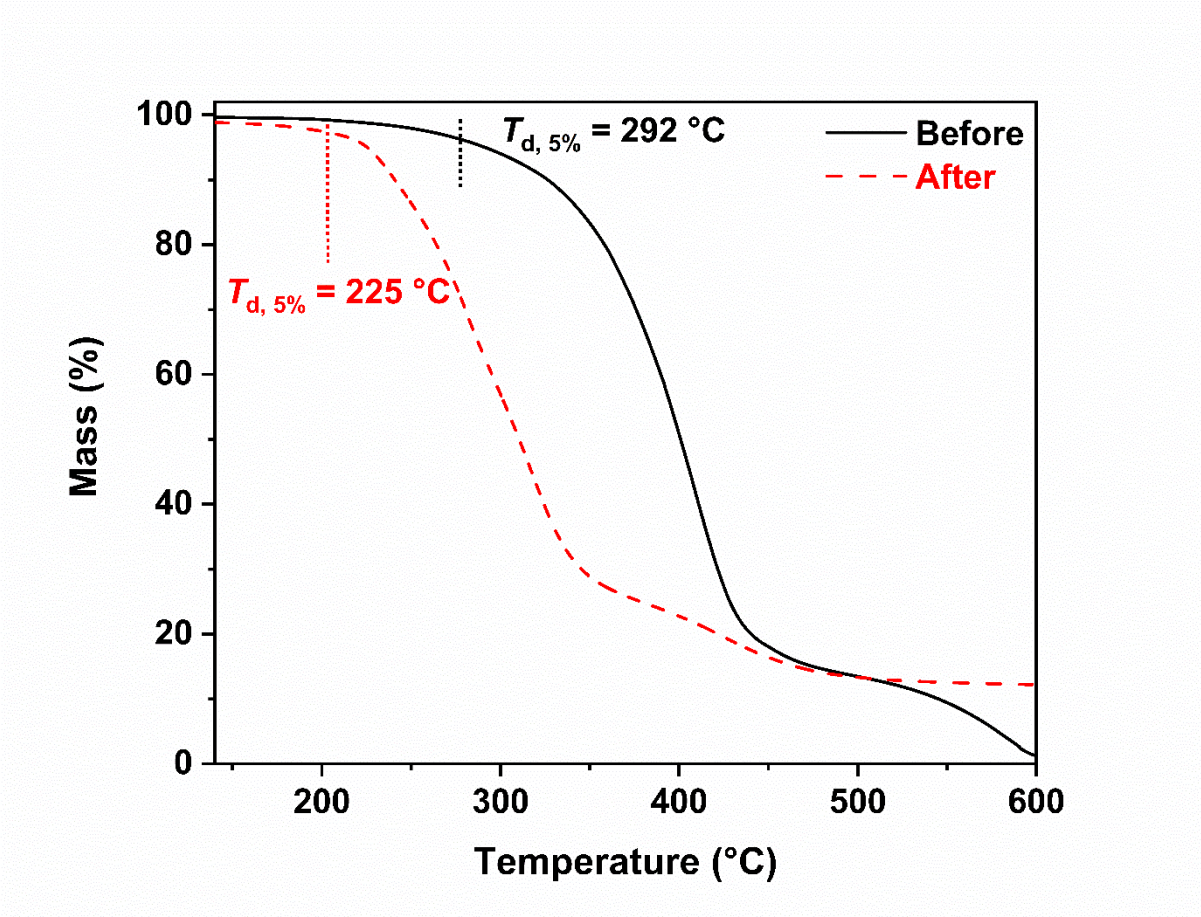


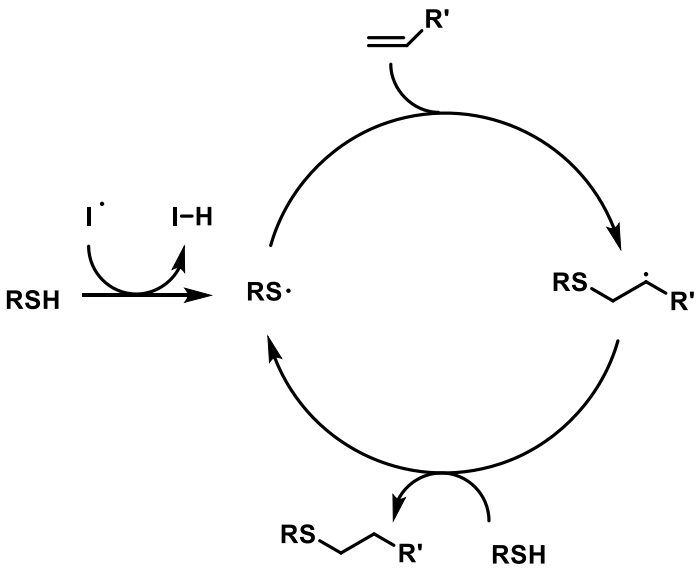
Figure 4.15. TGA data for poly(DTC-*b*-DGA-*alt*-AGE-*b*-DTC), before and after the diisocyanate coupling reaction.

Rheology was used to compare the mechanical properties of the polymers before and after the coupling reaction. A temperature sweep experiment quantified what was observed visually: the polymer was stiffer after coupling. At 30 °C, G' increased from 0.15 to 0.90 MPa; at 80 °C, G' increased from 6.9×10^{-5} to 0.013 MPa. This was consistent with the DSC data which showed a 9 °C increase in the polymer's T_g value after the coupling reaction. The longer, coupled polymer chains are more entangled and inclusion of diisocyanate units increases hydrogen bonding, resulting in a stiffer material with a greater storage modulus.

Whilst the utility of forming a polyurethane to improve mechanical properties was demonstrated, in this case the polymer became difficult to process so further characterisation of the polymer was challenging. In future, the optimisation of the extent of crosslinking with respect to mechanical properties, Li-ion conductivity and processability could be explored.

4.5.2. Polymer Post-Functionalisation

Functionalising polymers enables their properties to be tuned; this can achieve enhanced performance in specific applications. Pendant vinyl groups on polymer backbones can be used as a platform for thiol-ene addition reactions, allowing a range of functional groups to be incorporated. In this reaction, a thiyl-radical is generated from the reaction between a radical initiator and a thiol. The thiyl is subsequently added across the alkene bond in a two-step process: firstly, the thiyl radical adds to the alkene to produce a radical at the carbon atom; then, this radical adds to the thiol to produce a carbon-sulfur bond (Scheme 4.4). This reaction occurs rapidly and without by-products; it thus can be described as a 'click' reaction.[29]

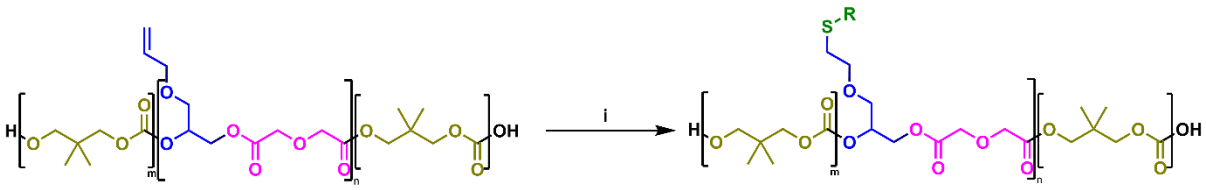


Scheme 4.4. General reaction mechanism for thiol-ene addition reactions.

Thiol-ene addition reactions have been reported for the post-functionalisation of polycarbonates: for example, Darensbourg and co-workers incorporated alcohol and carboxylic acid groups onto poly(2-vinyloxirane carbonate);[30] Greiner and co-workers incorporated ammonium salts, polyethylene glycol, carboxylate and ester groups onto poly(limonene carbonate) (PLC);[31] Konig and co-workers crosslinked PLC using multifunctional thiols;.[32, 33] Williams and co-workers functionalised poly(ester-*b*-carbonate) pentablock polymers with alcohol groups.[34] Here, functionalities have been incorporated into poly(DTC-*b*-DGA-*alt*-AGE-*b*-DTC) with the aim of improving their suitability for battery applications: fluorinated functionalities are hypothesised to improve electrochemical stability and Li-ion conductivity by enhancing salt dissociation; nitrile and sulfone functionalities are proposed to improve Li-salt dissociation and increase the lithium-ion transference number.[16, 35]

4.5.2.1. Functionalised Polymer Synthesis and Characterisation

Poly(DTC-*b*-DGA-*alt*-AGE-*b*-DTC) sample ABA(18, 0.20) was used: its electrolyte had the highest ionic conductivity of the compositions studied. The thiols used were 2,2,2-trifluoroethanethiol ($SHCH_2CF_3$, CF_3-functionalised), 3-mercaptopropanenitrile ($SH(CH_2)_2CN$, nitrile-functionalised), and 3-mercaptotetrahydrothiophene 1,1-dioxide ($SHCH(CH_2)_3SO_2$, sulfone-functionalised). Thiol-ene reactions were conducted, using UV light, with a DMPA photoinitiator (Scheme 4.5). The vinyl/thiol/DMPA ratio was 1/2/0.2; excess thiol was used to deliver complete functionalisation. Functionalised polymers were purified by precipitation with THF from Et_2O and were dried under reduced pressure.



Scheme 4.5. Functionalisation of P(DTC-*b*-DGA-*alt*-AGE-*b*-DTC). *i*: vinyl/thiol/DMPA = 1/2/0.2, THF, UV light, thiol R-SH, where R = CH_2CF_3, $(CH_2)_2CN$, $CH(CH_2)_3SO_2$.

Successful installation of the different functionalities was observed by ^{1}H NMR spectroscopy. In all three cases, the vinyl proton (5.85 ppm) on the starting polymer disappeared and the appearance of new peaks corresponding to the specific functionality were observed. For the CF_3-functionality, the new peaks were at 3.08, 2.73 and 1.84 ppm; for the nitrile, the peaks were at 2.95, 2.79, 2.67 and 1.84 ppm; and for the sulfone, the peaks were at 3.31, 3.12, 2.97, 2.67, 2.57, 2.12 and 1.85 ppm (Figure 4.16). The polymer molar mass was estimated by ^{1}H NMR spectroscopy, from the relative integrals of the initiator (7.34 ppm), polyester (4.60, 4.40 ppm) and polycarbonate blocks (1.01 ppm). In all cases, the polymers showed an increase in molar mass after functionalisation (Table 4.6). The SEC traces of the functionalised polymers were monomodal with narrow distributions (1.23 – 1.47), but only the polymers featuring CF_3 groups showed a mass increase, from 7.0 to 12.7 kg mol^{-1}. The polymers with nitrile and sulfone functionalities showed slight decreases in molar mass by SEC, with values of 6.8 and 5.8 kg mol^{-1}, respectively (Table 4.6). The SEC molar mass disparities are attributed to the functionalised polymers interacting differently with the column and eluent compared to the starting polymer and the polystyrene calibration standards.

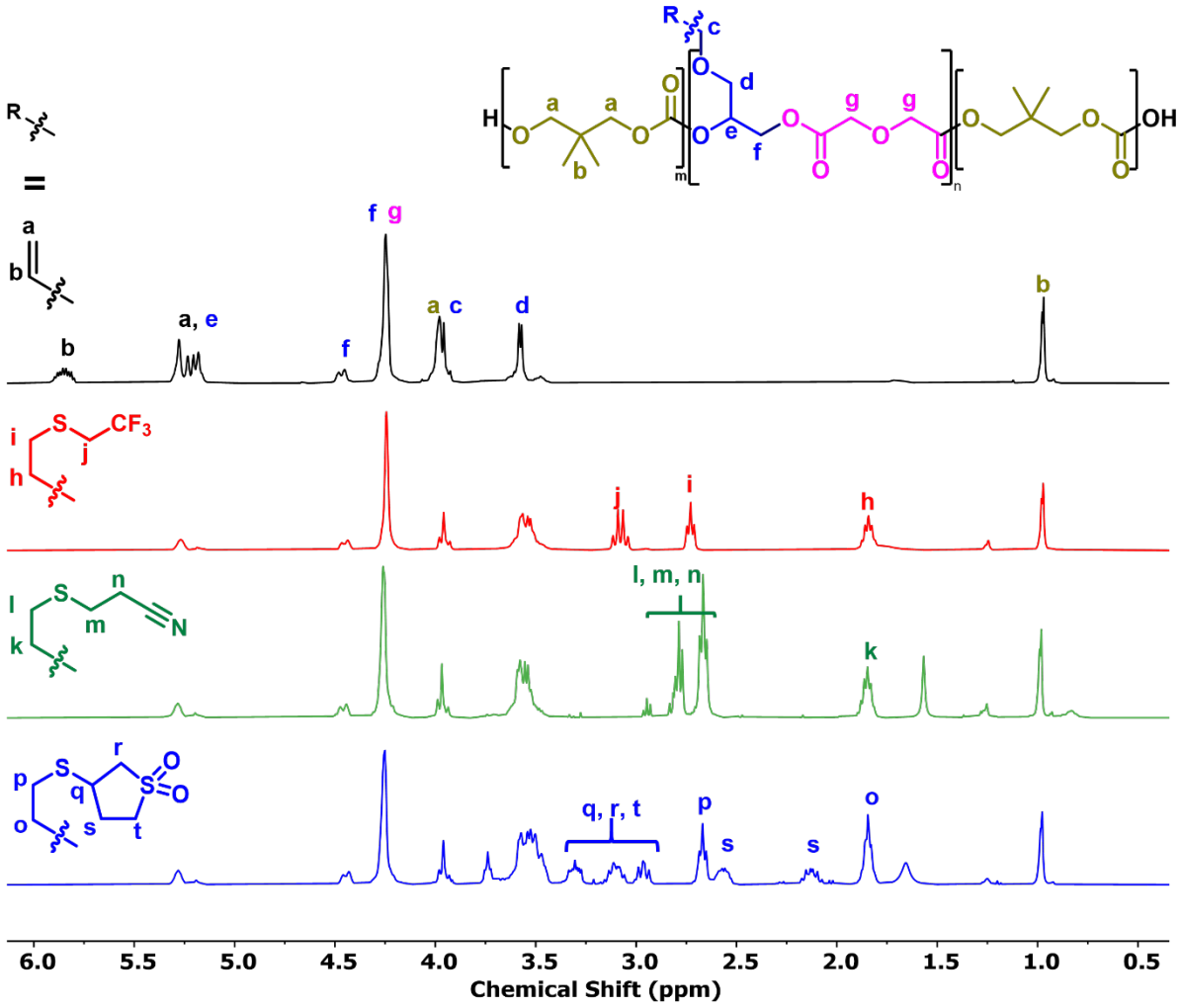


Figure 4.16. ^{1}H NMR spectra of P(DTC-*b*-DGA-*alt*-AGE-*b*-DTC), before and after functionalisation at the vinyl group.

Table 4.6. Characterisation Data for Functionalised Poly(DTC-*b*-DGA-*alt*-AGE-*b*-DTC) ABA(18, 0.20)

Functionality	$M_{n,calc}$ (kg mol^{-1}) [a]	$M_{n,NMR}$ (kg mol^{-1}) [b]	$M_{n,SEC}$ (kg mol^{-1}) [c]
Vinyl	-	19.5	7.0 [1.35]
CF_3	33.0	31.6	12.7 [1.43]
Nitrile	30.6	27.4	6.8 [1.47]
Sulfone	36.0	34.1	5.8 [1.23]

[a] M_n as calculated by the $M_{n,NMR}$ of the starting polymer and the mass of the functional units to be installed; [b] M_n as determined from the ^{1}H NMR spectra of the purified polymer by integration of the aromatic initiator resonance (7.34 ppm for BDM) against those of the polyester (4.60, 4.40 ppm) and the polycarbonate (1.01 ppm); [c] M_n determined by SEC, using THF eluent and polystyrene standards.

4.5.2.2 Functionalised Polymer Thermal-Mechanical Properties

Functionalised polymer electrolytes were prepared with LiTFSI, in the same manner as for the block copolymer electrolytes in section 4.4.2. There was a slight change to the polymers' thermal properties on functionalisation, as observed by DSC and TGA. Modest decreases in T_g were observed when the CF_3 and nitrile functionality were incorporated (from -5 °C for the vinyl, to -10 and -14 °C for the CF_3 and nitrile group, respectively). These functional groups are proposed to facilitate segmental motion and, therefore, they reduce the T_g. Conversely, the T_g increased to 11 °C when the sulfone group was incorporated (Table 4.7, Figure 4.17). This functionality restricts the segmental motion of the polymer, resulting in stiffening. Thermal stability was assessed using TGA; small variations were observed on changing functionality but in all cases, $T_{d,5\%}$ remained above 250 °C (Table 4.7, Figure 4.18).

Table 4.7. Thermal-Mechanical and Li-ion Conductivity Data for Poly(DTC-*b*-DGA-*alt*-AGE-*b*-DTC) Electrolytes, Before and After Functionalisation.

Functionality	T_g (°C) [a]	$T_{d,5\%}$ (°C) [b]	G', 30 °C (MPa) [c]	G', 70 °C (MPa) [c]	σ, 30°C (S cm^{-1}) [d]	σ, 70°C (S cm^{-1}) [d]
Vinyl	-5	264	0.15	1.9×10^{-4}	5.0×10^{-8}	5.3×10^{-5}
CF_3	-10	253	0.17	1.5×10^{-3}	3.1×10^{-7}	6.8×10^{-5}
Nitrile	-14	259	0.14	3.4×10^{-4}	1.8×10^{-7}	8.9×10^{-6}
Sulfone	11	273	31.4	3.2×10^{-2}	7.6×10^{-9}	3.0×10^{-7}

[a] Determined by DSC (10 °C min^{-1}), second heating curve; [b] The temperature at which 5% polymer mass loss is recorded, measured by TGA (20 °C min^{-1} heating rate); [c] Storage modulus G' obtained by oscillatory rheology temperature sweep (10 Hz, strain 10%); [d] Li-ion conductivity measured using impedance spectroscopy, with ionic conductivity being calculated from the resistance obtained by fitting the data to the equivalent circuit Q1+Q2/R2. Error = 34 and 35% at 30 and 70 °C, respectively.

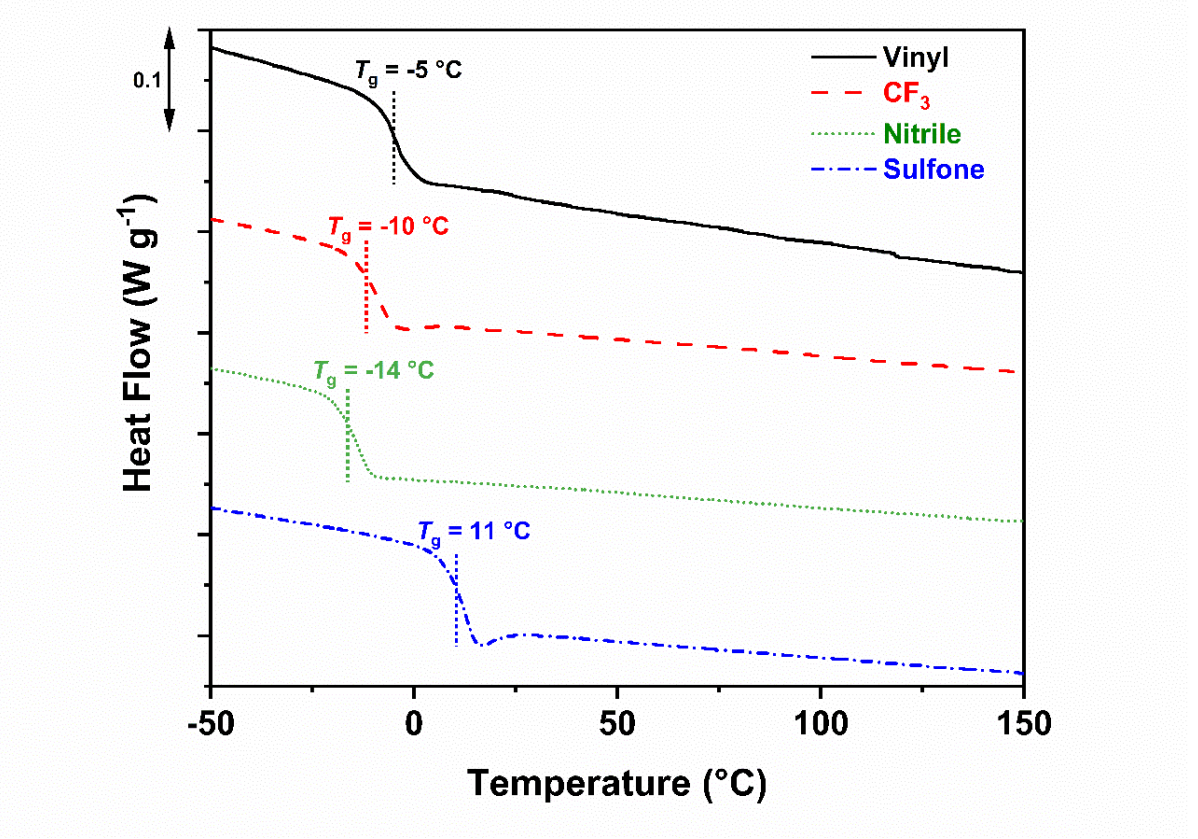


Figure 4.17. DSC traces for unfunctionalised (vinyl) and functionalised (CF_3, nitrile, and sulfone) polymer electrolytes, at a scan rate of 10 °C min^{-1}.

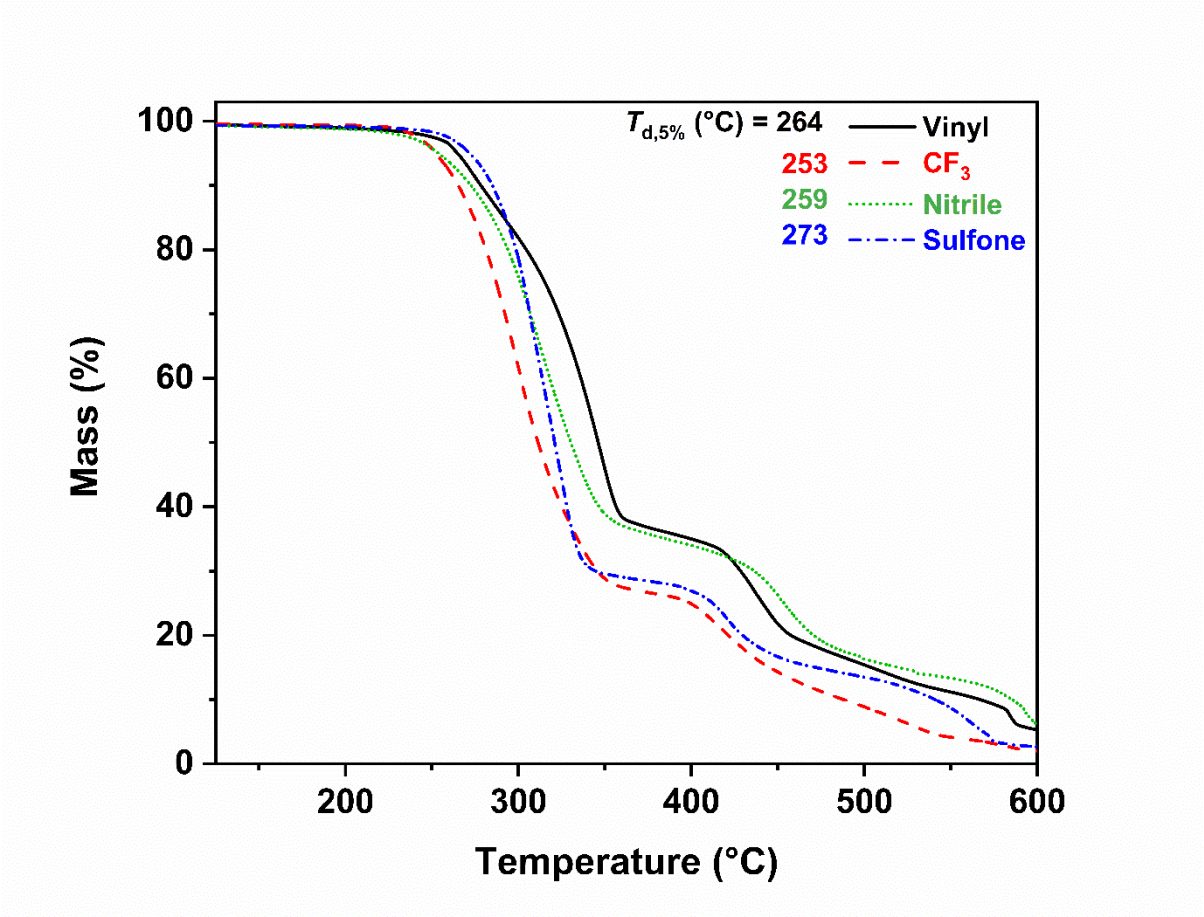


Figure 4.18. TGA data for the unfunctionalised (vinyl) and functionalised (CF_3, nitrile and sulfone) polymer electrolytes.

Rheology was used to study the mechanical properties of the functionalised polymer electrolytes. Storage and loss moduli (G', G'') were measured at temperatures 30 to 80 °C at an oscillation frequency of 10 Hz, and a strain of 10% (Table 4.7, Figure 4.19). This range was in the polymers' linear viscoelastic regions. At 30 °C, the CF_3- and nitrile-functionalised polymers exhibited similar mechanical properties to the unfunctionalised polymer (0.1 – 0.2 MPa). This finding is consistent with their similar T_g values (-10 and -14 for CF_3 and nitrile; -5 for vinyl). The CF_3 functionality had a greater storage modulus, G' than the unfunctionalised polymer at higher temperatures (4.7×10^{-4} MPa for CF_3; 6.9×10^{-5} MPa for the unfunctionalised electrolyte at 80 °C). The sulfone functionality showed a 100× increase in storage modulus across the temperature range; this was

consistent with the significantly higher T_g value (11 °C) of this polymer. The improved mechanical strength can aid battery safety and performance by inhibiting lithium dendrite formation and puncture, thus preventing short-circuits.[36]

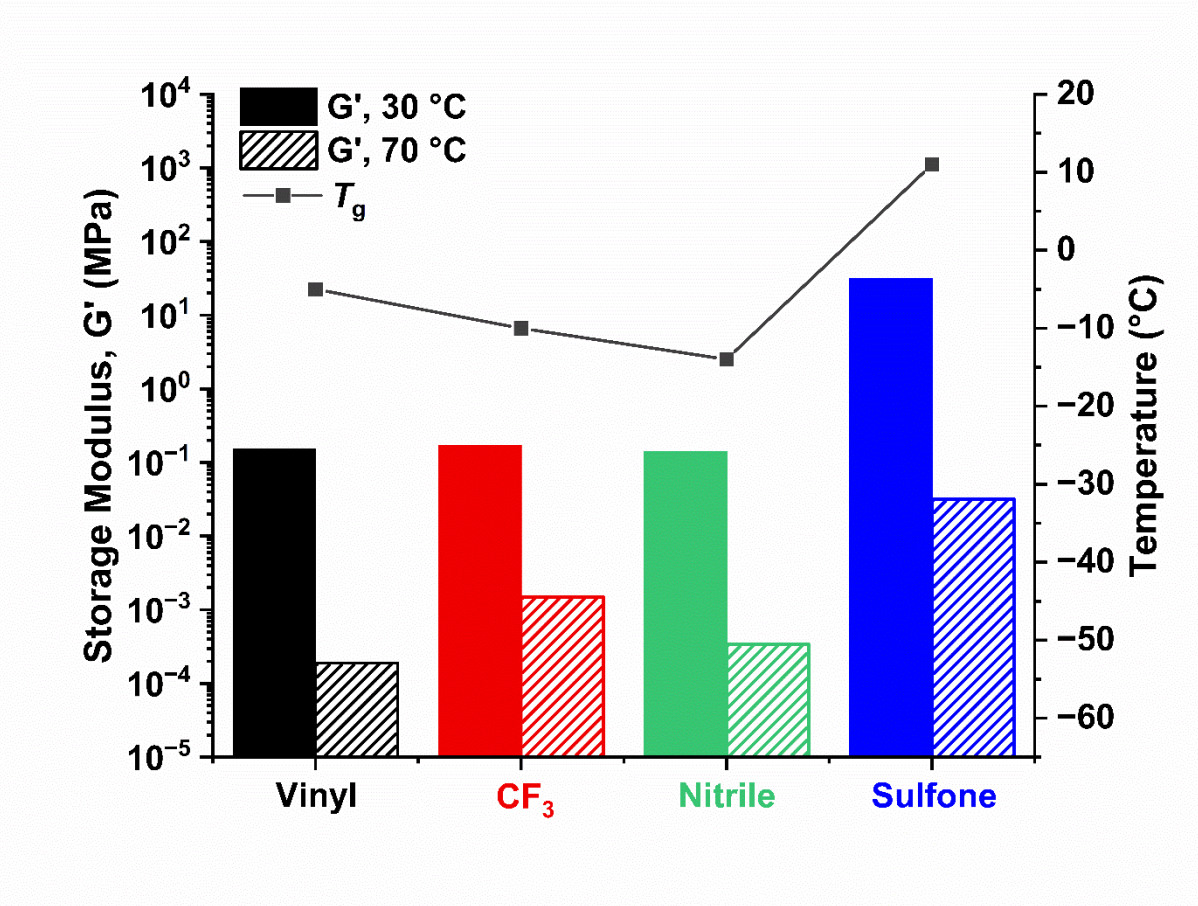


Figure 4.19. Storage moduli, G' at 30 °C and 70 °C; and the T_g values, for the unfunctionalised (vinyl) and functionalised (CF_3, nitrile, sulfone) polymer, ABA(18, 0.20), electrolytes.

4.5.2.3. Li-ion Conductivity of the Functionalised Polymers

The Li-ion conductivity of the functionalised and unfunctionalised polymer electrolytes were measured at 10 °C intervals between 30 and 70 °C (Table 4.7, Figure 4.20). At 70 °C, the CF_3-functionalised polymer had a Li-ion conductivity similar to the unfunctionalised polymer electrolyte (σ = 5.3 or 6.8 × 10^{-5} S cm^{-1} for the unfunctionalised and CF_3-functionalised

polymers, respectively). This is consistent with their similar T_g values. The nitrile and sulfone functionalities exhibited a 10× and 100× decrease in Li-ion conductivity, respectively ($\sigma = 8.9 \times 10^{-6}$, 3.03×10^{-7} S cm^{-1}). The sulfone-functionalised polymer had a T_g value 16 °C greater than the unfunctionalised polymer, resulting in more rigid chains which hindered Li-ion transport. The nitrile polymer had a lower T_g value of -14 °C. This loss of conductivity demonstrates that Li-ion conductivity depends on other factors other than just T_g – such as ion conduction pathways and salt solvation. These values are closely comparable to those reported by Balsara and Coates for poly(DGA-*alt*-AGE) ($\sigma = 2.5 \times 10^{-4}$ S cm^{-1} at 90 °C).

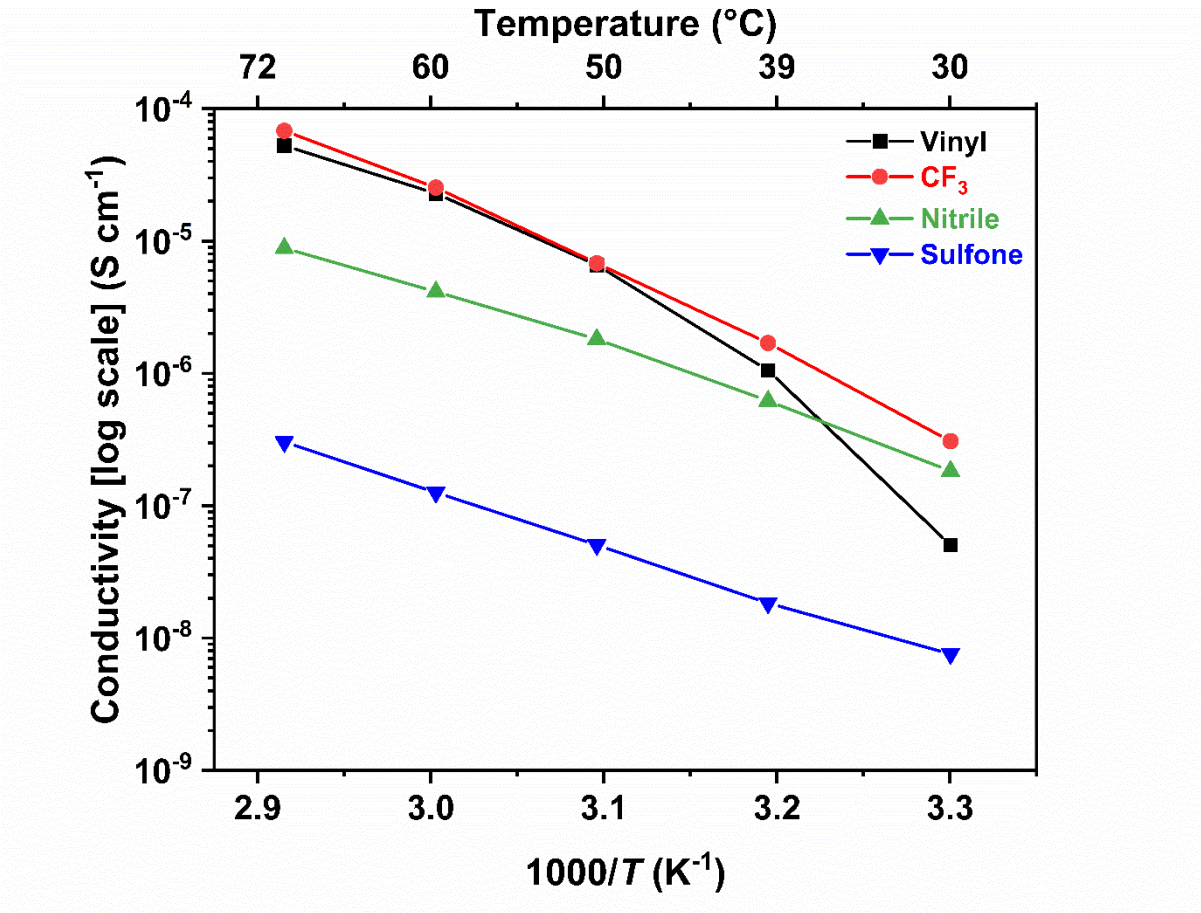


Figure 4.20. Li-ion conductivity as a function of temperature for the unfunctionalised (vinyl) and functionalised (CF_3, nitrile, sulfone) polymers, with Li-ion concentration $\rho = 0.22$.

4.6. Conclusions and Further Work

The switchable polymerisation of diglycolic anhydride (DGA), allyl glycidyl ether (AGE) and 2,2-dimethyltrimethylene carbonate (DTC) was achieved using the [L_{van}AlK(OAc)$_2$] catalyst. The polymerisations showed good control and a systematic series of ABA triblock copolymers were produced (A = P(DTC), B = P(DGA-*alt*-AGE)). The series contained polymers with molar masses of 4 – 19 kg mol^{-1} and hard (A-block) weight fractions of 0.2 – 0.5. Next, polymer electrolytes were produced (with ρ = 0.22, where this describes the Li-ion molar ratio) with all materials having T_g values < -10 °C and $T_{d,\,5\%}$ values > 265 °C. Polymers with the lower hard weight fraction, 0.2, showed 5× greater conductivity than polymers with a hard weight fraction 0.5. The polymer molar mass did not have a significant effect on Li-ion conductivity in this range. The polymer of molar mass 18 kg mol^{-1} and hard weight content of 0.2 had the highest Li-ion conductivity of $\sigma = 5.3 \times 10^{-5}$ S cm^{-1} at 70 °C. Fluorinated, sulfonated and nitrile functionalities were incorporated into a master batch of the polymer and the effect of these substituents on the thermomechanical properties and Li-ion conductivity were observed. Small improvements in ionic conductivity were achieved with the fluorinated functionality; a 10× increase at 30 °C but insignificant differences at higher temperatures. The sulfonated functionality decreased conductivity by approximately 100× but with a concomitant 100× increase in storage modulus.

There are two areas which should be prioritised for future exploration: 1, optimisation of the polymer composition and architecture; and 2, investigating the most conductive polymer in different types of battery.

1. Polymer Compositions and Architectures

P(DTC-*b*-DGA-*alt*-AGE-*b*-DTC) of a higher molar mass should be targeted in future in order to achieve block phase separation. This strategy may result in materials with elastomeric properties which might be desirable for application as cathode binders. To make such a polymer, one option would be to use organometallic catalysts since these can initiate polymers cleanly. The organometallic catalyst, L_{van}AlK(Cp) has been reported by the Williams group and should be studied for this polymerisation with the objective of producing higher molar mass polymers.[9]

In addition, the monomer purity could be improved as it is likely that protic impurities are present; these act as chain transfer agents thus reduce polymer molar mass. In this thesis, significant effort was made to purify the monomers, by multiple distillations, recrystallisations and sublimations of the monomers. In future, alternative monomers with more successful purification procedures could be explored. For example, using a propylene oxide (PO)/AGE epoxide mixture could improve molar mass whilst minimally affecting thermal and electrochemical properties – PO is significantly easier to purify than AGE.

The formation of polyurethanes should also be optimised in future to produce a processable polymer electrolyte. This work should prioritise different cross-link densities – at lower densities, it could be that the polymer would be more readily processable, whilst also resulting in materials with mechanical integrity. The polymer featuring the fluorinated functionality improved the Li-ion conductivity and warrants further investigation. A series of polymers with $-(CF_2)_nCF_3$ functionalities should be produced to determine the optimal side chain length for highest ionic conductivity. It would be expected that as the chain length increases, the polymer T_g may decrease and salt dissociation may increase. One issue would be that such side chains cannot coordinate Li-ions, therefore, the overall conductivity may decrease.[37] The performance of the polymer with fluorinated side chains could be compared to the corresponding polymers with alkyl chains. The lithium salt should be optimised: both the

type, and the amount. For example, LiTFSI-, LiFSI- and LiBOB-based polymer electrolytes could be tested systematically, with ρ varying from 0.05 to 0.5.

2. Battery Applications

The lead polymers should also be tested in battery applications; guided by the optimum mechanical properties, ionic conductivity and electrochemical stability. The testing could be as an electrolyte (gel, polymer or composite) or a cathode binder. The lead polymer in this chapter, ABA(18, 0.20), should be tested as a cathode binder, similarly to poly(vCHC-*b*-CL-*r*-TMC-*b*-vCHC) in the previous chapter. Furthermore, in-situ crosslinking of the polymer via the alkene groups might be feasible: such in situ cross-linking may improve contact between cathode components, thus reducing contact resistance and improving cycling performance.[38] The performance of cells incorporating three types of ABA(18, 0.20)-based binders should be studied: 1, ABA(18, 0.20); 2, ex-situ crosslinked ABA(18, 0.20); 3, in-situ cross-linked ABA(18, 0.20). This work would come after cross-link density optimisation, as previously described. Finally, as this polymer is produced in a one-pot method, with no reagent addition or atmosphere change, in-situ polymerisation should be studied to form a polymer electrolyte in the cathode directly. This approach might improve the contact between the cathode components, reducing the interfacial resistance. It would also reduce solvent use and may simplify cell fabrication.[39]

4.7. References

1. A. C. Deacy, G. L. Gregory, G. S. Sulley, T. T. D. Chen and C. K. Williams, *J. Am. Chem. Soc.*, 2021, **143**, 10021-10040.
2. C. Romain, Y. Zhu, P. Dingwall, S. Paul, H. S. Rzepa, A. Buchard and C. K. Williams, *J. Am. Chem. Soc.*, 2016, **138**, 4120-4131.

3. Y. Zhu, C. Romain and C. K. Williams, *J. Am. Chem. Soc.*, 2015, **137**, 12179-12182.

4. G. L. Gregory, G. S. Sulley, L. P. Carrodeguas, T. T. D. Chen, A. Santmarti, N. J. Terrill, K.-Y. Lee and C. K. Williams, *Chem. Sci.*, 2020, **11**, 4367-4378.

5. W. Luo, K. Deng, S. Wang, S. Ren, D. Han, Y. Wang, M. Xiao and Y. Meng, *Adv. Polym. Technol.*, 2020, **2020**, 5047487.

6. M. D. Konieczynska, X. Lin, H. Zhang and M. W. Grinstaff, *ACS Macro. Lett.*, 2015, **4**, 533-537.

7. D. M. Pesko, Y. Jung, A. L. Hasan, M. A. Webb, G. W. Coates, T. F. Miller and N. P. Balsara, *Solid State Ion.*, 2016, **289**, 118-124.

8. M. A. Webb, Y. Jung, D. M. Pesko, B. M. Savoie, U. Yamamoto, G. W. Coates, N. P. Balsara, Z.-G. Wang and T. F. Miller, *ACS Cent. Sci.*, 2015, **1**, 198-205.

9. W. T. Diment and C. K. Williams, *Chem. Sci.*, 2022, **13**, 8543-8549.

10. M. Jia, D. Zhang, G. W. de Kort, C. H. R. M. Wilsens, S. Rastogi, N. Hadjichristidis, Y. Gnanou and X. Feng, *Macromolecules*, 2020, **53**, 5297-5307.

11. T. Liu, T. L. Simmons, D. A. Bohnsack, M. E. Mackay, M. R. Smith and G. L. Baker, *Macromolecules*, 2007, **40**, 6040-6047.

12. A. Buchard, D. R. Carbery, M. G. Davidson, P. K. Ivanova, B. J. Jeffery, G. I. Kociok-Köhn and J. P. Lowe, *Angew. Chem. Int. Ed.*, 2014, **53**, 13858-13861.

13. F. Jing and M. A. Hillmyer, *J. Am. Chem. Soc.*, 2008, **130**, 13826-13827.

14. H. Keul, R. Bächer and H. Höcker, *Makromol. Chem.*, 1986, **187**, 2579-2589.

15. N.-S. Choi, Y.-G. Lee and J.-K. Park, *J. Power Sources*, 2002, **112**, 61-66.

16. S. Xie, A. Nikolaev, O. A. Nordness, L. C. Llanes, S. D. Jones, P. M. Richardson, H. Wang, R. J. Clément, J. Read de Alaniz and R. A. Segalman, *Macromolecules*, 2022, **55**, 5723-5732.

17. M. Viviani, N. L. Meereboer, N. L. P. A. Saraswati, K. Loos and G. Portale, *Polym. Chem.*, 2020, **11**, 2070-2079.

18. F. Ouhib, L. Meabe, A. Mahmoud, N. Eshraghi, B. Grignard, J.-M. Thomassin, A. Aqil, F. Boschini, C. Jérôme, D. Mecerreyes and C. Detrembleur, *J. Mater. Chem. A*, 2019, **7**, 9844-9853.

19. I. L. Johansson, D. Brandell and J. Mindemark, *Batter. Supercap.*, 2020, **3**, 527-533.

20. Y. Zhao, Y. Bai, W. Li, M. An, Y. Bai and G. Chen, *Chem. Mater.*, 2020, **32**, 6811-6830.

21. W. T. Diment, G. L. Gregory, R. W. F. Kerr, A. Phanopoulos, A. Buchard and C. K. Williams, *ACS Catal.*, 2021, **11**, 12532-12542.

22. S. Paul, Y. Zhu, C. Romain, R. Brooks, P. K. Saini and C. K. Williams, *Chem. Comm.*, 2015, **51**, 6459-6479.

23. B. V. Lebedev, T. y. G. Kulagina, V. I. Telnoy and V. G. Vasil'ev, *Macromol. Chem. Phys.*, 1995, **196**, 3487-3510.

24. M. A. Ratner and D. F. Shriver, *Chem. Rev.*, 1988, **88**, 109-124.

25. A. A. Teran, M. H. Tang, S. A. Mullin and N. P. Balsara, *Solid State Ion.*, 2011, **203**, 18-21.

26. J. Mindemark, M. J. Lacey, T. Bowden and D. Brandell, *Prog. Polym. Sci.*, 2018, **81**, 114-143.

27. D. G. Mackanic, X. Yan, Q. Zhang, N. Matsuhisa, Z. Yu, Y. Jiang, T. Manika, J. Lopez, H. Yan, K. Liu, X. Chen, Y. Cui and Z. Bao, *Nat. Commun.*, 2019, **10**, 5384.

28. Y. Zhu, M. R. Radlauer, D. K. Schneiderman, M. S. P. Shaffer, M. A. Hillmyer and C. K. Williams, *Macromolecules*, 2018, **51**, 2466-2475.

29. C. E. Hoyle and C. N. Bowman, *Angew. Chem. Int. Ed.*, 2010, **49**, 1540-1573.

30. D. J. Darensbourg and F.-T. Tsai, *Macromolecules*, 2014, **47**, 3806-3813.

31. O. Hauenstein, S. Agarwal and A. Greiner, *Nat. Commun.*, 2016, **7**, 11862.

32. C. Li, R. J. Sablong and C. E. Koning, *Eur. Polym. J.*, 2015, **67**, 449-458.

33. C. Li, M. Johansson, R. J. Sablong and C. E. Koning, *Eur. Polym. J.*, 2017, **96**, 337-349.

34. T. T. D. Chen, Y. Zhu and C. K. Williams, *Macromolecules*, 2018, **51**, 5346-5351.

35. Y. L. N. K. Mallela, S. Kim, G. Seo, J. W. Kim, S. Kumar, J. Lee and J.-S. Lee, *Electrochim. Acta*, 2020, **362**, 137141.

36. C. A. Angell, *Electrochim. Acta*, 2017, **250**, 368-375.

37. M. Ebadi, T. Eriksson, P. Mandal, L. T. Costa, C. M. Araujo, J. Mindemark and D. Brandell, *Macromolecules*, 2020, **53**, 764-774.

38. V. Vijayakumar, B. Anothumakkool, S. Kurungot, M. Winter and J. R. Nair, *Energy Environ. Sci.*, 2021, **14**, 2708-2788.

39. T. Liu, J. Zhang, W. Han, J. Zhang, G. Ding, S. Dong and G. Cui, *J. Electrochem. Soc.*, 2020, **167**, 070527.

CHAPTER 5

Outlook

5.1. Thesis Summary

This thesis has detailed the synthesis of poly(ester-*b*-carbonate)s by switch catalysis for battery applications. This highly-controlled synthesis approach facilitated systematic variation of polymer molar mass, composition and architecture; the effect of these variations on polymer properties were investigated.

In Chapter 2, systematic series of poly(carbonate-*b*-ester)s were prepared, to study the effect of molar mass ($26 < M_n < 69$ kg mol^{-1}), polycarbonate content ($0.26 < w_{PC} < 0.62$) and block structure (AB vs ABA) on Li-ion conductivity. The lead polymer had high electrochemical stability (5.2 V), good Li-ion conductivity (2.2×10^{-4} S cm^{-1} at 60 °C) and it demonstrated elastic recovery. It was applied as a composite cathode binder in an all-solid-state battery, resulting in high capacity (186 mAh g^{-1}) and excellent capacity retention (96.7% after 200 cycles), surpassing widely-used PTFE binders.

Chapter 3 produced polyester and poly(carbonate-*b*-ester-*b*-carbonate) electrolytes with unfluorinated or fluorinated backbones, and with oligoether side chains of different lengths, to investigate the effect on thermal and electrochemical properties. The block copolymers were produced by one-pot switch catalysis of anhydride/epoxide/cyclic carbonate. Generally, longer ether side chains and fluorinated backbones corresponded to increased ionic conductivity and decreased polymer T_g values, for both the block copolymers and polyesters. The best-performing block copolymer electrolyte had a high Li-ion conductivity of 5.6×10^{-4} S cm^{-1} at 80 °C.

In Chapter 4, the composition of a poly(carbonate-*b*-ester-*b*-carbonate) was optimised with respect to Li-ion conductivity, and the effect of post-polymerisation modifications was studied. The switch catalysis of anhydride/epoxide/cyclic carbonate from a one-pot monomer mixture was demonstrated, to produce polymers of molar mass 4 – 20 kg mol^{-1} and $w_{PC} = 0.2$

– 0.5. The optimum polymer had moderate conductivity, of 5.3×10^{-5} S cm^{-1} at 70 °C. It was crosslinked to improve mechanical integrity; and fluorinated, sulfonated and nitrile groups were introduced to affect thermomechanical properties and ionic conductivity. An improvement in Li-ion conductivity was observed on incorporation of the fluorinated functionality.

5.2. Outlook

This thesis has demonstrated the utility of switch catalysis to systematically produce poly(ester-*b*-carbonates) with control over molar mass, composition and architecture. This facilitated optimisation of polymer electrolytes, one of which was successfully applied as a composite cathode binder, and it elucidated structure-property relationships which can help to guide future polymer design for battery applications.

There is a wide range of monomers which can be applied to switchable polymerisations, including many which are heteroatom rich. Exploration of these could yield new, Li-ion conductive polymers. For example, alternative polycarbonate blocks could be produced by epoxide/CO_2 ROCOP, where the epoxide is cyclohexene oxide, allyl glycidyl ether, butylene oxide or limonene oxide.[1] The different T_g values of these polycarbonates will impart different thermal and mechanical properties onto the polymer electrolyte; the effect of this on ionic conductivity is of interest. Alternative lactone ROPs can be studied; poly(propiolactone) and poly(ethylene adipate) have both been reported as polyester electrolytes with good Li-ion conductivity.[2-4] As switch catalysis offers control over polymer molar mass and composition, these new polymers can then be optimised.

Work in Chapter 3 and 4 concluded that the inclusion of oligo(ethylene glycol) (PEG) or fluorinated side chain functionalities increased the Li-ion conductivity of poly(ester-*b*-carbonate) electrolytes. Therefore, it would be of interest to study a series of polymers with different types of oligomeric side chains: PEG, polyester, polycarbonate, fluorinated chains and alkyls, to observe the relationship between chemical structure and thermal and electrochemical properties. Alternative monomeric functionalities should be introduced to the lead polymers to observe if this improves their performance. Single Li-ion conducting polymer electrolytes tether the lithium salt's anion to the polymer chain, thus the Li-ion is solely responsible for ion transport and the Li-ion transference number can approach one. Therefore, anions should be introduced to the polymer backbone to observe how this improves electrochemical properties and battery performance.[5] Groups thought to improve adhesion, such as alcohol and carboxylic acids, can be incorporated to observe if this improves cycling performance by maintaining electrode contact; this could be tested at different stack pressures as many solid-state battery reports use stack pressures which are too high for practical or widespread adoption in an attempt to avoid contact loss.[6]

Polymer chain extension by polyurethane formation should be further explored and optimised. The optimum crosslink density would produce a polymer electrolyte with both mechanical integrity and processability, without compromise to Li-ion conductivity. The polymers studied in this thesis have been produced ex-situ, i.e., external to the battery. There is interest in producing polymers in-situ, to minimise solvent use and to improve cell performance by improving contact between components.[7] Switchable polymerization catalysis from an anhydride / epoxide / cyclic carbonate mixture, and polyurethane formation, can be

attempted in-situ to observe if this improves battery performance when compared to ex-situ approaches.

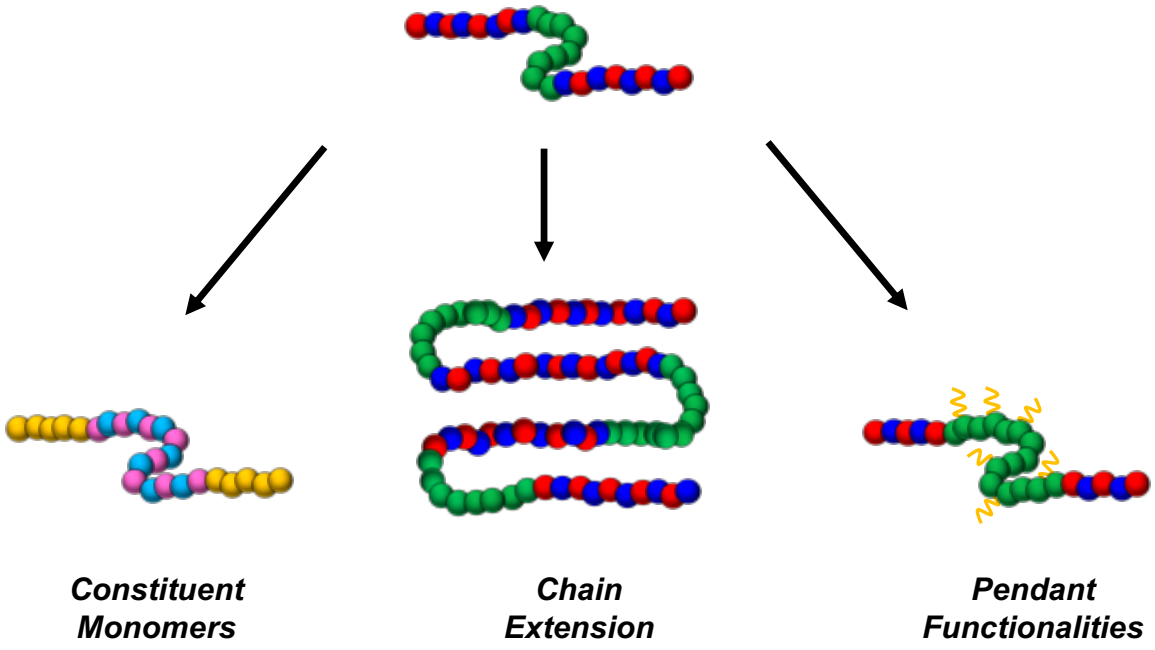


Figure 5.1. Strategies for producing new polymers for battery applications.

The lithium salt LiTFSI was primarily used in this work; it is widely use in polymer electrolyte research due to its thermal stability and effective charge delocalisation.[8] However, in Chapter 2, capacity retention was improved when an alternative salt was used, LiFSI. The effect of the salt on conductivity and cycling performance should be quantified and explained, to provide greater understanding and to aid optimisation of polymer electrolyte systems. $LiBF_4$, $LiCF_3SO_3$, $LiB(C_2O_4)_2$ (LiBOB) and $LiClO_4$ should be investigated; these salts regularly feature in polymer electrolyte studies and they may plasticise or rigidify the polymer to different extents and form different interfaces, thus affecting battery performance.[9-11] A post-mortem of the cell after cycling by X-ray photoelectron spectroscopy could identify the electrolyte interphase; perhaps the nature of this phase affects cycling performance.[12, 13]

The polymers studied in this thesis may be insufficiently conductive to be used as a standalone electrolyte. However, they could be an effective component of a solid composite electrolyte. Ceramic, or inorganic, electrolytes tend to have excellent ionic conductivity but poor processability and interfacial contact; the poly(ester-*b*-carbonate) electrolytes studied here had moderate ionic conductivity but can be readily processed and their excellent capacity retention suggests good interfacial contact.[14] A composite of these materials, therefore, could be applied as an electrolyte in all-solid-state batteries. Different polymer / inorganic ratios can be tested to find the optimum electrolyte, both for ionic conductivity and cycling performance.

There is pressure to reduce the cost and increase the capacity of Li-ion batteries, amidst concern regarding the abundance and global distribution of lithium and cobalt.[15] It would thus be wise to diversify and develop new battery chemistries. Sodium or potassium-ion batteries are purported as potential alternatives: they are more abundant in the Earth's crust (2.3 and 1.5 wt%, compared to 0.0017 wt% for Li); the raw materials are distributed worldwide; and they are cheaper than lithium.[16] There is a far smaller body of work for these chemistries, and indeed an even smaller body of work regarding polymers for these applications. The larger size of these cations presents challenges: volume change on cycling and ion diffusivity are both negatively affected.[16] Polymers should be developed and optimised for this specific application; it would be interesting to compare the optimum compositions for Li-, Na-, and K-ion batteries. Perhaps the polymers' mechanical properties – elasticity or adhesion – will be of greater importance when these larger cations are used.

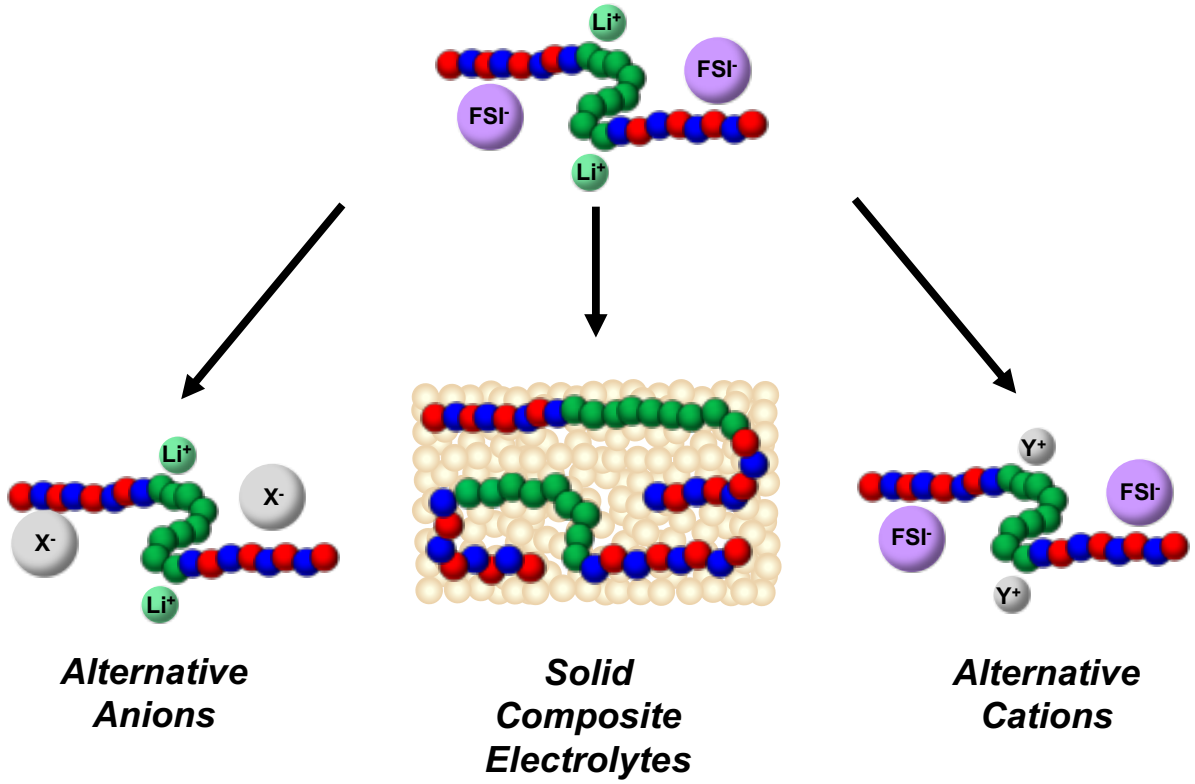


Figure 5.2. Strategies for producing new solid electrolytes for battery applications.

5.3. References

1. S. Paul, Y. Zhu, C. Romain, R. Brooks, P. K. Saini and C. K. Williams, *Chem. Commun.*, 2015, **51**, 6459-6479.
2. H. Xu, J. Xie, Z. Liu, J. Wang and Y. Deng, *MRS Energy Sustain.*, 2020, **7**, E2.
3. M. Watanabe, M. Togo, K. Sanui, N. Ogata, T. Kobayashi and Z. Ohtaki, *Macromolecules*, 1984, **17**, 2908-2912.
4. M. Lu, X. Zhu, X.-H. Li, X.-M. Yang and Y.-F. Tu, *Chinese J. Polym. Sci.*, 2017, **35**, 1051-1060.
5. D. Mecerreyes, L. Porcarelli and N. Casado, *Macromol. Chem. Phys.*, 2020, **221**, 1900490.
6. J. Janek and W. G. Zeier, *Nat. Energy*, 2023, **8**, 230-240.
7. C. Xuan, S. Gao, Y. Wang, Q. You, X. Liu, J. Liu, R. Xu, K. Yang, S. Cheng, Z. Liu and Q. Guo, *J. Power Sources*, 2020, **456**, 228024.
8. H. Zhang, Z. Song, W. Yuan, W. Feng, J. Nie, M. Armand, X. Huang and Z. Zhou, *ChemElectroChem*, 2021, **8**, 1322-1328.
9. C. Liu, X. Tang, Y. Wang, R. L. Sacci, W. Bras, J. K. Keum and X. C. Chen, *ACS Macro. Lett.*, 2022, **11**, 595-602.
10. Y. Zhao, Y. Bai, W. Li, M. An, Y. Bai and G. Chen, *Chem. Mater.*, 2020, **32**, 6811-6830.

11. Y. Tominaga, V. Nanthana and D. Tohyama, *Polym. J.*, 2012, **44**, 1155-1158.
12. S. Chattopadhyay, A. L. Lipson, H. J. Karmel, J. D. Emery, T. T. Fister, P. A. Fenter, M. C. Hersam and M. J. Bedzyk, *Chem. Mater.*, 2012, **24**, 3038-3043.
13. C. Xu, B. Sun, T. Gustafsson, K. Edström, D. Brandell and M. Hahlin, *J. Mater. Chem. A*, 2014, **2**, 7256-7264.
14. C. Yu, F. Zhao, J. Luo, L. Zhang and X. Sun, *Nano Energy*, 2021, **83**, 105858.
15. S. Sharma and A. Manthiram, *Energy Environ. Sci.*, 2020, **13**, 4087-4097.
16. K. Xi, X. Min, J. Xiao, M. Fang, W. Wang, Y. Zhao, Y.-g. Liu, A. Abdelkader, R. V. Kumar and Z. Huang, *Energy Environ. Sci.*, 2021, **14**, 2186-2243.

CHAPTER 6

Experimental

6.1. General

Materials. All solvents and reagents were purchased and used as obtained from commercial sources (Sigma Aldrich) unless stated otherwise. The synthesis of 4-tert-butyl-2,6-diformylphenol, $[H_4L](ClO_4)_2$ and H_2L were carried out in air. The synthesis of the catalyst, $[LZn_2(Ph)_2]$, monomer purification and subsequent polymerisations and depolymerisations were carried out under inert conditions using standard Schlenk line techniques and a nitrogen-filled glovebox. Vinyl cyclohexene oxide (98%, vCHO), ε-caprolactone (98%, ε-CL), HFA (97%) and ME_3MO were dried by stirring over CaH_2, distilled under reduced pressure (1 mbar at 40 °C for vCHO, 0.1 mbar at 60 °C for CL, 1 bar at 80 °C for HFA, 0.1 mbar at 90 °C for ME_3MO) and stored under nitrogen. Allyl glycidyl ether (99%, AGE) was distilled under reduced pressure (18 mbar at 60 °C) three times: firstly, it was dried by stirring over CaH_2 prior to distillation; secondly, it was dried over n-BuLi prior to distillation; thirdly, it was distilled without a drying agent. Diglycolic anhydride (97%, DGA) was obtained from Alfa Aesar and was recrystallised from acetic anhydride (twice) and sublimed under reduced pressure (twice, 60 °C, 0.1 mbar). 1,4-Benzene dimethanol (BDM) was recrystallised from toluene (three times) and stored under nitrogen. Diglyolic acid and hexafluoroglutaric acid were dried under vacuum at 80 °C prior to use. Trimethylene carbonate (98%, TMC) was purchased from TCI, recrystallised (dry Et_2O) under nitrogen and dried *in vacuo* before use. P_2-*t*-Bu was used as supplied, as a 2.0 M THF solution. $(PEG)_{12}$-MGE and $(PEG)_5$-MGE were purchased from Specific Polymers and were dried under vacuum at 80 °C prior to use. Research grade carbon dioxide (BOC, 99.99%) was passed through two drying columns (Micro Torr, Model number: MC1-804FV) prior to polymerisation. Single crystal NMC811 (MSE), Li_6PS_5Cl (MSE) and carbon nanofiber (Merck) were dried at 110 °C under vacuum (1×10^{-2} mbar).

6.2. Experimental Procedures

Synthesis of H_2L. The ligand was synthesised according to the published procedure.[1] $[H_4L](ClO_4)$ (5.0 g, 6.7 mmol) and MeOH (500 mL) were added to a round-bottom flask to obtain a red/orange solution. The solution was cooled to 0 °C, before the slow addition of $NaBH_4$ (7.58 g, 200 mmol) to yield a colourless solution. The solution was left stirring at room temperature, for 1 h, before water was added until precipitation was observed (400 mL). The resultant suspension was left standing for 10 h, before being filtered, washed with water and dried under vacuum (at 40 °C) to yield a white solid. The precipitate was crystallised from MeOH to yield white crystals (2.56 g, 4.63 mmol, 72%) (Figure 6.1).

^{1}H NMR (400 MHz, $CDCl_3$, 298 K): δ(ppm) = 6.93 (s, 4H, b), 3.73 (s, 8H, c), 2.52 (s, 8H, e), 1.25 (s, 18H, a), 1.01 (s, 12H, f).

Synthesis of $[LZn_2(Ph)_2]$ Catalyst. The catalyst was synthesised according to the published procedure.[1] Under anaerobic conditions, two separate solutions of $[H_2L]$ (0.40 g, 0.7 mmol) in THF (5 mL) and $ZnPh_2$ (0.25 g, 1.2 mmol) in THF (2 mL) were pre-cooled to -40 °C, before being added to a glass vial together to obtain a cloudy solution. The mixture was stirred for 25 h at 25 °C and filtered to obtain a white solid (260 mg, 0.31 mmol, 55%) (Figure 6.1).

^{1}H NMR (CD_2Cl_4, 400 MHz, 403 K): δ(ppm) = 7.40 (s, 5H, Ph), 7.00 (s, 4H, b), 4.81 (br m, 4 H, c), 3.37 (br d, 4H, d), 2.96 (br d, 4 H, f), 2.89 (br m, 4H, g), 2.47 (br m, 4H, e), 1.36 (s, 18H, a), 1.31 (s, 6H, h), 1.07 ppm (s, 6H, i).

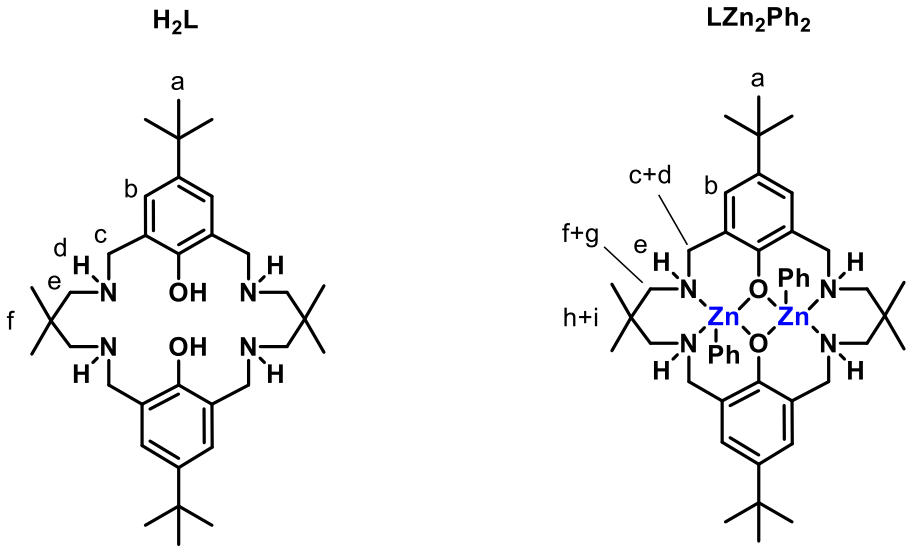


Figure 6.1. Structure of LH_2 and LZn_2Ph_2, with labelling corresponding to the ^1H NMR spectra assignment.

Synthesis of L_{van}AlOAc. The compound was synthesised according to the published procedure.[2] Under anaerobic conditions, $AlEt_3$ (162 mg, 1.42 mmol) was added to a stirring solution of $L_{van}H_2$ (500 mg, 1.35 mmol) in THF (5 mL) at ambient temperature and stirred for 2 hours. Glacial acetic acid was then added and the reaction was stirred for 16 hours at ambient temperature to form a yellow precipitate; which was isolated by centrifugation; washed with THF (1 × 10 mL) and hexane (1 × 10 mL); and dried under reduced pressure to yield [L_{van}AlOAc] as a pale-yellow precipitate (442 mg, 0.97 mmol, 72%) (Figure 6.2).

^1H NMR ($CDCl_3$, 400 MHz, 298 K): δ(ppm) = 8.10 (s, 2H, d), 6.92 (dd, 2H, c), 6.87, (dd, 2H, b), 6.62 (t, 2H, a), 3.87 (d, 2H, f), 3.80 (s, 6H, e), 3.28 (d, 2H, g), 2.03 (s, 3H, h), 1.14 (s, 3H, h), 0.93 (s, 3H, i).

Synthesis of [L_{van}AlK(OAc)$_2$] Catalyst. KOAc (95 mg, 0.97 mmol) was added to a stirring solution of [L_{van}AlOAc] (442 mg, 0.97 mmol) in chloroform at ambient temperature and stirred for 16 hours. The solution was then filtered and the solvent was removed under reduced pressure to yield [L_{van}AlK(OAc)$_2$] as a pale yellow powder (527 mg, 0.93 mmol, 96%) (Figure 6.2). The NMR spectra were consistent with those previously reported.[2]

^{1}H NMR ($CDCl_3$, 400 MHz, 298 K): δ(ppm) = 7.90 (s, 2H, d), 6.78 (dd, 2H, b), 6.63 (d, 2H, c), 6.52 (t, 2H, a), 3.75 (s, 4H, f), 3.39 (s, 6H, e), 1.53 (s, 6H, h), 1.20 (s, 6H, g).

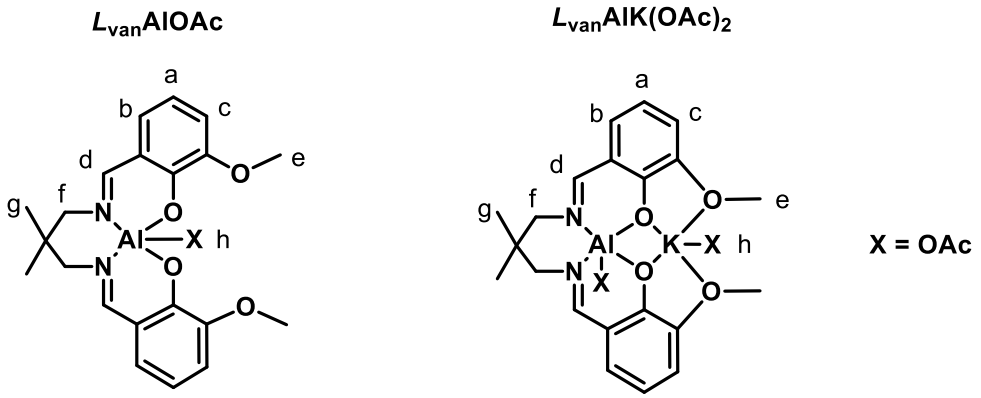


Figure 6.2. Structure of L_{van}AlOAc and L_{van}AlK(OAc)$_2$, with labelling corresponding to the ^{1}H NMR spectra assignment.

Synthesis of DTC. Under anaerobic conditions, CDI (12.6 g, 77.7 mmol) was added in six portions to a stirring solution of 2,2-dimethyl-1,3-propanediol (7.35 g, 70.6 mmol) in dry DCM (370 mL) over 2 hours and the reaction was stirred for a further 1 hour. The solution was washed (3 times with 1 M HCl), dried ($MgSO_4$), recrystallised (Et_2O) and sublimed under reduced pressure (0.1 mbar at 60 °C) (4.94 g, 38 mmol, 54%).

^{1}H NMR ($CDCl_3$, 400 MHz, 298 K): δ (ppm) = 4.06 (s, 4H), 1.11 (s, 6H).

Exemplar Switch Catalysis of vCHO, CO_2, TMC, and ε-CL. To a 100 mL Schlenk flask in a glove box (N_2 atmosphere), TMC (530 mg, 5.2 mmol), 1,4-BDM (11 mg, 0.08 mmol), ε-CL (2.30 mL, 20.8 mmol), vCHO (10.9 mL, 84 mmol), toluene (15 mL) and [LZn_2Ph_2] (20 mg, 0.024 mmol) were added. The flask was transferred to a triple manifold (vacuum/N_2/CO_2) Schlenk line and heated to 100 °C with rapid stirring. Once the temperature had reached 100 °C, the conditions were maintained for 1 h. The flask atmosphere was then switched from N_2 to CO_2, by partial removal of N_2, under vacuum, and refilling with 1 bar CO_2. After a further 22 h, the flask was cooled and exposed to air and the catalysis was quenched (benzoic acid in

chloroform). The conversion of ε-CL was determined by ^{1}H NMR spectroscopic analysis of the crude reaction mixture (92 % for ε-CL, 12% for vCHO, Figure 2.2). The reaction mixture was precipitated three times from methanol (3 × 200 mL) to yield a white gummy solid. The material was dried in vacuo and the triblock copolymer was isolated as a colourless solid (75%, 3.5 g) (Figure 6.3). Synthesis and characterisation data for all PvCHC-*b*-(CL-*r*-TMC)(-*b*-PvCHC) are detailed in Tables 6.1 and 6.2.

^{1}H NMR ($CDCl_3$, 400 MHz, 298 K): δ (ppm) = 7.32 (s, 2H, p), 5.74 (b s, 1*y*H, f), 5.01 (b s, 2*y*H, g), 4.87 (s, 1*y*H, a), 4.75 (s, 1*y*H, b), 4.15 (m, 0.2*x*(4H), m), 4.04 (t, 0.8*x*(2H), h), 2.41 (b s, 1*y*H, e), 2.28 (m, 0.2*x*(2H), l), 1.99 (m, 0.2*x*(2H), n), 1.83 (s, 4*y*H, c), 1.63 (b m, 0.8*x*(4H), i+k), 1.53 (b m, 0.2*x*(2H), n), 1.38 (b m, 0.8*x*(2H), j). SEC (THF, PS calib.): M_n = 35 kg mol^{-1}, Đ = 1.89.

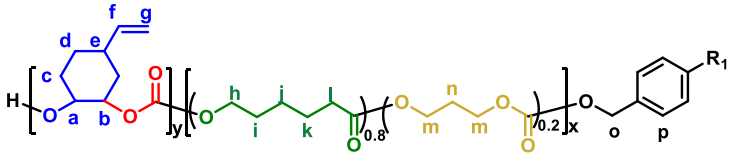


Figure 6.3. Structure of PvCHC-*b*-P(CL-*r*-TMC)-R_1, where R_1 corresponds to -CH_3 or CH_2-O-P(CL-*r*-TMC-*b*-vCHC), with labelling corresponding to the ^{1}H NMR spectra assignment.

Table 6.1. Reagent Quantities for the Synthesis of PvCHC-*b*-(CL-*r*-TMC)(-*b*-PvCHC).

Entry [a]	CTA [b] (mmol)	CL [c] (mmol)	TMC [c] (mmol)	vCHO [c] (mmol)	vCHO conversion [d] (%)
AB(26, 0.45)	0.154	17.6	4.4	84.0	15
AB(32, 0.51)	0.125	15.7	3.9	84.0	25
AB(45, 0.47)	0.089	17.0	4.2	84.0	15
AB(69, 0.58)	0.058	15.4	3.8	84.0	19
ABA(35, 0.52)	0.114	15.4	3.8	84.0	22
ABA(44, 0.53)	0.091	15.1	3.8	84.0	25
ABA(50, 0.47)	0.080	11.2	2.8	84.0	29
ABA(66, 0.52)	0.061	15.4	3.8	84.0	23
ABA(51, 0.26)	0.078	23.7	5.9	84.0	8
ABA(47, 0.30)	0.085	22.4	5.6	84.0	10
ABA(50, 0.35)	0.080	20.8	5.2	84.0	12
ABA(50, 0.62)	0.067	12.2	3.0	84.0	16

In all instances, 0.024 mmol of [LZn_2Ph_2] was used and 90–92% ε-CL was achieved. [a] Polymers labelled as ABA/AB (M_n, w_{PC}) where M_n = overall molar mass in kg mol^{-1} and w_{PC} = weight fraction of PvCHC; [b]

Quantity of chain transfer agent (CTA). Benzene dimethanol (BDM) was used to make triblock copolymers, methylbenzylalcohol (MeBnOH) was used to make diblock copolymers; [c] Quantity of CL, TMC and VCHO in the reaction mixture; [d] vCHO conversion at the end of the polymerisation, calculated by comparing the vCHO (3.20 ppm) and PvCHC (4.87 ppm) signals in the crude ^{1}H NMR spectra.

Table 6.2. Characterisation Data for PvCHC-*b*-(CL-*r*-TMC)(-*b*-PvCHC).

Entry [a]	Yield (%) [b]	DP_{PC}-DP_{PE}-DP_{PC} (calc) [c]	DP_{PC}-DP_{PE}-DP_{PC} (NMR) [d]	$M_{n,NMR,ABA}$ [d] (kg mol^{-1})	$M_{n,NMR}$ [d] (kg mol^{-1})	$M_{n,SEC}$ [e] (kg mol^{-1}) [Đ]
AB(26, 0.45)	75	88-152	77-139	13-15	26	26 [1.63]
AB(32, 0.51)	80	106-160	95-152	16-16	32	9 [1.80]
AB(45, 0.47)	80	100-151	71-120	12-13	45	45 [1.52]
AB(69, 0.58)	84	497-586	524-593	88-64	69	69 [1.68]
ABA(35, 0.52)	75	52-144-52	54-157-54	9-17-9	35	29 [1.69]
ABA(44, 0.53)	78	70-182-70	71-194-71	12-21-12	44	47 [1.56]
ABA(50, 0.47)	75	73-274-73	71-250-71	12-27-12	50	40 [2.03]
ABA(66, 0.52)	82	99-258-99	101-266-101	17-29-17	66	45 [1.58]
ABA(51, 0.26)	75	47-366-47	42-352-42	7-38-7	51	28 [1.75]
ABA(47, 0.30)	78	46-323-46	42-315-42	7-34-7	47	49 [1.52]
ABA(50, 0.35)	75	55-359-55	54-306-54	9-33-9	50	35 [1.89]
ABA(50, 0.62)	82	85-176-85	95-176-95	16-19-16	50	50 [1.85]

[a] Polymers labelled as ABA/AB (M_n, w_{PC}) where M_n = overall molar mass in kg mol^{-1} and w_{PC} = weight fraction of PvCHC.*)*; [b] Yield of the polymerisation, considering the mass of monomers used and the monomer conversions achieved vs the mass of polymer obtained after purification. [c] Calculated from the initial [CL + TMC + VCHO]$_0$/[BDM]$_0$ ratio and the monomer conversions; [d] Determined from the ^{1}H NMR spectra of the purified polymer by integration of the aromatic initiator resonance (7.34 ppm for 1,4-BDM, 7.17 ppm for Me-BnOH) against those of PvCHC (5.76 ppm) and P(CL-*r*-TMC) (2.00, 1.38 ppm); [e] M_n of the overall block copolymer determined by SEC with THF eluent, calibrated using PS standards.

Exemplar Catalysis of DGA and ME_3MO. To a 4 mL reaction vessel in a glovebox (N_2 atmosphere), DGA (140 mg, 1.21 mmol) was added to diglycolic acid (5.4 mg, 0.04 mmol), followed by dry degassed toluene (2 mL), ME_3MO (275 mg, 1.25 mmol) and P_2-*t*-Bu (2.0 M THF solution, 2.5 μL, 0.005 mmol). The reaction vessel was heated to 100 °C, with rapid stirring. After 16 h the reaction vessel was exposed to air, the catalysis was quenched (acetic acid) and the polymer solution was concentrated. The conversion of DGA and ME_3MO were determined by ^{1}H NMR spectroscopic analysis of the crude reaction mixture (100 % for DGA

and ME_3MO). The reaction mixture was precipitated three times from hexane (3 × 50 mL) and dried in vacuo to isolate the viscous polymer (310 mg, 75% yield) (Figure 6.4).

^{1}H NMR ($CDCl_3$, 400 MHz, 298 K): δ (ppm) = 5.28 (s, 1*x*H, e), 4.46 (m, 1*x*H, f), 4.24 (b m, 5*x*H, f+g), 4.00 (s, 1H, e (end group)), 3.64 (b m, 14*x*H, b+c+d), 3.38 (s, 3*x*H, a). SEC (THF, PS calib.): M_n = 3.0 kg mol^{-1}, $Đ$ = 1.42.

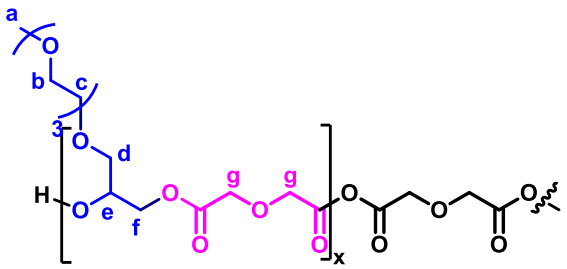


Figure 6.4. Structure of P(DGA-*alt*-ME_3MO), with labelling corresponding to the ^{1}H NMR spectra assignment.

Exemplar Catalysis of HFA and ME_3MO. To a 4 mL reaction vessel in a glovebox (N_2 atmosphere), HFA (266 mg, 1.21 mmol) was added to hexafluoroglutaric acid (9.6 mg, 0.04 mmol), followed by dry degassed toluene (2 mL), ME_3MO (275 mg, 1.25 mmol) and P_2-*t*-Bu (2.0 M THF solution, 2.5 µL, 0.005 mmol). The reaction vessel was heated to 100 °C, with rapid stirring. After 1 h the reaction vessel was exposed to air, the catalysis was quenched (acetic acid) and the polymer solution was concentrated. The conversion of ME_3MO was determined by ^{1}H NMR spectroscopic analysis of the crude reaction mixture; the conversion of HFA was determined by ^{19}F NMR spectroscopic analysis (100 % for HFA and ME_3MO). The reaction mixture was precipitated three times from hexane (3 × 50 mL) and dried in vacuo to isolate the viscous polymer (405 mg, 75% yield) (Figure 6.5). Synthesis and characterisation data for all polyesters synthesised in Chapter 3 are detailed in Tables 6.3 and 6.4.

^{1}H NMR ($CDCl_3$, 400 MHz, 298 K): δ (ppm) = 5.45 (s, 1*x*H, e), 4.68–4.41 (m, 2*x*H, f), 4.00 (s, 1H, e (end group)), 3.64 (b m, 14*x*H, b+c+d), 3.38 (s, 3*x*H, a). ^{19}F NMR ($CDCl_3$, 400 MHz,

298 K): δ (ppm) = -118.3 (b m, 4*x*F, -C**F**$_2$CF$_2$C**F**$_2$-), -123.8 (b m, 2*x*F -CF$_2$C**F**$_2$CF$_2$-). SEC (THF, PS calib.): M_n = 1.2 kg mol^{-1}, $Đ$ = 1.34.

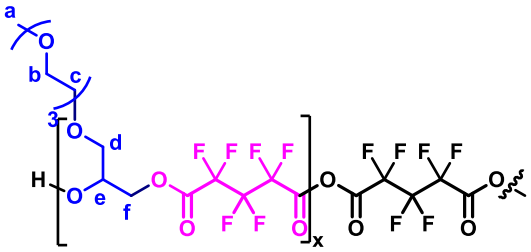


Figure 6.5. Structure of P(HFA-*alt*-ME$_3$MO), with labelling corresponding to the ^{1}H NMR spectra assignment.

Table 6.3. Reaction Conditions for the Polyesters Synthesised in Chapter 3.

Anhydride [a]	Anhydride [a] (mmol)	Epoxide [b]	Epoxide [b] (mmol)
DGA	1.21	ME$_3$MO	1.26
HFA	1.21	ME$_3$MO	1.25
DGA	1.21	(PEG)$_5$-MGE	1.25
HFA	1.21	(PEG)$_5$-MGE	1.25
DGA	1.21	(PEG)$_{12}$-MGE	1.25
HFA	1.21	(PEG)$_{12}$-MGE	1.25

In all instances, the amount of P$_2$-*t*-Bu, initiator and THF was 0.005 mmol, 0.04 mmol and 2 mL respectively. DGA conversion was 100% and epoxide conversion was >96%. When the anhydride was DGA, diglycolic acid was used as the initiator; when the anhydride was HFA, hexafluoroglutaric acid was used as the initiator; [a] Identity and quantity of the anhydride; [b] Identity and quantity of the epoxide.

Table 6.4. Characterisation Data for the Polyesters Synthesised in Chapter 3.

Anhydride	Epoxide	DP (calc) [a]	$M_{n,th}$ (kg mol^{-1}) [a]	DP (NMR) [b]	$M_{n,NMR}$ (kg mol^{-1}) [b]	$M_{n,SEC}$ (kg mol^{-1}) [c]
DGA	ME$_3$MO	30	10.0	15	5.0	3.0 [1.42]
HFA	ME$_3$MO	30	13.3	13	5.7	1.2 [1.34]
DGA	MGE-(PEG)$_5$	30	12.5	26	10.8	1.5 [1.25]
HFA	MGE-(PEG)$_5$	30	15.7	15	7.8	1.6 [1.77]
DGA	MGE-(PEG)$_{12}$	30	21.5	26	18.6	2.5 [1.34]
HFA	MGE-(PEG)$_{12}$	30	24.7	15	12.3	2.5 [1.58]

All polymerisations conducted at 100 °C under an anaerobic atmosphere, using a catalyst/CTA/anhydride/epoxide ratio of 1/8/240/250 and P$_2$-*t*-Bu catalyst of 2 mM concentration in toluene in all cases; the CTA was diglycolic acid when the anhydride was DGA; the CTA was hexafluoroglutaric acid when the anhydride was HFA; [a] DP and M_n as estimated by the initial reagent ratios and monomer conversions, where DGA conversion was monitored by comparing the monomeric signal at 4.41 ppm to the polymeric signal at 4.21 ppm, epoxide conversion was

determined by comparing the monomeric signal at 3.21 ppm to the polymeric signal at 5.36 ppm; [b] DP_n and M_n as determined from the ^{1}H NMR spectra of the purified polymer by integration of the polymeric end group resonance at 3.98 ppm against those of the polyester (5.28 – 4.24 ppm); [c] Determined by SEC using THF eluent and calibrated against narrow PS standards.

Exemplar Switch Catalysis of DGA, ME$_3$MO and DTC. To a 4 mL reaction vessel in a glovebox (N_2 atmosphere), DTC (202 mg, 1.55 mmol) and DGA (140 mg, 1.20 mmol) were added to diglycolic acid (5.4 mg, 0.04 mmol), followed by dry degassed toluene (2 mL), ME$_3$MO (275 mg, 1.25 mmol) and P_2-*t*-Bu (2.0 M THF solution, 2.5 µL, 0.005 mmol). The reaction vessel was heated to 100 °C, with rapid stirring. After 40 h the reaction vessel was exposed to air, the catalysis was quenched (acetic acid) and the polymer solution was concentrated. The conversion of DGA, ME$_3$MO and DTC were determined by ^{1}H NMR spectroscopic analysis of the crude reaction mixture (100 % for DGA, 72% for DTC, 100% for ME$_3$MO). The reaction mixture was precipitated three times from hexane (3 × 50 mL) and dried in vacuo to isolate the viscous polymer (400 mg, 75% yield) (Figure 6.6).

^{1}H NMR ($CDCl_3$, 400 MHz, 298 K): δ (ppm) = 5.28 (s, 1*x*H, g), 4.46 (m, 1*x*H, h), 4.24 (b m, 5*x*H, h+i), 3.96 (s, 4*y*H, a), 3.64 (b m, 14*x*H, d+e+f), 3.38 (s, 3*x*H, c), 0.98 (b m, 6*y*H, b), 0.84 (b m, 6H, b (end group)). SEC (THF, PS calib.): M_n = 3.5 kg mol^{-1}, $Đ$ = 1.36.

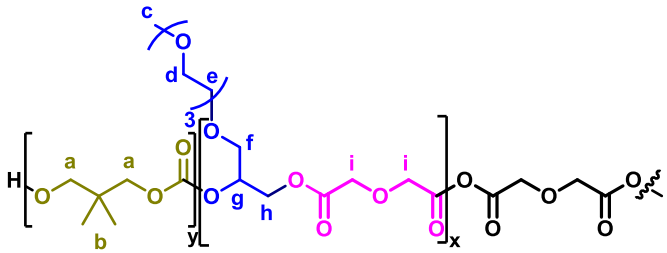


Figure 6.6. Structure of PDTC-*b*-P(DGA-*alt*-ME$_3$MO)-*b*-PDTC, with labelling corresponding to the ^{1}H NMR spectra assignment.

Exemplar Switch Catalysis of HFA, ME$_3$MO and DTC. To a 4 mL reaction vessel in a glovebox (N_2 atmosphere), DTC (202 mg, 1.55 mmol) and HFA (266 mg, 1.20 mmol) were added to hexafluoroglutaric acid (9.6 mg, 0.04 mmol), followed by dry degassed toluene

(2 mL), ME_3MO (275 mg, 1.25 mmol) and P_2-*t*-Bu (2.0 M THF solution, 2.5 µL, 0.005 mmol). The reaction vessel was heated to 100 °C, with rapid stirring. After 40 h the reaction vessel was exposed to air, the catalysis was quenched (acetic acid) and the polymer solution was concentrated. The conversions of ME_3MO and DTC were determined by ^{1}H NMR spectroscopic analysis of the crude reaction mixture; the conversion of HFA was determined by ^{19}F NMR spectroscopic analysis (100 % for HFA, 72% for DTC, 100% for ME_3MO). The reaction mixture was precipitated three times from hexane (3 × 50 mL) and dried in vacuo to isolate the viscous polymer (510 mg, 75% yield) (Figure 6.7). Synthesis and characterisation data for all block copolymers synthesised in Chapter 3 are detailed in Tables 6.5 and 6.6.

^{1}H NMR ($CDCl_3$, 400 MHz, 298 K): δ (ppm) = 5.45 (s, 1*x*H, g), 4.68–4.17 (m, 2*x*H, h), 3.96 (s, 4*y*H, a), 3.64 (b m, 14*x*H, d+e+f), 3.38 (s, 3*x*H, c), 1.00 (b m, 6*y*H, b), 0.84 (b m, 6H, b (end group)). ^{19}F NMR ($CDCl_3$, 400 MHz, 298 K): δ (ppm) = -118.3 (b m, 4*x*F, -C**F$_2$**CF_2C**F$_2$**-), -123.8 (b m, 2*x*F -CF_2C**F$_2$**CF_2-). SEC (THF, PS calib.): M_n = 2.9 kg mol^{-1}, $Đ$ = 1.89.

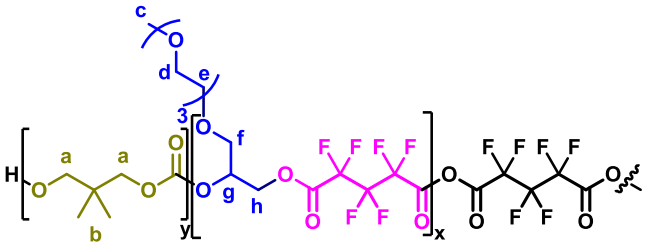


Figure 6.7. Structure of PDTC-*b*-P(HFA-*alt*-ME_3MO)-*b*-PDTC, with labelling corresponding to the ^{1}H NMR spectra assignment.

Table 6.5. Reaction Conditions for the Synthesis of the Block Copolymers in Chapter 3.

Anhydride [a]	Anhydride [a] (mmol)	Epoxide [b]	Epoxide [b] (mmol)	DTC [c] (mmol)
DGA	1.21	ME_3MO	1.25	1.15
HFA	1.21	ME_3MO	1.25	1.55
DGA	1.21	$(PEG)_5$-MGE	1.25	1.40
HFA	1.21	$(PEG)_5$-MGE	1.25	1.8
DGA	1.21	$(PEG)_{12}$-MGE	1.25	2.48
HFA	1.21	$(PEG)_{12}$-MGE	1.25	2.85

For all entries, the amount of P_2-*t*-Bu, initiator and toluene was 0.005 mmol, 0.04 mmol and 2 mL respectively. When the anhydride was DGA, diglycolic acid was used as the initiator; when the anhydride was HFA, hexafluoroglutaric acid was used as the initiator. In all instances, anhydride conversion was 100%, epoxide

conversion was >96%, and DTC conversion was 72–75%. [a] Identity and quantity of the anhydride; [b] Identity and quantity of the epoxide. [c] Quantity of DTC.

Table 6.6. Characterisation Data for the Block Copolymers Synthesised in Chapter 3.

Anhydride	Epoxide	DP_{PC}-DP_{PE}-DP_{PC} (calc) [a]	$M_{n,th}$ (kg mol^{-1}) [a]	DP_{PC}-DP_{PE}-DP_{PC} (NMR)[b]	$M_{n,NMR}$ (kg mol^{-1}) [b]	Hard wt fraction [b]	$M_{n,SEC,\ THF}$ (kg mol^{-1}) [c]
DGA	ME_3MO	10-30-10	12.5	8-22-8	9.3	0.22	3.5 [1.36]
HFA	ME_3MO	13-30-13	16.6	5-14-5	7.8	0.18	2.9 [1.89]
DGA	MGE-$(PEG)_5$	12-30-12	15.5	6-20-6	9.9	0.16	2.5 [1.46]
HFA	MGE-$(PEG)_5$	15-30-15	19.5	11-28-11	17.5	0.17	3.5 [1.52]
DGA	MGE-$(PEG)_{12}$	21-30-21	27.0	6-7-6	6.5	0.24	3.8 [1.26]
HFA	MGE-$(PEG)_{12}$	21-30-21	31.0	7-6-7	6.8	0.26	2.1 [1.41]

All polymerisations conducted at 100 °C under an anaerobic atmosphere, using a catalyst/CTA/anhydride/epoxide/DTC ratio of 1/8/240/250/X, where X is varied between 231 and 570 to target 0.20 hard weight block (P(DTC)) fraction. P_2-*t*-Bu catalyst was used at 2 mM concentration in toluene in all cases. When the anhydride was DGA, diglycolic acid was used as the initiator; when the anhydride was HFA, hexafluoroglutaric acid was used as the initiator. [a] M_n and DP as estimated by the initial reagent ratios and monomer conversions, where DGA conversion was monitored by comparing the monomeric signal at 4.41 ppm to the polymeric signal at 4.21 ppm, epoxide conversion was determined by comparing the monomeric signal at 3.21 ppm to the polymeric signal at 5.45 ppm, and DTC conversion was monitored by comparing the monomeric signal at 1.10 ppm to the polymeric signal at 0.97 ppm; [b] M_n, DP and hard weight fraction as determined from the ^{1}H NMR spectra of the purified polymers by integration of the polycarbonate end group signal (0.92 ppm) against those of the polyester (5.28, 4.46, 4.25, 3.64–3.37 ppm) and polycarbonate (3.96, 0.99 ppm); [c] Determined by SEC using THF eluent and calibrated against narrow PS standards.

Exemplar Switch Catalysis of DGA, AGE and DTC. To an 8 mL reaction vessel in a glovebox (N_2 atmosphere), DTC (543 mg, 4.18 mmol) and DGA (970 mg, 8.36 mmol) were added to 1,4-BDM (21 mg, 0.15 mmol), followed by dry degassed toluene (2 mL), AGE (2.30 mL, 19.76 mmol) and [L_{van}AlK(OAc)$_2$] (20 mg, 0.038 mmol). The reaction vessel was heated to 100 °C, with rapid stirring. After 24 h, the reaction vessel was exposed to air, the catalysis was quenched (acetic acid) and the polymer solution was concentrated. The conversions of

DGA and DTC were determined by ^{1}H NMR spectroscopic analysis of the crude reaction mixture (100% for DGA, 70–72% for DTC). The reaction mixture was precipitated three times from diethyl ether (3 × 50 mL), dialysed with H_2O and dried in vacuo to isolate the viscous polymer (1.08 g, 80% yield) (Figure 6.8). Synthesis and characterisation data for all poly(DTC-*b*-DGA-*alt*-AGE-*b*-DTC)s are detailed in Tables 6.7 and 6.8.

^{1}H NMR ($CDCl_3$, 400 MHz, 298 K): δ (ppm) = 7.34 (s, 2H, k), 5.83 (m, 1*x*H, d), 5.27–5.17 (m, 3*x*H, c+g), 4.45 (d, 1*x*H, h), 4.23 (b m, 5*x*H, h+i), 3.95 (m, 4*y*H+2*x*H, a+e), 3.56 (d, 2*x*H, f), 0.96 (b m, 6*y*H, b). SEC (THF, PS calib.): M_n = 4.8 kg mol^{-1}, $Đ$ = 1.67.

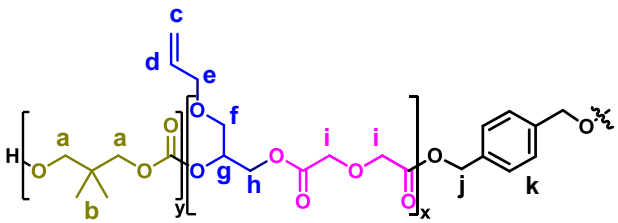


Figure 6.8. Structure of PDTC-*b*-P(AGE-*alt*-DGA)-*b*-PDTC, with labelling corresponding to the ^{1}H NMR spectra assignment.

Table 6.7. Reagent Quantities for the Synthesis of P(DTC-*b*-DGA-*alt*-AGE-*b*-DTC).

Entry [a]	DTC [b] (mmol)	DGA [b] (mmol)	AGE [b] (mmol)	AGE conversion [c] (%)
ABA(4, 0.20)	2.28	3.42	19.76	17
ABA(9, 0.22)	4.18	8.36	19.76	42
ABA(18, 0.20)	8.36	16.72	19.76	85
ABA(9, 0.43)	9.12	5.70	19.76	30
ABA(15, 0.47)	17.56	12.54	19.76	62

[a] Entries named *ABA(XX, 0.YY)* for triblock copolymers where *XX* is $M_{n,NMR}$ and *0.YY* is the hard wt. fraction. For all entries, the amount of $L_{van}AlK(OAc)_2$ and BDM was 0.038 and 0.15 mmol, and the conversion of DTC was 70–72%, and DGA was 100%; [b] Quantity of DTC, DGA and AGE. [c] Conversion of AGE, calculated by comparing the AGE (3.68 ppm) and P(DGA-*alt*-AGE) (3.55 ppm) signals in the crude ^{1}H NMR spectra

Table 6.8. Characterisation Data for P(DTC-*b*-DGA-*alt*-AGE-*b*-DTC).

Entry [a]	DP_{PC}-DP_{PE}-DP_{PC} (calc) [b]	$M_{n,th}$ [b] (kg mol^{-1})	DP_{PC}-DP_{PE}-DP_{PC} (NMR) [c]	$M_{n,NMR}$ [c] (kg mol^{-1})	Hard wt. fraction [c]	$M_{n,SEC,THF}$ [d] (kg mol^{-1}) [Đ]
ABA(4, 0.20)	4 – 15 – 4	4.5	3 – 13 – 3	3.8	0.20	3.5 [1.51]
ABA(9, 0.22)	8 – 37 – 8	10.6	7 – 30 – 7	8.7	0.22	4.8 [1.67]

ABA(18, 0.20)	16 – 73 – 16	21.0	14 – 62 – 14	17.9	0.20	6.7 [1.63]
ABA(9, 0.43)	17 – 25 – 17	10.2	15 – 22 – 15	9.0	0.43	5.7 [1.45]
ABA(19, 0.47)	28 – 55 – 28	19.9	27 – 53 – 27	19.2	0.47	6.5 [1.60]

[a] Entries named *ABA(XX, 0.YY)* for triblock copolymers where *XX* is $M_{n,NMR}$ and *0.YY* is the hard wt. fraction. [b] M_n and DP as calculated by the initial reagent ratios and monomer conversions, where DGA conversion was monitored by comparing the monomer signal at 4.41 ppm to the polymer signal at 4.21 ppm, AGE conversion was determined by comparing the monomer signal at 3.68 ppm to the polymer signal at 3.55 ppm and DTC conversion was determined by comparing the monomer signal at 1.10 ppm to the polymer signal at 0.97 ppm; [c] DP_n, M_n and hard weight fraction as determined from the ^{1}H NMR spectra of the purified polymer by integration of the aromatic initiator resonance (7.34 ppm for 1,4-BDM) against those of P(DGA-*alt*-AGE) (4.19, 3.52 ppm) and P(DTC) (0.92 ppm); [d] Determined by SEC, using THF eluent and calibrated against narrow PS standards.

^{31}P{^{1}H} NMR Spectroscopy for Polymer End-group Titration. A reported procedure for the analysis of hydroxyl end-groups was followed.[3] The polymer sample (40 mg) and stock solution (40 μL), in $CDCl_3$ (0.7 mL) were mixed in a 2 mL vial. Excess 2-chloro-4,4,5,5-tetramethyldioxaphospholane (40 μL) was then added to the vial and shaken to combine. The mixture was analysed by ^{31}P{^{1}H} NMR spectroscopy. The contents of the stock solution were bisphenol A (400 mg), $Cr(acac)_3$ (5.5 mg) and pyridine (10 mL).

Polymer Cross-Linking. Under anaerobic conditions, poly(DTC-*b*-DGA-*alt*-AGE-*b*-DTC) (986 mg, 0.0548 mmol, 1 eq.) was dissolved in DMF (0.1 M, 0.5 mL). Isophorone diisocyanate (IPDI, 35 μL, 0.16 mmol, 3 eq.) and dibutyltin dilaurate (DBTDL, 1 mg) were added and stirred at 85 °C for 3 h. Then, 1,6-hexanediol (13 mg, 0.11 mmol, 2 eq.) was added and the solution was stirred for a further 3 h. The polymer solution was exposed to air, concentrated and precipitated from diethyl ether to isolate the polymer in high yield (>95%) as a gummy free-standing solid.

Representative Thiol-ene Post-polymerisation Functionalisation. Under anaerobic conditions, poly(DTC-*b*-DGA-*alt*-AGE-*b*-DTC) (200 mg, 0.76 mmol, 1 eq.) was dissolved in

THF (4 mL). 2,2-Dimethoxyphenylacetophenone (DMPA) (38 mg, 0.15 mmol, 0.2 eq.) and thiol (1.48 mmol, 2 eq.) were added to the solution. The vial was stirred under UV irradiation (λ = 365 nm) for 2 hours, at which point the reaction was quenched by exposure to air. The crude material was precipitated from diethyl ether (3×20 mL) filtered and dried in vacuo to isolated the functionalised polymer in high yield (>95%) (Figure 6.9).

When thiol = 2,2,2-trifluoroethanethiol (CF_3): ^{1}H NMR ($CDCl_3$, 400 MHz, 298 K): δ (ppm) = 7.34 (s, 2H, k), 5.27 (s, 1*x*H, g), 4.45 (d, 1*x*H, h), 4.23 (b m, 5*x*H, h+i), 3.95 (m, 4*y*H+2*x*H, a+e), 3.56 (m, 2*x*H, f), 3.08 (q, 2*x*H, l), 2.73 (t, 2*x*H, c), 1.84 (b m, 2*x*H, d), 0.96 (b m, 6*y*H, b). SEC (THF, PS calib.): M_n = 12.7 kg mol^{-1}, $Đ$ = 1.43.

When thiol = 3-mercaptopropanenitrile (nitrile): ^{1}H NMR ($CDCl_3$, 400 MHz, 298 K): δ (ppm) = 7.34 (s, 2H, k), 5.27 (s, 1*x*H, g), 4.45 (d, 1*x*H, h), 4.23 (b m, 6*x*H, h+i), 3.95 (m, 4*y*H+2*x*H, a+e), 3.56 (m, 2*x*H, f), 2.95–2.67 (m, 6*x*H, c+l+m), 1.84 (b m, 2*x*H, d), 0.96 (b m, 6*y*H, b). SEC (THF, PS calib.): M_n = 6.8 kg mol^{-1}, $Đ$ = 1.47.

When thiol = 3-mercaptotetrahydrothiophene 1,1-dioxide (sulfone): ^{1}H NMR ($CDCl_3$, 400 MHz, 298 K): δ (ppm) = 7.34 (s, 2H, k), 5.27 (s, 1*x*H, g), 4.45 (d, 1*x*H, h), 4.23 (b m, 6*x*H, h+i), 3.95 (m, 4*y*H+2*x*H, a+e), 3.56 (m, 2*x*H, f), 3.31–2.97 (m, 5*x*H, m+l+o), 2.67 (t, 2*x*H, c), 2.57 (b m, 1*x*H, n), 2.13 (b m, 1*x*H, n), 1.85 (b m, 2*x*H, d), 0.96 (b m, 6*y*H, b). SEC (THF, PS calib.): M_n = 5.8 kg mol^{-1}, $Đ$ = 1.27.

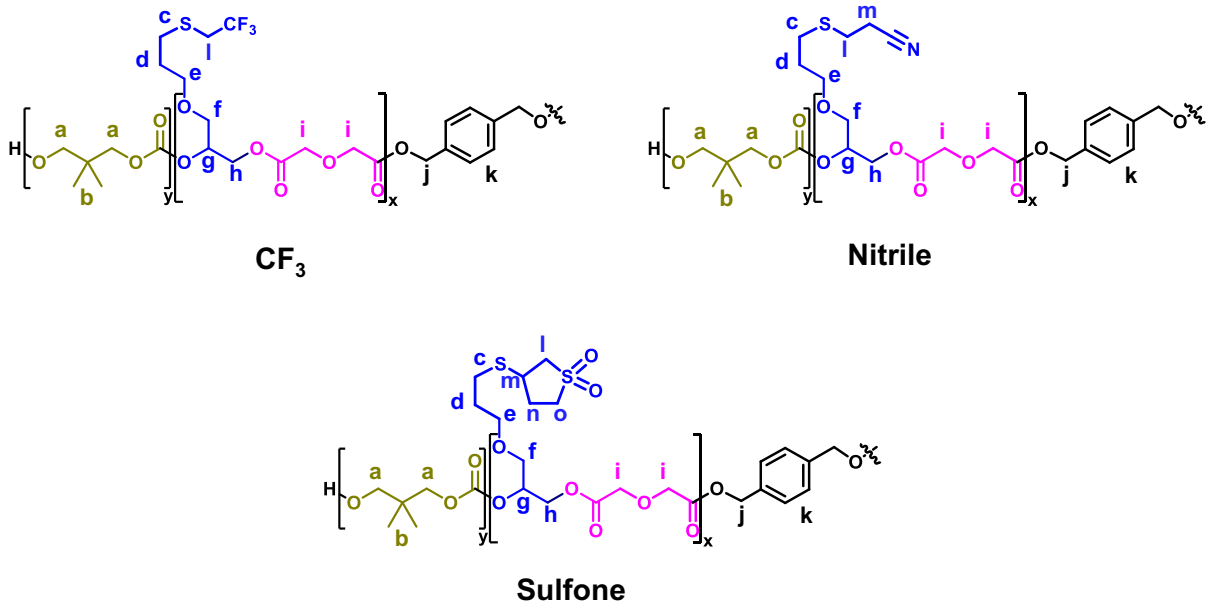


Figure 6.9. Structure of PDTC-*b*-P(AGE-*alt*-DGA)-*b*-PDTC with CF_3, nitrile, and sulfone functionalities incorporated, with labelling corresponding to the ^{1}H NMR spectra assignment.

6.3. Analytical Techniques

Nuclear Magnetic Resonance (NMR). ^{1}H, ^{19}F and $^{31}P\{H\}$ NMR spectra were obtained using a Bruker AVIII HD 400 NMR spectrometer. $^{13}C\{H\}$ NMR spectra were obtained using a Bruker AVII 500 NMR spectrometer.

Size Exclusion Chromatography (SEC). Data was obtained using a Shimadzu LC-20AD instrument, equipped with Refractive Index (RI) and UV-Vis detectors and two PSS SDV 5 µm linear M columns. HPLC grade THF was used as the eluent, flowing at 1.0 mL min^{-1}, at 30 °C. Monodisperse polystyrene standards were used for calibration. Samples were passed through 0.2 µm syringe filters prior to analysis.

Differential Scanning Calorimetry (DSC). A DSC3+ (Mettler-Toledo Ltd) instrument was used. A sealed, empty crucible was used as a reference and the DSC was calibrated using zinc and indium standards. Samples were cooled, from 25 °C to -80 °C, at a rate of 20 °C min^{-1}, under a N_2 flow (80 mL min^{-1}), followed by a 5-minute isotherm, at -80 °C. Samples were then heated to 200 °C, at a rate of 20 °C min^{-1}; kept at 200°C for a further 5 minutes; followed by a

cooling-heating procedure from 200 °C to -80 °C, at 10 °C min^{-1}. Glass transition temperatures (T_g) are reported as the midpoint of the transition taken from the second cycle.

Thermal Gravimetric Analysis (TGA). Data was collected on a TGA5500 System (TA Instruments), equipped with the TRIOS software package. For determination of thermal stability, polymer samples were heated from 30 to 500 °C, at a rate of 5 °C min^{-1}, under an N_2 flow (100 mL min^{-1}).

Rheology. Oscillatory rheology measurements were conducted on an ARES-G2 instrument (TA Instruments) equipped with 8 mm parallel plates. Frequency sweep analysis was conducted, at 10 °C intervals, between 30 and 130 °C, with $\gamma = 1\%$, and a logarithmic frequency ramp between 0.1 Hz and 100 Hz – under these conditions, the polymer was in its linear viscoelastic region. Temperature sweep analyses were conducted between 30 and 120 °C, with $\gamma = 1\%$, at an oscillation frequency of 1 Hz.

Tensile testing. Dumb-bell specimens were cut according to ISO 527-2, specimen type 5B with Zwick ZCP020 cutting press (length = 35 mm, gauge length = 10 mm, width = 2 mm). Uniaxial extension measurements were carried out on a Shimadzu EZ-LZ Universal testing instrument, at an extension rate of 10 mm min^{-1} to derive stress-strain relationships.

Electrochemical Impedance Spectroscopy (EIS). Ionic conductivity was measured by impedance spectroscopy using an MTZ-35 Impedance Analyzer (Biologic), over the frequency range 10 MHz – 0.01 Hz, with the amplitude set to 10 mV. The electrolytes were sandwiched between gold electrodes in a controlled environment sample holder which was then enclosed in an intermediate temperature system. Measurements were taken at 10 °C intervals, between 20 and 70 °C. The samples were equilibrated at each temperature for 20 min before a new recording was made. The resistance was calculated with EC-Labs, using a modified Debye equivalent circuit. Measurements were taken on three occasions and the error was recorded as a standard deviation.

Small-Angle X-ray Scattering (SAXS). Performed at beamLine station I-22, located at Diamond Light Source, Harwell, United Kingdom. Samples were mounted between two pieces of Kapton®. A monochromatic X-ray radiation (λ = 0.1 nm) and 2D SAXS detector (Pilatus P3-2M, DECTRIS Ltd.) were used for the experiments. 2D scattering patterns were reduced to 1D using Dawn software developed at the Diamond Light Source.[4]

Voltammetry. Linear sweep and cyclic voltammetry were conducted on a VMP2 (Bio-Logic). A 4 mm disc of ABA(50, 0.35) and a 3 mm lithium disc were sandwiched between two stainless steel discs. The cell was stabilised at the open circuit voltage (OCV) for 3 h at 60 °C, before cycling was performed at 0.5 mV s^{-1}. All procedures were carried out in an argon-filled glovebox.

Li-Ion Transference Number. All pulsed field gradient (PFG) nuclear magnetic resonance (NMR) measurements were completed at 9.45 T ($\upsilon_0(^{19}F)$ = 376.58, and $\upsilon_0(^{7}Li)$ = 155.53 MHz) on Bruker Avance III HD spectrometer, using a 5 mm single-axis diffusion probe with exchangeable ^{19}F and ^{7}Li ceramic heads. A stimulated echo pulse sequence was used, with an effective gradient pulse duration (δ) of between 1-3 ms, and a diffusion time (Δ) of 20-100 ms, with the gradient amplitude varying between 0.1 and 22 T/m. The experimental temperature was stabilised at 333.1 K, and a 5-second recycle delay was used throughout. All data is fitted to $f(x) = I_0 \times e^{-\gamma^2 g^2 \delta^2 \frac{(\Delta-\delta)}{3} D}$, where for ^{19}F; δ = 1-2 ms, Δ = 20-50 ms, and γ = 25172 rad/sG, and for ^{7}Li; δ = 1-3 ms, Δ = 20-100 ms, and γ = 10397 rad/sG. An R^2 of 0.999, errors of <1% (<1x10^{-14} m^2 s^{-1}) and normal distributions of the residuals were observed for all experiments.

Transference Number (Bruce-Vincent Method). Transference number measurements were performed on a VMP2 (Bio-Logic) connected to an oven operated at 60 °C. A 4 mm disc of ABA(50, 0.35) was sandwiched between two stainless steel discs. The cell was stabilised at the open circuit voltage (OCV) for 3 h at 60 °C. An impedance spectrum was recorded and the

cell was rested for 1 h before applying a voltage step of 50 mV and recording the current versus time. After 30 h, the impedance spectrum was measured again.

Polymer Electrolyte Processing. Polymer electrolyte films were processed into a powder using a Retsch CryoMill, cooled with liquid N_2. Small pieces of electrolyte film (1 – 3 mm diameter) were added to a 5 mL stainless steel jar, with 2 ball bearings of 7 mm diameter. The following cooling and milling procedure was conducted: 8 min pre-cooling at 5 Hz; 2 min milling step at 30 Hz; 0.5 min rest at 5 Hz; with 5 mill/rest cycles conducted. Once the procedure was complete, the jar was allowed to warm to ambient temperature yielding a white polymer electrolyte powder.

Composite Cathode Fabrication and Cell Assembly. Single crystal NMC811, Li_6PS_5Cl, polymer electrolyte, and carbon nanofiber (CNF, Merck) were mixed in a 70/23/5/2 wt% ratio by pestle and mortar. The resulting powder was pressed at 250 MPa with a layer of pure Li_6P_5SCl and a composite of $Li_4Ti_5O_{12}$ (LTO), Li_6PS_5Cl, and CNF in a glovebox filled with argon. The cells were assembled in a custom-designed module with a PEEK mould and two stainless steel plungers.

References

1. M. R. Kember, P. D. Knight, P. T. R. Reung and C. K. Williams, *J. Am. Chem. Soc.*, 2009, **48**, 931-933.
2. W. T. Diment, G. L. Gregory, R. W. F. Kerr, A. Phanopoulos, A. Buchard and C. K. Williams, *ACS Catal.*, 2021, **11**, 12532-12542.
3. A. Spyros, D. S. Argyropoulos and R. H. Marchessault, *Macromolecules*, 1997, **30**, 327-329.
4. J. Filik, A. W. Ashton, P. C. Y. Chang, P. A. Chater, S. J. Day, M. Drakopoulos, M. W. Gerring, M. L. Hart, O. V. Magdysyuk, S. Michalik, A. Smith, C. C. Tang, N. J. Terrill, M. T. Wharmby and H. Wilhelm, *J. Appl. Crystallogr.*, 2017, **50**, 959-966.

CHAPTER 7

Appendices

7.1. Chapter 2

Table 7.1.1. Thermal characterisation of P(vCHC-*b*-CL-*r*-TMC).

Entry [a]	T_g (°C) [b]	T_g (°C) [c]	$T_{d,5\%}$ (°C) [d]
AB(26, 0.45)	-49, 92	-52, 96	210
AB(32, 0.51)	-37, 88	-37, 84	226
AB(45, 0.47)	-54, 86	-19, 102	228
AB(69, 0.58)	-56, 113	-20, 94	231
ABA(35, 0.52)	-38, 89	-49, 101	204
ABA(44, 0.53)	-40, 102	-48, 102	235
ABA(50, 0.47)	-43, 84	-48, 100	242
ABA(66, 0.52)	-47, 98	-32, 100	231
ABA(51, 0.26)	-31, 81	-38, 98	233
ABA(47, 0.30)	-49, 95	-33, 66	240
ABA(50, 0.35)	-48, 89	-40, 100	241
ABA(50, 0.62)	-48, 94	-32, 85	230

[a] Polymers labelled as ABA/AB (M_n, w_{PC}) where M_n = overall molar mass in kg mol^{-1} and w_{PC} = weight fraction of PvCHC; [b] T_g of the polymer, estimated by DSC (10 °C min^{-1} heating rate), second heating curve; [c] T_g of the polymer electrolyte; [d] Thermal degradation temperature of the polymer electrolytes, determined by TGA. Recorded as the temperature at 5% mass loss.

Table 7.1.2. Summary of the SAXS data.

Sample [a]	*d* (nm) [b]	Observed *q*/q* [c]	Morphology [d]
ABA(35, 0.52)	44.4	1, 2, 3, 4	LAM
ABA(44, 0.53)	29.5	1	n.d.
ABA(50, 0.47)	27.3	1	n.d.
ABA(66, 0.52)	27.4	1	n.d.
ABA(51, 0.26)	12.6	1	n.d.
ABA(47, 0.30)	31.0	1, √3, (√4), √7	HEX
ABA(50, 0.35)	14.9	1, (√2), √3, (√4), (√5), (√6)	BCC/HEX
ABA(50, 0.47)	27.3	1	n.d.
ABA(50, 0.62)	32.5	1	n.d.

[a] Polymers labelled as ABA/AB (M_n, w_{PC}) where M_n = overall molar mass in kg mol^{-1} and w_{PC} = weight fraction of PvCHC. [b] Domain spacing d calculated from the principle scattering peak q*: d = 2π/q*. [c] Observed Bragg reflections, missing peaks in (). [d] Proposed phase morphology based on SAXS data. HEX = hexagonally packed spheres. BCC = body-centred cubic.

Table 7.1.3. Thermal and Ionic Conductivity Data for Poly(vCHC-*b*-CL-*r*-TMC) Electrolytes with 17 wt.% LiTFSI.

Entry [a]	$\sigma_{70\,°C}$ (S cm^{-1}) [b]	$\sigma_{30\,°C}$ (S cm^{-1}) [c]	E_a (kJ mol^{-1}) [d]	lnA [e]
AB(26, 0.45)	2.0×10^{-5}	1.5×10^{-6}	15.4	4.0
AB(32, 0.51)	1.9×10^{-5}	8.4×10^{-7}	23.6	12.5
AB(45, 0.47)	9.0×10^{-6}	2.0×10^{-7}	9.1	3.8
AB(69, 0.58)	7.0×10^{-7}	2.1×10^{-8}	8.8	0.9
ABA(35, 0.52)	1.6×10^{-5} *	6.6×10^{-7}	15.3	5.6
ABA(44, 0.53)	1.2×10^{-5}	9.8×10^{-7}	8.7	2.9
ABA(50, 0.47)	2.8×10^{-5}	2.6×10^{-6}	13.0	0.0
ABA(66, 0.52)	5.6×10^{-5} *	5.5×10^{-6}	12.8	6.3
ABA(51, 0.26)	4.4×10^{-5}	1.2×10^{-6}	16.0	7.3
ABA(47, 0.30)	2.6×10^{-5}	4.3×10^{-6}	11.2	2.5
ABA(50, 0.35)	2.2×10^{-4} *	5.9×10^{-6}	17.0	8.3
ABA(50, 0.47)	2.8×10^{-5}	2.6×10^{-6}	13.0	0.0
ABA(50, 0.62)	3.7×10^{-6}	1.8×10^{-7}	14.6	1.7

[a] Polymers labelled as ABA/AB (M_n, w_{PC}) where M_n = overall molar mass in kg mol^{-1} and w_{PC} = weight fraction of PvCHC; [b] Ionic conductivity at 70 °C, except for *, measured at 60 °C. Measured using impedance spectroscopy, values have a 9% error. The ionic conductivity was calculated from the resistance that was obtained by fitting the acquired data to a modified Debye circuit; [c] Li-ion

conductivity at 30 °C, values have an 11% error; [d] Activation energy of Li-ion transfer, obtained from the VFT fit; [e] Relative free charge carrier concentration of the polymer electrolyte, obtained from the VFT fit.

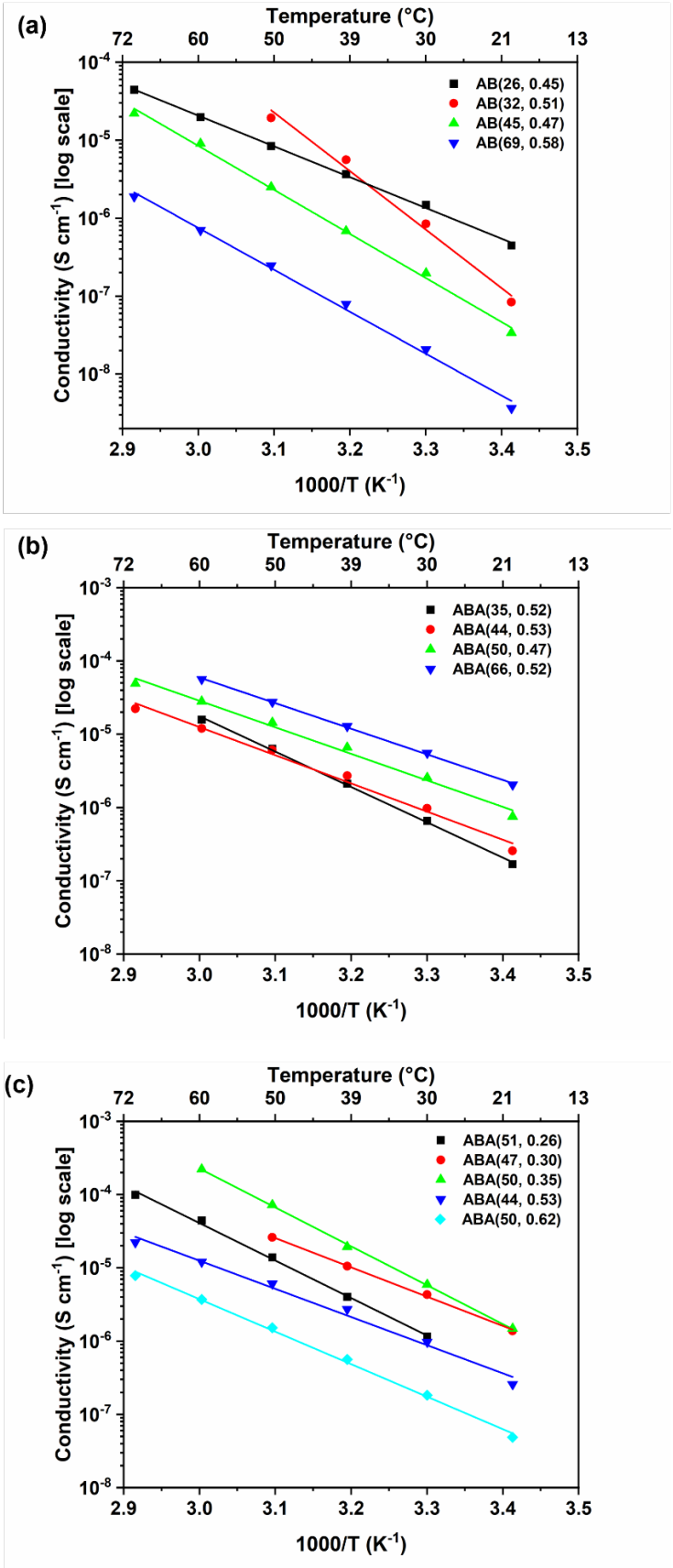


Figure 7.1.1. Li-ion conductivity as a function of temperature for (a) Series I, AB(M_n, 0.5), (b) Series II, ABA(M_n, 0.5), and (c) Series III, ABA(50, w_{PC}), all with 17 wt% LiTFSI.

Table 7.1.2. Pulsed-Field Gradient NMR Data for ABA(50, 0.35) Electrolyte.

Nucleus	Chemical Shift (ppm)	Assignment	D (m^2 s^{-1}) [a]	t_{Li+} [b]
^{7}Li	0.85	P(CL-*r*-TMC)	5.7×10^{-13}	0.44
^{7}Li	2.73	PvCHC	4.6×10^{-13}	0.52
^{19}F	-78.8	P(CL-*r*-TMC)	7.4×10^{-13}	0.44
^{19}F	-77.0	PvCHC	4.2×10^{-13}	0.52

[a] Diffusion coefficient; [b] Li-ion transference number.

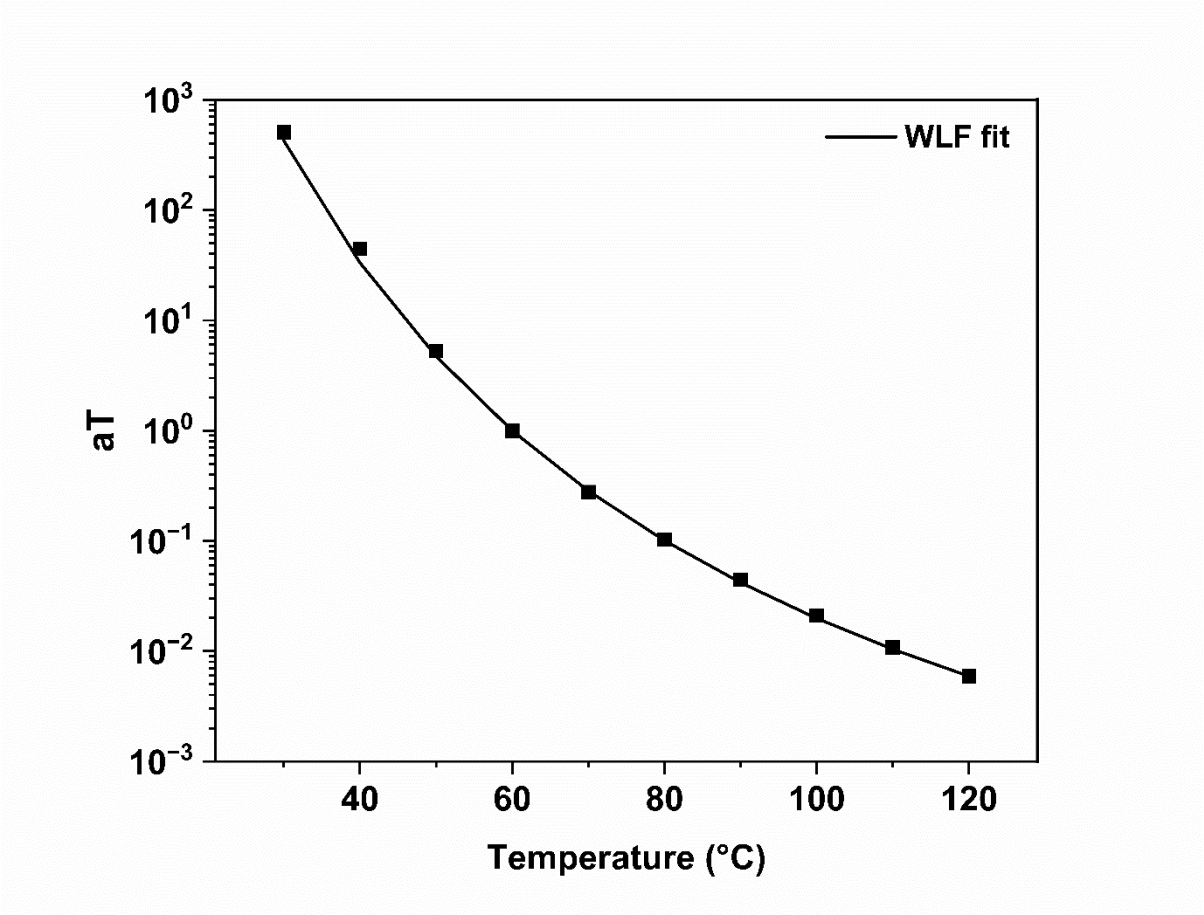


Figure 7.1.2. The shift factors (aT) versus temperature (data points), fitted to the WLF equation (line): $log(aT) = \frac{-c_1(T-T_r)}{c_2(T-T_r)}$, where $c_1 = 5.799$, $c_2 = 96.2$ K. and $T_r = 60$. Shift factors were applied to dynamic frequency sweep data obtained at different temperatures to produce a master curve of modulus vs frequency (Figure 2.27) for ABA(50, 0.35)/17 wt.% LiTFSI.

7.2. Chapter 3

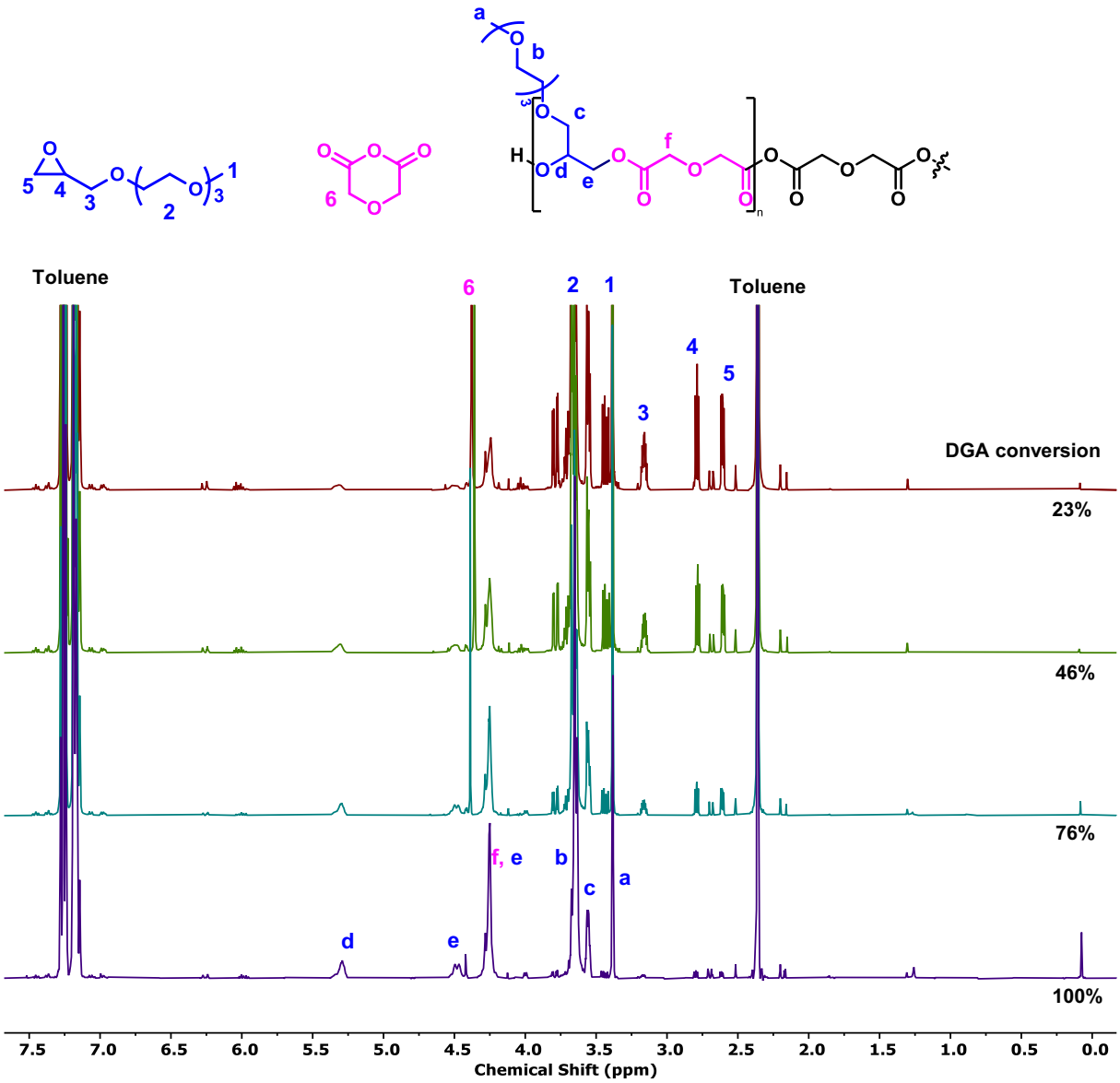


Figure 7.2.1. ^{1}H NMR spectra ($CDCl_3$, 500 MHz) from aliquots from DGA/ME_3MO ROCOP at 23%, 46%, 76% and 100% DGA consumption, depicting the consumption of DGA and ME_3MO monomer and formation of poly(DGA-*alt*-ME_3MO).

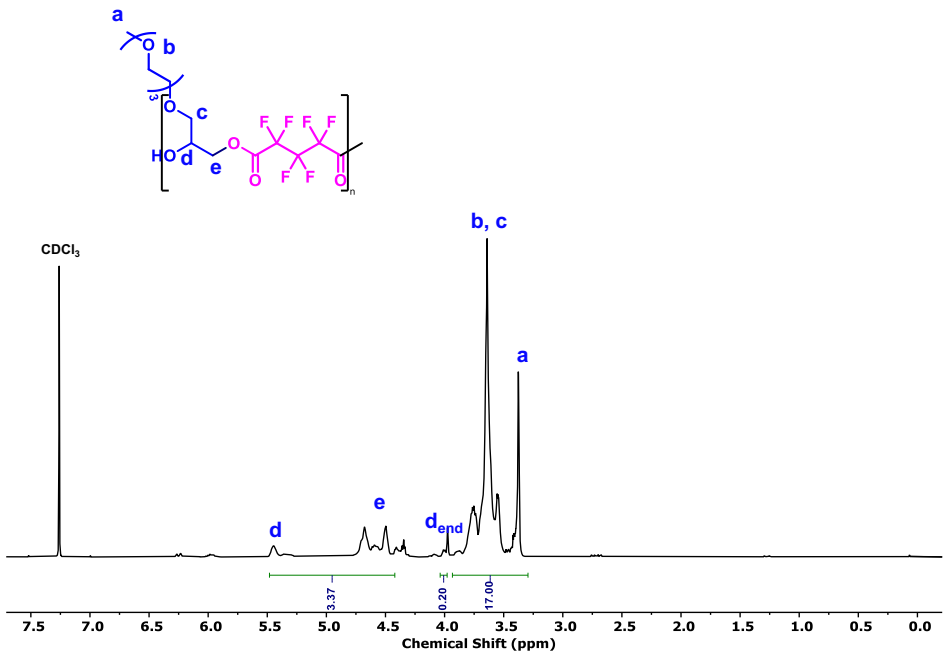


Figure 7.2.2. Assigned ^{1}H NMR spectrum ($CDCl_3$, 500 MHz) of the purified polymer, poly(HFA-*alt*-ME_3MO).

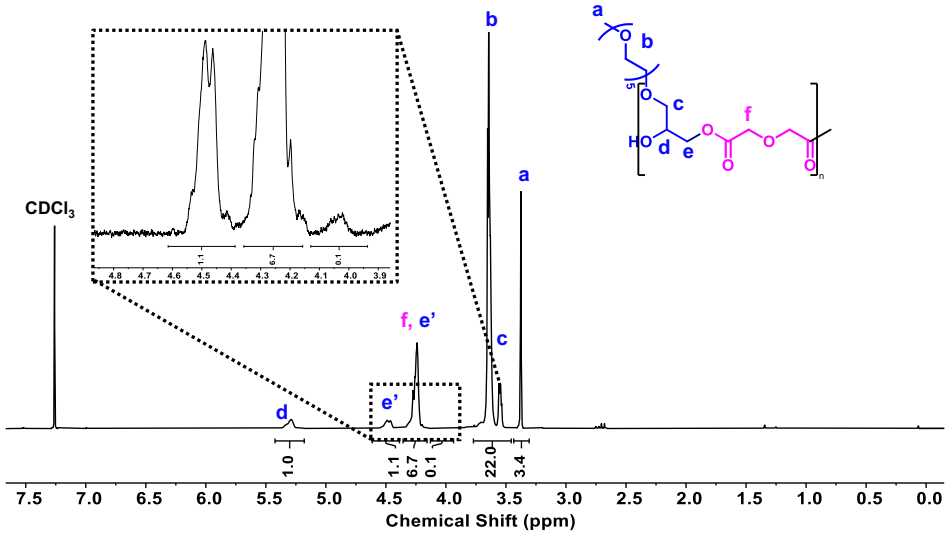


Figure 7.2.3. Assigned ^{1}H NMR spectrum ($CDCl_3$, 500 MHz) of the purified polymer, poly(DGA-*alt*-MGE-$(PEG)_5$).

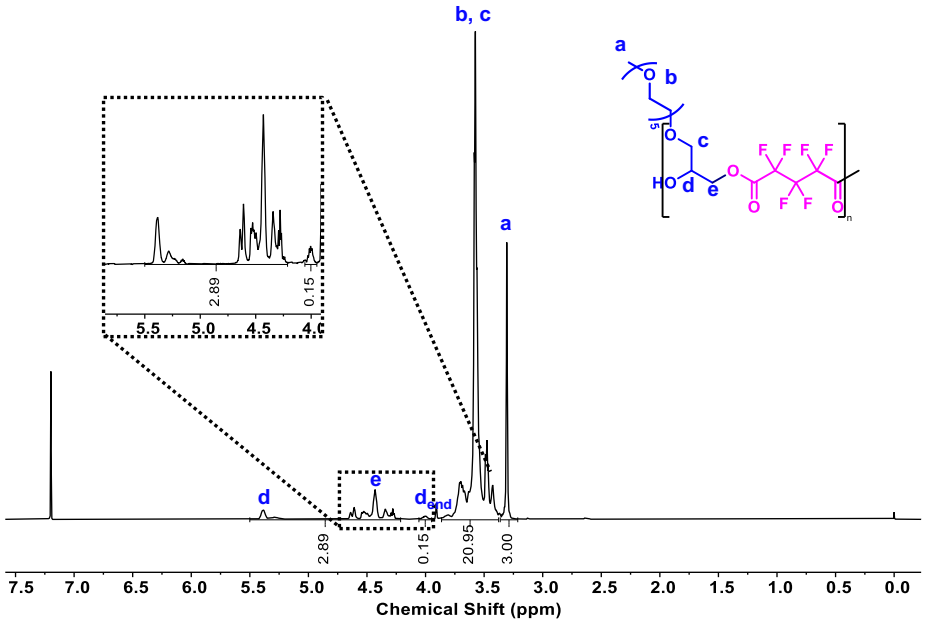


Figure 7.2.4. Assigned ^{1}H NMR spectrum ($CDCl_3$, 500 MHz) of the purified polymer, poly(HFA-*alt*-MGE-$(PEG)_5$).

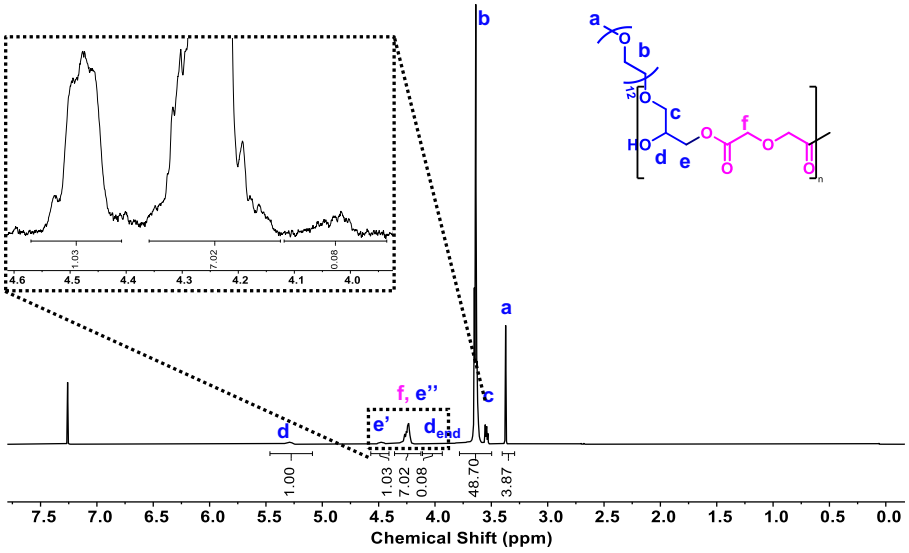


Figure 7.2.5. Assigned ^{1}H NMR spectrum ($CDCl_3$, 500 MHz) of the purified polymer, poly(DGA-*alt*-MGE-$(PEG)_{12}$).

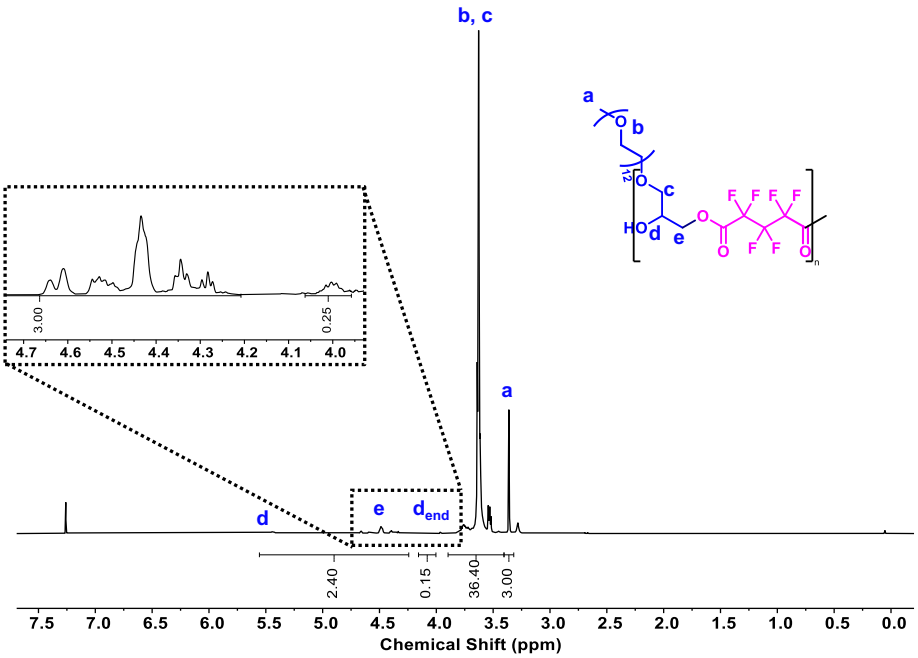


Figure 7.2.6. Assigned ^{1}H NMR spectrum ($CDCl_3$, 500 MHz) of the purified polymer, poly(HFA-*alt*-MGE-$(PEG)_{12}$).

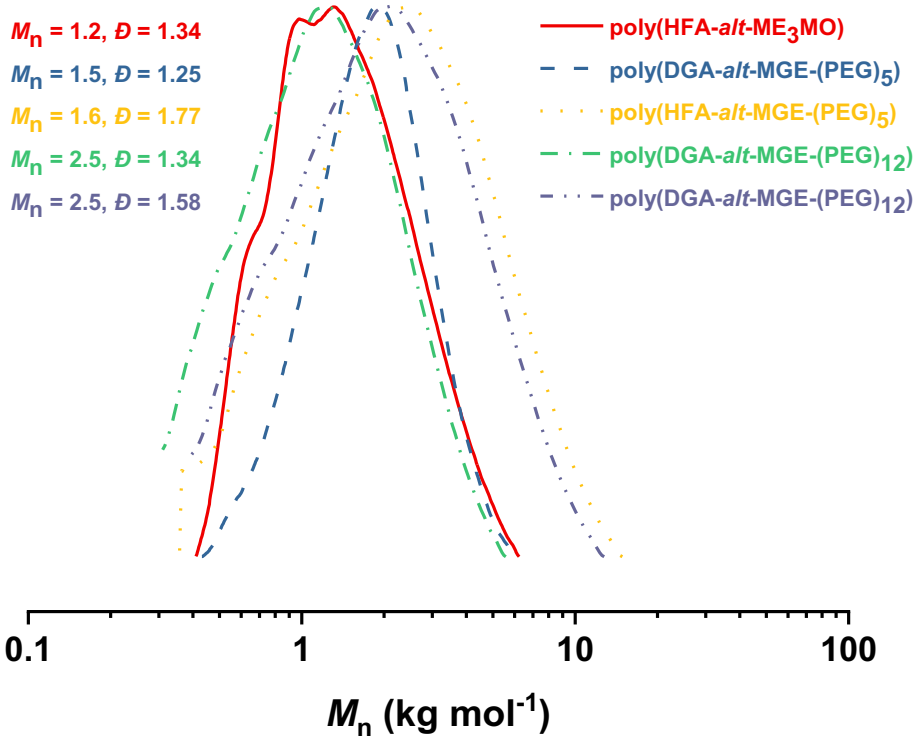


Figure 7.2.7. SEC traces for the purified polymer polyesters, measured in THF with an RI detector vs. narrow PS standards.

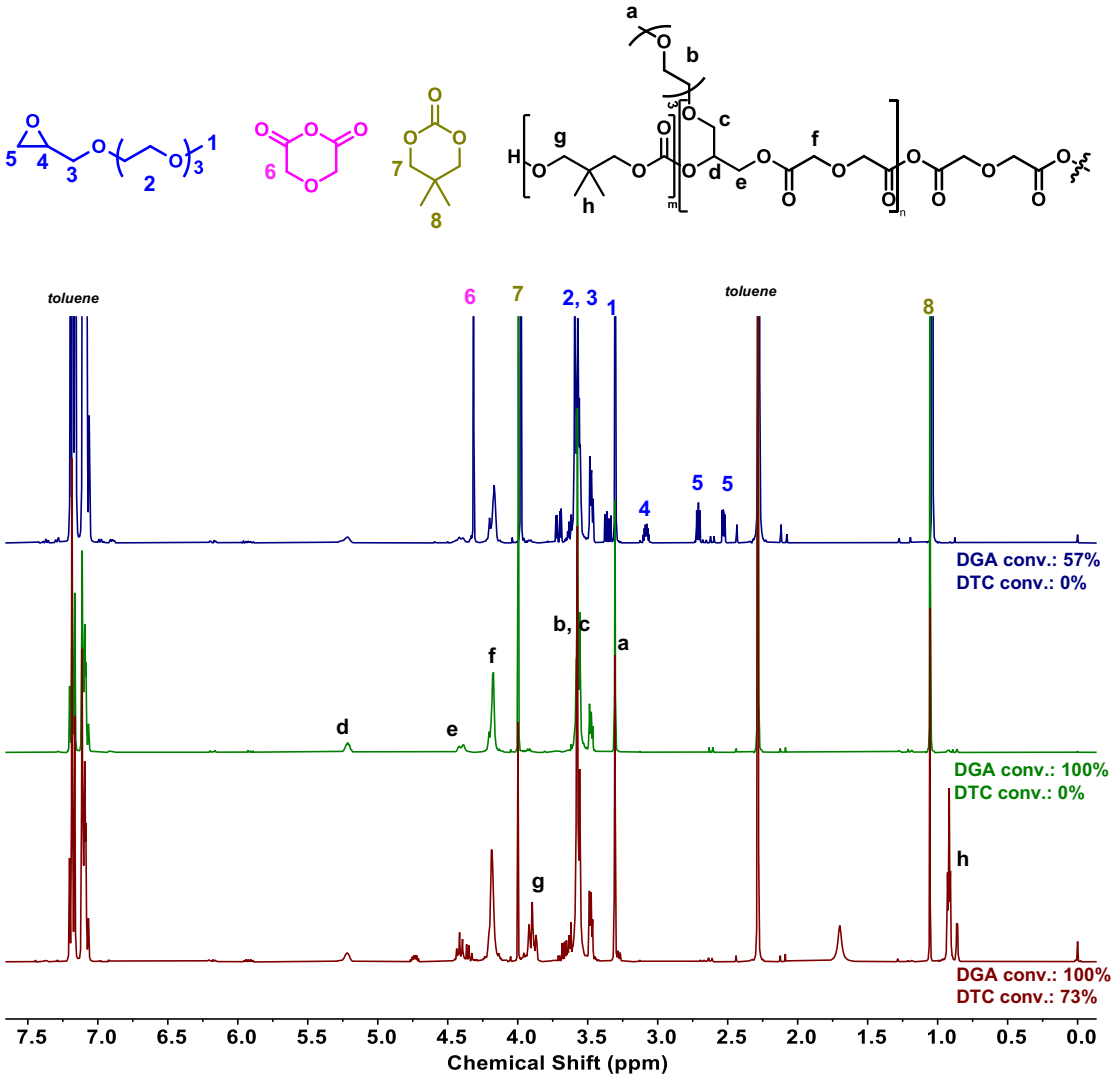


Figure 7.2.8. ^{1}H NMR spectra ($CDCl_3$, 500 MHz) of DGA/ME_3MO/DTC ROCOP at 57% DGA, 0% DTC; 100% DGA, 0% DTC; and 100% DGA, 73% DTC conversion, depicting the consumption of DGA, ME_3MO and DTC monomer and formation of poly(DTC-*b*-DGA-*alt*-ME_3MO-*b*-DTC).

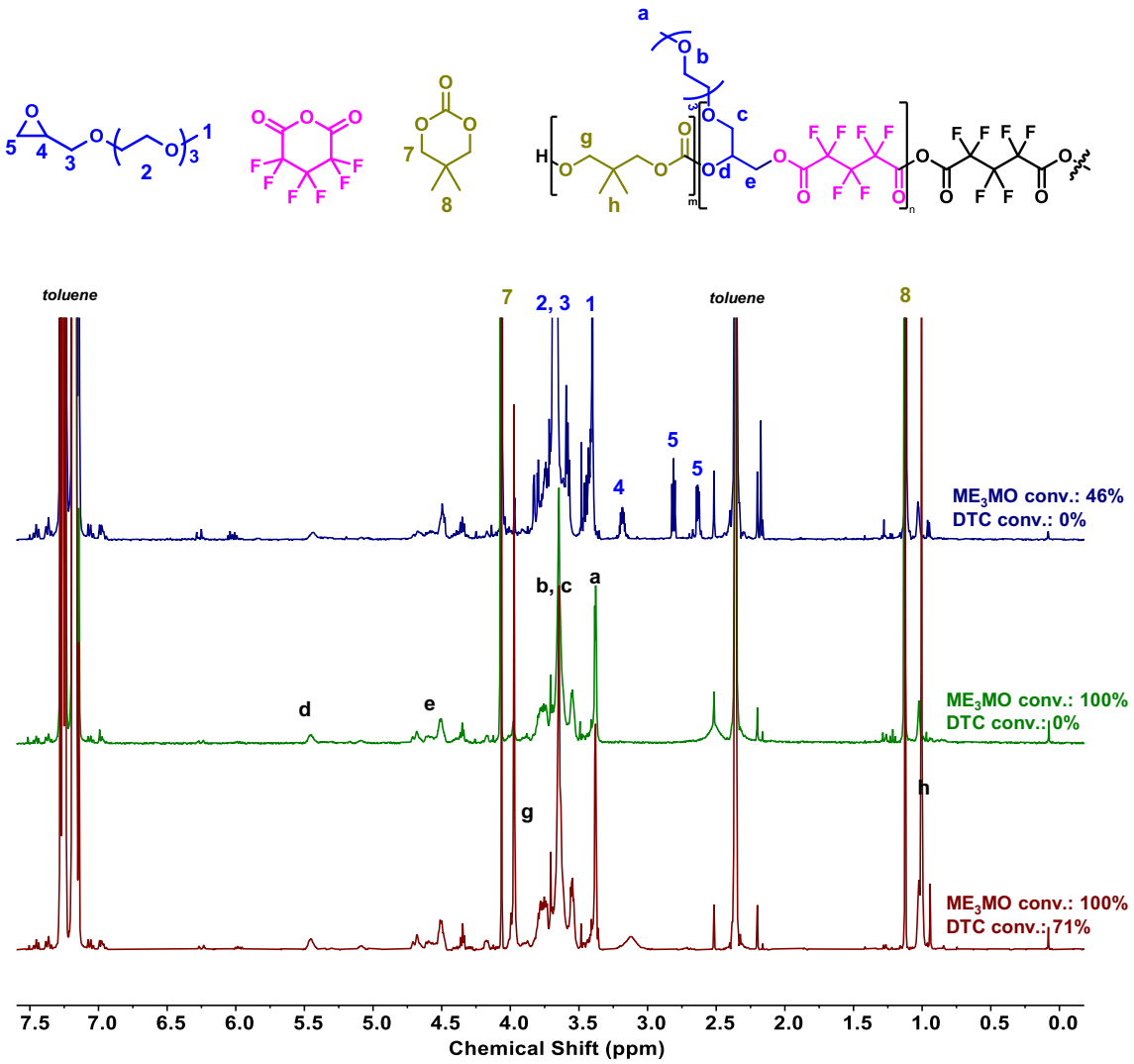


Figure 7.2.9. ^{1}H NMR spectra ($CDCl_3$, 500 MHz) of HFA/ME_3MO/DTC ROCOP at 46% ME_3MO, 0% DTC; 100% ME_3MO, 0% DTC; and 100% ME_3MO, 71% DTC conversion, depicting the consumption of ME_3MO and DTC monomer and formation of poly(DTC-*b*-HFA-*alt*-ME_3MO-*b*-DTC).

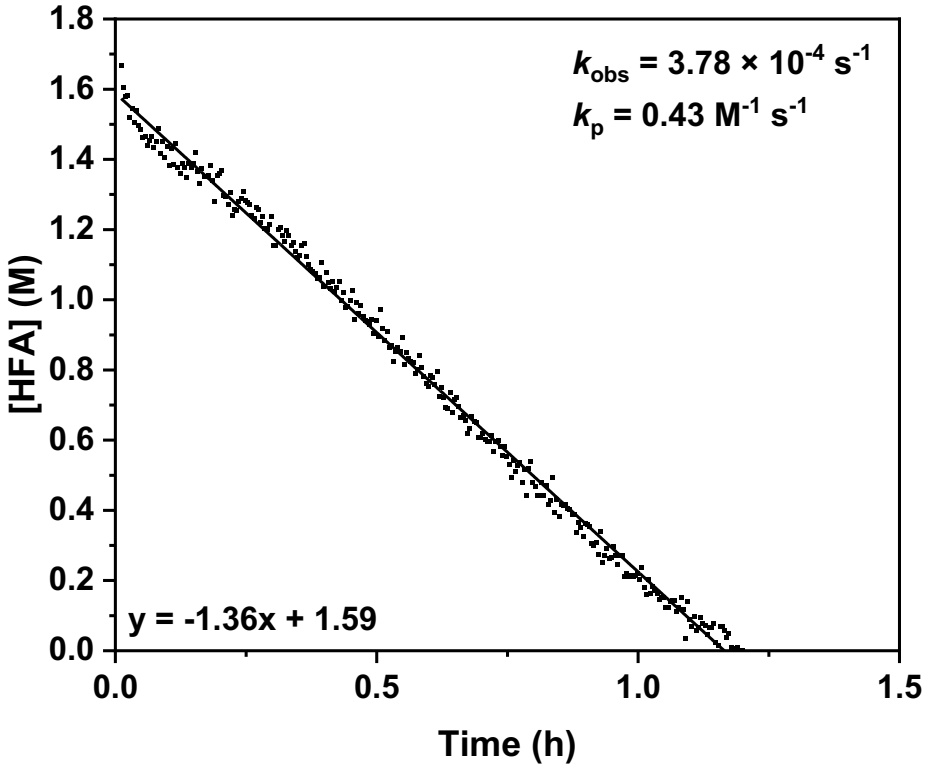


Figure 7.2.10. [HFA] vs time for HFA/ME_3MO ROCOP during HFA/ME_3MO/DTC switchable polymerization catalysis. Linear fit applied (R^2 = 0.996), to find k_{obs} ($[HFA]_t = -k_{obs}t + [HFA]_0$).

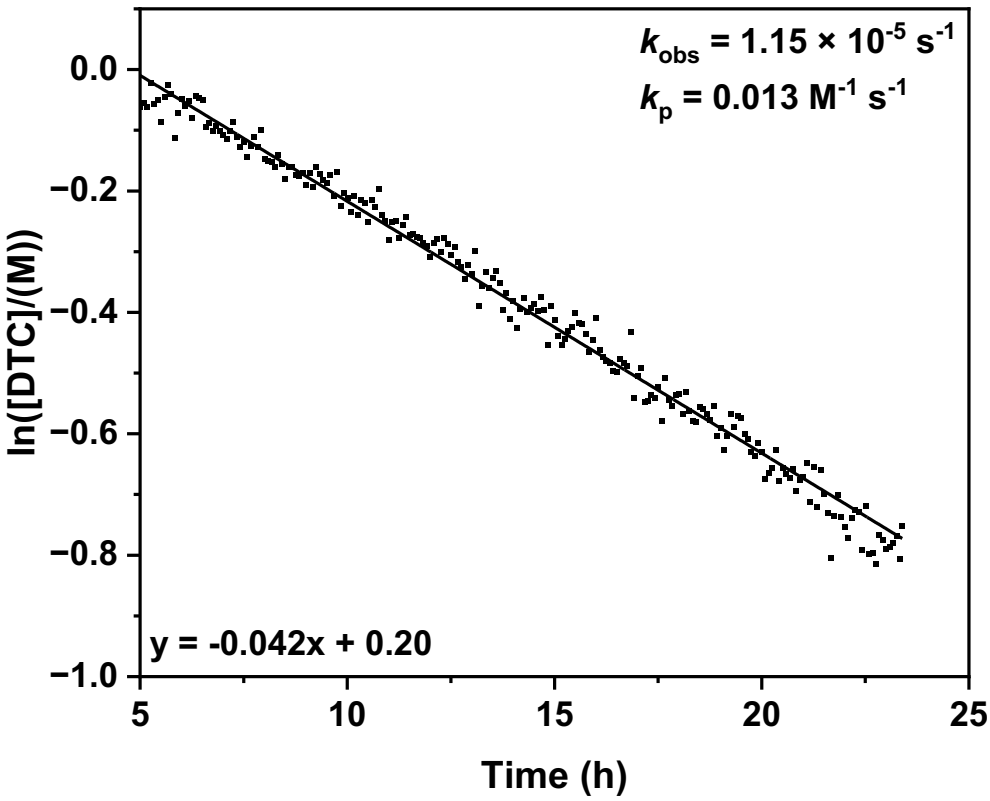


Figure 7.2.11. ln([DTC]) vs time for DTC ROP during HFA/ME_3MO/DTC switchable polymerization catalysis. Linear fit applied, R^2 = 0.989, to find k_{obs} ($\ln[DTC]_t = -k_{obs}t + [DTC]_0$).

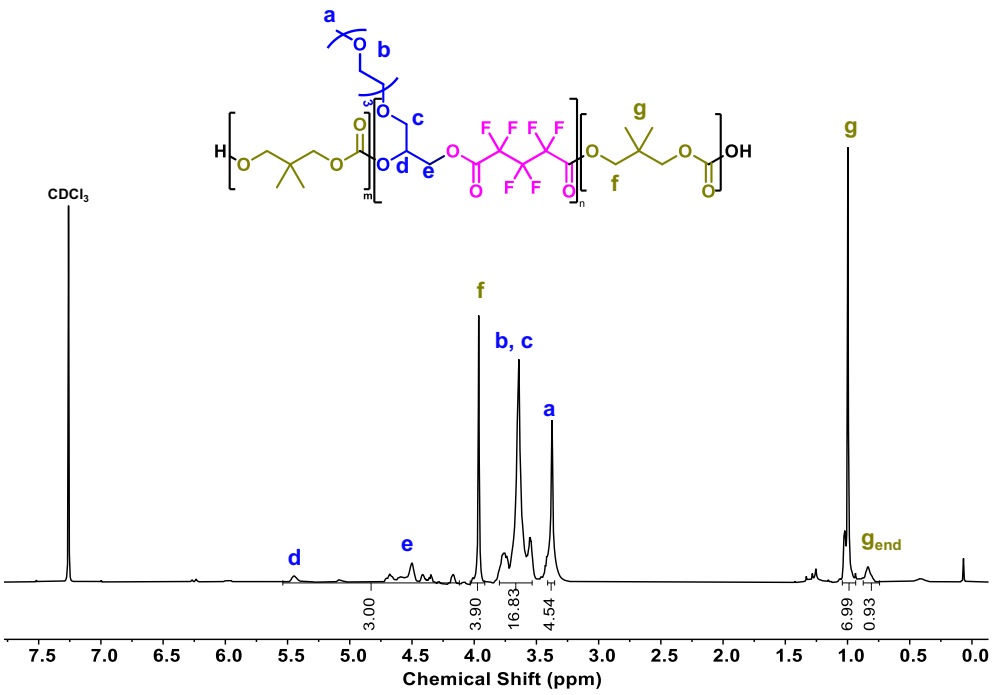


Figure 7.2.12. Assigned ^{1}H NMR spectrum ($CDCl_3$, 500 MHz) of the purified polymer, poly(DTC-*b*-HFA-*alt*-ME_3MO-*b*-DTC).

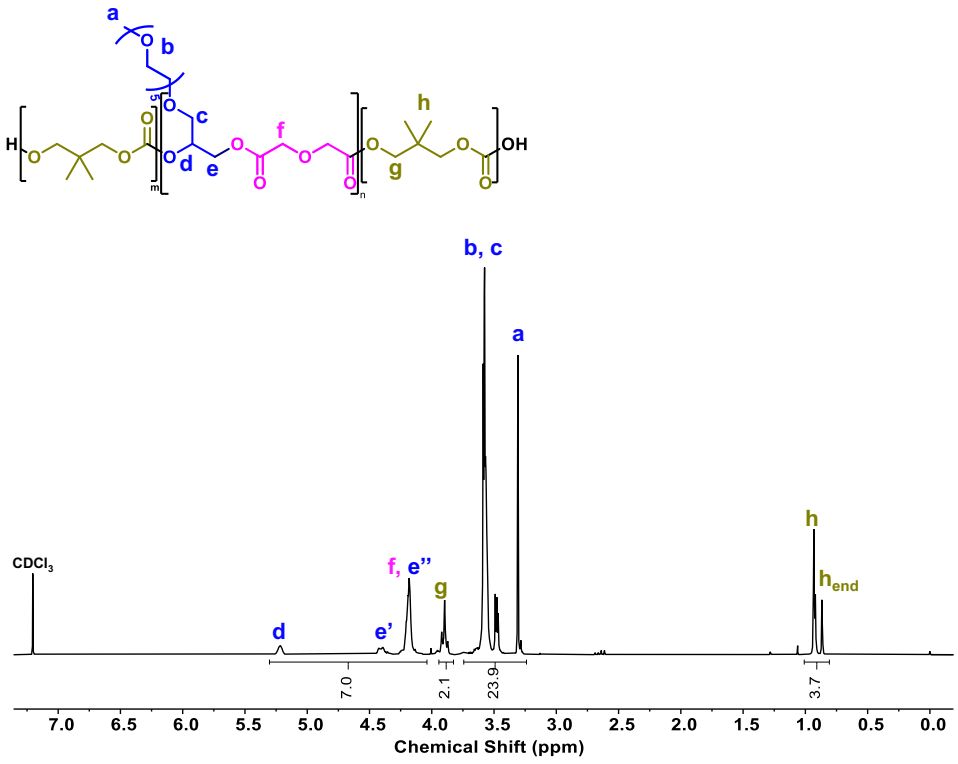


Figure 7.2.13. Assigned ^{1}H NMR spectrum ($CDCl_3$, 500 MHz) of the purified polymer, poly(DTC-*b*-DGA-*alt*-MGE-$(PEG)_5$-*b*-DTC).

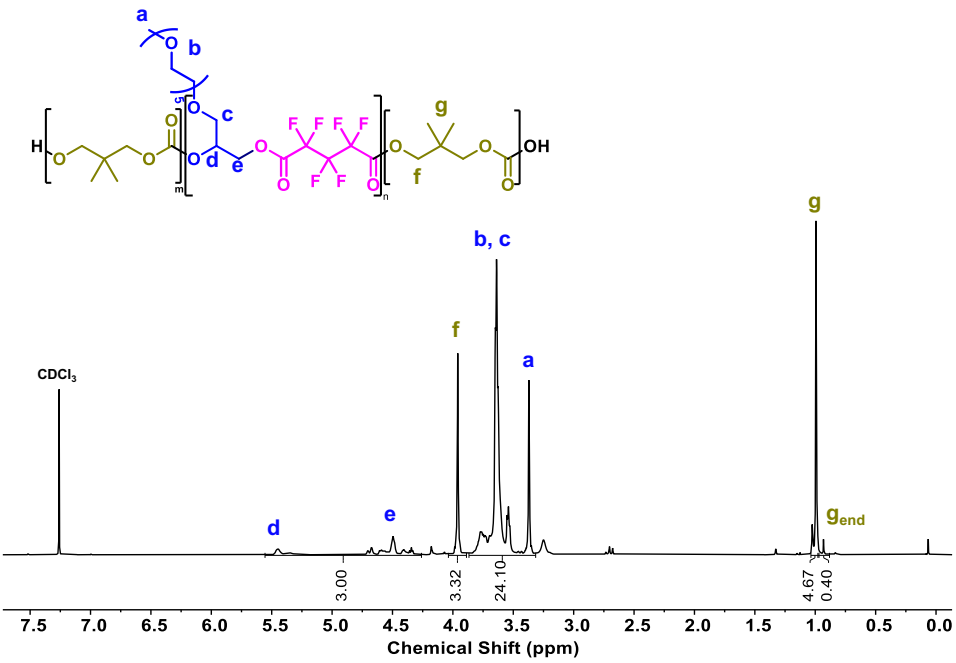


Figure 7.2.14. Assigned ^{1}H NMR spectrum ($CDCl_3$, 500 MHz) of the purified polymer, poly(DTC-*b*-HFA-*alt*-MGE-$(PEG)_5$-*b*-DTC).

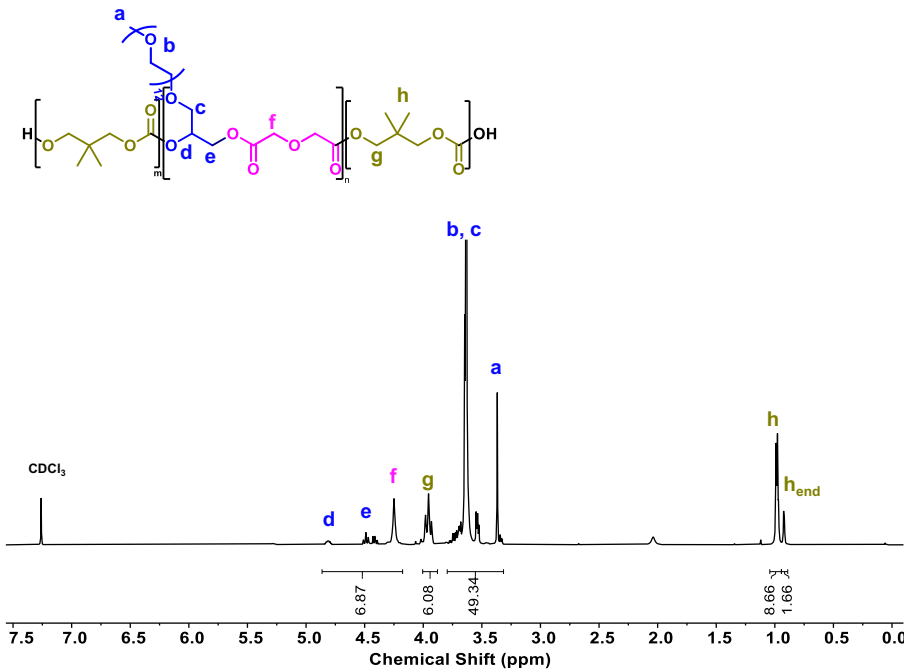


Figure 7.2.15. Assigned ^{1}H NMR spectrum ($CDCl_3$, 500 MHz) of the purified polymer, poly(DTC-*b*-DGA-*alt*-MGE-$(PEG)_{12}$-*b*-DTC).

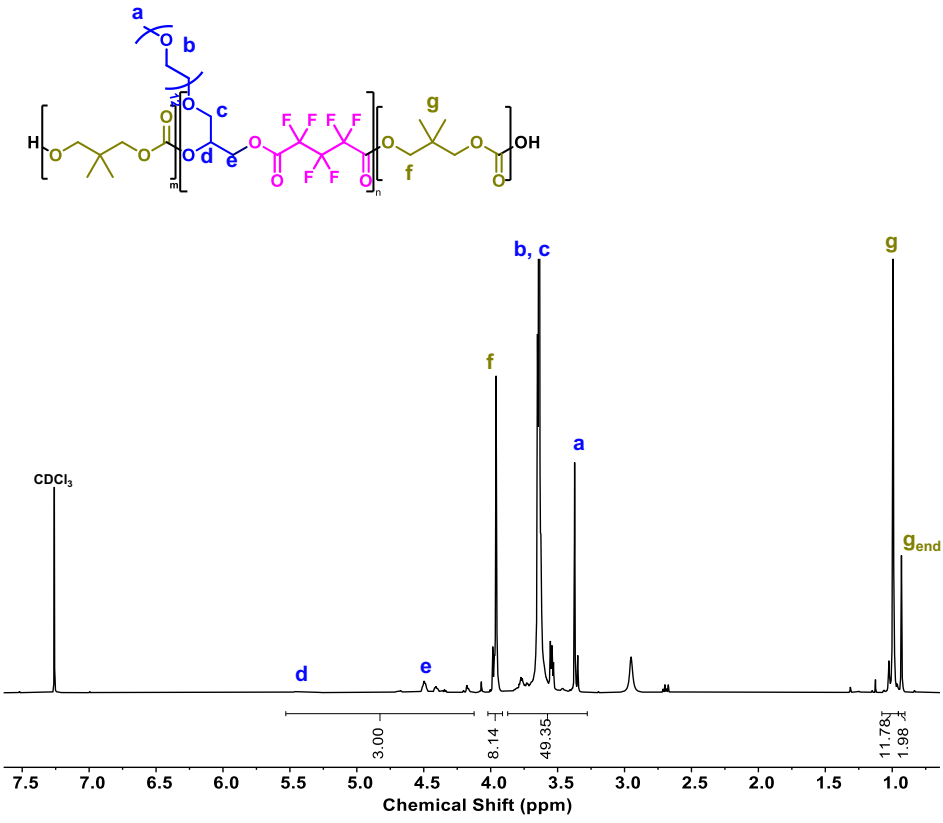


Figure 7.2.16. Assigned ^{1}H NMR spectrum ($CDCl_3$, 500 MHz) of the purified polymer, poly(DTC-*b*-HFA-*alt*-MGE-$(PEG)_{12}$-*b*-DTC).

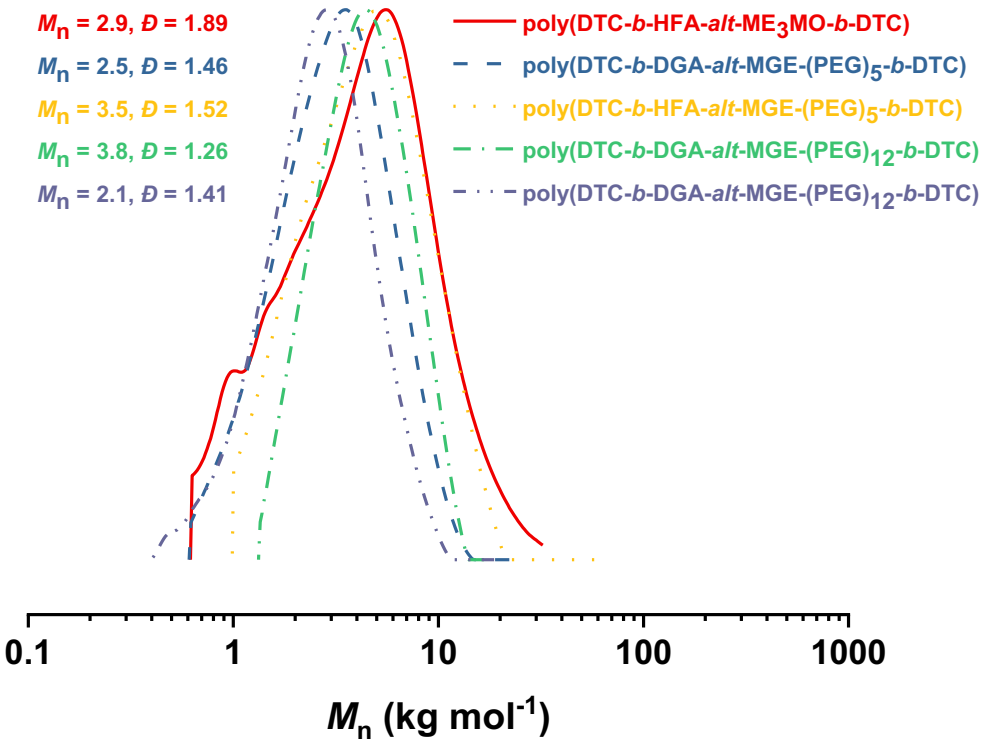


Figure 7.2.17. SEC traces for the purified block copolymers, measured in THF with an RI detector vs. narrow PS standards.

7.3. Chapter 4

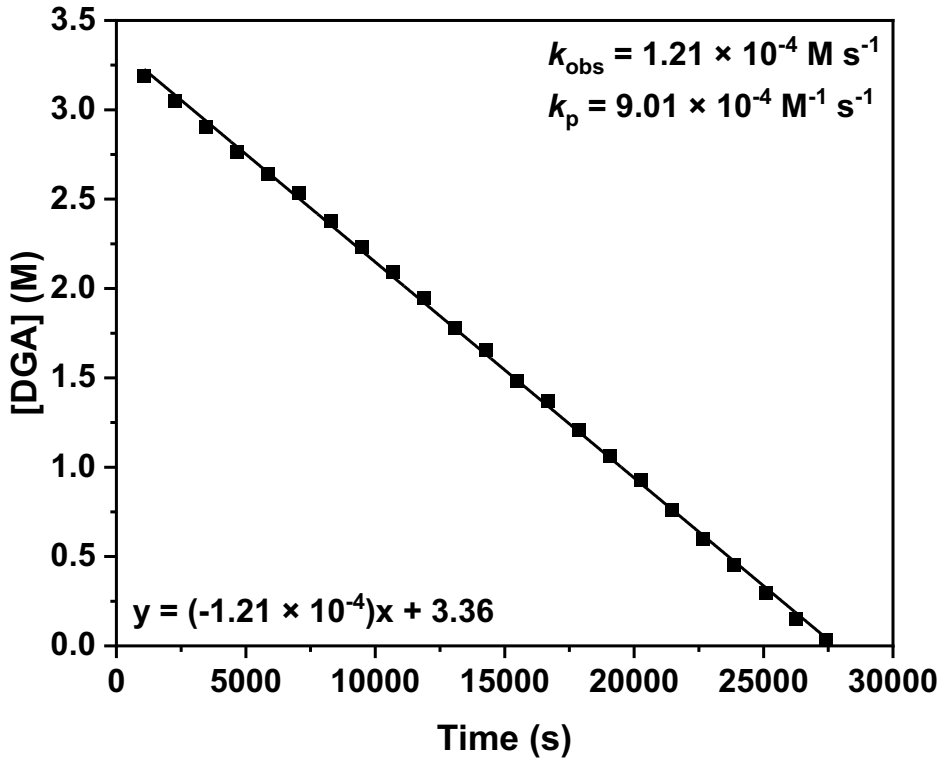


Figure 7.3.1. [DGA] vs time for DGA/AGE ROCOP during DGA/AGE/DTC switchable polymerization catalysis. Linear fit applied (R^2 = 0.999), to find k_{obs} ($[DGA]_t = -k_{obs}t + [DGA]_0$).

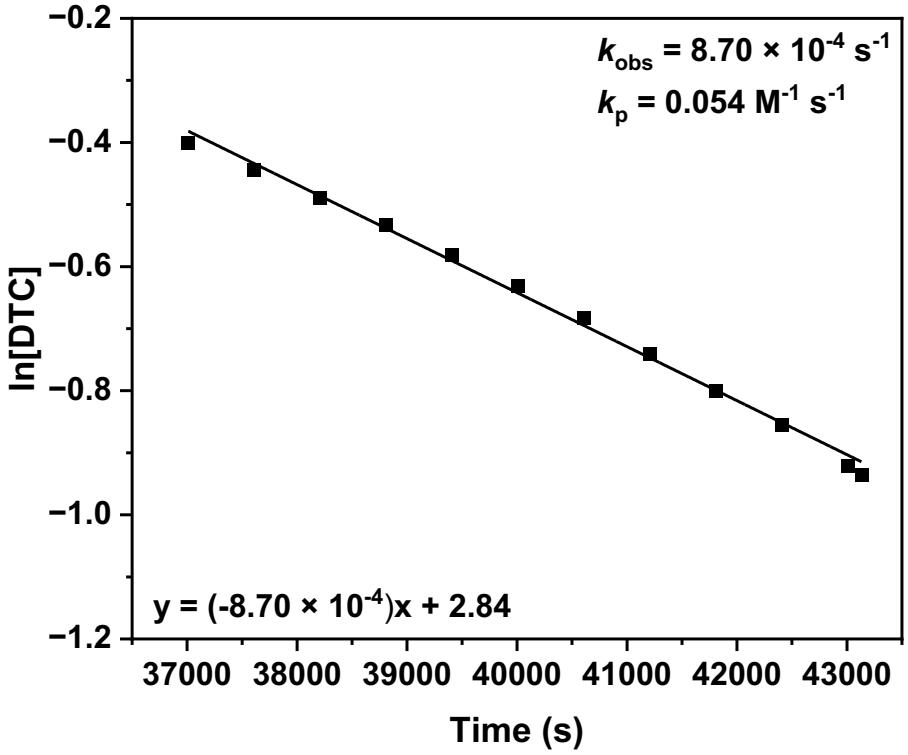


Figure 7.3.2. ln([DTC]) vs time for DTC ROP during DGA/AGE/DTC switchable polymerization catalysis. Linear fit applied, $R^2 = 0.996$, to find k_{obs} ($\ln[DTC]_t = -k_{obs}t + [DTC]_0$).